UNIVERSITAT POLITÈCNICA DE CATALUNYA
Departament d'Enginyeria de la Construcció

A non-linear coupled model for the analysis of reinforced concrete sections under bending, shear torsion and axial forces

Doctoral Thesis by:

Jesús Miguel Bairán García

Supervisor:
Prof. Antonio Marí Bernat

Barcelona, October 2005

Doctoral Thesis:

“ A non-linear coupled model for the analysis of reinforced concrete sections under bending, shear, torsion and axial forces”

Author:
Jesús Miguel Bairán García

Supervisor:
Prof. Antonio Marí Bernat

Barcelona, October 2005

Universitat Politècnica de Catalunya
School of Civil Engineering
Department of Construction Engineering
Doctoral Program in Construction Engineering

A non-linear coupled model for the analysis of reinforced concrete sections under bending, shear, torsion and axial forces

Thesis submitted for the degree of
Doctor Engineer

by: Jesús Miguel Bairán García
Civil Engineer
M.Sc. Structual and Mechanical Eng.
Dipl. of Advanced Studies in Construction Eng.

Supervisor: Prof. Antonio Marí Bernat
Doctor Civil Engineer

Acknowledgements

This thesis would not have been possible without the constant support of my parents Consuelo and Omar, my brothers Carlos and Omar and, of course, with the support and encouragement of my beloved wife Rosangel. To them I want to express all my love and my gratitute since all I am is because of them.

I would like to express my sincere gratitude to my supervisor Prof. Antonio Marí for proposing me the subject of this research, for his numerous good advices and suggestions and specially for being an excellent mentor and friend from whom I have learned a lot. I also thank Prof. Marí for allowing me to collaborate in numerous researches carried out in the Department of Construction Engineering which were important parts of my research education.

I thank Prof. Paolo E. Pinto, from the University of Rome-"*La Sapienza*", who accepted me as a visiting Ph.D. student at the Department of Structural and Geotechnical Engineering. Particularly, I am very grateful to Prof. Pinto, Dr. Paolo Franchin and Dr. Alessio Lupoi for the many fruitful advices and suggestions, all the knowledge I received from them and for being excellent and kind persons.

I want to acknowlege Prof. Ferdinando Auricchio, from the University of Pavia and ROSE School, who was kindly available for discussions and adviced me with the formal presentation of the model, for the many consulting hours while I was in Pavia and by e-mails back in Barcelona. I also want to thank professors Rui Pinho and Gian Michele Calvi for accepting me at

ROSE School.

During my stay in Barcelona, many persons have contributed in a direct or indirect manner through many interesting conversations and suggestions. Particularly I would like to acknowledge Vicente Alegre, Prof. Enrique Mirambell, Prof. Francisco Lopez-Almansa and Dr. Diego Cobo. My gratitude is also extended to all the professors and staff of the Department of Construction Engineering.

A very special mention must be done to all my colleagues with whom I shared a wonderful time during the realization of this Ph.D., an unselfish friendship and help. Specially to Mariela Cordero, Manuel Jara, Jesús Alvarez, Felipe Mora, José Luis Rangel, Tulio de la Cruz, Ulises Mena, Selma Chan, Rodrigo Franklin, Francisco Alonso and Alvaro Viviescas. I extent this acknowledgement to my fellow companions while I was a visiting student at Rome, Marko Schotanus and Giorgo Lupoi.

I am very grateful to Prof. Juan José Arenas from the University of Cantabria who was my master thesis supervisor and encouraged me to do a Ph.D.

I want to thank professors Juan Miguel Canet and Ramón Codina who received me when I arrived to the UPC and adviced me during my first months at this school.

Finally, I thank God for giving me health and allowing me to carry out this thesis.

This thesis was carried out with the support of the "Departament d'Universitats, Recerca i Societat de la Informació" of the Catalan Government through the 2002 FI-00502 fellowship and the Spanish Ministry of Education through the R+D Project MAT2002-00615.

I want to express my gratitude to FI fellowship of the "Departament d'Universitats, Recerca i Societat de la Informació" that allowed me to carry out this doctoral thesis and the stay at the University of Rome. I also thank the Marie Curie Fellowships Association for the financial support to do a stay at ROSE School.

Summary

Most RC structures are subjected to combined normal and tangential forces, such as bending, axial load, shear and torsion. Concrete cracking, steel yielding and other material nonlinearities produce an anisotropic sectional response that results in a coupling between the effects of normal and shear forces, i.e. normal force or bending moments may produce shear strains and vice versa. Although this interaction is sometimes taken into account, in a simplified manner, in the design of RC structures, a deep analysis of the coupling effects of RC sections using fiber models has not yet been made for arbitrary shape sections under general 3D loading.

The main objective of this thesis is to generalize the fiber-like sectional analysis of reinforced concrete elements, to make it capable of considering the coupled non-linear response under tangential and normal internal forces, from a general 3D loading. Similarly, it is desired to obtain, for torque and shear forces, the same capacity and versatility in reproducing complex geometry and materials combination that fiber-like sectional representations offers for bending and stretching.

The first problematic lies in finding a proper representation of the section's kinematics under such general loading. Except for in-plane normal strains, there is no single kinematical theory capable of a-priori representing the correct distribution of the others strains or stresses satisfying, at the same time, inter-fiber equilibrium and continuity. On the other hand, for rather anisotropic materials, such as cracked concrete, all internal forces are, in general, coupled. It is also required that distortion is allowed for the section's kinematics in order to guarantee satisfaction of internal equilibrium.

The problem is dealt in a general form considering arbitrary shaped sections and any material behaviour. Starting from the differential equilibrium of a solid, an inter-fiber equilibrium system (equilibrium at the sectional level) was deduced. This system, which is complementary to the standard equilibrium problem of a beam-column, allows to recuperate information of the three-dimensional problem that is generally lost when solving a beam problem.

Further, a solution of the equilibrium at the sectional level is proposed in which the section's warping and distortion are posed as a function of the generalized beam-column strains (axial and shear strains, bending and torsion curvatures). No additional degrees of freedom are required at the structural level nor a-priori hypotheses on the distribution of the internal strains or stresses.

After the theoretical formulation, a planar finite element model for cross-sectional analysis is developed. The model can be used as a constitutive law for general beam-column elements at their integration points.

A series of constitutive models have been implemented for several materials. In particular, a triaxial constitutive model for cracked concrete is implemented considering crack-induced anisotropy and a multiaxial failure criterion.

The sectional formulation is validated by means of various theoretical and experimental case studies. Non-linear coupled response under normal and tangential internal forces is reproduced with accuracy, as can be seen both in the predicted internal force-strain curves and in the sectional stiffness matrixes.

Finally, the conclusions drawn from the current research are summarized and recomendations for future works are given.

Resumen

La mayoria de las estructuras de hormigón armado se someten a solicitaciones combinadas de esfuerzos axiles, flexión, cortante y torsión. La fisuración del hormigón, plastificación de las armaduras y otros efectos no-lineales hacen que las secciones transversales de estos elementos presenten un comportamiento anisótropo que deriva en el acoplamiento de los esfuerzos normales y tangenciales. Es decir, esfuerzos normales o momentos flectores pueden producir deformaciones de corte y vice versa. Aunque en algunas ocaciones, esta interacción es considerada de forma simplificada en el dimensionamiento de estructuras, hasta el momento no se ha realizado un análisis profundo de los efectos acoplados en secciones de forma arbitraria bajo cargas 3D generales utilizando modelos de fibras.

El objetivo principal de esta tesis es generalizar el análisis de secciones de hormigón armado mediante fibras, de forma que se pueda reproducir la respuesta no-lineal acoplada frente a esfuerzos normales y tangenciales bajo solicitaciones tridimensionales generales. De igual forma, se pretende obtener, para los esfuerzos cortante y torsión, la misma capacidad de representación de geometrías y combinación de materiales que ofrecen los modelos de fibras para esfuerzos de flexo-compresión.

La primera problemática estriba en representar adecuadamente la cinemática de la sección transversal. Con la excepción de las deformaciones normales contenidas en el plano de la sección, no existe una teoría cinemática que a priori pueda dar la distribución del resto de deformaciones o tensiones en la sección, sin dejar de satisfacer las condiciones de equilibrio interno o continuidad entre las fibras que componen la misma. Por otra parte, para

materiales anisótropos, como el hormigón fisurado, en general todos los esfuerzos internos pueden estar acoplados. Además, es preciso considerar la distorsión de la sección transversal para satisfacer el equilibrio entre fibras.

El problema se aborda de forma general, considerando una sección de forma y materiales cualesquiera. Se parte del problema diferencial de equilibrio de un sólido con el que se ha podido deducir un sistema de equilibrio entre fibras (equilibrio a nivel sección). Se puede demostrar que éste es complementario al problema estándar de vigas. El sistema complementario permite recuperar información tridimensional que normalmente se pierde al resolver un problema de vigas.

Posteriormente, se propone una solución interna del problema complementario, en la que el alabeo y la distorsión de la sección quedan expresados como una función de las deformaciones generalizadas de una viga: deformaciones axil y cortantes, curvaturas de flexión y torsión. No son necesarios grados de libertad adicionales a nivel estructura ni hipótesis a-priori sobre la forma de los campos de deformación o tensión interna.

A partir de la formulación teórica, se desarrolla un modelo de elementos finitos plano de la sección transversal. El modelo está preparado para servir como respuesta constitutiva de cualquier tipo de elemento viga en sus puntos de integración.

Se implementan una serie de modelos constitutivos para distintos materiales. En particular, se implementa un modelo constitutivo triaxial para hormigón fisurado, considerando la anisotropía inducida por la fisuración e incluyendo la superficie de rotura según un criterio multiaxial.

La formulación seccional es validada mediante varios casos de estudio teóricos y experimentales. La respuesta no-lineal acoplada bajo diversas combinaciones de esfuerzos normales y tangenciales es reproducida con precisión, lo cual queda patente tanto en las curvas esfuerzo-deformación obtenidas como en las matrices de rigidez seccionales.

Finalmente, se recopilan las conclusiones derivadas de la presente investigación y se ofren recomendaciones para futuros trabajos.

Contents

List of Symbols

$()'$ Derivative with respect to the beam's axis.

Latin letters

A	Area.
$\mathbf{A}^*$	Sectional modes of distortion.
$\mathbf{B}^{ps}$	Operator to interpolate the plane-section strain tensor from $\mathbf{e}_s$.
$\mathbf{B}^{ps*}$	Operator to interpolate the plane-section strain tensor from $\mathbf{e}_s^*$.
$\mathbf{B}^w$	Operator to obtain the warping-distortion strain tensor.
$\mathbf{B}^w_{yz}$	Interpolation matrix of the warping-distortion strain tensor in the finite element model.
$\mathbf{d}^w$	Vector of nodal warping-distortion values.
$\mathbf{d}_{XY}$	Damage tensor in global coordinates.
$\mathbf{d}_{12}$	Damage tensor in local coordinates.
$\mathbf{D}$	Constitutive matrix in global coordinates.
$\mathbf{D}_{12}$	Constitutive matrix in local coordinates.
$\mathbf{e}_s$	Vector of sectional generalized strains: $[\varepsilon_0, \gamma_y, \gamma_z, \phi_x, \phi_y, \phi_z]^T$.
$\mathbf{e}_s^*$	Subvector of sectional generalized strains: $[\varepsilon_0, \phi_x, \phi_y, \phi_z]^T$.
E	Longitudinal modulus.
E_0	Initial longitudinal modulus.
E_1	Yielded longitudinal modulus.
E_i	Longiturinal modulus in local direction i.
f_c	Compression strength.
f_t	Tension strength.

f_y	Yielding stress.
G	Shear modulus.
G_{ij}	Shear modulus in local plane $i-j$.
$\mathbf{K}_s$	Sectional stiffness matrix.
$\mathbf{L}$	Linear operator to obtain the gradient of a 3D vector.
$\mathbf{L}_x$	Linear operator to obtain the gradient of a 3D vector with respect to the beam's axis.
$\mathbf{L}_{yz}$	Linear operator to obtain the gradient of a 3D vector with respect to the section's plane.
$\mathbf{N}^{ps}$	Operator to obtain the plane-section displacement field.
$\mathbf{N}^{w}$	Operator to obtain the warping displacement field.
$\mathbf{T}_{\boldsymbol{\varepsilon}}$	Strain tensor rotation matrix.
$\mathbf{T}_{\boldsymbol{\sigma}}$	Stress tensor rotation matrix.
$\mathbf{s}_s$	Vector of sectional generalized stresses: $[N_x, V_y, V_z, T_x, M_y, M_z]^T$.
$\mathbf{u}$	Displacement vector: $[u, v, w]^T$.
$\mathbf{u}^{ps}$	Plane-section displacement field.
$\mathbf{u}^{w}$	Warping-distortion (or 3D distortion) displacement field.
$\mathbf{u}_s$	Beam displacement vector: $[u_0, v_0, w_0, \theta_x, \theta_y, \theta_z]^T$.
$\mathbf{r}_0$	Coordinates of the beam's axis in the sectional plane.
$\mathbf{r}_{cs}$	Coordinates of the section's center of shear forces.

Greek letters

$\boldsymbol{\varepsilon}$	Strain tensor in global coordinates: $[\varepsilon_x, \varepsilon_y, \varepsilon_z, \gamma_{xy}, \gamma_{xz}, \gamma_{yz}]^T$.
$\boldsymbol{\varepsilon}_{12}$	Strain tensor in the principal directions.
$\boldsymbol{\varepsilon}^{ps}$	Plane-section strain tensor.
$\boldsymbol{\varepsilon}^{w}$	Warping-distortion strain tensor.
$\boldsymbol{\varepsilon}^{m}$	Mechanical strain tensor.
$\boldsymbol{\varepsilon}^{nm}$	Non-mechanical strain tensor.
ε_0	Concrete strain at peak stress.
$\boldsymbol{\varepsilon}^{e}$	Elastic strain tensor.
$\boldsymbol{\varepsilon}^{p}$	Plastic strain tensor.
$\boldsymbol{\varepsilon}^{p}_{XY}$	Plastic strain tensor in global coordinates.
$\boldsymbol{\varepsilon}^{p}_{12}$	Plastic strain tensor in the principal directions.

$\boldsymbol{\varepsilon}^{\nu}_{XY}$	Poisson strain offset in global coordinates.
$\boldsymbol{\varepsilon}^{\nu}_{12}$	Poisson strain offset in the principal directions.
$\boldsymbol{\gamma}_0$	Vector of generalized shear strains in the reference axis: $[\gamma_y, \gamma_z]^T$.
$\boldsymbol{\gamma}_{rc}$	Vector of generalized shear strains in the center of shear forces.
$\boldsymbol{\gamma}_m$	Vector of mean shear strains.
$\boldsymbol{\sigma}$	Stress tensor in global coordinates: $[\sigma_x, \sigma_y, \sigma_z, \tau_{xy}, \tau_{xz}, \tau_{yz}]^T$.
$\boldsymbol{\sigma}_{12}$	Stress tensor in the principal directions.
$\boldsymbol{\sigma}^{ps}$	Plane-section stress tensor.
$\boldsymbol{\sigma}^{w}$	Warping-distortion stress tensor.
ν	Poisson coefficient.
ν_{ij}	Poisson coefficient in the $i-j$ plane.
$\boldsymbol{\xi}^*$	Vector of generalized strains: $\left[\varepsilon_0, \phi_x, \phi_y, \phi_z, \varepsilon_0', \phi_x', \phi_y', \phi_z'\right]^T$.
$\boldsymbol{\xi}$	Vector of generalized strains: $\left[\varepsilon_0, \phi_x, \phi_y, \phi_z, \phi_y', \phi_z'\right]^T$.
$\boldsymbol{\Xi}$	Transformation matrix from $\boldsymbol{\xi}$ vector to $\boldsymbol{\xi}^*$.
$\boldsymbol{\Omega}$	Transformation matrix from $\mathbf{e}_s$ vector to $\boldsymbol{\xi}$.

List of Figures

List of Tables

Chapter 1

Introduction and objectives

1.1 Motivation and problem statement

All real structures are three dimensional and are subjected to multiaxial stress states. However, many of them can be assimilated to strucutal systems composed by linear elements either because one dimension is much larger than the other two or the stress in one direction is higher than in the other two. In that case, the structure can be simulated as a planar or space frame, as shown in figure 1.1, so that the response of each point in the linear element is defined by the cross section mechanical characteristics.

Using this type of representation it is possible to derive simpler governing equations than in the case of complex solid three-dimensional formulations. In the same way, model generation and results interpretation is usually easier, more versatile and more directly related to engineers reasoning.

This fact, together with the higher computational costs and engineering-time demanded by three-dimensional finite element modeling, compared to one-dimensional elements, makes frame type elements the most employed in structural engineering analysis and simulations.

The demand more accurate design procedures that could produce safer and more economical structures, made necessary to simulate the structural performance under all load levels, including the inelastic range until failure.

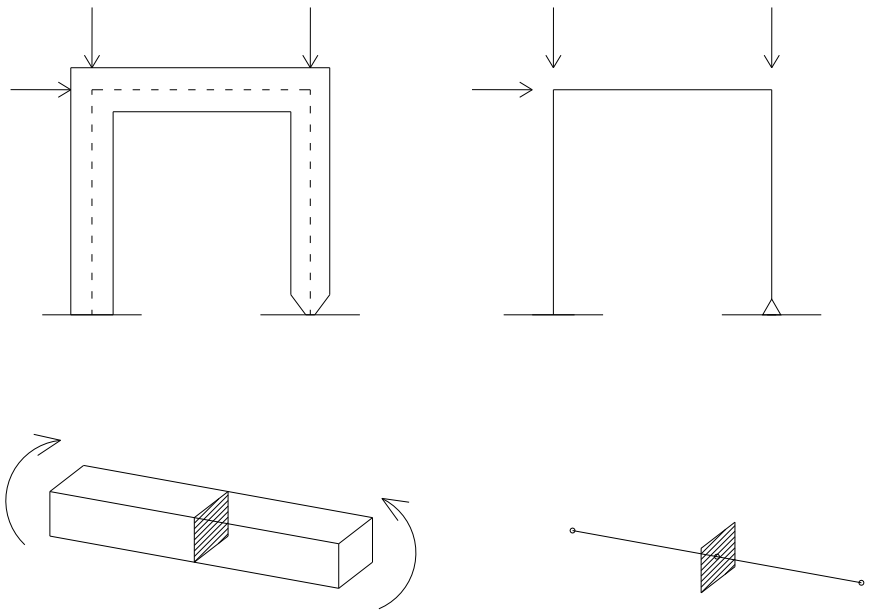

Figure 1.1: Frame structure.

This necessity is even more evident if constructions are designed against accidental and seismic loads, where good non-linear performance is the key to assure safety in a reliable and economic way. Most of the state-of-the-art on seismic design and assessment procedures proposed recently for common engineering practice require some kind of non-linear analysis either dynamic or static.

These non-linear analyses are mostly carried out using frame elements with different levels of accuracy. The most basic type of non-linear analysis using frame elements assumes that the inelastic behaviour is lumped at a series of fixed points with given generalized force-displacements characteristics, such as moment-rotation ($M-\theta$) or axial force-elongation ($N-u$), called plastic hinges. These approaches are referred, in general, as lumped-inelasticity.

More general procedures consider the fact that inelastic behaviour can occur in any point of the structures. These approaches are generally referred to as smeared-inelasticity. The first possibility is to use given generalized non-linear force-strains curves, for instance moment-curvature ($M-\phi$), axial force-elongation ($N-\varepsilon_0$), etc., at every integration point within the beam

element. The frame non-linear response is obtained by direct integration along the element's length.

The previous two approaches present an important drawback in the case of RC beam-column elements. This is given by the dependency of the axial load on the moment-curvature curves or moment-rotation in the axial load and vice-versa (coupling). More realistic results are obtained by means of the so-called fiber beam elements, figure 1.2.

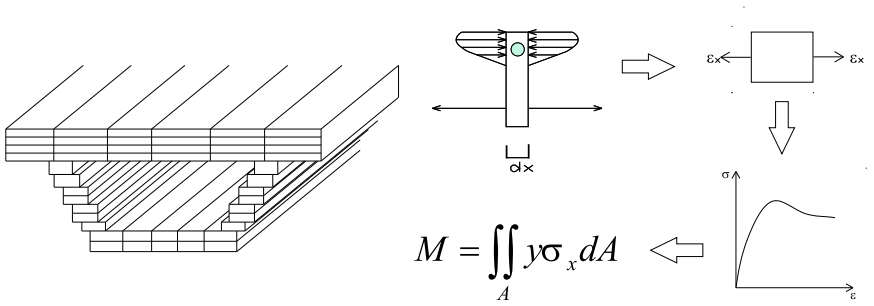

Figure 1.2: Fiber beam element cross section.

Fiber beam elements have been developed since more than twenty years and successfully applied in the non-linear analysis of all levels of normal forces, i.e. bending moments and axial force. These elements are based on the cross section discretization in a series of point elements or fibers characterized by a tributary area and a non-linear uniaxial constitutive model. Uniaxial strain at each fiber is computed from the generalized strains by means of the plane-section (PS) hypothesis. Generalized strains are thus directly integrated with as much accuracy as fine the section mesh is. When fiber discretization is combined with a flexibility based element, the highest degree of accuracy and stability is obtained in a frame structural model at the current state of knowledge.

Though normal solicitations are frequently dominant in the behaviour of frame structures, they are not the only type of stresses that can act on them. In the general case of loading, a beam cross section can subjected to a maximum of six stress resultants: three generalized normal forces (one axial force and two bending moments) and three tangential forces (one torsional moment and two shear forces). Fiber elements, as described above, are not

capable of considering shear stresses, therefore shear forces and torsion can not be integrated as is done with normal forces.

Usually, when a member is subjected to combined loading, the effect of normal and shear stresses are treated separately. A fiber sectional approach is used to integrate normal stresses ignoring the presence of shear stresses. Sectional response to shear forces is considered, in an uncoupled fashion, by means of a given generalized force-deformation curve or simply is considered as perfect elastic. In any case, the level of accuracy achieved in considerable less than the obtained with the concomitant normal stresses, figure 1.3.

More important than the difference in accuracy is the fact that the interaction between tangential and normal stresses is not being taken into account, neither in strength nor in the overall non-linear behaviour. Moreover, the accuracy apparently achieved in normal forces by means of the fiber integration scheme can be reduced in some cases.

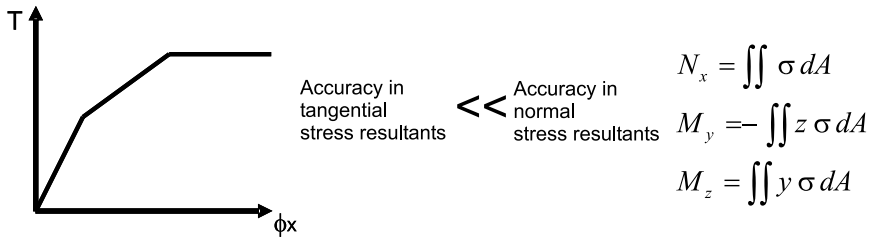

Figure 1.3: Different treatment for non-linear tangential and normal generalized stresses.

In the case of reinforced concrete (RC) structures in general (also for prestressed concrete structures) the described phenomena are of relevant importance. It is well known that cracked concrete exhibits anisotropic behaviour, so called crack-induced anisotropy. Post-cracking coupling between shear related forces (torsion and shear forces) and axial related forces (axial force and bending moments) takes place. Figure 1.4 shows a representation of this phenomenon.

If, for instance, a concrete section is subjected to torsion, diagonal cracks will form at a certain cracking load and the stresses in the two principal directions can not longer be equal; then shear stresses can not be developed

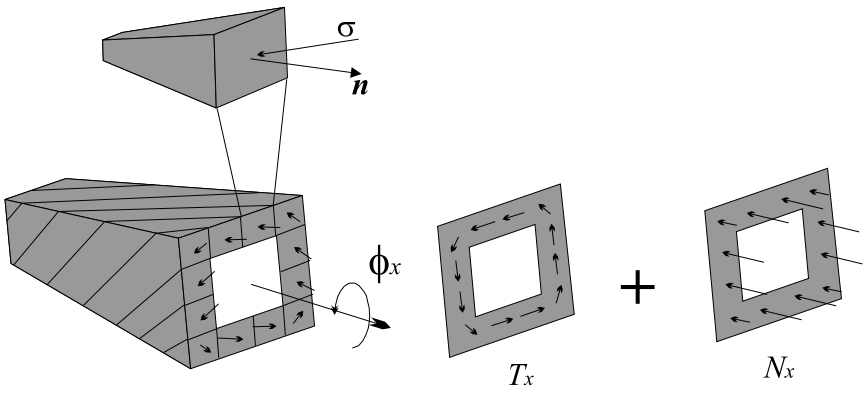

Figure 1.4: Generalized stresses coupling in a cracked RC beam.

unless volumetric compression is supplied by the reinforcements. Coupling between tangential and normal forces occurs and the equilibrium conditions among fibers have to be satisfied in the three dimensions. It is precisely this coupling that loads transversal reinforcement allowing, the element to resist higher shear stresses after cracking.

As another example, consider the case of shear-bending interaction in a cracked RC beam. As will be seen in the next chapter, it is recognized in the current design codes the existance of an increment of tensile stresses in the longitudinal bending reinforcements due to the presence of a concomitant shear force, $\Delta T_s = f(V)$. Nevertheless, it is reasonable to think, and so is reflected by the experimental evidence, that a concomitant bending moment produces an increment of stresses in the transverse reinforcements $\Delta T_t = f(M)$ in the presence of inclined cracks. However, this phenomenon is not considered in current design approaches.

The problem of non-linear coupled axial-bending of concrete sections is considered nowadays *solved*, since plane-section hypothesis allows a rational sectional analysis producing fairly good results. However, the same statement can not be said about the non-linear shear and torsion problems. From the above paragraph it is clear that, in order to do a rational evaluation of the behaviour of cracked concrete sections in shear and torsion, the inter-fiber equilibrium must be suitably considered.

The aim of developing a rational theory to analyse concrete sections under shear and torsion is not new. The most frequently used method of analysis was stated more than a century ago by Ritter and extended by Morsch. Even though, there is no shear theory equivalent to the plane-section hypothesis in axial-bending loading. This is evident from differences in the approaches given in the design codes of several countries and also by the series of historical and recent failures in shear that have been occurred.

This is the case of a series of American Air Force warehouses that failed in shear during 1955 and 1956 that strongly influenced the 1963 ACI code shear provisions. More recently in the summer of 1998, a parking garage collapsed in Toronto due to shear failure.

Figure 1.5: American Air Force warehouse shear failure.

The case of shear forces coming from cyclic or seismic loading is less understood, Paulay and Priestley (1992), Petrangeli, Pinto and Ciampi (1999), Ranzo (2000). Even slender members, that mainly work in flexure with apparently moderate shear, have failed in cyclic shear because of the bending interaction at high levels of ductility demand. It could be stated that in the late great earthquakes occurred in the last years, most failure observed in concrete structures were related to shear. Some remarkable examples

were observed in Loma Prieta (1989), Northridge (1994), Kobe (1995) and Taiwan (1999) earthquakes.

Figure 1.6: Shear failure of Hanshin express piers during Kobe earthquake 1995.

Figure 1.7: Shear failure of squat bridge pier during Taiwan 1999 earthquake.

Some dramatic cases deserving a special mention are the Cypress viaduct, that collapsed in Loma Prieta, and the more than $600m$ of the Hanshin

expressway, that collapsed in the 1995 Kobe earthquake (Japan) due to lack of concrete confinement and shear strength of the piers. Particularly in the case of Hanshin expressway in Kobe, it must be noticed that these piers were rather slender members (shear span to section's depth ratio was greater than 3). In the 1999 Taiwan earthquake, shear failures of bridge piers were observed also in squat elements.

Currently, most modern design codes recognize the influence of flexure ductility-demand in shear resistance.

During the last twenty years, several researches were conducted with the aim of developing rational models for RC in shear. The joint ACI-ASCE Committee 445 *"Shear and Torsion"* published a state of the art report in 1998 (ACI-ASCE Committee 445, 1998) where these research works were comprehensibly reviewed. Even though, it was also recognized that the performance of RC members subjected to severe shear demand is still not fully understood and more research is called for. The need for improvements in the design regulations for torsional strength was also identified as the next challenge to be faced.

In the last two decades several coupled in-plane bending-shear sectional models were developed and good agreement with the experimental evidence was obtained for this particular loading case. A description of the some of these models will be presented in the next chapter. However, there is no rational sectional model capable of considering the situation of full coupled loading (with the six generalized stresses components) for any cross section shape or reinforcement arrangement, both longitudinal and transverse (stirrups).

With respect to this last statement, it has been observed, Bigaj (1999), that the non-linear rotation capacity of beams is very influenced by the reinforcement arrangement. Particularly, in order to have a ductile RC structure, the reinforcement arrangement should be related to the member size. Adequate detailing of reinforcements represents the difference between adequate or poor rotation capacity of beams in the presence of a shear force.

It is apparent that, in order to achieve a beam theory with equivalent level

of thoroughness for tangential and normal 3D loading, good estimation of the full 3D stress tensor distribution in the cross section domain is essential. It has been recognized that in a beam model the main assumptions, such as that of PS in flexure, are more important than the details on more specific aspects related to the materials behaviour.

Precisely, the major drawback presented in the current shear-bending models, that disables their applicability in full 3D loading, is the way in which shear stresses are computed. Mainly two approaches have been used: either a fixed strain shape of the in-plane shear strains are used or shear stresses are computed from 2D fiber equilibrium considering the gradients of the axial stresses.

The first approach is somehow arbitrary and not justified for non-linear analysis of concrete-sections. Besides being strongly affected by the section's geometry, the shear strain distribution experiences important shape changes influenced by cracks distribution, width, slope, inelastic response of reinforcements and compressed concrete. As a result, these approaches tend to exaggerate shear stresses in the compression zone of the beam and underestimate the effects of the transversal reinforcements.

The second approach is based on explicitly considering the equilibrium betweeen each fiber, thus predicting more accurate stress-strain fields than the latter. The inconvenience is that straightforward application of this procedure is only possible for 2D loading. Strictly, this approach should only be used in situations where bending moments and shear forces are contained in a plane of symmetry. This limitation exists because the inter-fiber equilibrium equations are statically defined only for 2D loading.

The interest of determining the distribution of all stress tensor components in a beam's section is shared by other structural technologies besides that of concrete. In particular, for composite laminate structures this problem is of relevant importance. Composite laminates present an anisotropic coupled response of extension, bending and shear. Furthermore, accurate evaluation of interlaminar out-of-plane stresses (shear an axial stresses in the thickness direction originated from inter-layers equilibrium) is needed to prevent

delamination, which strongly limits the performances of composites. Some advanced beam theories are available in this field, basically they can be included in two classes of theories: equivalent single layer theories and multilayer theories. These approaches will be discussed in the state of the art chapter as well as their advantages and disadvantages.

The described problematic motivated the development of this thesis with the goal of contributing in the achievement of a fully coupled sectional model capable of correctly reproducing the response under all possible 3D loading situations. Although mainly inspired in the problematic of cracked concrete frame sections, a contribution of this type could be useful to other structural technologies with strong anisotropic behaviour.

1.2 Objectives

General objective

The main objective of this thesis is to develop an analytical model capable of capturing the response of arbitrary shaped reinforced concrete cross-sections subjected to general coupled loading: biaxial bending and shear with axial force and torsion. It is desired to obtain similar level of accuracy and generality than in the analysis under pure normal forces (i.e. bending and axial loading) when transversal internal forces are included (i.e. shear loading and torsion). Namely, direct integration of the generalized stresses from a fiber-like discretization is aimed.

Specific objectives

As it was explained in the previous section, in the case of full 3D loading, several difficulties exist in comparison with the 2D problem of in-plane bending-shear-axial loading making the former considerably more involved than the latter. Particularly in the case of reinfoced concrete sections, additional complexity arises from the need of considering all components of the 3D stress and strain tensors. In order to achieve the general goal with an

adequate balance of accuracy, the following set of specific objectives are also considered:

- To develop a rational methodology to compute the actual distribution of three-dimensional stress and strain tensors in the cross section's domain made of an arbitrary anisotropic material.
- To express the rational model as a function of the beam's generalized strains in order to make it independent of any beam element formulation.
- To model post-cracking coupling of transversal and normal generalized forces; namely, include the effects of cracking inclination in the response of concrete sections.
- To model the effects of transversal reinforcements in the response of concrete sections: confinement and resistance to shear and torsion.
- To implement the mathematical model in a suitable numerical formulation to make possible, with similar versatility as a fiber sectional discretization, its utilization in sections of arbitrary geometry, material heterogeneity and reinforcement arrangement.
- To evaluate the accuracy that can be obtained with the proposed formulation.
- To study the non-linear behaviour of reinforced concrete sections under combined normal and tangential loading.

1.3 Research significance

In this thesis the problem of non-linear coupled behaviour of reinforced concrete-sections has been investigated. The problem is dealt in a general form considering any anisotropic material. Subsequently, non-linear cracked concrete was included as a particular case by means of suitable constitutive equations. This approach makes the model versatile and suitable of analysing structures made of any type of materials.

The resulting model is independent of any frame element formulation. In fact, one objective was that the proposed formulation could be posed as function of solely the generalized strains of the single section. Thus it can be implemented as sectional constitutive law into any frame element in the standard form: input consisting of generalized strains and output consisting of generalized stresses and a set of state variables.

Neither fixed a-priori kinematic constraints nor dual-section analysis is required. Accurate evaluation of the three-dimensional stress and strain tensor is achieved by the superposition of a warping-distortion field to the section's deformability. From inter-fiber equilibrium and compatibility equations, the new displacement field was effectively expressed as a function of the components of the generalized strains by means of an original procedure in which non-local effects, such as stress increments, are evaluated from the sectional characteristics derivatives.

The sectional formulation is considered the main contribution of this investigation. Though coupled shear-bending loading and torsion-bending model exist in the current state of the art of concrete sectional analysis, to the knowledge of the author, no sectional model was capable of handling the full coupled problem (biaxial bending, shear, torsion and axial load) for any geometry, satisfying all mechanical conditions of equilibrium and compatibility at the same time.

In fact, the formulation produces full three-dimensional information in a sectional bidimensional analysis. With a model of this characteristics, three-dimensional effects that traditionally were analyzed using expensive solid element models are now at the reach of frame element analysis at the expense of some simplifications but with the advantages of a simple system of monodimensional elements and a set of bidimensional sectional analysis.

It is recognized that the resulting model is more computationally demanding than a traditional uniaxial fiber sectional model. The interest of the this sectional model is evident when three-dimensional effects are of relevant importance and traditional uniaxial fiber sectional discretization fails to produce correct results.

On the other hand, the problem size is smaller than solid finite element models since the proposed formulation is in the *middle way* of the two previous approaches. Moreover, computational cost optimization can be easily done in a frame element model thanks to the versatility of the sectional analysis. Thus, traditional fiber elements could be used in structure regions known to be dominated by normal solicitation, while the proposed 3D sectional model can be used only at the sections known to be dominated by combined tangential loading or other three-dimensional effects.

1.4 Contents of this document

This thesis is divided in seven chapters, being the current introduction the first of them.

In the second chapter a brief review of the state of the art is presented. Emphasis is given in highlighting the problems arising from the non-linear 3D coupled analysis of RC sections. A review of simulation methodologies to include shear and torsion in RC sectional analysis is presented. Similar interests were found between the general coupled problem of RC sections and the analysis of composite laminate sections; some methodologies for the accurate determination of the stress fields of these type of sections are also commented. Finally a critical analysis of the state of the art is presented.

In chapter three, a mathematical framework, in the form of general hypotheses and unified notations, for the representation of beam theories is offered. Some classical and modern beam approaches are presented as particular cases that can be casted in the presented framework. After commenting the applicability of the available approaches in general loading situations of concrete sections, a generalized beam theory capable of considering the full three-dimensional state is proposed based on mechanical conditions: equilibrium and compatibility. No a-priori fixed kinematical constraint is required.

In chapter four, the proposed sectional model is implemented in a 2D finite element formulation. The developed numerical formulation and algorithm are deeply explained. The resulted finite element code constitute a sectional

subroutine capable of analysing any type of cross-section with any shape and constitutive material with independence of the frame element formulation used at the structural level. Full 3D inter-fiber equilibrium is satisfied for any normal-tangential loading combination or anisotropic material behaviour. A library of finite elements was developed in order to properly discretize a wide number of sectional typologies; the formulation of these elements are given in the second part of this chapter.

Chapter five describes a series of four material models that were implemented together with the sectional model. In general 3D material constitutive equations are required for the solid matrix elements while a uniaxial constitutive equation is enough for the reinforcement elements. The developed materials include a 3D orthotropic linear elastic material, a linear-brittle material that allows for cracking along principal tensile directions thus crack-induced anisotropy. A 3D constitutive model for concrete was also developed after state-of-the-art knowledge of this material behaviour. Finally a uniaxial elasto-plastic model has been developed for reinforcement elements.

Validation of the model is carried out in chapter six by performing a series of case studies with the developed sectional model. The chapter is composed of two parts, where theoretical and experimental studies are analysed respectively.

Finally, conclusions are summarized in chapter seven. Recommendations of future researches that could be carried out after this work are also given in order to improve the proposed formulation or to use it as an aid in the understanding of concrete-sections under complex load combinations.

Chapter 2

State of the art

2.1 Non-linear analysis of RC elements under bending and axial loads

The problem of non-linear analysis of RC frame structures under bending and axial loads has been extensively investigated. In general the plane-section hypothesis has proved to be a suitable approximation of the section's kinematics in all range of loading. As a result, available formulations present robustness and generality, being the most versatile the ones based on direct integration of the cross-section discratization based on fiber or layer elements. These formulations have been successfully employed to study complex non-linear and time-dependent phenomena on RC and prestressed elements, such as those proposed by Kang and Scordelis (1980), Buckle and Jackson (1981), Chan (1983), Mari (1984) (2000) and Ulm et. al. (1994).

Effects of segmental construction process have been investigated using similar approaches by Ghali and Elbadry (1985), Kang and Scordelis (1990), Abbas and Scordelis (1993), Ketchum (1986), Murcia and Herkenhoff (1994), Cruz, Mari and Roca (1998) and Mari (2000).

Virtually "*exact*" solutions for non-linear analysis of frame structures can be obtained, independently of the discretizaton mesh, by means of equilibrium or flexibility based frame elements. These are a generalization of the

matrix flexibility formulations that, in contrast to displacement based elements, frame deformation shapes are a result of the exact integration of the equilibrium and compatibility equations of a beam element. An historical presendent of this approach can be found in Baron (1961). More recent formulations were proposed by Backlund (1976), Grelat (1978). Carol and Murcia (1989) extended the flexibility-based elements to non-linear time-dependent analysis. Carrascon et al (1987) generalized the formulation to curve elements in space with variable sections.

Spacone, Ciampi and Filippou (1996) used the flexibility formulation for earthquake analysis and also proposed an specific integration scheme at element level. Molins, Roca and Mari (1995) applied the formulation to mansory structures and in Molins, Roca and Barbat (1995) a virtually "*exact*" mass matrix for the element was developed.

2.2 Behaviour of RC elements under shear and torsion

2.2.1 Shear resistance mechanism

Beams without transverse reinforcement

Shear forces in a beam element always act in combination with bending moments to produce a multi-axial stress state. When principal tension stress reaches the tensile strength a crack pattern at an approximate inclination of 45 °. Frequently shear cracks are extensions of vertical cracks previously formed in the tension zone of the beam due to bending. Park and Paulay (1994).

Drawing the free body of a beam cut across the inclined crack (figure 2.1), the following sources of shear forces shows:

- Shear stresses transfered in the uncracked compression zone of the beam.

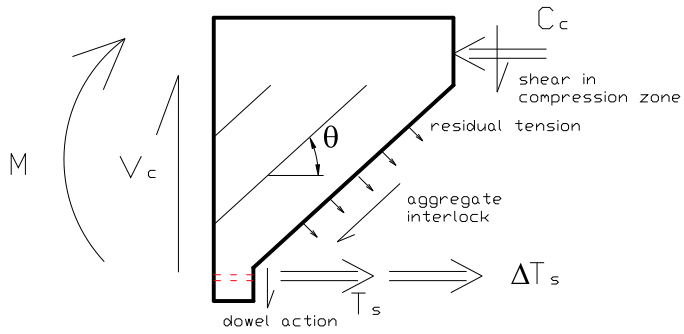

Figure 2.1: Mechanism of concrete shear resistance

- Shear stresses transfered along the crack plane by means of friction and aggregate interlock.
- Dowel action of the longitudinal reinforcements.
- Residual tensile stresses transfered across the crack plane, as a unperfect discontinuity (ASCE-ACI Commitee 445, 1998).

Note that, from equilibrium analysis, the longitudinal reinforcing steel is governed by the moment acting on the section at upper end of the crack, therefore it must account for an increment in tension force of value:

$$\Delta T_s = V \cot \theta$$

In beams without transverse reinforcement, dowel action can not be developed to important terms since this force reacts directly on the concrete cover which is lost at low dowel forces.

Considering the total variation of bending moments ($M = zT$):

$$V = \frac{dM}{dx} = \frac{\partial M}{\partial T}\frac{dT}{dx} + \frac{\partial M}{\partial z}\frac{dz}{dx} = z\frac{dT}{dx} + T\frac{dz}{dx}$$

Where z is the effective lever arm between internal tension and compression resultant forces. The term considering the variation of tensile force for constant lever arm is referred to as beam action and represents the mechanisms previously descrived. The variation of the lever arm at constant tensile force represents an additional mechanism for resisting shear forces reffered to as

arch-action. Arch-action, represented in figure (2.2) is only important when longitudinal steel presents bond-slip or begins to yield.

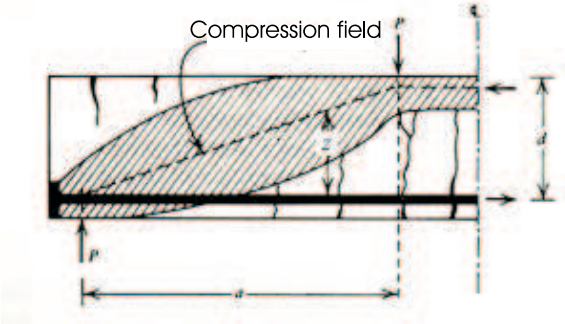

Figure 2.2: Arch action

Beams with transverse reinforcement

Transverse reinforcement is beneficial to RC beams by providing support to the dowel action of longitudinal bars, limiting the crack width thus augmenting the aggregate interlock effect and enhancing bond resistance as well as confiniment on the compression zone. More important to these effects is the fact that transverse streel introduces a new resisting mechanism known as truss-action. The first rational model considering this mechanism was described by Ritter in the late XIX century and latter improved by Morsch.

This mechanism can be explained by considering the field of compression stresses in concrete that forms parallel to the cracks. This field is anchored against the longitudinal and transverse reinforcements producing an effectively shear bearing mechanism that resembles a truss, figure (2.3).

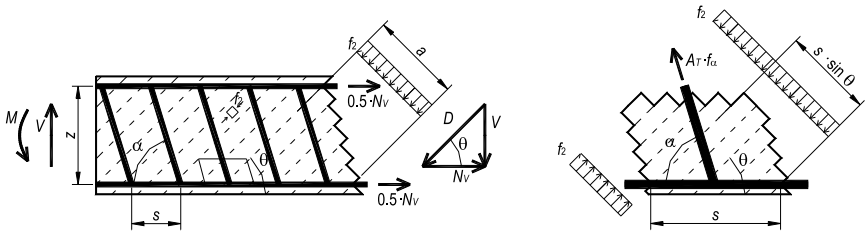

Figure 2.3: Truss mechanism of shear resistance

It can be noticed (figure 2.4) that by means of the truss analogy, longitudinal reinforcements must account for an additional tensile force of:

$$\Delta T_s = \frac{1}{2} V_s \left(\cot\theta - \cot\alpha\right)$$

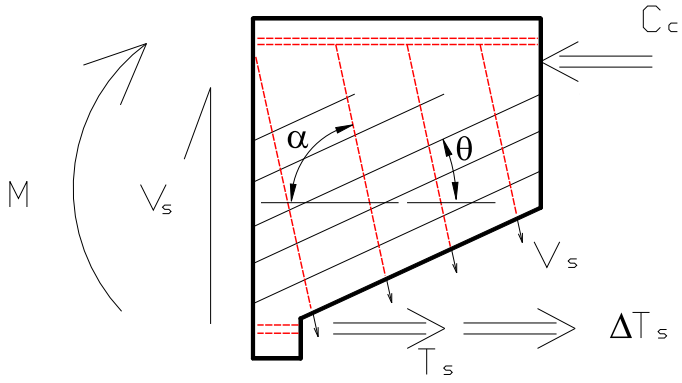

Figure 2.4: Mechanism of transverse reinforcement shear resistance

The stirrups arrangement influences the distribution of the compression field. This effect can be important in wide beams with stirrups around the perimeter, figure 2.5. In this case, only the bars in the corners tend to anchor the compression field.

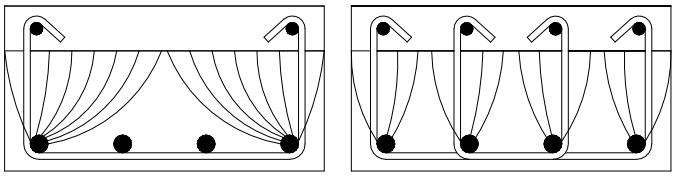

Figure 2.5: Influence of stirrups arrangement on the post-cracked in-plane shear flow of a wide RC section

2.2.2 Torsion resistance mechanism

Before cracking, the response of a concrete section under torsion can be reasonably predicted by the elastic theory of Saint-Venant. However, cracking occurs at relatively low torque values producing a sudden and brittle collapse of the element. The behaviour does not change much if the beam is reinforced with longitudinal bars, it was observed that, with this type of

reinforcement, ultimate torsion rarely exceeds the cracking moment in more than 15% (Hsu, 1984).

When transverse and longitudinal reinforcements are used together, an alternative torsion bearing mechanism is developed after cracking. Similarly to shear resistance, the new mechanism can be interpreted as a spatial truss as seen in figure 2.6.

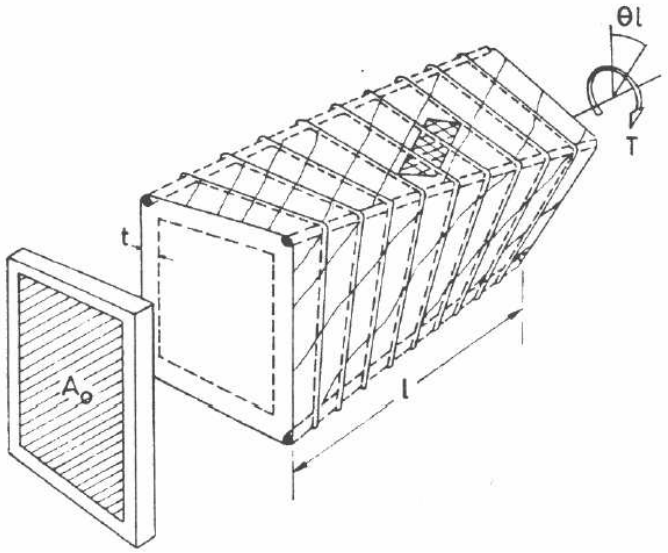

Figure 2.6: Truss mechanism of torsion resistance

In experimental observations, Onsongo (1978) and Hsu (1984) noticed that the beam's length increases under augmenting torque. This stretching is required to produce tensile stresses in the longitudinal reinforcements in order to provide anchorage to the diagonal struts of the spatial truss mechanism. Distortion of the section's shape is also required in order to produce tensile stresses in the transverse reinforcements. These phenomena also take place in shear loading.

The post-cracking stiffness of a hollow concrete section and a solid one with similar external dimensions are of similar magnitude. This observations reinforces the spatial-truss analogy. An analitical expression for torsion stiffness of cracked concrete sections was proposed in Lampert (1973).

2.3 RC sectional analysis under combined loading

2.3.1 Preamble

In general, the analysis of a cross section requires two main ingredients: a constitutive model of the materials and a suitable representation of the sectional kinematics in order to obtain the distribution of strains in the section. If the load produces shear stresses, the difficulty of the problem increases considerably both in the constitutive model to be used (which must be multi-axial) and the adoption of valid kinematical hypotheses.

Modeling the behaviour of concrete under multi-axial loading is a difficult task. Under rather small values of stresses, concrete exhibits non-linear tensile cracking and stress-strain relationships. Time dependent shrinkage and creep under sustained loads, complex stress-strain curves under cyclic loading and dilatation under high compressions are also phenomena related to concrete behaviour. Particularly, the markedly different behaviour on tension and compression is the source of anisotropic behaviour under multi-axial stresses.

Many constitutive models have been proposed in the last decades for the analysis of concrete structures. These models can be generally classified into non-linear elasticity (Elwi and Murray, 1979), plasticity models (Chen, 1982; Simo et al., 1988]), damage and fracture mechanics (Bažant and Oh, 1983, Mazars, 1982, Saouridis and Mazars, 1992) and micro-plane models (Bažant and Prat, 1988, Carol et al., 1990), among others. Damage with directionality have also been considered, hence producing anisotropic behaviour, some recent works on this subject can be found in Jefferson (2000), Luccioni and Oller (2003), amog others. Combination of the previous models have also been carried out. A comprehensive review can be found in CEB (1996).

Among the available spectrum of constitutive models for concrete, those that handle cracking as a distributed effect with directionality are particularly suitable for sectional analysis under combined loading. This is so, because in this approach cracked concrete is simulated as a continuos medium with

anisotropic characteristics, hence in an integration point there is enough information of the directionality of the response. In general, these models are referred to as "*smeared cracks approaches*".

In the next section, a review of some constitutive models for reinforced concrete suitable for sectional analysis under combined loading will be presented. Further, the available methods for integration the sectional are examinated.

2.3.2 Smeared-crack approaches to material response modeling

Two basic possibilities exist for the smeared crack approaches, referred to as *rotating crack* and *fixed crack* approaches if the cracking directions are allow to change with the load direction or not. Combining the two methodologies is also possible. General discussions of these approaches are available in Bažant (1983) and Petrangeli and Ozbolt (1996).

In the following some extensively used smeared crack constitutive models will be presented.

Modified Compression Field Theory (MCFT)

The Modified Compression Field Theory (MCFT) was originally developed in Vecchio and Collins (1982) and Vecchio and Collins (1986) with further changes in Collins and Mitchell (1987). It is a constitutive model to evaluate the stress-strain response of RC material points under shear and axial stresses. The MCFT is also a further development of the Comprression Field Theory (CFT), developed by Mitchell and Collins (1974), in orther to account for the influence of tensile stresses in the shear loading of cracked concrete. Both CFT and MCFT were developed in the University of Toronto and were inspired in the solution, proposed by H. A. Wagner in 1929, to the problem of shear loading of metal beams with very thin webs.

The MCFT was formulated after experimental tests carried out in bidimen-

sional RC panels subjected to plane-stress loading. These tests were carried out on specially built panel-tester.

Originally the MCFT was developed for plane-stress monotonic loading and neglecting the so-called "*Poisson-effect*". Further extensions to 3D loading (Vecchio and Selby, 1991; Vecchio, 1992; Selby and Vecchio, 1997), cyclic loading (Vecchio, 1999; Palermo and Vecchio, 2003) and confinement effects (Vecchio, 1992; Montoya, Vecchio and Sheik, 2001) were carried out. In the following the basic formulation is explained.

The main assumptions of the MCFT are that cracks are considered distributed in the concrete and the the principal directions of the stress and strain tensor coincide; therefore, it can be called a smeared-crack model with rotating-cracks. Reinforcing steel is also considered smeared in the concrete. It is recognized that the local stresses in both concrete and steel vary from point to point in the cracked concrete. Therefore, equilibrium and compatitibility equations are evaluated with the average value of the stress and strain in the crack plane and in the concrete in between cracks. Additionally, to account for the probable fact of steel yielding first at the crack location than in its average value, a local check of the stress state at the crack plane is required. Figure 2.7 summarizes the main aspects of the MCFT.

For clarity of the exposition, it has been considered that reinforcing steels are located in the global directions $(X - Y)$.

Reinforcing steel The response of reinforcing steel is considered by means of a bilinear elasto-plastic $\sigma - \varepsilon$ curve as shown in figure 2.7. Besides the mechanical properties, the steel in each direction will be characterized by the steel-concrete volume ratio: ρ_x and ρ_y.

Concrete in compression It was early recognized, since the CFT formulation, that the compression $\sigma - \varepsilon$ relationship in cracked concrete differs from that of uniaxial loading. In the MCFT, the maximum stress that cracked concrete can resist in the principal direction (f_{2max}) is considered a

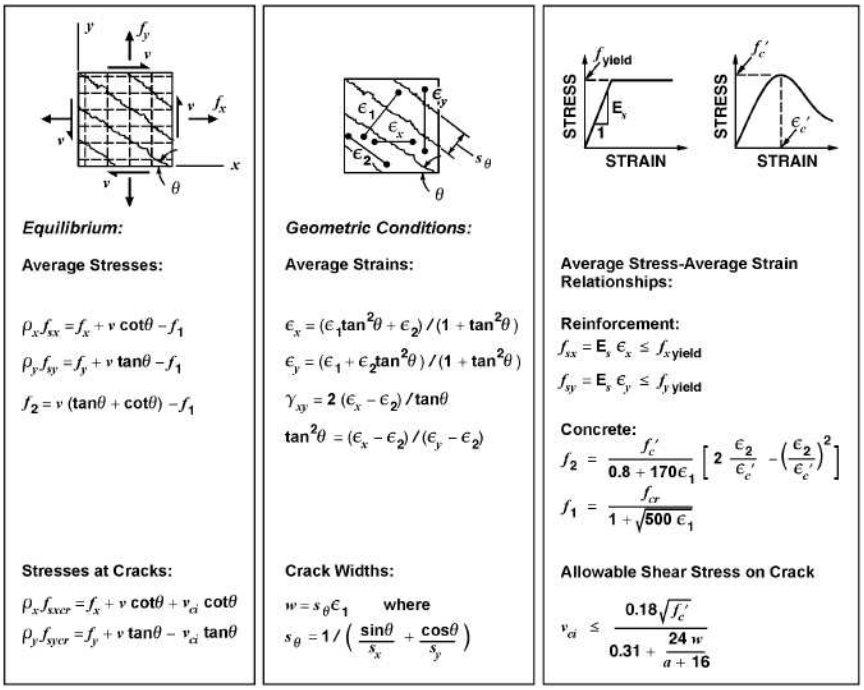

Figure 2.7: Summary of the Modified Compression Field Theory

function of the concomitant transverse tensile strain (ε_1) as follows:

$$f_{2max} = \frac{f_c}{0.8 + 170\varepsilon_1} \leq f_c \text{ [MPa]} \tag{2.1}$$

where f_c is the uniaxial strength.

The $\sigma - \varepsilon$ response is computed using the following parabolic equation:

$$\sigma_2 = f_{2max}\left[2\left(\frac{\varepsilon_2}{\varepsilon_0}\right) - \left(\frac{\varepsilon_2}{\varepsilon_0}\right)^2\right] \tag{2.2}$$

Where ε_0 is the strain at peak stress. More sophisticated expressions, see eq. (5.8), have also been used to account for the change of shape of the $\sigma - \varepsilon$ curve depending on the concrete strength (Selby and Vecchio, 1997).

Concrete in tension A tensile $\sigma - \varepsilon$ relationship was included feature of the MCFT that marked the main difference between it and the CFT; this relationship was requiered to account for the tension-stiffening effect and its influence in shear resistance. The original equation (Vecchio and Collins,

1982) was based on 30 experimental results from tests on $70mm$ thick shear panel elements. The proposed equation was:

$$\sigma_1 = \frac{f_t}{1 + \sqrt{200\varepsilon_1}} \text{ [MPa]} \tag{2.3}$$

Latter, tests were conducted on larger panels ($285mm$ thick). It was found that adjustments in the previous equation was requiered to fit the new series of data. Therefore, Collins and Mitchell (1987) proposed the following modified expression:

$$\sigma_1 = \frac{f_t}{1 + \sqrt{500\varepsilon_1}} \text{ [MPa]} \tag{2.4}$$

Moreover, equation (2.4) was not able to fit properly the test results carried out in the University of Houston on $178mm$ thick elements and different reinforcement ratio. To fit these data, a factor of 1500 is required in the previous equations.

This problem was explained recently in Bentz (2005) as a size effect phenomenon. Bentz proposed the following new equation for the tension response considering the size-effect:

$$\sigma_1 = \frac{f_t}{1 + \sqrt{3.6M\varepsilon_1}} \text{ [MPa]} \tag{2.5}$$

Where M is a size effect parameter (expressed in mm) computed as:

$$M = \frac{A_c}{\sum d_b \pi} \text{ [mm]} \tag{2.6}$$

here d_b is the diameter of the reinforcing bar and A_c is the tributary area of concrete for each reinforcing bar.

Crack-check The local stress state in the crack plane must be investigated to check if the averaged stresses can be transmitted across the crack. To perform this checking, the actual complex crack pattern is idealized as a series of parallel cracks, spaced at s_θ. If τ_{xy} is the shear stress in the $X-Y$ system and τ_{ci} the shear at the crack plane, the stresses in the reinforcing steel can be determined form equilibrium perfoming a cut along the crack

plane as follows:

$$\begin{aligned} \rho_x \sigma_{sxcr} &= \tau \cot(\theta) + \tau_{ci} \cot(\theta) \\ \rho_y \sigma_{sycr} &= \tau \tan(\theta) - \tau_{ci} \tan(\theta) \end{aligned} \tag{2.7}$$

The maximum shear stress that can be transfered across a concrete crack is computed by means of the model proposed by Walraven (1981), equation (2.8), after tests on different concrete up to a cube strengths of 59 MPa. It must be considered that for concrete of very high strength, the cracks tend to cut the coarse aggregates, therefore, equation (2.8) might not be appropiate for such concretes.

$$\tau_{ci} \leq \frac{0.18\sqrt{f_c}}{0.3 + \frac{24w}{a+16}} \text{ [MPa, mm]} \tag{2.8}$$

In the above equation, a is the size of the coarse aggregate. On the other hand, the averaged stress of the steel and concrete are related by equilibrium conditions that can be derived by using the Mohr circle:

$$\begin{aligned} \rho_x \sigma_{sx} &= \tau \cot(\theta) - \sigma_1 \\ \rho_y \sigma_{sy} &= \tau \tan(\theta) - \sigma_1 \\ \sigma_2 &= \tau \left(\tan(\theta) + \cot(\theta)\right) - \sigma_1 \end{aligned} \tag{2.9}$$

At high loads, reinforcement will typically yield, both the local stress at the carck plane and in the average stress, thus right hand side of the first two equations in (2.9) will equal the right hand side of (2.7) and can be equated; doing so and substituting τ_{ci} from (2.8), the following limit to the concrete principal tensile stress is obtained:

$$\sigma_1 \leq \frac{0.18\sqrt{f_c}\tan(\theta)}{0.3 + \frac{24w}{a+16}} \text{ [MPa, mm]} \tag{2.10}$$

This crack check is of particular relevance in the MCFT, since it limits the tension stiffening effects of equations (2.3), (2.4) and (2.5), which predicts rather important tensile stresses, by taking into account the possibility of failure of the aggregate interlock. If this check is not considered or properly performed the MCFT will produce unsafe results.

Disturbed Stress Field Model (DSFM)

In year 2000 Vecchio presented the Disturbed Stress Field Model (DSFM) as an extension of the MCFT, Vecchio (2000). It is a smeared-crack model with a hybrid formulation in between a fully rotating-crack approach and a fixed-crack approach. The implementation and validation of the model was published latter in Vecchio (2001) and Vecchio, Lai and Schim (2001). For clarity of the exposition, in the following it has been considered that reinforcing steel bars are located in the global directions $(X - Y)$.

This new model was motivated by some deficiencies observed in the MCFT when compared to some experimental results of shear panels and beams, namely:

- Underestimation of the shear strength and stiffness in heavily reinforced panels in both directions and subjected to high concomitant compression stresses.
- Overestimation of the shear strength and stiffness in uniaxially reinforced panels.
- Overestimation of the ductility and both overestimation or understimation of the strength in beams with little or null transverse reinforcements.

Nevertheless, in Vecchio (2000) it is also stated that the MCFT remains a simple but powerful model applicable with enough accuracy in most practical situations.

These deficiencies were attributed to hypothesis of coincidence of stress and strain principal directions used in the MCFT. It was noticed from the experimental observations that after cracking and yielding both stress and strain tensors experimented reorientation of the principal directions, but in general, strains rotate more than stresses. Therefore, a "*lag*" exists in the stress rotation. It was observed that this lag is usually between 5° and 10°.

This difference in the strains orientation can be assimilated as a rigid shear slip in the crack plane and taken into account explicitly in the compatibility

equations as an elastic strain offset in the following form:

$$\boldsymbol{\varepsilon} = \boldsymbol{\varepsilon}_c + \boldsymbol{\varepsilon}^s \tag{2.11}$$

Where $\boldsymbol{\varepsilon}$ if the total strain tensor, $\boldsymbol{\varepsilon}_c$ is the strain tensor directly related to stresses in concrete, also referred to as non-mechanical strain, $\boldsymbol{\varepsilon}^s$ is the strain offset due to rigid shear slip along the crack plane.

To compute the $\boldsymbol{\varepsilon}^s$ tensor lets consider the shear slip occuring in the crack plane with orthogonal direction defined by the angle θ, figure 2.8. A local shear strain associated to this slip can be defined as:

$$\gamma_s = \frac{\delta_s}{s} \tag{2.12}$$

Where δ_s is the crack slip and s the crack spacing.

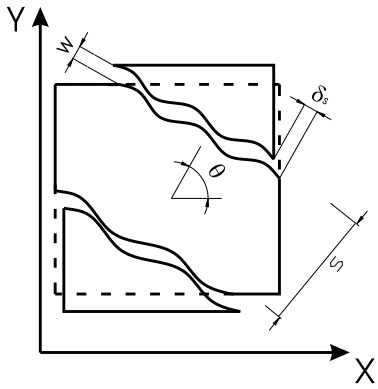

Figure 2.8: Rigid shear-slip in a cracked concrete element

By rotating this strain to the reference coordinate system, the strain offset tensor is defined as:

$$\begin{aligned} \varepsilon_x^s &= -\frac{\gamma_s}{2}\sin(2\theta) \\ \varepsilon_y^s &= \frac{\gamma_s}{2}\sin(2\theta) \\ \varepsilon_x^s &= \gamma_s \cos(2\theta) \end{aligned} \tag{2.13}$$

The shear slip (δ_s) is related to the local shear stress in the crack and the crack width (w) by means of the crack shear-slip model proposed by Walraven (1981):

$$\delta_s = \frac{\tau_{ci}}{1.8w^{-0.8} + (0.234w^{-0.707} - 0.20)\, f_{cc}} \text{ [MPa, mm]} \tag{2.14}$$

Where f_{cc} is the concrete cube strength.

On the other hand, based on the experimental observations, the lag angle is limited to a maximum value of θ_l:

$$\theta_\sigma - \theta_\varepsilon \leq \theta_l \tag{2.15}$$

Where θ_l is 5° for elements reinforced in both directions, 7.5° for elements reinforced in one direction and 10° for non-reinforced elements.

Rotating-Angle Softened Truss Model (RA-STM)

The Rotating-Angled Softened-Truss Model (RA-STM) is a smeared-crack constitutive model for reinforced concrete elements with a rotating crack approach in which reinforcements are also considered smeared in the concrete. It was developed in the University of Houston by the research group lead by T. Hsu based on shear panel tests similar to those carried out in the University of Toronto. Detailed explanation of this element can be found in Belarbi and Hsu (1994), (1995) and Pang and Hsu (1995) (1996). For clarity of the exposition, in the following it has been considered that reinforcing steels are located in the global directions $(X - Y)$.

Many of the hypothesis of the MCFT are shared by the RA-STM, namely: stresses and strains are considered to have the same principal directions, compressed concrete experiences softening after cracking occurs in an orthogonal direction.

Different softening model and stress-strain relationships are used for the cracked concrete under compression. The expressions for concrete in compression are taken as:

$$\begin{aligned} \sigma_2 &= \zeta_{\sigma 0} f_c \left[2\left(\frac{\varepsilon_2}{\zeta_{\varepsilon 0}\varepsilon_0}\right) - \left(\frac{\varepsilon_2}{\zeta_{\varepsilon 0}\varepsilon_0}\right)^2 \right] \forall \frac{\varepsilon_2}{\zeta_{\varepsilon 0}\varepsilon_0} \leq 1 \\ \sigma_2 &= \zeta_{\sigma 0} f_c \left[1 - \left(\frac{\frac{\varepsilon_2}{\zeta_{\varepsilon 0}\varepsilon_0} - 1}{\frac{2}{\zeta_{\varepsilon 0}} - 1} \right)^2 \right] \forall \frac{\varepsilon_2}{\zeta_{\varepsilon 0}} > 1 \end{aligned} \tag{2.16}$$

Where $\zeta_{\sigma 0}$ is the concrete softening parameter to be computed as:

$$\begin{aligned} \zeta_{\sigma 0} &= \frac{0.9}{\sqrt{1+400\varepsilon_1}} \quad \text{for proportional loading} \\ \zeta_{\sigma 0} &= \frac{0.9}{\sqrt{1+250\varepsilon_1}} \quad \text{for sequential loading} \end{aligned} \tag{2.17}$$

$\zeta_{\varepsilon 0}$ defines the strain of maximum stress in the $\sigma - \varepsilon$ curve and it is computed as:

$$\begin{aligned} \zeta_{\varepsilon 0} &= \frac{1}{\sqrt{1+500\varepsilon_1}} \quad \text{for proportional loading} \\ \zeta_{\varepsilon 0} &= 1 \quad \text{for proportional loading} \end{aligned} \tag{2.18}$$

The concrete post-cracked behaviour in tension is simulated by the following tension-stiffening equation:

$$\sigma_1 = \frac{f_{cr}}{(12500\varepsilon_1)^{0.4}} \text{ [MPa]} \tag{2.19}$$

Another important difference with the MCFT is that the RA-STM does not requires a check of the stress-state in the crack location. Instead, this model adjusts the average stress-strain curve of the reinforcement to account for the possibility of local yielding in at the crack. The $\sigma - \varepsilon$ curve for the steel are as follows:

$$\begin{aligned} &\sigma_s = E_s \varepsilon_s \forall \varepsilon_s \leq \varepsilon_n \\ &\sigma_s = f_y \left[(0.91 - 2B) + (0.02 + 0.25B) \frac{E_s}{f_y} \varepsilon_s \right] \left[1 - \frac{2 - \frac{\alpha_2}{45}}{1000\rho} \right] \forall \varepsilon_s > \varepsilon_n \end{aligned} \tag{2.20}$$

Where ε_n is the average strain producing local yielding at the cracks. It is computed as:

$$\varepsilon_n = \frac{f_y}{E_s} (0.93 - 2B) \left[1 - \frac{2 - \frac{\alpha_2}{45}}{1000\rho} \right] \tag{2.21}$$

B is a tension-stiffening parameter defined as:

$$B = \frac{\left(\frac{f_{cr}}{f_y}\right)^{1.5}}{\rho} \tag{2.22}$$

In the above expressions, α_2 is the angle between the initial crack direction and the longitudinal reinforcement, ρ is the reinforcement ratio, f_y is the

reinforcement yielding stress, E_s is the elastic modulus of reinforcement, f_{cr} is the concrete cracking stress.

In general the RA-STM and the MCFT give similar predictions for low amounts of reinforcements. For high reinforcement ratios, the MCFT predicts somewhat higher stresses than the RA-STM.

Cyclic versions of the above stress-strain equations for concrete and steel were presented latter in Mansour et al (2001).

Fixed-Angle Softened Truss Model (FA-STM)

In addition to the RA-STM, Hsu and his colleagues have proposed the Fixed-Angle Softened Truss Model (FA-STM), Pang and Hsu (1996). This model assumes that concrete struts remain parallel to the initial cracks direction; which in turn are defined by the concrete principal stress directions in the moment of cracking.

The model uses three different coordinate systems, as shown in figure 2.9, namely: the reference coordinate system $(X-Y)$, the local coordinate system at the cracks $(1-2)$ defined by the angle ϕ, and the coordinate system of the current principal stress directions in concrete $(1'-2')$ defined by the angle θ. During loading the angle ϕ is remains fixed after craking has occured while the angle θ changes constantly with the current stress-state. For clarity of the exposition, in the following it has been considered that reinforcing steels are located in the global directions $(X-Y)$.

The same stress-strain expressions of the RA-STM for concrete in tension and compression are used in this model. The important difference is that these stresses are defined now in the local crack coordinate system $(1-2)$. Since this is not necessary a principal direction, both shear stress and strain will generally exist in the crack plane, these quantities are related by the following expression:

$$\tau_{21}^{c} = \tau_{21m}^{c}\left[1-\left(1-\frac{\gamma_{21}^{c}}{\gamma_{210}}\right)^{6}\right] \tag{2.23}$$

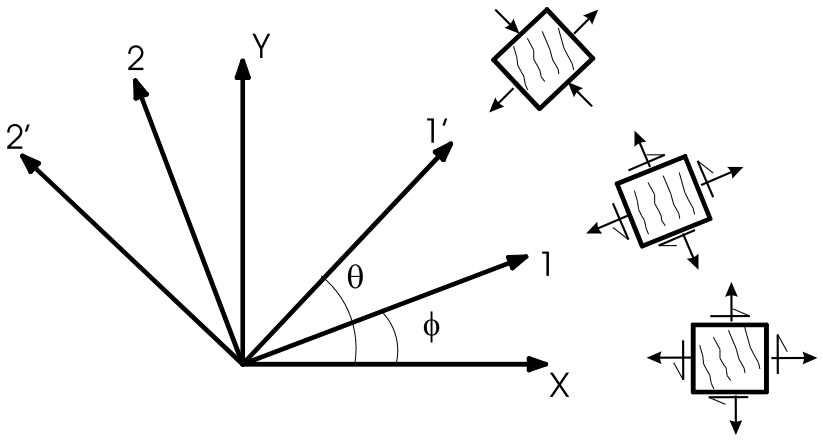

Figure 2.9: Coordinate systems in the Fixed-Angle Softened Truss Model

where

$$\gamma_{210} = 0.85\varepsilon_{x0}\left[1 - \frac{\rho_y f_{y,y} - \sigma_y}{\rho_x f_{y,x} - \sigma_x}\right] \tag{2.24}$$

and

$$\tau^c_{21m} = \frac{1}{2}\left[(\rho_y f_{y,y} - \sigma_y) + (\rho_x f_{y,x} - \sigma_x)\right]\sin(2\phi) + \tau_{ltm}\cos(2\phi) \tag{2.25}$$

Where τ^c_{21} and γ^c_{21} are the shear stress and strain in the local crack directions $(1-2)$. τ^c_{21m} and γ_{210} are the concrete maximum shear stress and strain respectively. τ_{ltm} is the maximum shear stress applied in the plane where the longitudinal and transverse reinforcement, notice in this exposition this plane is coincides with the reference coordinate system $(X-Y)$. $f_{y,x}$ and $f_{y,y}$ are the reinforcement yielding stress in the X and Y directions respectively.

Latter in Zhu, Hsu and Lee (2001), a different scheme for determining the crack shear behaviour was proposed where an explicit $\tau^c_{21} - \gamma^c_{21}$ relationship is not necessary. This approach was based on an explicit shear modulus original developed for rotating-crack approaches, Bažant (1983), equation (2.26).

$$G^c_{21} = \frac{\tau^c_{21}}{\gamma^c_{21}} = \frac{1}{2}\frac{\sigma^c_1 - \sigma^c_2}{\varepsilon^c_1 - \varepsilon^c_2} \tag{2.26}$$

Other smeared-crack approaches to concrete

Recently, many other smeared crack formulations for concrete have been proposed. An interesting formulation, similar to the ones explained above, for 2D monothonic loading with smeared-reinforcements was proposed by Belleti et al. (2001).

Balan, Filippou and Popov (1997) proposed a 3D smeared crack formulation for concrete that allows for cyclic loading and confinement effects.

2.3.3 Integration of the sectional response

Once a suitable constituive model for concrete is available, in principle it is possible to deduce the response of the cross-section by direct integration over all material points. As shown above, this procedure was straightforward when the RC section was only subjected to bending moments and axial forces since the Navier-Bernoulli (NB) hypotheses produce a suitable kinematic constraint between the cross-section deformations and the normal strains at every point in the section. In addition, it has been observed that this hypothesis remain valid for all range of loading.

When in addition to normal forces, the section is subjected to an in-plane shear force, the distribution of shear stresses required to keep together all fibers in the section was deduced by D. J. Jourawski in 1856. The process considered by Jourawski is sketched in figure 2.10.

As it is known from equilibrium considerations, the presence of a shear force implies an increment of the bending moments along the beam's axis; therefore, along the horizontal direction a fiber will be subjected to normal stress and an increment of axial stress which must be equilibrated by horizontal out-of-plane shear stresses. These horizontal shear stresses are in equilibrium with the in-plane vertical components by beams of moment equilibrium. The equilibrium of a fiber will be given by the following equation:

$$\frac{\partial \sigma_x}{\partial x} + \frac{\partial \tau_{xz}}{\partial z} = 0 \tag{2.27}$$

Equation (2.27) can be solved directly resulting that the shear stress at any

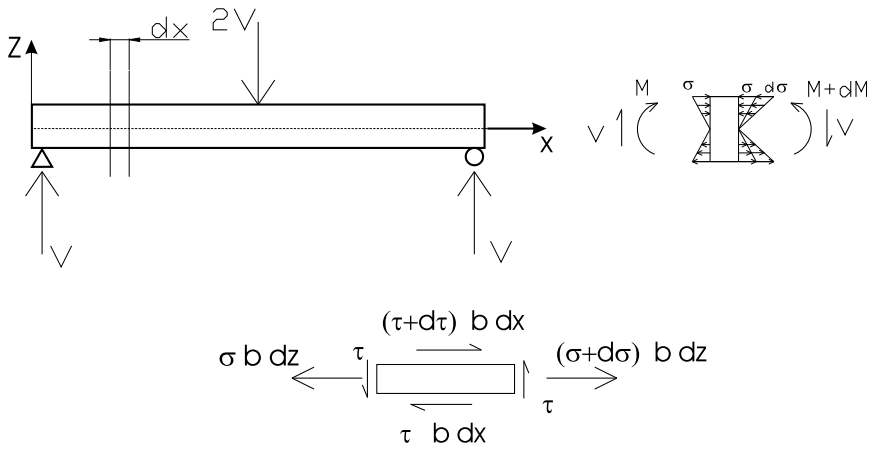

Figure 2.10: Jourawski solution for in-plane shear stresses in a beam

point of the beam can be computed as:

$$\tau_{xz}(z) = -\frac{1}{b}\int_{-c}^{z}\frac{\partial\sigma}{\partial x}bdz \tag{2.28}$$

Where $-c$ is the coordinate of the bottom fiber. If the beam is homogenous and made of an isotropic-elastic material, the previous integral reduces to the well-known equation:

$$\tau_{xz}(z) = -\frac{1}{b}\int_{-c}^{z}\frac{Vbz}{I}dz = \frac{VQ(z)}{Ib(z)} \tag{2.29}$$

$Q(z)$ is the first moment of area integrated from the bottom of the section to point z, $b(z)$ is the section's width in coodinate z. Keeping the previous constitutive assumptions, the shear strain in the point will depend exclusively on the shear stress and the elastic tangential modulus ($\tau_{xz} = G\gamma_{xz}$), therefore:

$$\gamma_{xz}(z) = \frac{1}{Gb}\int_{-c}^{z}\frac{Vbz}{I}dz = \frac{1}{G}\frac{VQ(z)}{Ib(z)} \tag{2.30}$$

Using the concept of effective shear area ($A_e = \alpha A = \frac{V}{G\gamma_0}$), the following constraint between the section shear deformation and the shear strain in a fiber can be stated:

$$\gamma_{xz}(z) = \frac{\alpha AQ(z)}{Ib(z)}\gamma_0 \tag{2.31}$$

After manipulating the equilibrium equation and introducing the constitutive relationships, a kinematic constraint (i.e. only geometric parameters

are present) between the generalized sectional shear deformation (γ_0) and the shear strain at a point of the cross section was obtained in equation (2.31).

Nevertheless, some remarks must be mentioned about this solution. Firstly, unlike the Navier-Bernoulli kinematic constraint for normal forces, this constraint varies with the sectional geometry. In praticular, for a rectangular section, equation (2.31) reduces to the following parabola:

$$\gamma_{xz}(z) = \frac{5}{4h^2}\left(h^2 - 4z^2\right)\gamma_0 \tag{2.32}$$

On the other hand, even though the final solution only includes geometric quantities, implicitly, it is material dependent. Recall that it was derived from an internal equilibrium equation in which isotropic linear material was assumed. In fact, the assumption that shear stresses are decoupled from normal stresses (suitable for isotropic materials and orthotropic materials along the planes of material symmetry) was what allowed the step from equation (2.29) to (2.30).

Particularly this last remark represents the first issue that makes the simulation of the non-linear response of RC sections with tangential forces considerably more involved than the case of bending and stretching.

It is known that concrete under combined normal-shear loading develops crack patterns that in general are not parallel to the section's plane. Since cracked concrete exhibits considerably different non-linear response along compression and tension directions, it will present strong anisotropic behaviour resulting in general coupling of normal and tangential stress and strains. This situation is schematized in figure 2.11 where a stress σ_x is applied to fiber with an oblique crack pattern; as a result, this fiber will be distorted (shear strain) as well as deformed in the $(X-Y)$ plane. It is evident that, if a correct kinematic constraint for the shear strains can be deduced in this case, it must be a function of all generalized sectional strains, including the elongation and bending curvatures.

Finally, consider the possibility of a bidimensional shear stress flow in a section. This case is more frequent than it might seem in a first instance.

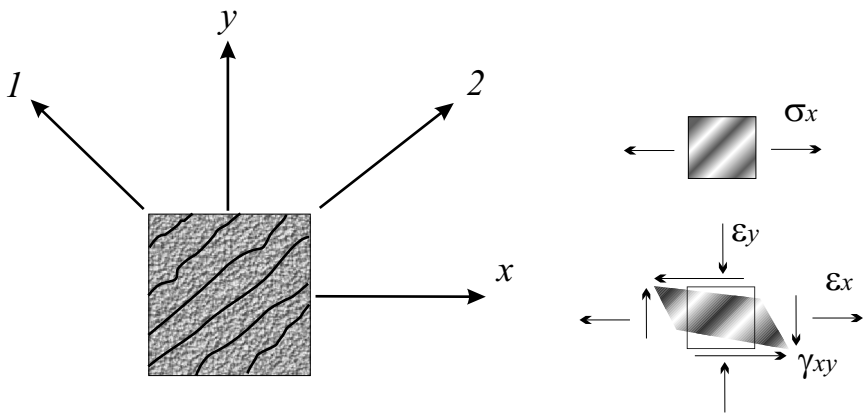

Figure 2.11: Crack induced anisotropy phenomenon

2D shear flows not only occurs in beams under torsion, but also in beams that are not loaded along a symmety plane (biaxial bending), see figure 2.12. Transverse reinforcement arrangement also influences the shear flow of cracked sections, which can be strongly bidimensional for moderately wide beams (figure 2.5).

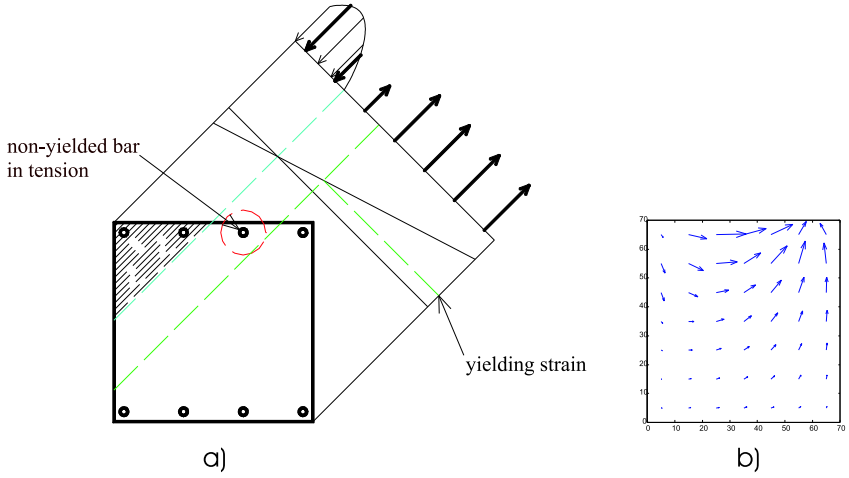

Figure 2.12: Skew shear force in a RC section. a) normal stresses situation. b) 2D flow of shear stresses.

Under this situation the increment of longitudinal stress will be equilibrated by the two components of shear stresses indicated in figure 2.13. Instead of

equation (2.27), the differential equation to be solved will be the following:

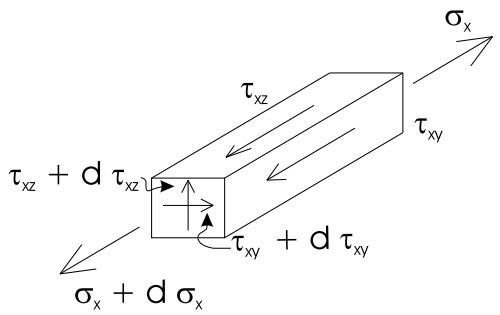

Figure 2.13: Free body under biaxial shear flow

$$\frac{\partial \sigma_x}{\partial x} + \frac{\partial \tau_{xy}}{\partial y} + \frac{\partial \tau_{xz}}{\partial z} = 0 \tag{2.33}$$

Unlike equation (2.27), the differential equation (2.13) is statically indeterminate, there are two unknowns (shear modulus and direction) and only one equation. Hence, compatibility conditions must be explicitly considered in order to solve the correct 2D shear flow. This was not necessary for the 1D case.

The solution of this problem for an elastic isotropic beam was obtained by Saint-Venant, first for pure torsion in 1855 and then for an elastic beam with arbitrary load at its boundaries in 1856, Timoshenko and Goodier (1972).

In the last two decades there have been considerable efforts in extending the capabilities of frame elements to loading combinations more general than bending and extension. Therefore, some models for integrating the sectional response in RC sections with shear forces or torsion have been proposed in this period. As a necessity, these models require some procedures for estimating the shear stress or strain distribution. In general, the approaches available are based either on an a-priori fixed kinematic constraint during the whole loading process (equivalent to a displacement based sectional model) or the explicit consideration of the inter-fiber equilibrium (equivalent to a force based sectional model). In the following, some of the most extensively used proposals for RC sections will be described.

Fixed pattern approaches

The most direct procedure to estimate the internal shear stress-strain distribution in the cross section is by a-priori assuming a fixed pattern either for the shear stress or strain and taking it as constant during the whole loading process. Thus, the stress or strain at a point is considered as the value of the assumed pattern multiplied by a generalized quantity of the cross-section state.

Formally, one of the equations (2.34) or (2.35) is assumed. In the first case a compatibility constraint is considered, while in the second a mean-equilibrium constraint is used. Although only the case of shear load has been represented in the mentioned equations, in principle, any type of load can be casted in this approaches, including torsion.

$$\gamma(y,z) = F_\gamma(y,z)\gamma_0 \tag{2.34}$$

$$\tau(y,z) = F_\tau(y,z)V \tag{2.35}$$

These approaches have been used by many authors both for the case of shear and torsion loading: Mitchell and Collins (1974), Onsongo (1978), Hsu (1984), Lopez (1987), Vecchio and Collins (1988), Rahal and Collins (1995), Petrangeli, Pinto and Ciampi (1999), Rahal and Collins (2003), Recupero et al. (2003), Recupero et al. (2005), among others.

Particularly, the formulation in equation (2.35) is more suitable for development of simple procedures. Therefore, some design code guidelines (AASHTO, 2001; ACI-318, 1999) are based on this type of approach including the spanish design provisions for structural concrete EHE (1999). From a plasticity point of view, the pattern in (2.34) will produce an upper-bound value of the failure load while approach (2.35) gives a lower-bound value of the ultimare load. Nevertheless, the assimilation of concrete as a plastic material is only possible in some situations since concrete has limited ductility. Therefore, the plasticity theorems must be carefully applied and attention

must be paid to the type of pattern chosen.

The choice of an adequate pattern is not always an easy task since it will depend on the section's shape, reinforcement arragements, etc. Fortunately, for most common situations in practice guidelines are somewhat available. It is worth to mention the case of pure torsion in a solid section and the usual assimilation of it to a thin-walled section.

Note that the role of the patterns is to fix the direction of the shear (stress or strain) flow at each fiber both in terms of direction and relative value with respect to a generalized sectional quantity. By knowing this information, each fiber can be considered to be in plane-stress along the respective direction.

Fixed strain patterns: The choice of a strain pattern is usually based on the elastic solution of strain field. When coupled with the NB kinematic constraints in the axial strain field, the pair $(\varepsilon_x, \gamma_{xz})$ is known in any point as a function of the generalized stretching, curvature, shear deformation and, if it is the case, torsion curvature:

$$(\varepsilon_x, \gamma_{xz}) \leftarrow (\varepsilon_0, \gamma_{xz}, \phi_z)$$

For simplicity, only the process for shear loading is sketched bellow. The procedure for torsion has equivalent steps.

A suitable constitutive model is invoked resulting the following set of stress components at each fiber: $(\sigma_x, \sigma_z, \tau_{xz})$.

The presence of a vertical normal stress violates the equilibrium along the vertical direction. Equilibrium is reestablished by computing the corresponding vertical elongation that cancels the total normal stress in the vertical direction taking into account the presence of a lateral reinforcement across the fiber, figure 2.14. Recalling that in cracked concrete normal and shear stresses are typically coupled, the increment of vertical normal stresses is computed considering perfect bond between concrete and lateral steel:

$$\begin{aligned} \sigma_z^c &= D_{21}\varepsilon_x + D_{22}\varepsilon_z + D_{23}\gamma_{xz} && \text{(on concrete)} \\ \sigma_z^s &= E_s\varepsilon_z && \text{(on lateral reinforcement)} \end{aligned} \tag{2.36}$$

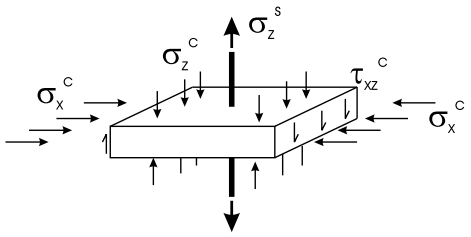

Figure 2.14: Fiber equilibrium in the transverse direction inducing distortion.

The equilibrium along the vertical direction is set out as:

$$\Sigma\sigma_z = \sigma_z^c + \rho_T \sigma_z^s = D_{21}\varepsilon_x + D_{22}\varepsilon_z + D_{23}\gamma_{xz} + \rho_T E_s \varepsilon_z = 0 \qquad (2.37)$$

where ρ_T is the ratio of transverse reinforcement. The following vertical strain results:

$$\varepsilon_z = -\frac{D_{21}\varepsilon_x + D_{23}\gamma_{xz}}{D_{22} + \rho_T E_s} \qquad (2.38)$$

It should be noticed that this vertical strain implies that the distortion of the section's shape is needed to achieve internal equilibrium. It is also remarkable that this process is what loads the transverse reinforcement and sets up the shear bearing mechanism of reinforced concrete; this reflects the importance of a suitable evaluation of the section's distortion.

Although compatibility of the section's warping can be always guaranteed by choosing a suitable strain pattern in equation (2.34), the compatitiblity along the vertical direction (involving the section's distortion) is not explicitly considered. This is not a problem in the case of 1D analysis (compatible strains are always obtained), but it does affect the 2D problem. On the other hand, fiber equilibrium in the vertical direction, equations (2.27) and (2.33), are not explicitly considered. Therefor, the integrity of the section (all fibers are kept together) is not verified.

Fixed stress patterns: In this case, the constrained quantities in the fiber are: ε_x and τ_{xy}. The material constitutive model is invoked to compute normal stress: σ_x. Similarly to the fixed-strain-approach, the vertical axial strain at each fiber is computed to restablish the equilibrium along the

vertical direction. The following transverse and shear strains result at each fiber:

$$\varepsilon_z = \frac{(D_{23}D_{31} - D_{33}D_{21})\,\varepsilon_x - D_{23}\tau_{xz}}{\hat{D_{22}}D_{33} - D_{23}D_{32}} \tag{2.39}$$

$$\gamma_{xz} = \frac{\left(D_{32}D_{21} - \hat{D_{22}}D_{31}\right)\varepsilon_x + \hat{D_{22}}\tau_{xz}}{\hat{D_{22}}D_{33} - D_{23}D_{32}} \tag{2.40}$$

where $\hat{D_{22}} = D_{22} + \rho_T E_s$

In this approach strain compatitibility is not explicitly guaranteed neither in the warping component nor in the distortion (transverse) component. As for the fixed strain pattern approach the internal fiber equilibrium is not directly verified.

Approaches considering the inter-fiber equilibrium

To satisfy the internal equilibrium among fibers for a non-linear material such as reinforced concrete, the shear stress and strain distributions should be a state-dependent property of the section and hence change during loading process.

For in-plane loading, the fiber equilibrium equation can be statically determinated from direct evaluation of the integral (2.28) along the section's depth. In the general cases where bidimensional shear flows are important, to author's knowledge, no formulation has been presented in the context of RC structural analysis to explicitly guarantee the internal fiber equilibrium.

It has been proved that the satisfaction of internal fiber equilibrium strongly influences the shear stress and strain distribution, Ranzo (2000). Although the failure load can be reasonably estimated in some cases with the fixed-pattern approaches, the predicted failure mode and the overall non-linear behaviour often do not reflect the real response. This effect can can be seen in figure 2.15, Vecchio and Collins (1988), where the shear stress-strain pattern to satisfy equilibrium is compared to a fixed stress pattern approach and a fixed strain approach applied to a RC section under a high shear force.

It can be seen that the fixed strain pattern tends to concentrate the shear

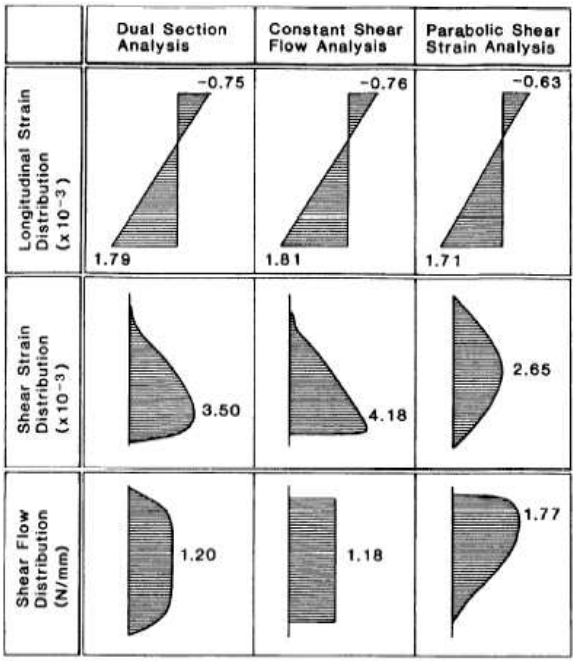

Figure 2.15: Comparision of different approaches for the estimation of shear distribution. *Vecchio and Collins (1988)*

stresses in the compression side thus underestimating the effects of the stirrups and the strain in the tension side. On the contrary, a reasonably chosen fixed shear-pattern produces a good strain distribution, slightly overestimating the strains and underestimating the stresses.

Currently, two type of approaches have been presented in the specialized litarature differing each other in the way the gradient of normal stresses ($\frac{\partial \sigma_x}{\partial x}$) of equation (2.28) is computed at each fiber. These methods are presented next.

Dual-section analysis: The Dual-section analysis was first presented in Vecchio and Collins (1988) and also was used by Ranzo (2000) to extend the capabilities of the fixed strain pattern model proposed by Petrangeli et al. (1999) to achieve internal fiber equilibrium. In this method, the gradient of normal stress of expression (2.28) is approximately computed by finite differences of the normal stress value on each side of a finite-length fiber, see

figure (2.17).

$$\frac{\partial \sigma_x}{\partial x} \approx \frac{\sigma_x(x_2) - \sigma_x(x_1)}{S} \tag{2.41}$$

Where $\sigma_x(x_1)$ and $\sigma_x(x_2)$ are the normal stresses of the fiber in the two analysed sections, S is the distance between the sections. Vecchio and Collins (1988) recomended a value of $S \approx \frac{H}{6}$ being H the beam's depth.

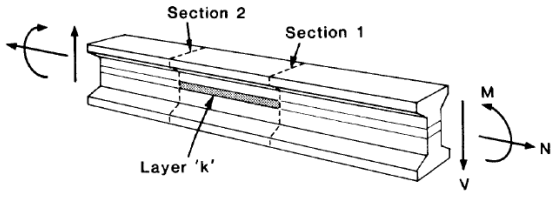

Figure 2.16: Dual section analysis scheme. *Vecchio and Collins (1988)*

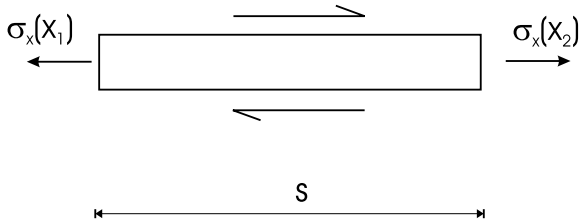

Figure 2.17: Free body diagram of a finite fiber in 2D

Note that in this method, the response of the section depends on information from outside of the section's geometric plane, therefore it can be said that the approach is *non-local*. If this scheme is to be implemented within a frame analysis, some conditions are required on the beam element. Hence, a special beam element formulation has to be developed for this sectional model. As it is seen in figure 2.18, a minimum of two integration points are required for flexure. Besides, shear has to be computed on different points, being always one less than for bending, and further be translated to the two adjacent flexure points.

It is evident that, from the point of view of implementing a sectional analysis procedure within a frame element (as the constitutive generalized stress-

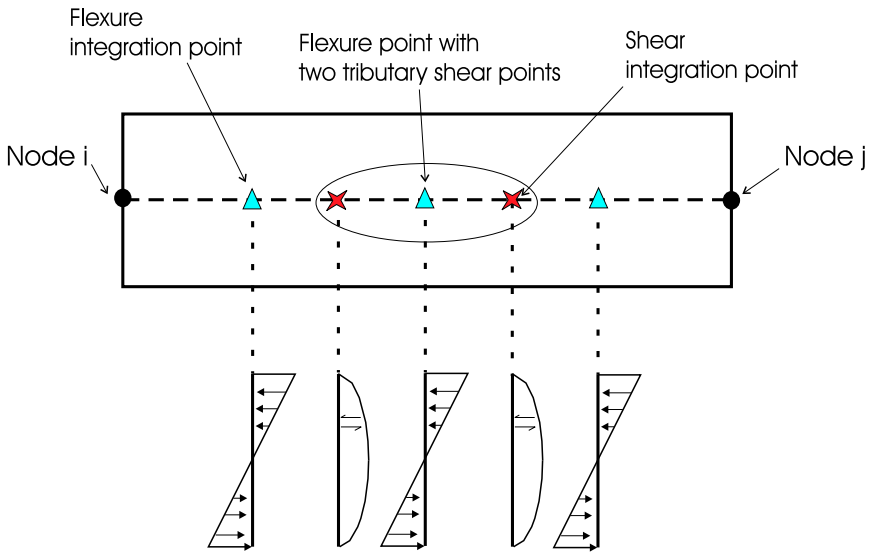

Figure 2.18: Dual section analysis implemented in a frame element

strain model of a frame), it would be preferred that all the information required by the sectional model is contained in a single integration point of the frame. If this is achieved, the sectional analysis model will be independent of the frame element used. Moreover, an independent sectional model is also interesting in order to take advantage of the flexibility based frame elements which, as mentioned above, give *exact* solution for the frame problem and are, therefore, free from shear-locking phenomenon.

On the other hand, it has been noticed, Bentz (2000), that the dual-section analysis has inherent difficulties in accurately evaluating the shear stress profile on the two sections in a stable manner. Particullarly, the method requires that the two sections are evaluated to the same value of axial forces and shear with high accuracy. Even a small difference of axial force, that would have been acceptable for the evaluation of the internal normal forces resultants, implies a spurious distributed load on the beam that might have important effects in the distribution of shear stresses, see figure 2.19. Hence, discontinuities on the shear stresses or non-closed shear diagrams are produced.

This approach explicitly considers the inter-fiber equilibrium in non-linear

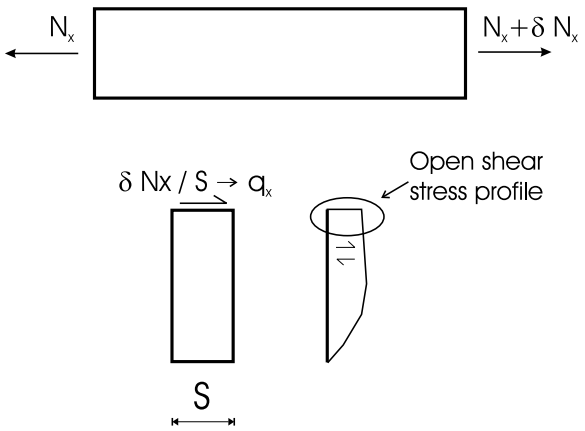

Figure 2.19: Effect of unbalanced axial forces in dual section analysis

analysis. However, the same comments about continuity, sectional warping and distortion mentioned above are also applicable.

Longitudinal stiffness method: The longitudinal stiffness method was proposed by Bentz (2000) in order to solve accuracy and instability problems noticed in the Dual-section analysis method. It was noticed that the influence of the distance separating the two sections influenced the results of the dual-section scheme.

In the longitudinal stiffness method, the gradient of normal stress is effectively computed as the derivative of the stress with respect to the element's axis by means of the *chain-rule*. Although the method was explained slightly different in Bentz (2000), it will be presented here in a more compact-formal format which in essence is equivalent.

The method requires an initial shear strain pattern as a function of the *mean* sectional shear deformation ($\gamma_{xz}(z) = F_\gamma(x,z)\gamma_m$). For the first load step this pattern can be taken as the elastic Jourawski solution:

$$\gamma_{xz}(z) = \frac{AQ(z)}{Ib(z)}\gamma_m \tag{2.42}$$

note that in eq. (2.42) γ_m is the the mean shear strain of the section, i.e. considereing the complete area of the section instead of the shear effective area. For further load steps, the previously obtained profile is used.

Combining the NB hypothesis to compute the axial strain and the current strain pattern, the strains at any fiber can be computed from the section's elongation, curvature and mean shear strain:

$$\begin{bmatrix} \varepsilon_x \\ \gamma_{xz} \end{bmatrix} = \begin{bmatrix} 1 & z & 0 \\ 0 & 0 & F_\gamma(y,z) \end{bmatrix} \begin{bmatrix} \varepsilon_0 \\ \phi_y \\ \gamma_m \end{bmatrix} \tag{2.43}$$
$$\boldsymbol{\varepsilon}(z) = \mathbf{B}(z)\mathbf{e}_s$$

At each fiber, the differential increment of stress can be computed as follows:

$$\begin{bmatrix} d\sigma_x \\ d\sigma_z \\ d\tau_{xz} \end{bmatrix} = \frac{\partial \boldsymbol{\sigma}}{\partial \boldsymbol{\varepsilon}} \begin{bmatrix} d\varepsilon_x \\ d\varepsilon_z \\ d\gamma_{xz} \end{bmatrix} \tag{2.44}$$
$$d\boldsymbol{\sigma} = \mathbf{D}_t d\boldsymbol{\varepsilon}$$

Where $\mathbf{D}_t$ is the tangent stiffness matrix of a fiber, recall that, because of the post-crack anisotropic behaviour, tangent constitutive matrix of concrete will be in general full. Therefore the derivatives must be taken with respect to every strain component:

Further, transverse equilibrium is imposed independently at each fiber by condensing the σ_z component in (2.44).

$$\begin{bmatrix} d\sigma_x \\ d\tau_{xz} \end{bmatrix} = \hat{\mathbf{D}}_t \begin{bmatrix} d\varepsilon_x \\ d\gamma_{xz} \end{bmatrix} \tag{2.45}$$

Where $\hat{\mathbf{D}}_t$ is the condensed $[2 \times 2]$ constitutive matrix of the fiber including the reinforcing steel smeared in it. Now it is possible to compute the derivative of the normal and shear stress with respect to X by means of the chain rule and using equations (2.43) and (2.45):

$$\frac{\partial \boldsymbol{\sigma}}{\partial x} = \frac{\partial \boldsymbol{\sigma}}{\partial \boldsymbol{\varepsilon}} \frac{\partial \boldsymbol{\varepsilon}}{\partial \mathbf{e}_s} \frac{d\mathbf{e}_s}{dx} = \hat{\mathbf{D}}_t \mathbf{B}(z) \frac{d\mathbf{e}_s}{dx} \tag{2.46}$$

The derivatives of the generalized stresses are computed by direct integration

as:

$$\begin{bmatrix} \frac{d\mathbf{N}_x}{dx} \\ \frac{d\mathbf{M}_y}{dx} \\ \frac{d\mathbf{V}}{dx} \end{bmatrix} = \iint_A \begin{bmatrix} 1 & 0 \\ z & 0 \\ 0 & 1 \end{bmatrix} \begin{bmatrix} \frac{\partial \sigma_x}{\partial x} \\ \frac{\partial \tau_{xz}}{\partial x} \end{bmatrix} dA$$
$$\frac{d\mathbf{s}_s}{dx} = \iint_A \mathbf{A}(z)\hat{\mathbf{D}}_t\mathbf{B}(z)dA\frac{d\mathbf{e}_s}{dx} = \mathbf{K}_s\frac{d\mathbf{e}_s}{dx} \tag{2.47}$$

In the above equations, the **A** matrix is used to integrate the stress of a point to a generalized sectional force, while **B** is used to interpolate local strains from the generalized sectional strains. Since in this approach matrixes **A** and **B** are different, the resulting sectional matrix will always be asymmetric. It can be also demostrated, that the obtained pair of generalized stress and strains is not energetically consistent with the actual distribution of stress and strain.

Considering that a shear force $V = \frac{dM_y}{dx}$ is applied to the section, the corresponding increment of generalized strains can be computed as:

$$\frac{d\mathbf{e}_s}{dx} = \begin{bmatrix} \frac{d\varepsilon_0}{dx} \\ \frac{d\phi_y}{dx} \\ \frac{d\gamma_m}{dx} \end{bmatrix} = \mathbf{K}_s^{-1} \begin{bmatrix} 0 \\ \frac{d\mathrm{M}_y}{dx} = V \\ 0 \end{bmatrix} \tag{2.48}$$

The normal stress gradient ($\frac{\partial \sigma_x}{\partial c}$) required in equation (2.29) is directly obtained by substituting the previous result in equation (2.46).

This formulation is an effective local sectional model (it only requires information of a single point of the frame) that satisfies inter-fiber equilibrium. Therefore this formulation is more susceptible than the dual-section analysis to be implemented within frame element. However, in this approach only monodimensional shear flows are possible. Therefore it can only be applied for in-plane bending and shear. Besides, as commented above, the stiffness matrix for this cross-section, although reflecting the coupling of tangential and normal internal forces, will be asymmetric in all cases.

Nevertheless, the type of sectional model looked for in this research is in the same line of the "*Longitudinal stiffness method*" but extended to three dimensional loading and arbitrary sectional geometry. To achive this tasks,

compatibility and equilibrium must be considered and a suitable framework of the cross-section mechanics be stablished.

2.4 Sectional analysis of composite laminated structures

A composite material is formed by the combination of two or more different materials to obtain a new material with enhanced properties, either mechanical (higher strength and stiffness, less weight, etc.), thermic (higher or less conductivity), accustic isotlation, chemical (durability, corrosion resistance), etc. In this sense, plain concrete is a composite material formed by aggregates and cement. When more than one reinforcing material is used, the composite is called hybrid, this is the case of reinforced concrete.

Other modern composite materials are made with metal, ceramic or polymer matrix reinforced with a variety of fibers or particles (for instance: fiberglass, graphite, etc.). Composite laminates are constructed by stacking layers of different composite materials or fiber orientations, typically forming thin-panel members.

Extensively explanation of the mechanical behaviour of these materials can be found in: Nettles (1994), Reddy (1997), Barbero (1998), Oller (2002) among others.

The use of modern composite materials has been notably increasing in the last decades in all types of engineering structures: aerospace, automobile, medical prosthesis, etc. In civil engineering, these materials have been traditionally used as repairing reinforcements: Priestley, Seible and Calvi (1996); Fam, et al. (2002); Oller, Cobo and Mari (2004). Although scant, they have also been used as the main material in some bridges: Cobo et al (2000), Sobrino and Pulido (2002).

As a rule, composite laminates present anisotropic response with strong coupling of bending, extension and shear. The stack arrangement produces irregular stress distribution on the cross-section and out-of-plane stresses

(auto-equilibrated shear stresses and normal stress in transverse direction) producing delamination, effect that strongly limits the performance of these materials. The sectional analysis of this type of structures must be capable of reproducing these multi-axial stress state.

Currently, several laminate sectional models are available in the literature, in general these approaches can be classified in two groups: equivalent single layer theories and layerwise theories. In the following an overview of these approaches is presented.

Equivalent single layer theories (ESL)

Equivalent single layer theories (ESL) are derivations of the 3D elastic problem based on suitable fixed patterns of the deformation or the stress fields along the laminate thickness. Therefore, they are equivalent to the *fixed-pattern approaches* described above. These assumptions allow the reduction of the problem dimension, from 3D to 2D in plate problems and from 3D to 1D in beam problems.

The simplest ESL theory available is the "*Classical laminated theory*" (CLT) which is an extension of the NB beam theory (for beams) or the Kirshoff theory (for plates) to composite structures. In this theory, shear deformation is neglected. It is followed by the "*First order shear deformation theory*" (FSDT) which in turn is an extension of the Timoshenko theory of beams and the Reissner-Mindlin theory of plates. This theory accounts for shear deformation keeping the plane-section hypothesis.

In both theories mentioned above, the inextensibility along the element thickness (or section distortion) can be removed to account for delamination.

Although considering the shear deformation, FSDT requires shear correction factors which are difficult to determine for arbitrary laminated sections. This is so because the shear correction factor not only depends on the lamaninate geometry, but also on the loading and boundary conditions, this aspects gain importance because of the anisotropic behaviour of the composite.

Higher order theories have been developed to describe more complicated

displacement fields along the thickness in order to eliminate the need of a shear correction factor. However, additional unknowns are often introduced that are difficult to interpret in physical terms.

One high order theory is the "*Reddy's third order theory*", Reddy (1996) and Reddy (1997). Reddy's approach is to use a third order field for the section's normal displacement obtaining a parabolic strain profile. The theory eliminates the need of a shear correction factor without introducing additional unknowns. This approach can be classified as a particular case of a fixed-strain pattern approach in which a second order shear strain profile is used. By energetically consistant integration of the shear forces there's no need of shear correction factors.

Auricchio and Sacco (2003) have proposed a series of mixed variational ESLT formulations where shear correction factors are also eliminated. In these formulations shear stress profile are represented by either independent quadratic functions or by satisfying the 3D equilibrium and compatibility in a weak fashion from a variational principle.

Although FSDT represent a good compromise between accuracy and simplicity, their applicability to all composite structure problem is limited. The accuracy of the global predicted response tends to degrade with the mainate thickness. Also, these models often fail to describe the state of stress and strain near geometric and material discontinuities (so called "*free edge effect*"), structural zones were concentration of stresses typically take place.

Layerwise theories (LWT)

Layerwise teories (LWT) explicitely consider the equilibrium and compatitibility at the inter-fiber level. These theories are obtained assuming independent deformation within each layer; linear piecewise functions are typically considered to describe the section's displacement field.

LWT are capable of much more correct kinematic representation of moderate to severe section's warping associated to thick laminates. On the other hand, the number of unknowns functions to be solved depend on the number of

layers of the laminate. Some LWT formulations have been proposed, among others, by Barbero (1992), Reddy (1996), Carrera (1999).

Other approaches

The "*Variational asymptotic beam sectional analysis*" (VABS) (Cesnik and Hodges, 1994; Yu et al., 2002) is a procedure that splits the full 3D problem into a 2D sectional analysis and a 1D beam analysis. This is done by means of a suitable scheme to asymptotically approximate the strain energy up to any desire order (in the mentioned work a second order approximation of the strain energy is used) so called "*Variational asymptotic method*".

2.5 Discussion about the state of the art

The understanding of shear resistant mechanisms of RC beam elements have experienced considerable increase in the last three decades. After a suitable characterization of the material response, models for the cross-section analysis have been developed with different degree of thoroughness and accuracy. Currently, there is no sectional theory that has been proved to suitable evaluate the complete 3D interactions among the possible six internal forces and general geometry and reinforcement arrangement that is generated after cracking.

In the simplified models presented, the influence of transverse reinforcement arragement and other sources of bidimensional shear flows are limited by the approach of layer discretization and the fact that the compatibility is not satisfied along the distortion field. Implicitly, the discretization and/or the fixed-pattern used implicitly contains a-priori hypotheses on the shear flow direction and the way the effects of transverse reinforcement is effectively distributed.

In reinforced concrete, the role of section's distortion is crucial. In a first instance because it is the distortion of the sectional shape that makes possible that transverse reinforcements be loaded. On the other hand, the stresses

that a reinforcing bar transmits to concrete in a point are effectively distributed to other fibers thanks to compatibility of the fiber's distortion. The efficiency of a transverse reinforcement arrangement and the evolution of the bearing mechanisms from pre-cracking to collapse can only be simulated in an objective way if distortion is considered in the sectional model.

High level sectional analysis models have also been developed to accurately analyse composite laminated structures. The relevance of a correct sectional displacement field for these highly anisotropic materials has been recognized, mostly in a 1D domain to account for delamination of the stack of laminae. To this extent, it was considered worthy to include transverse distortion in some sectional analysis theories. Although due to different causes, the interesest of an accurate sectional model capable of representing the behaviour of complex materials is common to several specializations of structural engineering.

It is considered that a more sophisticated cross-sectional model that could take into account the sectional distortion considering the cross section as a 2D domian was of special importance for achieve a realistic and accurate analysis of general RC sections. Moreover, to propertly analyze the evolution of damage in the material the warping and distortion should be non-fixed.

An original proposal to compute the sectional displacement field is presented in the next chapter based on the the satisfaction of 3D mechanical principles in a variational form especially derived to this matter. An advantage of the proposal is that it does not requires additional degrees of freedom different from those associated to traditional generalized deformation of a frame element.

Chapter 3

A generalized beam theory

3.1 Introduction

The most basic theory capable of analyzing beam-column elements is the Navier-Bernoulli (NB) approach. It is based on the assumption that plane sections (PS) remain plane after the deformation and orthogonal to the beam's axis.

The use of the NB theory for beam-columns is well extended since it is capable of reproducing correctly the actual response of this type of members under combined axial forces and bending moments (referred to as normal generalized stresses).

The drawback of the NB theory is its incapability of accounting for shear forces and torsion moments in a general way (referred to as tangential generalized stresses). When tangential stress effects are important in the response of the element, more refined theories must be used.

Several beam theories are available to consider tangential stress effects with different levels of generality. After setting a general hypotheses framework, in the following, some of the most important approaches will be described with the aim of identifying their common aspects, differences, benefits and drawbacks.

The presentation of these theories will be organized distinguishing between "*classical approaches*" (i.e. theories which can be found in the classical strength of materials or theory of elasticity literature) and "*new approaches*" (i.e. theories which have been presented more recently in the literature).

It is worthy to emphasize that, besides the NB theory, all the more-advanced models available can be obtained by superimposing an additional distortion field to the PS displacement field. In other words, the total displacement field on the section is enhanced, with respect to the PS, in order to enable a more accurate description of the tangential stress effects in the modeling. It will be seen that by choosing particular forms for the distortion field, the described beam theories can be deduced. In general, the different forms of the distortion field give exact solution for particular loading cases under assumptions of isotropy and homogeneity.

Finally, a beam theory is proposed that generalizes the use of the distortion field as an enhancement of the PS field for heterogeneous and anisotropic beam elements under general 3D loading. The aim is to account for 3D effects that occurs under the mentioned situations using a beam approach.

In the following, the section is defined in the plane $y - z$ with normal x parallel to the beam axis, see fig. 3.1. The beam axis intersects the section in point defined by the position vector $\mathbf{r}_0$. At this position, there are six generalized section displacements defined: three rigid body translations in each direction (u_0, v_0, w_0) and the corresponding rigid body rotations (θ_x, θ_y, θ_z).

3.2 General hypotheses

Firstly, the general assumptions common to all beam theories are developed. These assumptions are presented in a general fashion; then, specific theories are deduced introducing more restrictive considerations on the displacement/strain fields.

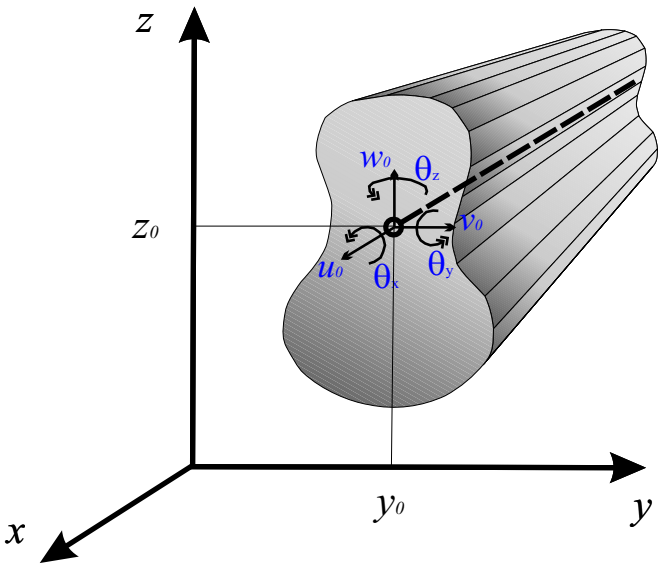

Figure 3.1: Local axes in the sectional domain

Displacement decomposition

The displacement field is decomposed in two parts as indicated in equation (3.1), see fig. 3.2.

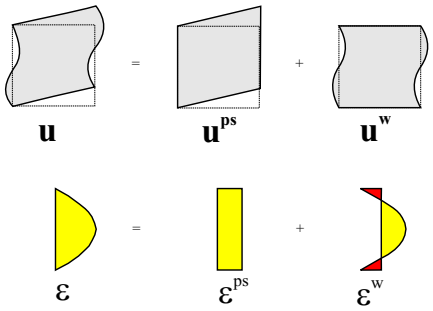

Figure 3.2: Typical PS-distortion decomposition

$$\mathbf{u} = \mathbf{u}^{ps} + \mathbf{u}^{w} \tag{3.1}$$

Where $\mathbf{u}^{ps}$ is a "plane-section" (PS) displacement field, consistent with the beam theory of Navier-Bernoulli which will be described bellow.

The other component of the displacement ($\mathbf{u^w}$) is a 3D field which are referred to, equivalently, as "*3D distortion*", or "*warping-distortion*". Since $\mathbf{u^w}$ is a three component field, it actually can reproduce both out-of-plane warping and section's change of shape.

It should be noticed that, in this work, warping is considered as any displacement additional to the PS field of the Navier-Bernoulli beam theory. Therefore, it can be itself a planar deformation in some theories. This is the case of the Timoshenko beam theory.

Small strains

Strains are considered small. Therefore, they are computed as linear combination of the first derivatives of the displacement field by means of the standard linear operator $\mathbf{L}$ as follows:

$$\boldsymbol{\varepsilon} = \mathbf{L}\mathbf{u} \tag{3.2}$$

$\mathbf{L}$ can be further divided in the following two linear operators:

$$\mathbf{L} = \mathbf{L}_x + \mathbf{L}_{yz} \tag{3.3}$$

Where:

$$\mathbf{L}_x = \begin{bmatrix} \frac{\partial}{\partial x} & 0 & 0 & 0 & 0 & 0 \\ 0 & 0 & 0 & \frac{\partial}{\partial x} & 0 & 0 \\ 0 & 0 & 0 & 0 & \frac{\partial}{\partial x} & 0 \end{bmatrix}^T = \mathbf{E}_x \frac{\partial}{\partial x} \tag{3.4}$$

$$\mathbf{L}_{yz} = \begin{bmatrix} 0 & 0 & 0 & \frac{\partial}{\partial y} & \frac{\partial}{\partial z} & 0 \\ 0 & \frac{\partial}{\partial y} & 0 & 0 & 0 & \frac{\partial}{\partial z} \\ 0 & 0 & \frac{\partial}{\partial z} & 0 & 0 & \frac{\partial}{\partial y} \end{bmatrix}^T \tag{3.5}$$

Considering the displacement decomposition (3.1) and the linearity of the $\mathbf{L}$ operator, the strain field can be also decomposed in an additive way in a part arising from the PS displacements and another part due to the section's distortion.

$$\boldsymbol{\varepsilon} = \mathbf{L}\mathbf{u}^{ps} + \mathbf{L}\mathbf{u}^{w} = \boldsymbol{\varepsilon}^{ps} + \boldsymbol{\varepsilon}^{w} \tag{3.6}$$

Stresses

Following (3.6) we introduce a similar decomposition also for the stress field $\boldsymbol{\sigma}$, i.e.:

$$\boldsymbol{\sigma} = \boldsymbol{\sigma}^{ps} + \boldsymbol{\sigma}^{w} \tag{3.7}$$

Where $\boldsymbol{\sigma}^{ps}$ is the stress field detected in a Navier-Bernoulli beam theory and $\boldsymbol{\sigma}^{w}$ is the enhanced stress. It is interesting to observe that relation (3.7) is trivially satisfied for the case of linear elastic materials. However, for more general conditions (such as inelastic materials), it is possible to prove the validity of equation (3.7) in an incremental format which still makes possible to use it.

3.3 Classical approaches

3.3.1 Theory of Navier-Bernoulli

The theory of beams of Navier-Bernoulli is based on the assumption that plane cross-sections remain plane after deformation and orthogonal to the beam axis. This statement imposes the following relationship between the beam's axis deflections and rotations:

$$v_0' - \theta_z = 0 \qquad w_0' + \theta_y = 0 \tag{3.8}$$

Where v_0 and w_0 are the beam axis deflections in the y and z directions respectively. θ_y and θ_z are the section rotations along y and z axis respectively.

In this theory the displacement field is completely defined using only the previous assumptions. Hence, the distortion field in (3.1) is null, $\mathbf{u}^{w} = \mathbf{0}$.

Vector $\mathbf{u}^{ps}$ is computed, using (3.8), as follows:

$$\begin{bmatrix} u^{ps} \\ v^{ps} \\ w^{ps} \end{bmatrix} = \begin{bmatrix} 1 & 0 & 0 & 0 & z & -y \\ 0 & 1 & 0 & -z & 0 & 0 \\ 0 & 0 & 1 & y & 0 & 0 \end{bmatrix} \begin{bmatrix} u_0 \\ v_0 \\ w_0 \\ \theta_x \\ \theta_y = -w_0' \\ \theta_z = v_0' \end{bmatrix} \tag{3.9}$$

$$\mathbf{u}^{ps}(x,y,z) = \mathbf{N}^{ps}(y,z)\mathbf{u}_s(x)$$

In (3.9) $\mathbf{u}_s$ is a vector whose components are the displacements and rotations of the beam's axis.

The strain field resulting from $\mathbf{u}^{ps}$ is, after applying the $\mathbf{L}$ operator, as follows:

$$\boldsymbol{\varepsilon}^{ps} = \mathbf{L}_x\mathbf{u}^{ps} + \mathbf{L}_{yz}\mathbf{u}^{ps} = \begin{bmatrix} u^{ps\prime} \\ 0 \\ 0 \\ v^{ps\prime} \\ w^{ps\prime} \\ 0 \end{bmatrix} + \begin{bmatrix} 0 \\ 0 \\ 0 \\ -\theta_z \\ \theta_y \\ -\theta_x + \theta_x \end{bmatrix} = \begin{bmatrix} u_0' + z\theta_y' - y\theta_z' \\ 0 \\ 0 \\ v_0' - z\theta_x' - \theta_z \\ w_0' + y\theta_x' + \theta_y \\ 0 \end{bmatrix}$$

Taking into account (3.8), one may write

$$\boldsymbol{\varepsilon}^{ps} = \begin{bmatrix} u_0' + z\theta_y' - y\theta_z' \\ 0 \\ 0 \\ -z\theta_x' \\ y\theta_x' \\ 0 \end{bmatrix}$$

The previous equation can be rearranged in a matrix form

$$\begin{bmatrix} \varepsilon_x^{ps} \\ \varepsilon_y^{ps} \\ \varepsilon_z^{ps} \\ \gamma_{xy}^{ps} \\ \gamma_{xz}^{ps} \\ \gamma_{yz}^{ps} \end{bmatrix} = \begin{bmatrix} 1 & 0 & 0 & 0 & z & -y \\ 0 & 0 & 0 & 0 & 0 & 0 \\ 0 & 0 & 0 & 0 & 0 & 0 \\ 0 & 0 & 0 & -z & 0 & 0 \\ 0 & 0 & 0 & y & 0 & 0 \\ 0 & 0 & 0 & 0 & 0 & 0 \end{bmatrix} \begin{bmatrix} \varepsilon_0 \\ \gamma_{0y} \\ \gamma_{0z} \\ \phi_x \\ \phi_y \\ \phi_z \end{bmatrix} \tag{3.10}$$

$$\boldsymbol{\varepsilon}^{ps} = \mathbf{B}^{ps}(y,z)\mathbf{e}_s(x)$$

Where $\mathbf{B}^{ps}(y,z)$ is the strain interpolation matrix according to the PS hypothesis. The vector of generalized strains of the section or beam's strains has been defined as:

$$\mathbf{e}_s(x) = \begin{bmatrix} \varepsilon_0 \\ \gamma_{0y} \\ \gamma_{0z} \\ \phi_x \\ \phi_y \\ \phi_z \end{bmatrix} \tag{3.11}$$

In $\mathbf{e}_s$, ε_0 is the beam axis elongation, γ_{0y} and γ_{0z} are the generalized shear deformation in the directions y and z, ϕ_x is the beam torsion curvature, ϕ_y and ϕ_z are the bending curvatures along y and z axis.

Notice that only the subset of the generalized strains:

$$\mathbf{e}_s^*(x) = \begin{pmatrix} \varepsilon_0 \\ \phi_x \\ \phi_y \\ \phi_z \end{pmatrix} \tag{3.12}$$

is relevant in the Navier-Bernoulli beam theory. A shorter form of equation 3.10 is:

$$\begin{bmatrix} \varepsilon_x^{ps} \\ \varepsilon_y^{ps} \\ \varepsilon_z^{ps} \\ \gamma_{xy}^{ps} \\ \gamma_{xz}^{ps} \\ \gamma_{yz}^{ps} \end{bmatrix} = \begin{bmatrix} 1 & 0 & z & -y \\ 0 & 0 & 0 & 0 \\ 0 & 0 & 0 & 0 \\ 0 & -z & 0 & 0 \\ 0 & y & 0 & 0 \\ 0 & 0 & 0 & 0 \end{bmatrix} \begin{bmatrix} \varepsilon_0 \\ \phi_x \\ \phi_y \\ \phi_z \end{bmatrix} \tag{3.13}$$

$$\boldsymbol{\varepsilon}^{ps} = \mathbf{B}^{ps*}(y,z)\mathbf{e}_s^*(x)$$

The following aspects are remarkable:

- The strains components related to section's change of shape or distortion, namely ε_y^{ps}, ε_z^{ps} and γ_{yz}^{ps}, are always null for this theory.
- The in-plane shear strains, γ_{xy}^{ps} and γ_{xz}^{ps}, are simply linear functions of the torsion curvature. This constraint only produces correct solutions, under tangential interal forces, in the case of circular shafts under pure torsion without shear forces.

3.3.2 Timoshenko's theory for shear forces

The Timoshenko beam theory allows considering the effects of the generalized shear strains, in a simplified manner, by means of a constant shear strain distribution along the section. The main statement of this theory is that cross-sections remain plane after deformation but not orthogonal to the beam's axis.

The angle between the cross-section and the plane orthogonal to the beam's axis is considered equal to the generalized shear strain on the corresponding plane:

$$v_0' - \theta_z = \gamma_{0y} \qquad w_0' + \theta_y = \gamma_{0z} \tag{3.14}$$

Equation (3.14) implies that the distortion field, $\mathbf{u}^{\mathbf{w}}$, has only a component in the out-of-plane direction. This additional displacement is linear and proportional to the generalized shear strain of the beam.

$$\begin{bmatrix} u^w \\ v^w \\ w^w \end{bmatrix} = \begin{bmatrix} y\gamma_{0y} + z\gamma_{0z} \\ 0 \\ 0 \end{bmatrix} = \begin{bmatrix} 0 & y & z & 0 & 0 & 0 \\ 0 & 0 & 0 & 0 & 0 & 0 \\ 0 & 0 & 0 & 0 & 0 & 0 \end{bmatrix} \begin{bmatrix} \varepsilon_0 \\ \gamma_{0y} \\ \gamma_{0z} \\ \phi_x \\ \phi_y \\ \phi_z \end{bmatrix} \tag{3.15}$$

$$\mathbf{u}^w = \mathbf{N}^w \mathbf{e}_s$$

The strain field associated to this form of $\mathbf{u}^w$ is:

$$\begin{bmatrix} \varepsilon_x^w \\ \varepsilon_y^w \\ \varepsilon_z^w \\ \gamma_{xy}^w \\ \gamma_{xz}^w \\ \gamma_{yz}^w \end{bmatrix} = \begin{bmatrix} 0 \\ 0 \\ 0 \\ \gamma_{0y} \\ \gamma_{0z} \\ 0 \end{bmatrix} = \begin{bmatrix} 0 & 0 & 0 & 0 & 0 & 0 \\ 0 & 0 & 0 & 0 & 0 & 0 \\ 0 & 0 & 0 & 0 & 0 & 0 \\ 0 & 1 & 0 & 0 & 0 & 0 \\ 0 & 0 & 1 & 0 & 0 & 0 \\ 0 & 0 & 0 & 0 & 0 & 0 \end{bmatrix} \begin{bmatrix} \varepsilon_0 \\ \gamma_{0y} \\ \gamma_{0z} \\ \phi_x \\ \phi_y \\ \phi_z \end{bmatrix} \tag{3.16}$$

$$\boldsymbol{\varepsilon}^w = \mathbf{B}^w \mathbf{e}_s(x)$$

The following aspects from the Timoshenko shear theory must be remarked:

- The distortion field only takes into account the warping of the section. Actual distortion of the shape is not considered by this theory.
- The in-plane shear strains due to the distortion field, γ_{xy} and γ_{xz}, are enhanced with respect to the PS. The current theory considers a constant distributionof the in-plane shear strains that are linearly dependent on the generalized shear deformation.

3.3.3 Saint-Venant's theory for torsion

Saint-Venant theory of torsion solves, in an "*exact*" way, the problem of an homogeneous isotropic shaft of constant cross-section with torsion moments on its ends.

Under these conditions, the distortion field consists only on the out-of-plane warping expressed by:

$$\begin{bmatrix} u^w \\ v^w \\ w^w \end{bmatrix} = \begin{bmatrix} 0 & 0 & 0 & \Psi(y,z) & 0 & 0 \\ 0 & 0 & 0 & 0 & 0 & 0 \\ 0 & 0 & 0 & 0 & 0 & 0 \end{bmatrix} \begin{bmatrix} \varepsilon_0 \\ \gamma_{0y} \\ \gamma_{0z} \\ \phi_x \\ \phi_y \\ \phi_z \end{bmatrix} \tag{3.17}$$

$$\mathbf{u}^w = \mathbf{N}^w \mathbf{e}_s$$

With the torsion curvature, ϕ_x, is constant.

The corresponding strain field is:

$$\begin{bmatrix} \varepsilon_x^w \\ \varepsilon_y^w \\ \varepsilon_z^w \\ \gamma_{xy}^w \\ \gamma_{xz}^w \\ \gamma_{yz}^w \end{bmatrix} = \begin{bmatrix} 0 \\ 0 \\ 0 \\ \frac{\partial \Psi}{\partial y}\phi_x \\ \frac{\partial \Psi}{\partial z}\phi_x \\ 0 \end{bmatrix} = \begin{bmatrix} 0 & 0 & 0 & 0 & 0 & 0 \\ 0 & 0 & 0 & 0 & 0 & 0 \\ 0 & 0 & 0 & 0 & 0 & 0 \\ 0 & 0 & 0 & \frac{\partial \Psi}{\partial y} & 0 & 0 \\ 0 & 0 & 0 & \frac{\partial \Psi}{\partial z} & 0 & 0 \\ 0 & 0 & 0 & 0 & 0 & 0 \end{bmatrix} \begin{bmatrix} \varepsilon_0 \\ \gamma_{0y} \\ \gamma_{0z} \\ \phi_x \\ \phi_y \\ \phi_z \end{bmatrix} \tag{3.18}$$

$$\boldsymbol{\varepsilon}^w = \mathbf{B}^w \mathbf{e}_s(x)$$

3.3.4 Saint-Venant's theory for stretching, bending and shear

Saint-Venant theory for stretching, bending and shear solves, in an "*exact*" way, the problem of an homogeneous isotropic shaft of constant cross-section with shear and bending moments on the extremes.

Saint-Venant assumes that the field of normal stress $\boldsymbol{\sigma}_x$ has the same distribution as in the PS hypothesis. Shear stresses exist on the cross-section which can be resolved in their components τ_{xy} and τ_{xz}. The fields of σ_y, σ_z and τ_{yz} stresses are assumed to be null. The distortion results in an out-of-plane constant warping, proportional to the shear loads and the change of shape of the cross-section due to Poisson effects.

$$\begin{bmatrix} u^w \\ v^w \\ w^w \end{bmatrix} = \begin{bmatrix} 0 & \hat{a}(y,z) & \hat{b}(y,z) & 0 & 0 & 0 \\ \hat{c}(y,z) & 0 & 0 & 0 & \hat{d}(y,z) & \hat{e}(y,z) \\ \hat{f}(y,z) & 0 & 0 & 0 & \hat{g}(y,z) & \hat{h}(y,z) \end{bmatrix} \begin{bmatrix} \varepsilon_0 \\ \gamma_{0y} \\ \gamma_{0z} \\ \phi_x \\ \phi_y \\ \phi_z \end{bmatrix} \tag{3.19}$$

$$\mathbf{u}^w = \mathbf{N}^w \mathbf{e}_s$$

The total strain field consists on the same as the PS hypothesis plus the strains due to distortion that has the following form:

$$\begin{bmatrix} \varepsilon_x^w \\ \varepsilon_y^w \\ \varepsilon_z^w \\ \gamma_{xy}^w \\ \gamma_{xz}^w \\ \gamma_{yz}^w \end{bmatrix} = \begin{bmatrix} 0 & 0 & 0 & 0 & 0 & 0 \\ A(y,z) & 0 & 0 & 0 & B(y,z) & C(y,z) \\ D(y,z) & 0 & 0 & 0 & E(y,z) & F(y,z) \\ 0 & G(y,z) & H(y,z) & 0 & 0 & 0 \\ 0 & I(y,z) & J(y,z) & 0 & 0 & 0 \\ 0 & 0 & 0 & 0 & 0 & 0 \end{bmatrix} \begin{bmatrix} \varepsilon_0 \\ \gamma_{0y} \\ \gamma_{0z} \\ \phi_x \\ \phi_y \\ \phi_z \end{bmatrix} \tag{3.20}$$

$$\boldsymbol{\varepsilon}^w = \mathbf{B}^w \mathbf{e}_s(x)$$

It should be noted that the strain field of γ_{yz} are always zero. This is so because the stress field τ_{yz} is null and the considered material is isotropic, i.e. shear stresses are decoupled from all other components.

3.4 Recent approaches

3.4.1 Reddy's third-order beam theory

The distortion field in the Reddy Third-Order Beam Theory consists on two third order polynomials along the directions y and z proportional to the two shear generalized strains respectively.

$$\begin{bmatrix} u^w \\ v^w \\ w^w \end{bmatrix} = \begin{bmatrix} \alpha_y y^3 \gamma_{0y} + \alpha_z z^3 \gamma_{0z} \\ 0 \\ 0 \end{bmatrix} = \begin{bmatrix} 0 & \alpha_y y^3 & \alpha_z z^3 & 0 & 0 & 0 \\ 0 & 0 & 0 & 0 & 0 & 0 \\ 0 & 0 & 0 & 0 & 0 & 0 \end{bmatrix} \begin{bmatrix} \varepsilon_0 \\ \gamma_{0y} \\ \gamma_{0z} \\ \phi_x \\ \phi_y \\ \phi_z \end{bmatrix}$$

$$\mathbf{u}^w = \mathbf{N}^w \mathbf{e}_s \tag{3.21}$$

Where

$$\alpha_y = \frac{4}{3} b^3 \qquad\qquad \alpha_z = \frac{4}{3} h^3$$

b and h are the section's width and height respectively.

The corresponding strain field is:

$$\begin{bmatrix} \varepsilon_x^w \\ \varepsilon_y^w \\ \varepsilon_z^w \\ \gamma_{xy}^w \\ \gamma_{xz}^w \\ \gamma_{yz}^w \end{bmatrix} = \begin{bmatrix} 0 \\ 0 \\ 0 \\ \alpha_y y^2 \gamma_{0y} \\ \alpha_z z^2 \gamma_{0z} \\ 0 \end{bmatrix} = \begin{bmatrix} 0 & 0 & 0 & 0 & 0 & 0 \\ 0 & 0 & 0 & 0 & 0 & 0 \\ 0 & 0 & 0 & 0 & 0 & 0 \\ 0 & \alpha_y y^2 & 0 & 0 & 0 & 0 \\ 0 & 0 & \alpha_z z^2 & 0 & 0 & 0 \\ 0 & 0 & 0 & 0 & 0 & 0 \end{bmatrix} \begin{bmatrix} \varepsilon_0 \\ \gamma_{0y} \\ \gamma_{0z} \\ \phi_x \\ \phi_y \\ \phi_z \end{bmatrix} \tag{3.22}$$

$$\boldsymbol{\varepsilon}^w = \mathbf{B}^w \mathbf{e}_s$$

3.5 General remarks on the presented approaches

The plane section hypothesis (PS) is a fixed kinematical constraint that gives a unique distribution of strains in the cross section as functions of the generalized strains. For general 3D loading and section's shape, the PS strains distribution is not correct. Under certain assumptions, namely homogeneity and isotropy, some *exact* solutions are available for the strain distribution in the cross-section domain.

The application of these solutions in the case of anisotropic and heterogeneous medium, as can be the case of a cracked reinforced concrete element, is necessarily an approximation.

Therefore, a beam theory general enough to consider these special cases is proposed in the following section.

3.6 Proposed beam theory for coupled 3D loading

3.6.1 Equilibrium equations

Consider the set of 3D differential equilibrium equations:

$$\mathbf{L}^T\boldsymbol{\sigma} = \mathbf{0}$$

$$\begin{aligned}
\frac{\partial \sigma_x}{\partial x} + \frac{\partial \tau_{xy}}{\partial y} + \frac{\partial \tau_{xz}}{\partial z} = 0 \\
\frac{\partial \tau_{xy}}{\partial x} + \frac{\partial \sigma_y}{\partial y} + \frac{\partial \tau_{yz}}{\partial z} = 0 \\
\frac{\partial \tau_{xz}}{\partial x} + \frac{\partial \tau_{yz}}{\partial y} + \frac{\partial \sigma_z}{\partial z} = 0
\end{aligned} \tag{3.23}$$

It can be shown that the following weighted residual form is equivalent to the previous equation.

$$\begin{aligned}
\iiint_\Omega \delta\mathbf{u}^T\mathbf{L}^T\boldsymbol{\sigma}dxdydz = 0 \\
\int_L \left(\iint_A \delta\mathbf{u}^T\mathbf{L}^T\boldsymbol{\sigma}dA \right) dx = 0
\end{aligned} \tag{3.24}$$

In the term between parentheses one can identify the equilibrium residual of a differential element of beam.

$$R(x) = \iint_A \delta\mathbf{u}^T\mathbf{L}^T\boldsymbol{\sigma}dA \tag{3.25}$$

After integrating by parts equation (3.25) in the $y-z$ domain, the following

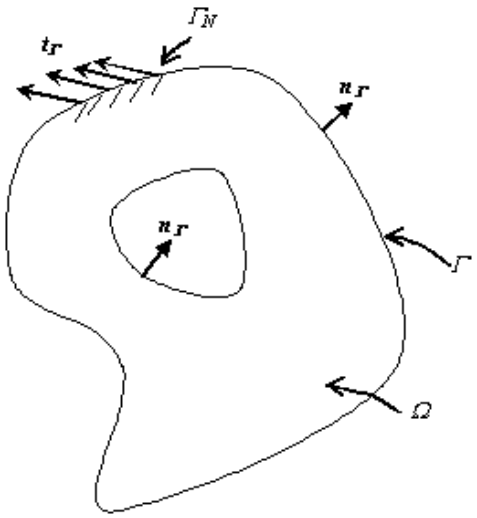

Figure 3.3: Neuman boundary conditions

result is obtained:

$$\begin{aligned} R(x) &= \iint_A \delta\mathbf{u}^T \mathbf{L}_x^T(\boldsymbol{\sigma})\, dA - \iint_A \mathbf{L}_{yz}\,(\delta\mathbf{u})^T \boldsymbol{\sigma} dA \\ &= \iint_A \delta\mathbf{u}^T \mathbf{E}_x^T \boldsymbol{\sigma}' dA - \iint_A \mathbf{L}_{yz}\,(\delta\mathbf{u})^T \boldsymbol{\sigma} dA \end{aligned}$$

$$R(x) = G(\boldsymbol{\sigma}') - F(\boldsymbol{\sigma}) \tag{3.26}$$

Where

$$G(\boldsymbol{\sigma}') = \iint_A \delta\mathbf{u}^T \mathbf{E}_x^T \boldsymbol{\sigma}' dA \tag{3.27}$$

$$F(\boldsymbol{\sigma}) = \iint_A \mathbf{L}_{yz}\,(\delta\mathbf{u})^T \boldsymbol{\sigma} dA \tag{3.28}$$

Equation (3.26) represents the projection of the equilibrium equations on the space of the displacement field used. It means that a generic body is in equilibrium in the $\mathbf{u}$ space if the overall residual along direction x is null.

If the $\mathbf{u}$ space is not general enough, there might be important equilibrium terms not captured by the space of solution. These terms exist in the exact solution space as components orthogonal to $\mathbf{u}$. Therefore, even if the residual (3.26) is null, exact solution, equation (3.23), wont be achieved.

The equilibrium residual when the PS space is used will be analyzed next.

Residual on the plane-section displacement field

In this section we shall compute the equilibrium residual by using the PS displacement field. This is, the projection of the residual on the space of $\mathbf{u}^{ps}$ computed from the PS hypothesis:

$$\mathbf{u}^{ps} = \mathbf{N}^{ps}(y,z)\mathbf{u}_s(x)$$

Substituting the variation of this field in equation (3.26):

$$\begin{aligned} R^{ps}(x) &= G^{ps}(\boldsymbol{\sigma}') - F^{ps}(\boldsymbol{\sigma}) \\ G^{ps}(\boldsymbol{\sigma}') &= \delta\mathbf{u}_s{}^T \iint_A \mathbf{N}^{psT}\mathbf{E}_x^T\boldsymbol{\sigma}' dA \\ F^{ps}(\boldsymbol{\sigma}) &= \delta\mathbf{u}_s{}^T \iint_A \mathbf{L}_{yz}\left(\mathbf{N}^{ps}\right)^T\boldsymbol{\sigma} dA \end{aligned} \tag{3.29}$$

Expanding G^{ps} and F^{ps}:

$$G^{ps} = \delta\mathbf{u}_s{}^T \iint \begin{bmatrix} \sigma_x' \\ \tau_{xy}' \\ \tau_{xz}' \\ -z\tau_{xy}' + y\tau_{xz}' \\ z\sigma_x' \\ -y\sigma_x' \end{bmatrix} dA$$

$$F^{ps} = \delta\mathbf{u}_s{}^T \iint \begin{bmatrix} 0 \\ 0 \\ 0 \\ 0 \\ \tau_{xz} \\ -\tau_{xy} \end{bmatrix} dA$$

$$R^{ps}(x) = \delta\mathbf{u}_s{}^T\mathbf{s}_s' - \delta\mathbf{u}_s{}^T \begin{bmatrix} \mathbf{0} \\ \mathbf{V}\times\mathbf{i} \end{bmatrix}$$

It can be noticed that, by making $R^{ps}(x)$ zero in each cross section for all $\delta\mathbf{u}_s$, the residual (3.29) coincides with the system of equilibrium differential equations of a beam element.

$R^{ps}(x) = 0$ represents the equilibrium among sections of the beam. It accounts for the integrity of the beam, assuming that it can only be dissociated through its vertical cross-sections. The integrity of each section itself, the equilibrium among all fibers in the section, is not considered in $R^{ps}(x)$ since, when projecting the residual (3.25) to displacement field $\mathbf{u}^{ps}$, this part of the 3D equilibrium is lost.

Tangential forces, i.e. shear forces and torsion moments, produce stresses that tends to dissociate the section's fibers, figure 3.4. It is possible then to call equilibrium at the *beam level*, or *structure level*, the one among entire sections of the beams or frames. On the other hand, the one among inner fibers will be referred to as equilibrium at the *section level*.

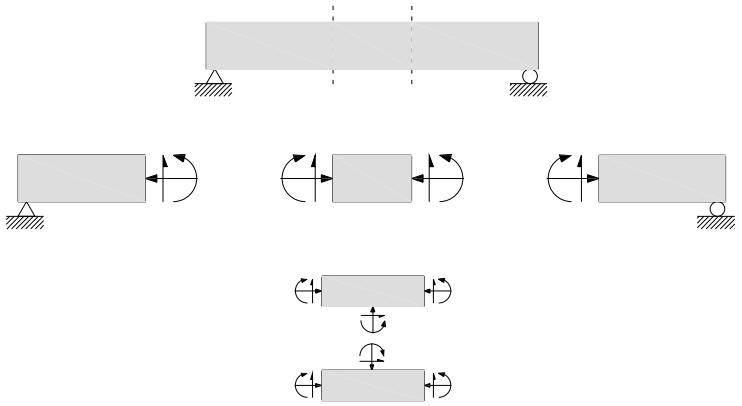

Figure 3.4: Equilibrium at the beam and sectional levels

Residual on the distortion displacement field

To consider equilibrium at the section level in a beam formulation, one needs an enhanced displacement field which allows more general deformation modes than $\mathbf{u}^{ps}$. In particular one may consider the total displacement field

as the superposition of the PS displacement field and a distortion field as the one in equation (3.1):

$$\mathbf{u} = \mathbf{u}^{ps} + \mathbf{u}^{w}$$

The decomposition of the displacement field implies, in the same way, the decomposition of the strain fields and thus of the stress field.

$$\boldsymbol{\varepsilon} = \boldsymbol{\varepsilon}^{ps} + \boldsymbol{\varepsilon}^{w}$$

$$\boldsymbol{\sigma} = \boldsymbol{\sigma}^{ps} + \boldsymbol{\sigma}^{w}$$

It should be clear that, in the limit, if the most general displacement field is chosen, the resulting formulation will be equivalent to a full 3D theory both in accuracy and in computational cost. The goal is now to properly enhance the beam's displacement field, to consider inter-fiber equilibrium, maintaining a beam element formulation.

After computing the residual (3.26) in the space of the section's distortion, $\mathbf{u}^{w}$, results:

$$R^{w}(x) = G^{w}(\boldsymbol{\sigma}') - F^{w}(\boldsymbol{\sigma}) \tag{3.30}$$

Where

$$G^{w}(\boldsymbol{\sigma}') = \iint_{A} \delta\mathbf{u}^{w\,T}\mathbf{E}_{x}^{T}\boldsymbol{\sigma}' dA \tag{3.31}$$

$$F^{w}(\boldsymbol{\sigma}) = \iint_{A} \mathbf{L}_{yz}\,(\delta\mathbf{u}^{w})^{T}\boldsymbol{\sigma} dA \tag{3.32}$$

The complete 3D equilibrium at the structure and section levels is governed by the following system of functionals. Notice that it is also an implicit system of equations with unknowns $\mathbf{u}^{ps}$ and $\mathbf{u}^{w}$.

$$\begin{aligned}\mathbf{R}^{ps}(x) &= G^{ps}(\boldsymbol{\sigma}') - F^{ps}(\boldsymbol{\sigma}^{ps}) - F^{ps}(\boldsymbol{\sigma}^{w}) = 0\\ \mathbf{R}^{w}(x) &= G^{w}(\boldsymbol{\sigma}') - F^{w}(\boldsymbol{\sigma}^{ps}) - F^{w}(\boldsymbol{\sigma}^{w}) = 0\end{aligned} \tag{3.33}$$

The system (3.33) can be weighted along the length of the element. However, following such approach will produce a system of differential beam equilibrium equations on $\mathbf{u}^{ps}$ and $\mathbf{u}^{w}$ and thus, a beam element with more degrees of freedom in general, since $\mathbf{u}^{w}$ must be discretized along the beam's length.

An alternative way to solve (3.33) is to impose $\mathbf{R}^{w}(x) = 0$ at each cross section and obtain the $\boldsymbol{\sigma}^{w}$ field as a function of $\mathbf{u}^{ps}$ at each section:

$$\begin{aligned}\boldsymbol{\sigma}^{w} &= F^{w-1}\left\{G^{w}(\boldsymbol{\sigma}') - F^{w}(\boldsymbol{\sigma}^{ps})\right\}\\ &= H^{w}\left(\boldsymbol{\sigma}', \boldsymbol{\sigma}^{ps}\right)\end{aligned} \tag{3.34}$$

This stress component can now be replaced in $\mathbf{R}^{ps}$, which represents the traditional beam equilibrium equations. The important difference is that, now the two components of stress fields are effectively considered.

Equation (3.34) can be used to define a cross-section constitutive relation. The equilibrium at the structure level can be solved using beam-column elements formulated in the standard fashion. The resulting formulation will be similar to an equivalent single layer theory (ESLT) of higher order, see chapter 2. However, no fixed shape strain or stress fields are needed, instead strain patterns they are computed directly from inter-fiber equilibrium and continuity conditions in the sectional-level.

3.6.2 Distortion spaces

Additional assumptions have to be done on the form of the distortion function in order to reduce the space of possible solutions. It is evident that if one take a completely general distortion function the beam formulation will reduce to the full 3D continuum problem.

In this section orthotropic linear elastic materials have been assumed for performing the derivations. This should not imply a lack of generality on the following analyses since extension to non-linear inelastic materials is straightforward in an incremental form.

Boundary conditions on the distortion field

To avoid trivial solutions of the equilibrium equation (3.30), a field $\mathbf{u^w}$ free of rigid body movements, must be used. In fact, it may be noticed that a $\mathbf{u^w}$ consisting on rigid translation along the three directions as well as a rigid rotation along x axis do not produce any deformation when the operator (3.5) is applied to it (this is not the case for plane rotation along axes y and z since they produce constant shear strains). One can notice that these displacements coincide with the subset of generalized displacements contained in the PS hypothesis: $\left[u_0, v_0, w_0, \theta_x\right]^T$.

In principle, the previous four displacement modes can be reproduced both by the distortion field and the PS field. This situation will produce redundancy on the total displacement (3.1) not guaranteeing a unique displacement solution. The possible redundancies can be eliminated if the distortion field satisfies the following equations:

$$\begin{bmatrix} u^R \\ v^R \\ w^R \\ \theta_x^R \end{bmatrix} = \iint_A \begin{bmatrix} 1 & 0 & 0 \\ 0 & 1 & 0 \\ 0 & 0 & 1 \\ 0 & -z & y \end{bmatrix} \begin{bmatrix} u^w \\ v^w \\ w^w \end{bmatrix} dA = \begin{bmatrix} 0 \\ 0 \\ 0 \end{bmatrix} \qquad (3.35)$$

$$\mathbf{u}^R = \mathbf{R}(\mathbf{u}^w) = \mathbf{0}$$

Relation (3.35) requires $\mathbf{u}^w$ to be orthogonal to the PS displacement, see figure 3.6.2, coming from $\mathbf{u}_s$ excluding θ_y and θ_z.

The previous condition is equivalent to impose the projection of $\mathbf{u}^R$ on any arbitrary variation of the rigid displacement $\delta\mathbf{u}^R$ to be null.

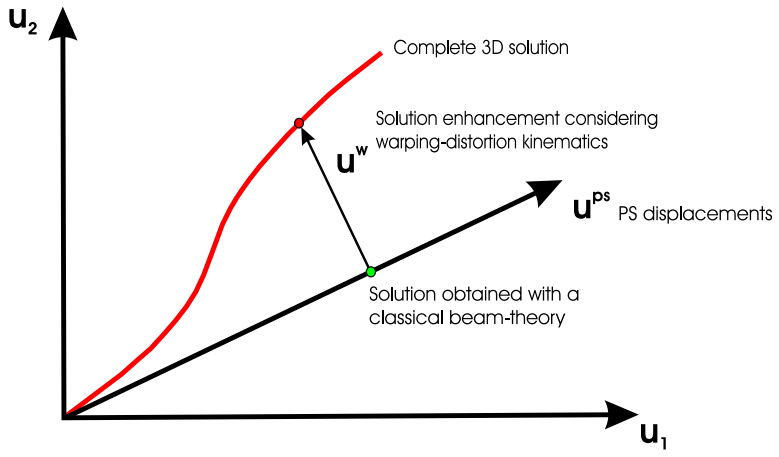

Figure 3.5: Typical solution on the PS-distortion system

$$\delta \mathbf{u}^{R^T} \mathbf{u}^R = \mathbf{R}(\delta \mathbf{u}^w)^T \mathbf{R}(\mathbf{u}^w) = 0 \tag{3.36}$$

Distortion as implicit function of the beam's strains

Assume the following form for the distortion function:

$$\mathbf{u}^w = \mathbf{U}(y,z)\hat{\mathbf{a}} \tag{3.37}$$

$\mathbf{U}$ is a collection of functions in the section's space weighted by a vector of coefficients, $\hat{\mathbf{a}}$, defining the distortion of the section. In addition, these coefficients are independent of X.

$$\begin{aligned} \boldsymbol{\varepsilon}^w &= \mathbf{L}_x \mathbf{U}(y,z)\hat{\mathbf{a}} + \mathbf{L}_{yz}\mathbf{U}(y,z)\hat{\mathbf{a}} \\ &= \mathbf{L}_{yz}\mathbf{U}(y,z) \\ \boldsymbol{\varepsilon}^{w\prime} &= 0 \end{aligned} \tag{3.38}$$

Computing the residual along this space, by substituting this distortion in (3.30) and equating to zero, one obtains:

$$R^w = \left[\iint_A \mathbf{U}^T\mathbf{E}_x^T\mathbf{D}\mathbf{B}^{ps*}dA\right]\mathbf{e}_s^{*\prime} - \left[\iint_A \mathbf{L}_y z(\mathbf{U})^T\mathbf{D}\mathbf{B}^{ps*}dA\right]\mathbf{e}_s^* - \left[\iint_A \mathbf{L}_y z(\mathbf{U})^T\mathbf{D}\mathbf{L}_y z(\mathbf{U})dA\right]\hat{\mathbf{a}} = 0 \tag{3.39}$$

The former functional equation is linear on $\mathbf{U}$. $\mathbf{e}_s^*$ is the subvector of the section's generalized strains that are relevant for the Navier-Bernoulli beam theory:

$$\mathbf{e}_s^*(x) = \begin{pmatrix} \varepsilon_0 \\ \phi_x \\ \phi_y \\ \phi_z \end{pmatrix}$$

$\mathbf{B}^{ps*}$ is the corresponding strain interpolation matrix for $\mathbf{e}_s^*$:

$$\mathbf{B}^{ps*} = \begin{bmatrix} 1 & 0 & z & -y \\ 0 & 0 & 0 & 0 \\ 0 & 0 & 0 & 0 \\ 0 & -z & 0 & 0 \\ 0 & y & 0 & 0 \\ 0 & 0 & 0 & 0 \end{bmatrix}$$

Let $\mathbf{A}_1$, $\mathbf{B}_a$ and $\mathbf{C}_1$ be the following matrixes:

$$\mathbf{A}_1 = \iint_A \mathbf{U}^T\mathbf{E}_x^T\mathbf{D}\mathbf{B}^{ps*}dA \tag{3.40}$$

$$\mathbf{B}_1 = \iint_A \mathbf{L}_y z(\mathbf{U})^T\mathbf{D}\mathbf{B}^{ps*}dA \tag{3.41}$$

$$\mathbf{C}_1 = \iint_A \mathbf{L}_y z(\mathbf{U})^T\mathbf{D}\mathbf{L}_y z(\mathbf{U})dA \tag{3.42}$$

By means of the residual in equation (3.39), the following equation can be deduced:

$$\mathbf{C}_1\hat{\mathbf{a}} = \mathbf{A}_1\mathbf{e}_s^{*\prime} - \mathbf{B}_1\mathbf{e}_s^* \tag{3.43}$$

and $\hat{\mathbf{a}}$ can be solved as:

$$\begin{aligned}\hat{\mathbf{a}} &= \mathbf{C}_1^{-1}\left\{\mathbf{A}_1\mathbf{e}_s^{*\prime} - \mathbf{B}_1\mathbf{e}_s^*\right\} \\ &= \mathbf{H}_1\begin{bmatrix}\mathbf{e}_s^* \\ \mathbf{e}_s^{*\prime}\end{bmatrix}\end{aligned} \tag{3.44}$$

Defining:

$$\boldsymbol{\xi}^* = \begin{bmatrix} \mathbf{e}_s^* \\ \mathbf{e}_s^{*\prime} \end{bmatrix} \tag{3.45}$$

the section's distortion results:

$$\mathbf{u}^w = \mathbf{U}(y,z)\mathbf{H}_1\boldsymbol{\xi}^*$$

The following remarks can be made:

- $\mathbf{u}^w$ is a linear function of the generalized strains relevant for the PS hypothesis ($\mathbf{e}_s^*$) and theirs derivatives with respect to x ($\mathbf{e}_s^{*\prime}$).
- Even that $\mathbf{u}^w$ is only function of y and z, in general there can be different fields for every section since on each one will depend on the values of $\mathbf{e}_s^*$ and $\mathbf{e}_s^{*\prime}$ who in general vary along the beam's length. This variation is neglected with this distortion function.
- The distortion field on a section is univocally determined from information on the same x coordinate.
- Non-local information is obtained from the derivatives of the generalized strains.

3.6.3 Localization of the distortion solution

The sectional distortion can be posed as a set of functions in the plane (y,z) times the four generalized strains that are relevant in the PS hypothesis and their derivatives. The distortion solution requires non-local information that appears in the form of the generalized strains derivatives. The fact that the section's distortion depends also on some generalized strains derivatives might seem odd as a first impression. This is due to dependence of the shear stress distribution on the increment of longitudinal stresses.

The goal of this section is to make $\mathbf{u}^w$ a function only of the complete vector generalized strains ($\mathbf{e}_s$). This is possible since an equilibrium relationship exists between the derivatives of generalized forces due to normal stresses and the generalized shear forces. This relationship in forces, will be used to

derive a transformation from generalized strains derivatives to generalized shear strains.

On the other hand, from (3.29) it results that the terms in $\mathbf{e}_s^{*\prime}$ are not independent, but have to satisfy certain equilibrium requirements in the domain of the beam element. The aim of this section is then to state the relationship between the generalized strains derivatives and the complete vector of generalized strains ($\mathbf{e}_s^{*\prime} \leftarrow \mathbf{e}_s$).

Particularly ε_0' and ϕ_x' can be obtained from the condition that $N_x' = 0$ and $T_x' = 0$, hence they can be *condensed* in the domain of the cross-section. ϕ_y' and ϕ_z' must satisfy a relationship with γ_{0y} and γ_{0z} implicit in the mentioned equation.

Since the generalized shear strains ($\boldsymbol{\gamma_{0s}}$) are not an input argument in the non-local solution of distortion, the relationship (3.29) can be used to obtain $\boldsymbol{\gamma_{0s}}$ given $\mathbf{e_s^*}$ and $\mathbf{e_s^{*\prime}}$.

After the previous arguments, consider that a relationship between $\mathbf{e_s}$, $\mathbf{e_s^*}$ and $\mathbf{e_s^{*\prime}}$ can be written in the following form:

$$\mathbf{e}_s = \mathbf{Q}^{-1}(\mathbf{e}_s^*, \mathbf{e}_s^{*\prime}) \tag{3.46}$$

with the inverse relationship:

$$(\mathbf{e}_s^*, \mathbf{e}_s^{*\prime}) = \mathbf{Q}\mathbf{e}_s \tag{3.47}$$

Using this expression it is possible to write:

$$\mathbf{u}^w = \mathbf{A}(\mathbf{e}_s) \tag{3.48}$$

Computation of the distortion strains is straight forward. The distortion stresses are computed as in (3.50).

$$\begin{aligned} \boldsymbol{\varepsilon}^w &= \mathbf{L}\mathbf{A}(\mathbf{e}_s) \\ \boldsymbol{\varepsilon}^w &= \mathbf{B}^w\mathbf{e}_s \end{aligned} \tag{3.49}$$

$$\begin{aligned} \boldsymbol{\sigma}^{ps} &= \int \mathbf{D} d\boldsymbol{\varepsilon}^{ps} \\ \boldsymbol{\sigma}^{w} &= \int \mathbf{D} d\boldsymbol{\varepsilon}^{w} \\ \boldsymbol{\sigma} &= \boldsymbol{\sigma}^{ps} + \boldsymbol{\sigma}^{w} \end{aligned} \tag{3.50}$$

3.6.4 Generalized stresses

The generalized stresses in the mixed (PS-distortion) displacement field can be defined by means of the Principle of Virtual Works (PTW). This is as follows:

$$\int_L \delta \mathbf{e}_s^T \mathbf{s}_s dx = \int_L \iint_A \delta \boldsymbol{\varepsilon}^T \boldsymbol{\sigma} dA dx$$

Identifying the the work densities as:

$$\delta \mathbf{e}_s^T \mathbf{s}_s = \iint_A \delta \boldsymbol{\varepsilon}^T \boldsymbol{\sigma} dA$$

$$= \iint_A \delta \boldsymbol{\varepsilon}^{psT} \boldsymbol{\sigma} dA + \iint_A \delta \boldsymbol{\varepsilon}^{wT} \boldsymbol{\sigma} dA$$

$$= \delta \mathbf{e}_s^T \left[\textstyle\iint_A \mathbf{B}^{psT} \boldsymbol{\sigma} dA + \iint_A \mathbf{B}^{wT} \boldsymbol{\sigma} dA \right]$$

The vector of generalized stress is defined as follows. Notice that it involves the traditional PS generalized stress plus an additional term that represents the stress projection on the distortion space.

$$\begin{aligned} \mathbf{s}_s &= \iint_A \mathbf{B}^{psT} \boldsymbol{\sigma} dA + \iint_A \mathbf{B}^{wT} \boldsymbol{\sigma} dA \\ \mathbf{s}_s &= \mathbf{s}_s^{ps} + \mathbf{s}_s^{w} \end{aligned} \tag{3.51}$$

3.6.5 Section's stiffness matrix

The stiffness or constitutive matrix of the cross-section can be computed by linearization of equation (3.51).

$$\dot{\mathbf{s}_s} = \iint_A \mathbf{B}^{psT}\mathbf{D}\dot{\boldsymbol{\varepsilon}}d\mathrm{A} + \iint_A \mathbf{B}^{wT}\mathbf{D}\dot{\boldsymbol{\varepsilon}}dA$$

Where $\mathbf{D}$ is a material constitutive matrix which can be of any type, in general anisotropic.

$$\dot{\mathbf{s}_s} = \iint_A \mathbf{B}^{psT}\mathbf{D}\dot{\boldsymbol{\varepsilon}}^{ps}dA + \iint_A \mathbf{B}^{psT}\mathbf{D}\dot{\boldsymbol{\varepsilon}}^{w}dA + \cdots$$
$$\iint_A \mathbf{B}^{wT}\mathbf{D}\dot{\boldsymbol{\varepsilon}}^{ps}dA + \iint_A \mathbf{B}^{wT}\mathbf{D}\dot{\boldsymbol{\varepsilon}}^{w}dA$$

$$\dot{\mathbf{s}_s} = \iint_A \left[\mathbf{B}^{psT}\mathbf{D}\mathbf{B}^{ps} + \mathbf{B}^{psT}\mathbf{D}\mathbf{B}^{w} + \mathbf{B}^{wT}\mathbf{D}\mathbf{B}^{ps} + \mathbf{B}^{wT}\mathbf{D}\mathbf{B}^{w}\right] dA\dot{\mathbf{e}_s}$$

Resulting that the section's stiffness matrix is defined as:

$$\mathbf{K}_s = \iint_A \left[\mathbf{B}^{psT}\mathbf{D}\mathbf{B}^{ps} + \mathbf{B}^{psT}\mathbf{D}\mathbf{B}^{w} + \mathbf{B}^{wT}\mathbf{D}\mathbf{B}^{ps} + \mathbf{B}^{wT}\mathbf{D}\mathbf{B}^{w}\right] dA \quad (3.52)$$

3.6.6 Special considerations for non-linear analysis

In the previous analysis sectional generalized stresses, strains and the corresponding stiffness matrix were presented as the projection of the 3D solution in a smaller space formed by the PS field and a distortion field. Passing from the full 3D domain to the PS-distortion space is possible by means of $\mathbf{B}^{ps}$ and $\mathbf{B}^{w}$ matrixes, while the former is an a priori fixed matrix, the latter is deduced from internal equilibrium at each fiber.

In case the material has a non linear behaviour, it is obvious that the *transformation* matrix, $\mathbf{B}^{w}$, can not remain fixed and still satisfy the load internal equilibrium at every load step. On the other hand using the updated matrixes to compute the new generalized stress will result in an unconsistency since the generalized stress definition; hence at each new step or iteration one might be comparing two generalized stresses defined in different spaces.

To avoid this inconsistency, when working in a non-linear problem, the matrixes used in equations (3.51) and (3.52) must belong to the same space.

This means that they should remain fixed for the whole analysis. An internal iteration is still needed to eliminate the residual R^w of equation (3.39) and then assure that the solution is also satisfied in a distortion space currently parallel to the PS space.

3.6.7 Remarks on the proposed scheme

- Isotropy or anisotropy can be directly included by using the proper form of the constitutive matrix, **D**.
- The implications in the shape of the strains ditributions are considered by means of the warping-distortion kinematics.
- Complete 3D inter-fiber equilibrium is explicitly considered.
- Different degrees of accuracy can be achieved by means of more complex spaces of the distortion field.
- Neglecting the variation of distortion along the length is a very common assumption on slender beams with compact cross-section based on the Saint-Venant Principle. This can be achieved by means of the distortion space presented in 3.6.2.
- Higher order distortion fields along x would allow to consider warping strains normal to the beam axis. Two main practical application are of interest for this effect: "warping torsion" (mentioned in the previous remark), and "shear-lag", which is rather a 2D elasticity problem than a beam problem. For these reasons such possibility is not considered in this work and it is left as possible future developments.

3.7 Closure

In general, the use of beam theories implies partial satisfaction of the full 3D equilibrium equations (3.23). It was shown that if the functional given in equation (3.26) is equated to zero only on the PS displacement space,

the system of differential equations of a beam element, in its strong form, is obtained (*equilibrium at the beam level*).

Beam differential equation satisfies the equilibrium between vertical sections without considering the equilibrium among fibers inside the section (*equilibrium at the sectional level*). To consider the latter, the functional residual must be computed in a more complex space, referred to as warping-distortion.

All beam theories derived only to satisfy the beam's differential equation neglect the portion of the equilibrium condition in the sectional level. The complete 3D equilibrium can be posed as the dual equilibrium system in equation (3.33). Where $\mathbf{R}^{ps} = 0$ represents the traditional beam equilibrium system and $\mathbf{R}^{w} = 0$ is an enhancement to recuperate the inter-fiber equilibrium, lost in the former system. Hence, the simultaneous solution of the exact solution of these two systems is equivalent to the full 3D equilibrium.

The proposed scheme consists on expressing the distortion field as a function of the generalized stresses by means of the condensation of new set of equations ($\mathbf{R}^{w} = 0$) at each section. The equilibrium among fibers can be then considered locally in the sectional domain by means of a cross-section constitutive model. The problem is separated from the beam formulation. Any beam element formulation can then be used together with the resulting sectional model.

By choosing the distortion field from specific function spaces increasing complexity it is possible to account for different effects from the full 3D problem.

Generalized stresses are consistently defined and the section's stiffness matrix is deduced by means of the Principle of Virtual Works.

Chapter 4

Cross-section numerical model

4.1 Introduction

In the previous chapter, a generalized beam theory was proposed that was able to consider the full 3D stress state due to combined loading conditions of beams with arbitrary shapes and material composition. The proposition aims to satisfy inter-fiber equilibrium conditions that traditionally beam theory is not able to achieve. This is done by considering that the complete displacement field of the section is the superposition of the traditional plane-section (PS) displacement field, used by standard beam theories, and an additional 3D field to consider the section's warping-distortion.

The problem is then defined in a dual space (plain section and warping-distortion) were equilibrium is to be imposed by means of variational methods, i.e. integral forms. It was shown that if the chosen weak form, equation (3.26), is applied to the PS displacement field, the standard set of equilibrium equations of a beam element in space is obtained.

All frame elements formulations existing in literature are derived to solve this set of equations in some way achieving different degrees of accuracy. In the context of this work, the mentioned set of equations were called *equilibrium*

at the structural level.

On the other hand there is the equilibrium in the distortion-warping space which complements the former, so each fiber is in equilibrium and compatibility among each other and maintain section's integrity. It is this proposal's aim to solve this part of the equilibrium internally in the cross-section space given the vector of sectional generalized strains:

$$\mathbf{e}_s = \begin{bmatrix} \varepsilon_x & \gamma_y & \gamma_z & \phi_x & \phi_y & \phi_z \end{bmatrix}^T$$

Therefore, a suitable cross-section model is required.

Developing of frame elements to solve the equilibrium of in the structural level is not in the scope of this work. Instead, it has been considered this part of the equilibrium can be suitably solved by means of any frame structure model while the sectional level problem is internally handled by the proposed scheme.

Solving the sectional equilibrium problem usually will require complex calculations specially if the materials have a non-linear behaviour or general shaped sections are to be analysed. The need of implementing the theory in a numerical model allowing a systematic and versatile use of it is evident.

One possibility to carry out this task is to use the finite elements method in the sectional problem. Geometrically the problem to be solved is in a bidimensional domain, i.e. the cross-section's plane, so 2D discretizations are used although the theory allows the full 3D material state to be computed as described before.

This chapter is divided in two parts. The first part deals with the implementation of the proposed model specifically in a finite element environment. In the last part, the implementation of three types of elements is described, namely:

- 2D element to simulate solid matrix materials.
- 1D element to simulate transversal reinforcements.
- Point element to simulate longitudinal reinforcements.

The last to elements are typically applied in reinforced concrete sections in whose applications this work is mainly oriented.

4.2 Finite element model

Consider the finite element (FE) discretization of the distortion field:

$$\mathbf{u}^w = \mathbf{N}^w(y,z)\mathbf{d}^w \tag{4.1}$$

Where $\mathbf{d}^w$ is the vector of distortion nodal values and $\mathbf{N}(y,z)$ is the interpolation matrix containing the shape functions.

The distortion strain field can be computed as:

$$\begin{aligned}\boldsymbol{\varepsilon}^w(y,z) &= \mathbf{L}_x\mathbf{N}^w(y,z)\mathbf{d}^w + \mathbf{L}_{yz}\mathbf{N}^w(y,z)\mathbf{d}^w \\ &= \mathbf{L}_{yz}\mathbf{N}^w(y,z)\mathbf{d}^w \\ &= \mathbf{B}^w_{yz}\mathbf{d}^w\end{aligned} \tag{4.2}$$

with

$$\mathbf{B}^w_{yz} = \mathbf{L}_{yz}\mathbf{N}^w(y,z) \tag{4.3}$$

Note that the derivatives of this strain field with respect to x are null.

The nodal values of the distortion field ($\mathbf{d}^w$) are computed to satisfy both Dirichlet type conditions and internal equilibrium at the sectional level.

The Dirichlet boundary condition shown in (3.36) guarantees that the solution is unique by imposing, in a weak-manner, that the warping-distortion displacements are orthogonal to those belonging to the PS field.

$$\delta\mathbf{u}^{R^T}\mathbf{u}^R = \mathbf{R}(\delta\mathbf{u}^w)^T\mathbf{R}(\mathbf{u}^w) = 0$$

Where the rigid body movement of the distortion field is:

$$\mathbf{R}(\mathbf{u}^w) = \iint_A \begin{bmatrix} 1 & 0 & 0 \\ 0 & 1 & 0 \\ 0 & 0 & 1 \\ 0 & -z & y \end{bmatrix} \begin{bmatrix} u^w \\ v^w \\ w^w \end{bmatrix} dA$$

As shown before, full 3D equilibrium is satisfied if the unbalanced stresses are null in the PS and in the distortion spaces, see equations (3.29) and (3.39). After the former the classical equilibrium equation of a beam element is deduced. This condition was referred to as equilibrium at the beam level. The latter represents the part of the equilibrium which is neglected by the classical beam theory casted in the following equation.

$$\begin{aligned} R^w = &\iint_A \delta\mathbf{U}^T \mathbf{E}_x^T \mathbf{D}\mathbf{B}^{ps*} dA \mathbf{e}_s^{*\prime} - \iint_A \mathbf{L}_y z(\delta\mathbf{U})^T \mathbf{D}\mathbf{B}^{ps*} dA \mathbf{e}_s^* \\ &- \iint_A \mathbf{L}_y z(\delta\mathbf{U})^T \mathbf{D}\mathbf{L}_y z(\mathbf{U}) dA = 0 \end{aligned}$$

With $\mathbf{e}_s^*$ being the subset of generalized strains relevant in the Navier-Bernoulli beam theory as defined in (3.12). $\mathbf{B}^{ps*}$ is the corresponding operator to compute strains in the PS space, defined in (3.13).

4.2.1 Dirichlet boundary conditions

By substitution of the finite element discretization in equation (4.1) on the equation of rigid body movement one obtains the projection of $\mathbf{u}^w$ on the PS space.

$$\mathbf{u}^R = \mathbf{R}(\mathbf{N}^w)\mathbf{d}^w = \iint_A \begin{bmatrix} 1 & 0 & 0 \\ 0 & 1 & 0 \\ 0 & 0 & 1 \\ 0 & -z & y \end{bmatrix} \mathbf{N}^w(y,z) dA \mathbf{d}^w$$

The weak condition to be satisfied can be posed as:

$$\mathbf{R}(\mathbf{N}^w)^T\mathbf{R}(\mathbf{N}^w)\mathbf{d}^w = \mathbf{0} \tag{4.4}$$

4.2.2 Equilibrium in the sectional level

After substituting the finite element discretization (4.1) the equilibrium in the sectional level is written as:

$$\begin{aligned} R^w = \delta\mathbf{d}^{wT} \iint_A \mathbf{N}^{wT}\mathbf{E}_x^T\mathbf{D}\mathbf{B}^{ps*}dA\mathbf{e}_s^{*\prime} - \delta\mathbf{d}^{wT} \iint_A \mathbf{B}_{yz}^{w\ T}\mathbf{D}\mathbf{B}^{ps*}dA\mathbf{e}_s^* \\ - \delta\mathbf{d}^{wT} \iint_A \mathbf{B}_{yz}^{w\ T}\mathbf{D}\mathbf{B}_{yz}^{w}dA\mathbf{d}^w = 0 \end{aligned}$$

Since the previous equation must be satisfied for any arbitrary virtual variation $\delta\mathbf{d}^w$:

$$\begin{aligned} &\iint_A \mathbf{N}^{wT}\mathbf{E}_x^T\mathbf{D}\mathbf{B}^{ps*}dA\mathbf{e}_s^{*\prime} - \iint_A \mathbf{B}_{yz}^{w\ T}\mathbf{D}\mathbf{B}^{ps*}dA\mathbf{e}_s^* \\ &- \iint_A \mathbf{B}_{yz}^{w\ T}\mathbf{D}\mathbf{B}_{yz}^{w}dA\mathbf{d}^w = \mathbf{0} \end{aligned} \tag{4.5}$$

4.2.3 Non-local solution

By subtracting equations (4.4) and (4.5) we arrive to the following system of equations with $\mathbf{d}^w$ as the only unknown:

$$\begin{aligned} &\iint_A \mathbf{N}^{wT}\mathbf{E}_x^T\mathbf{D}\mathbf{B}^{ps*}dA\mathbf{e}_s^{*\prime} - \iint_A \mathbf{B}_{yz}^{w\ T}\mathbf{D}\mathbf{B}^{ps*}dA\mathbf{e}_s^* \\ &- \iint_A \mathbf{B}_{yz}^{w\ T}\mathbf{D}\mathbf{B}_{yz}^{w}dA\mathbf{d}^w - \mathbf{R}(\mathbf{N}^w)^T\mathbf{R}(\mathbf{N}^w)\mathbf{d}^w = \mathbf{0} \end{aligned} \tag{4.6}$$

Defining:

$$\mathbf{K}_{\Delta ps} = -\iint_A \mathbf{N}^{wT}\mathbf{E}_x^T\mathbf{D}\mathbf{B}^{ps*}dA \tag{4.7}$$

$$\mathbf{K}_{ps} = \iint_A \mathbf{B}_{yz}^{w\ T}\mathbf{D}\mathbf{B}^{ps*}dA \tag{4.8}$$

$$\mathbf{K}_{ww} = \iint_A \mathbf{B}_{yz}^{w\ T}\mathbf{D}\mathbf{B}_{yz}^{w}dA + \mathbf{R}(\mathbf{N}^w)^T\mathbf{R}(\mathbf{N}^w) \tag{4.9}$$

Equation (4.6) is written as:

$$\mathbf{K}_{ps}\mathbf{e}_s^* + \mathbf{K}_{\Delta ps}\mathbf{e}_s^{*\prime} + \mathbf{K}_{ww}\mathbf{d}^w = \mathbf{0} \tag{4.10}$$

Solving for $\mathbf{d}^w$:

$$\begin{aligned} \mathbf{d}^w &= -\mathbf{K}_{ww}^{-1}\mathbf{K}_{ps}\mathbf{e}_s^* - \mathbf{K}_{ww}^{-1}\mathbf{K}_{\Delta ps}\mathbf{e}_s^{*\prime} \\ &= \mathbf{A}_1^*\mathbf{e}_s^* + \mathbf{A}_2^*\mathbf{e}_s^{*\prime} = \mathbf{A}^*\boldsymbol{\xi}^* \end{aligned} \tag{4.11}$$

Where:

$$\mathbf{A}_1^* = -\mathbf{K}_{ww}^{-1}\mathbf{K}_{ps} \tag{4.12}$$

$$\mathbf{A}_2^* = -\mathbf{K}_{ww}^{-1}\mathbf{K}_{\Delta ps} \tag{4.13}$$

$$\boldsymbol{\xi}^* = \begin{bmatrix} \mathbf{e}_s^* \\ \mathbf{e}_s^{*\prime} \end{bmatrix} \tag{4.14}$$

4.2.4 Local Solution

Finite element solution obtained in (4.11) requires information of stresses from the surroundings of the section, this is obtained by means of $\mathbf{e}_s^{*\prime}$, see figure 4.1.a. A completely local solution will solely involve information of the cross section, as shown in figure 4.1.b.

Using equilibrium conditions at the beam level (3.29) it is possible to define a relationship between $\mathbf{e}_s^{*\prime}$ and the complete vector of generalized strains $\mathbf{e}_s$. Hence only local variables are required to compute the distortion field. The procedure followed involves the reduction of the number of required degrees of freedom in the non-local model from 8 to 6 by means of static condensation. In second place, a constraint between the bending curvatures and the shear generalized strains is obtained using the equilibrium relationship between shear forces and the derivatives of the bending moments.

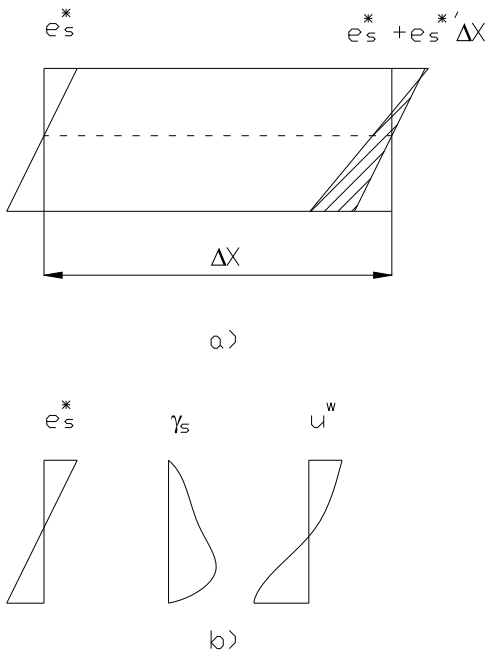

Figure 4.1: Internal equilibrium solutions: a) non-local solution b)local solution

Reduction of the required degrees of freedom

Notice that in (4.11) the distortion field is a linear function of the eight component vector $\boldsymbol{\xi}^* = \left[\mathbf{e}_s^* \quad \mathbf{e}_s^{*\prime}\right]^T$. Even though eight variables appear in the internal 3D equilibrium equation, it should be noticed that two of these components are not independent since increments of generalized axial force and torsion should be produced only by applied distributed loads. By a static condensation process, it results that only six independent variables are needed. From equation (3.29) one can write:

$$\iint_A \sigma' dA = 0$$
$$\iint_A \left(-z\tau'_{xy} + y\tau'_{xz}\right) dA = 0$$

Or equivalently

$$\iint_A \begin{bmatrix} 1 & 0 & 0 & 0 & 0 & 0 \\ 0 & 0 & 0 & -z & y & 0 \end{bmatrix} \mathbf{DB}_1^{ps*} dA \begin{bmatrix} \varepsilon_0' \\ \phi_x' \end{bmatrix} + \dots$$
$$\iint_A \begin{bmatrix} 1 & 0 & 0 & 0 & 0 & 0 \\ 0 & 0 & 0 & -z & y & 0 \end{bmatrix} \mathbf{DB}_2^{ps*} dA \begin{bmatrix} \phi_y' \\ \phi_z' \end{bmatrix} = \begin{bmatrix} 0 \\ 0 \end{bmatrix}$$

$$\bar{\mathbf{P}}_1 \begin{bmatrix} \varepsilon_0' \\ \phi_x' \end{bmatrix} + \bar{\mathbf{P}}_2 \begin{bmatrix} \phi_y' \\ \phi_z' \end{bmatrix} = \mathbf{0}$$

$$\begin{bmatrix} \varepsilon_0' \\ \phi_x' \end{bmatrix} = -\bar{\mathbf{P}}_1{}^{-1} \bar{\mathbf{P}}_1 \begin{bmatrix} \phi_y' \\ \phi_z' \end{bmatrix} = \mathbf{P} \begin{bmatrix} \phi_y' \\ \phi_z' \end{bmatrix} \tag{4.15}$$
$$\mathbf{e}_{s1}^{*\prime} = \mathbf{P} \mathbf{e}_{s2}^{*\prime}$$

Vector $\boldsymbol{\xi}^*$ can be univocally defined from the six components vector $\boldsymbol{\xi}$ as:

$$\begin{bmatrix} \mathbf{e}_s^* \\ \mathbf{e}_{s1}^{*\prime} \\ \mathbf{e}_{s2}^{*\prime} \end{bmatrix} = \begin{bmatrix} \mathbf{1} & \mathbf{0} \\ \mathbf{0} & \mathbf{P} \\ \mathbf{0} & \mathbf{1} \end{bmatrix} \begin{bmatrix} \mathbf{e}_s^* \\ \mathbf{e}_{s2}^{*\prime} \end{bmatrix} \tag{4.16}$$
$$\boldsymbol{\xi}^* = \boldsymbol{\Xi} \boldsymbol{\xi}$$

Generalized shear strains

In the proposed scheme, there is no need of a-priori kinematic constraints between the shear strain pattern and the generalized shear strains: γ_{0y} and γ_{0z}. Instead, the full 3D stress-strain field is computed solely from internal equilibrium conditions. This procedure has clear benefits in terms of correctness of the solution, accuracy and capabilities of the sectional model to reproduce more complex phenomena (i.e. non-linear shear loading might change the correct shear strain pattern, influence of different stirrups arrangements, sectional confinement or sectional distortion).

Because of the mentioned generality, the sectional generalized shear deformations are not required in the model, instead curvatures derivatives are used. Nevertheless, in order to build a standard sectional formulation and

also to know the corresponding shear deformation applicable to a frame element using this sectional model, suitable γ_{0y} and γ_{0z} shall be defined, figure 4.2.

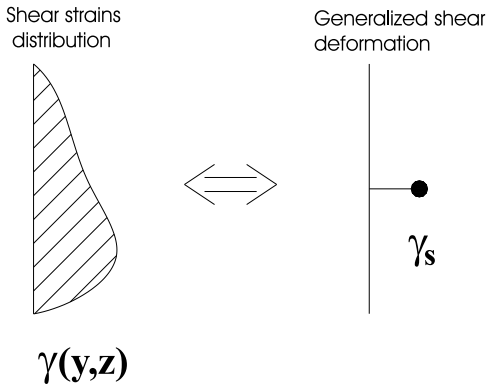

Figure 4.2: One-to-one transformation of the shear strain distribution to a generalized shear deformation of the whole section.

Basically we will use two new generalized strains that allow the standard vectors of generalized forces and strains to balance the internal virtual work (VW) performed by the stresses and strains. It is also necessary to consider compatibility requirements between torsion twist curvature (ϕ_x) and generalized shear strains located at the beam's axis ($\mathbf{r}_0 = \begin{bmatrix} y_0 & z_0 \end{bmatrix}$) since, as shown in figure (4.3), in general this point won't coincide with the shear center ($\mathbf{r}_{cs} = \begin{bmatrix} y_{cs} & z_{cs} \end{bmatrix}$); and specially on a non-linear analysis the shear center might be state dependent, i.e. not on a fixed location. This compatibility requirement is:

$$\boldsymbol{\gamma}_0 = \boldsymbol{\gamma}_{cs} + \phi_x \left(\mathbf{r}_{cs} - \mathbf{r}_0 \right) \times \mathbf{i} \tag{4.17}$$

Where $\boldsymbol{\gamma}_0$ is a vector defined by the two generalized shear strains located at the beam's axis, $\boldsymbol{\gamma}_{cs}$ is the vector of the two generalized shear strains located at the center of shear forces (i.e., point where a shear force does not produce a twist of the beam) of the section, $\mathbf{i}$ is a unit vector parallel to the beam's axis. By applying unit shear forces in the two orthogonal directions the components of $\boldsymbol{\gamma}_0$ are defined as the mean shear strain in the corresponding direction times a constant for each direction.

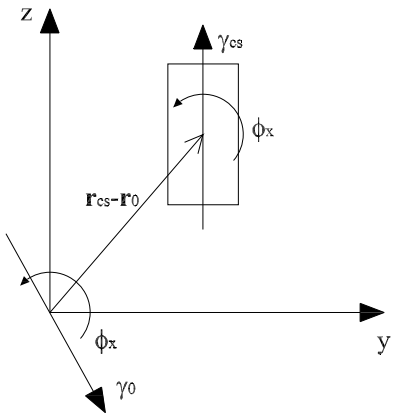

Figure 4.3: Compatibility between shear and torsion deformations

$$\boldsymbol{\gamma}_m = \frac{1}{\iint_A dA} \iint_A \begin{bmatrix} \gamma_{xy} \\ \gamma_{xz} \end{bmatrix} dA$$

$$\boldsymbol{\gamma}_{cs} = \mathbf{k}\boldsymbol{\gamma}_m$$

Where $\mathbf{k}$ is a diagonal matrix whose components are defined to guarantee energetic balance between the sectional and continuous models. Namely, the density of virtual work done by the strain and stress field shall be balanced by the density of virtual work done by the generalized stresses and strains, evaluated in the center of shear forces. Therefore, to compute the i^{th} component of $\mathbf{k}$ consider that a pure shear force is applyed to the section so that it is parallel to the i^{th} direction (at this stage the shear force is applied by means of the corresponding bending moment derivative). The virtual work produced in the sectional domain is the following:

$$VW = \iint_A \delta\boldsymbol{\varepsilon} \cdot \boldsymbol{\sigma} dA \Delta L = \delta\mathbf{e}_s \cdot \mathbf{s}_s \Delta L$$

Where $\delta\mathbf{e}_s \cdot \mathbf{s}_s$ shall be called the virtual work density and represented by VW'. The i^{th} component of $\mathbf{k}$ is found to be:

$$\iint_A \delta\boldsymbol{\varepsilon}\cdot\boldsymbol{\sigma}dA = \begin{bmatrix}\delta\varepsilon_0\\ \delta\phi_x\\ \delta\phi_y\\ \delta\phi_z\end{bmatrix}\cdot\begin{bmatrix}N_x\\ T_x\\ M_y\\ M_z\end{bmatrix} + k_i\begin{bmatrix}\delta\gamma_{my}\\ \delta\gamma_{mz}\end{bmatrix}\cdot\begin{bmatrix}V_y\\ V_z\end{bmatrix}$$

$$k_i = \frac{VW' - \delta\mathbf{e}_s^*\cdot\mathbf{s}_s^*}{\delta\boldsymbol{\gamma}_m\cdot\mathbf{V}} = \frac{SW'}{\delta\boldsymbol{\gamma}_m\cdot\mathbf{V}} \tag{4.18}$$

Where SW' is the density of virtual work performed by the shear forces.

Replacing the previous result into (4.17) the generalized shear strain can be computed for every component of $\boldsymbol{\xi}$ defining the following 6×6 matrix:

$$\begin{bmatrix}\varepsilon_0\\ \gamma_{0y}\\ \gamma_{0z}\\ \phi_x\\ \phi_y\\ \phi_z\end{bmatrix} = \begin{bmatrix}1 & 0 & 0 & 0 & 0 & 0\\ a_1 & a_2 & a_3 & a_4 & a_5 & a_6\\ a_7 & a_8 & a_9 & a_{10} & a_{11} & a_{12}\\ 0 & 1 & 0 & 0 & 0 & 0\\ 0 & 0 & 1 & 0 & 0 & 0\\ 0 & 0 & 0 & 1 & 0 & 0\end{bmatrix}\begin{bmatrix}\varepsilon_0\\ \phi_x\\ \phi_y\\ \phi_z\\ \phi_y'\\ \phi_z'\end{bmatrix}$$

$$\mathbf{e}_s = \boldsymbol{\Omega}^{-1}\boldsymbol{\xi}$$

The previous relation can be inverted as:

$$\begin{bmatrix}\varepsilon_0\\ \phi_x\\ \phi_y\\ \phi_z\\ \phi_y'\\ \phi_z'\end{bmatrix} = \begin{bmatrix}1 & 0 & 0 & 0 & 0 & 0\\ 0 & 0 & 0 & 1 & 0 & 0\\ 0 & 0 & 0 & 0 & 1 & 0\\ 0 & 0 & 0 & 0 & 0 & 1\\ b_1 & b_2 & b_3 & b_4 & b_5 & b_6\\ b_7 & b_8 & b_9 & b_{10} & b_{11} & b_{12}\end{bmatrix}\begin{bmatrix}\varepsilon_0\\ \gamma_{0y}\\ \gamma_{0z}\\ \phi_x\\ \phi_y\\ \phi_z\end{bmatrix} \tag{4.19}$$

$$\boldsymbol{\xi} = \boldsymbol{\Omega}\mathbf{e}_s$$

Which has the following closed-form solution:

$$
\begin{aligned}
b_1 &= \frac{a_6 a_7 - a_1 a_{12}}{a_5 a_{12} - a_{11} a_6} & b_7 &= \frac{a_1 a_{11} - a_5 a_7}{a_5 a_{12} - a_{11} a_6} \\
b_2 &= \frac{a_{12}}{a_5 a_{12} - a_{11} a_6} & b_8 &= -\frac{a_{11}}{a_5 a_{12} - a_{11} a_6} \\
b_3 &= -\frac{a_6}{a_5 a_{12} - a_{11} a_6} & b_9 &= \frac{a_5}{a_5 a_{12} - a_{11} a_6} \\
b_4 &= \frac{a_8 a_6 - a_2 a_{12}}{a_5 a_{12} - a_{11} a_6} & b_{10} &= \frac{a_8 a_5 - a_2 a_{11}}{a_5 a_{12} - a_{11} a_6} \\
b_5 &= \frac{a_6 a_9 - a_3 a_{12}}{a_5 a_{12} - a_{11} a_6} & b_{11} &= \frac{a_3 a_{11} - a_5 a_9}{a_5 a_{12} - a_{11} a_6} \\
b_6 &= \frac{a_6 a_{10} - a_4 a_{12}}{a_5 a_{12} - a_{11} a_6} & b_{12} &= \frac{a_4 a_{11} - a_5 a_{10}}{a_5 a_{12} - a_{11} a_6}
\end{aligned}
$$

Note that for the case of an isotropic material and if the position of the reference coordinate system coincides with the center of shears of the section, shear forces are uncoupled from all generalized stresses and only a_5, a_6, a_{11} and a_{12} will be non-zero.

Furthermore, if the section is double-symmetric then only a_6 and a_{11} will be non-zero, these two are the components linking the shear forces and the derivative of bending moments around their orthogonal direction in the simplest uncoupled case. In all situations the inverted form of eq. (4.19) is well posed.

4.2.5 Generalized stresses

The generalized stresses of the cross section, or sectional forces, are defined as the energetically equivalent forces in the space of sectional strains ($\mathbf{e}_s$). Hence the virtual work density performed by the generalized stresses, must balance the virtual work density of the stress field in the section.

$$\delta \mathbf{e}_s^T \mathbf{s}_s = \iint_A \delta \boldsymbol{\varepsilon}^T \boldsymbol{\sigma} dA \tag{4.20}$$

According to our previously posed hypotheses, both the plane section (PS) and distortion (w) components of the strain field can be written respectively as:

$$\boldsymbol{\varepsilon}^{ps} = \mathbf{B}^{ps}\mathbf{e}_s \tag{4.21}$$

and

$$\boldsymbol{\varepsilon}^{w} = \mathbf{B}^{w}_{yz}\mathbf{d}^{w} \tag{4.22}$$

Where $\mathbf{B}^{ps}$ was defined in (3.10). The virtual work density is then decomposed as:

$$\delta\mathbf{e}_s^T\mathbf{s}_s = \delta{\mathbf{e}_s}^T \iint_A \mathbf{B}^{psT}\boldsymbol{\sigma}dA + \delta{\mathbf{d}^w}^T \iint_A {\mathbf{B}^w_{yz}}^T\boldsymbol{\sigma}dA \tag{4.23}$$

The nodal values of the distortion field ($\mathbf{d}^w$) can be written as a function of the generalized strains, as was shown in section 4.2.4. The complete process included three transformations concerning internal equilibrium, condensation of redundant degrees of freedom and definition of generalized shear strains.

$$\mathbf{d}^w = \mathbf{A}^*\boldsymbol{\Xi}\boldsymbol{\Omega}\mathbf{e}_s \tag{4.24}$$

The previous transformation can be introduced in (4.23), resulting:

$$\delta\mathbf{e}_s^T\mathbf{s}_s = \delta{\mathbf{e}_s}^T \iint_A \mathbf{B}^{psT}\boldsymbol{\sigma}dA + \delta{\mathbf{e}_s}^T\boldsymbol{\Omega}^T\boldsymbol{\Xi}^T\mathbf{A}^{*T} \iint_A {\mathbf{B}^w_{yz}}^T\boldsymbol{\sigma}dA$$

and the following generalized stress definition:

$$\mathbf{s}_s = \iint_A \mathbf{B}^{psT}\boldsymbol{\sigma}dA + \boldsymbol{\Omega}^T\boldsymbol{\Xi}^T\mathbf{A}^{*T} \iint_A {\mathbf{B}^w_{yz}}^T\boldsymbol{\sigma}dA \tag{4.25}$$

A special mention must be done however in the case of non linear analysis, see also section 3.6.6. Transformation (4.24) was defined after tangent material properties at each point, namely the tangent constitutive matrix, center of shear forces, etc. Hence, as these material properties changes in a non-linear analysis the transformation (4.23) will also change; in other words, it is state-dependent.

To keep a consistent definition of the generalized stresses during a non-linear analysis, they should be computed using equation (4.25) and the initial values of $\mathbf{\Xi}$, $\mathbf{\Omega}$ and $\mathbf{A}^*$ fixed for all load steps. However, the stress field must satisfy internal equilibrium equation (4.5) at all load step. An internal iteration process on the nodal distortion vector is needed to satisfy this requirement.

4.2.6 Sectional constitutive matrix

Computing the increment of the sectional forces from equation (4.25) and taking into account the equation (4.24) one gets:

$$\dot{\mathbf{s}_s} = \mathbf{K}_s \dot{\mathbf{e}_s}$$

Where $\mathbf{K}_s$ is the sectional constitutive matrix (or sectional stiffness matrix) which can be computed as:

$$\begin{aligned}\mathbf{K}_s = &\iint \mathbf{B}^{ps\,T} D \mathbf{B}^{ps} dA + \iint \mathbf{B}^{ps\,T} D \mathbf{B}^{w}_{yz} dA \mathbf{A}^* \mathbf{\Xi\Omega} + \\ &\mathbf{\Omega}^T \mathbf{\Xi}^T \mathbf{A}^{*T} \iint \mathbf{B}^{w\,T}_{yz} D \mathbf{B}^{ps} dA + \\ &\mathbf{\Omega}^T \mathbf{\Xi}^T \mathbf{A}^{*T} \iint \mathbf{B}^{w\,T}_{yz} D \mathbf{B}^{w}_{yz} dA \mathbf{A}^* \mathbf{\Xi\Omega}\end{aligned} \tag{4.26}$$

In the previous sectional matrix, three-dimensional effects due to inter-fiber interaction are indeed included, integrated and characterized as functions of the beam generalized strains. As a result the matrix is in general full with terms out of the principal diagonal producing the coupling of any degrees of freedom contrary to typical sectional matrixes computed solely from PS hypothesis and uniaxial material behaviour, where only bending and axial force coupling can be captured.

The last statement is easily demonstrated noticing that the first integral in equation (4.26) is the stiffness matrix obtained using exclusively a PS displacement field in the cross-section.

Consider the following uniaxial tangent constitutive matrix:

$$\mathbf{D} = \begin{bmatrix} E & 0 & 0 & 0 & 0 & 0 \\ 0 & 0 & 0 & 0 & 0 & 0 \\ 0 & 0 & 0 & 0 & 0 & 0 \\ 0 & 0 & 0 & 0 & 0 & 0 \\ 0 & 0 & 0 & 0 & 0 & 0 \\ 0 & 0 & 0 & 0 & 0 & 0 \end{bmatrix}$$

after substituting it, as well as the $\mathbf{B}^{ps}$ matrix, the following PS sectional matrix results:

$$\mathbf{K}_s^{ps} = \iint \mathbf{B}^{psT} D \mathbf{B}^{ps} dA = \iint \begin{bmatrix} E & 0 & 0 & 0 & Ez & -Ey \\ 0 & 0 & 0 & 0 & 0 & 0 \\ 0 & 0 & 0 & 0 & 0 & 0 \\ 0 & 0 & 0 & 0 & 0 & 0 \\ Ez & 0 & 0 & 0 & Ez^2 & -Eyz \\ -Ey & 0 & 0 & 0 & -Eyz & Ey^2 \end{bmatrix} dA$$

In the previous integrals, if the uniaxial modulus (E) linear elastic and the section is homogenous, the sectional linear elastic mechanical properties (area, first and second moments of inertia) can be identified. If this is not the situation, this quantities are not obtained. Nevertheless, the following set of mechanical quantities are defined with the physical meaning of sectional tangent stiffness:

$$\bar{EA} = \iint E dA$$
$$\bar{EQ}_y = \iint Ez dA$$
$$\bar{EQ}_z = \iint Ey dA$$
$$\bar{EI}_{yy} = \iint Ez^2 dA$$
$$\bar{EI}_{zz} = \iint Ey^2 dA$$
$$\bar{EI}_{yz} = \iint Eyz dA$$

Where $(\bar{\bullet})$ stands to highlight that these are tangent sectional stiffness quantities coming from a sectional integration; hence they are not the multipli-

cation of the elastic modulus times the sectional mechanical quantities.

This stiffness matrix is identical to the one obtained from traditional uniaxial fiber sectional discretization. Note that the terms corresponding to the degrees of freedom of shear and torsion (2^{nd}, 3^{rd} and 4^{th} rows and columns) are not considering by this matrix. The only coupling that can be reproduced is between bending moments and axial forces due to geometric matters. If this matrix is referred to the section's center of gravity and along their principal axes, the matrix will only have terms in the principal diagonal.

$$\mathbf{K}_s^{ps} = \begin{bmatrix} \bar{EA} & 0 & 0 & 0 & \bar{EQ}_y & -\bar{EQ}_z \\ 0 & 0 & 0 & 0 & 0 & 0 \\ 0 & 0 & 0 & 0 & 0 & 0 \\ 0 & 0 & 0 & 0 & 0 & 0 \\ \bar{EQ}_y & 0 & 0 & 0 & \bar{EI}_{yy} & -\bar{EI}_{yz} \\ -\bar{EQ}_z & 0 & 0 & 0 & -\bar{EI}_{yz} & \bar{EI}_{zz} \end{bmatrix}$$

It can be seen that the former matrix is a particular case of the one resulting from the proposed sectional scheme, equation (4.26). Note that any type of constitutive matrix ($\mathbf{D}$), either isotropic or anisotropic, can be used in the proposed formulation. Three additional integrals contribute to the sectional stiffness compared to the traditional fiber section formulation allowing to properly handle inter-fiber three-dimensional processes.

The proposed sectional matrix is in general full and is able to take into account all internal forces couplings due to sectional anisotropies (namely initially anisotropic materials or cracked induced anisotropy typical on RC sections under normal and tangential loading) or section's kinematics while internal equilibrium and compatibility are both satisfied.

4.3 Algorithm

To have a compact description of the implemented algorithm, it is useful to unify all internal variables of the lower level calculations in a single vector as follows:

$$\mathbf{d} = \begin{bmatrix} \boldsymbol{\xi}^* \\ \mathbf{d}^w \end{bmatrix} \tag{4.27}$$

At a higher level computations, the *input-output* variables are the generalized sectional strains

$$\mathbf{e}_s = \begin{bmatrix} \varepsilon_0 & \gamma_y & \gamma_z & \phi_x & \phi_y & \phi_z \end{bmatrix}^T$$

The input of the algorithm will be a new $\mathbf{e}_s$ vector which can be transformed into a $\mathbf{d}$ vector in the following form:

$$\mathbf{d} = \mathbf{B}_{ds}\mathbf{e}_s \tag{4.28}$$

where, as can be seen in equations (4.16), (4.19) and (4.24), $\mathbf{B}_{ds}$ is

$$\mathbf{B}_{ds} = \begin{bmatrix} \boldsymbol{\Xi\Omega} \\ \mathbf{A}^*\boldsymbol{\Xi\Omega} \end{bmatrix} \tag{4.29}$$

In the above equations, $\mathbf{B}_{ds}$ gives a set of deformation modes for $\boldsymbol{\xi}^*$ and $\mathbf{d}^w$ for each component of $\mathbf{e}_s$. These modes are used to define the generalized stresses and stiffness matrix of the section. It was mentioned in section 3.6.6 that to be consistent with a single energetic definition of the generalized stresses in the case of non-linear behaviour, $\mathbf{B}_{ds}$ is computed only once at the beginning of the analysis with the initial state. Throughout the whole analysis, this matrix is maintained constant as a sectional property.

Latter in this section it will be shown that both internal equilibrium and consistency can be achieved if the increments of $\mathbf{d}$ resulting from non-linear iteration process are assured to be orthogonal to the deformation modes defined in $\mathbf{B}_{ds}$.

From an arbitrary given $\mathbf{d}$ vector, the generalized strains can be computed using the mean values of the strain field given by $\boldsymbol{\xi}^*$ and $\mathbf{d}^w$. In general, this transformation will be in the form of the following matrix:

$$\mathbf{e}_s = \mathbf{B}_{sd}\mathbf{d} = \begin{bmatrix} \mathbf{B}1_{sd} & \mathbf{B}2_{sd} \end{bmatrix} \begin{bmatrix} \boldsymbol{\xi}^* \\ \mathbf{d}^w \end{bmatrix} \tag{4.30}$$

Where matrix

$$\mathbf{B}1_{sd} = \begin{bmatrix} 1 & 0 & 0 & 0 & 0 & 0 & 0 & 0 \\ 0 & z_{cs} & 0 & 0 & 0 & 0 & 0 & 0 \\ 0 & -y_{cs} & 0 & 0 & 0 & 0 & 0 & 0 \\ 0 & 1 & 0 & 0 & 0 & 0 & 0 & 0 \\ 0 & 0 & 1 & 0 & 0 & 0 & 0 & 0 \\ 0 & 0 & 0 & 1 & 0 & 0 & 0 & 0 \end{bmatrix} \tag{4.31}$$

gives the contribution of ξ^* to the vector $\mathbf{e}_s$. Note that the first four components of ξ^* are present in the $\mathbf{e}_s$ vector. From the shear-torsion compatibility condition, see equation (4.17), torsion curvature affects the values of the shear generalized strains located in the reference coordinate $\mathbf{r}_0$. Quantities y_{cs} and z_{cs} are the coordinates of the center of shear forces with respect to the beam's reference axis:

$$\begin{bmatrix} y_{cs} \\ z_{cs} \end{bmatrix} = \mathbf{r}_{cs} - \mathbf{r}_0 \tag{4.32}$$

The distortion contribution to $\mathbf{e}_s$ is evaluated by the following matrix:

$$\mathbf{B}2_{sd} = \begin{bmatrix} \mathbf{0} \\ \mathbf{k}\mathbf{B}_{\gamma m} \\ \mathbf{0} \\ \mathbf{0} \\ \mathbf{0} \end{bmatrix} \tag{4.33}$$

where $\mathbf{B}_{\gamma m}$ is a matrix that extracts the mean values of the in-plane shear strain field given a distortion vector $\mathbf{d}^w$. This matrix can be computed as:

$$\mathbf{B}_{\gamma m} = \frac{1}{A} \begin{bmatrix} 0 & 0 & 0 & 1 & 0 & 0 \\ 0 & 0 & 0 & 0 & 1 & 0 \end{bmatrix} \iint \mathbf{B}^w_{yz} dA \tag{4.34}$$

$\mathbf{k}$ is a $[2 \times 2]$ diagonal matrix containing shear effective coefficients on the non-zero terms. Each component is computed as indicated in equation (4.18).

Note that given a vector of generalized strains $\mathbf{B}_{ds}$ gives a $\mathbf{d}$ vector according to certain criteria, formed from a combination of mode shapes. While, on

the other hand, $\mathbf{B}_{sd}$ extracts a vector of generalized strains from an arbitrary $\mathbf{d}$ vector just taking into consideration the mean strain values. It can be verified, and also follows from the previous reasoning, that the following product will always result in an identity matrix:

$$\mathbf{B}_{sd}\mathbf{B}_{ds} = \mathbf{I} \tag{4.35}$$

The verification will be as follows: consider a vector of internal degrees of freedom formed from a combination of modes after a certain set of sectional strains: $\bar{\mathbf{d}} = \mathbf{B}_{ds}\mathbf{e}_s$. If the generalized strains are extracted from this vector, one should obtain the same set of generalized strains given in first instance: $\mathbf{e}_s = \mathbf{B}_{sd}\bar{\mathbf{d}} = \mathbf{B}_{sd}\mathbf{B}_{ds}\mathbf{e}_s$. From which equation (4.35) results.

However, the complementary product does not give an identity matrix:

$$\mathbf{B}_{ds}\mathbf{B}_{sd} \neq \mathbf{I} \tag{4.36}$$

which means that the generalized strains extracted from an arbitrary $\mathbf{d}$ vector by means of mean values of the strain field, may not be a combination of modal shapes contained in $\mathbf{B}_{ds}$.

The previous result is important since it can be used to decompose any $\mathbf{d}$ vector into a part belonging to the space of fixed mode shapes, after which the generalized stresses are defined, and a part orthogonal to this space. This will be done in the following way: let $\mathbf{d}$ be an arbitrary vector of internal variables, then after equation (4.36)

$$\bar{\mathbf{d}} = \mathbf{B}_{ds}\mathbf{B}_{sd}\mathbf{d}$$

is the part of $\mathbf{d}$ that can be formed by a superposition of fixed mode shapes and

$$\mathbf{d} - \bar{\mathbf{d}} = (\mathbf{I} - \mathbf{B}_{ds}\mathbf{B}_{sd})\,\mathbf{d}$$

is orthogonal to all fixed mode shapes, will have null generalized strains.

To prove this statement lets extract the generalized strains from the previous vector:

$$\begin{aligned}\bar{\mathbf{e}_s} &= \mathbf{B}_{sd}\bar{\mathbf{d}} \\ &= \mathbf{B}_{sd}\left(\mathbf{I} - \mathbf{B}_{ds}\mathbf{B}_{sd}\right) \\ &= \mathbf{B}_{sd} - \mathbf{B}_{sd}\mathbf{B}_{ds}\mathbf{B}_{sd} \\ &= \mathbf{B}_{sd} - \mathbf{B}_{sd} = 0\end{aligned}$$

The previous result is useful to assure that during internal iterations of $\mathbf{d}$ there are no spurious changes of the generalized strains $\mathbf{e}_s$.

The algorithm to compute the state of a cross-section is described in the flow chart shown in figure 4.5.

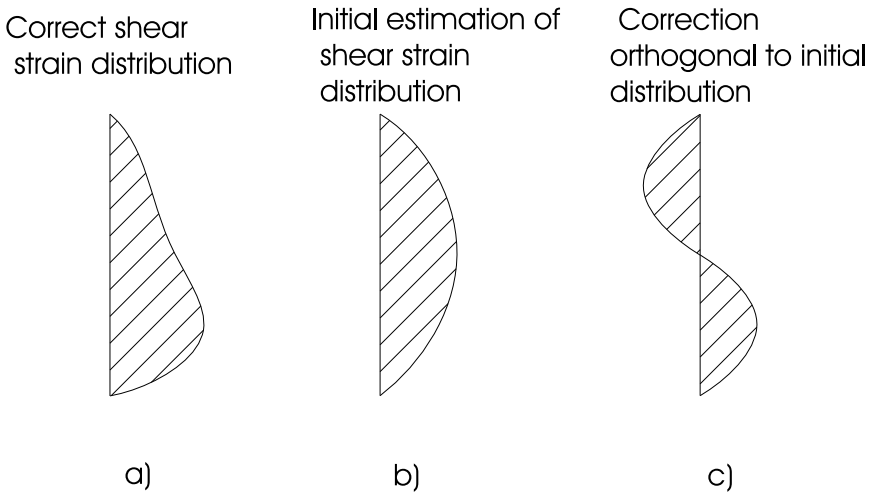

Figure 4.4: Strain field decomposition. a) Total strain field, b) strain combined from fixed mode shaped, c) orthogonal iterative component

4.4 Library of finite elements

A computer code was written to implement the presented cross-section model. As was already mentioned, this model uses a specific plane finite element model to compute the section's distortion. A full 3D stress-strain state is obtained at every point of the section. This is successfully done by means of the proposed scheme for the 3D equilibrium conditions described above. Virtually, this procedure offers the same level of information as a

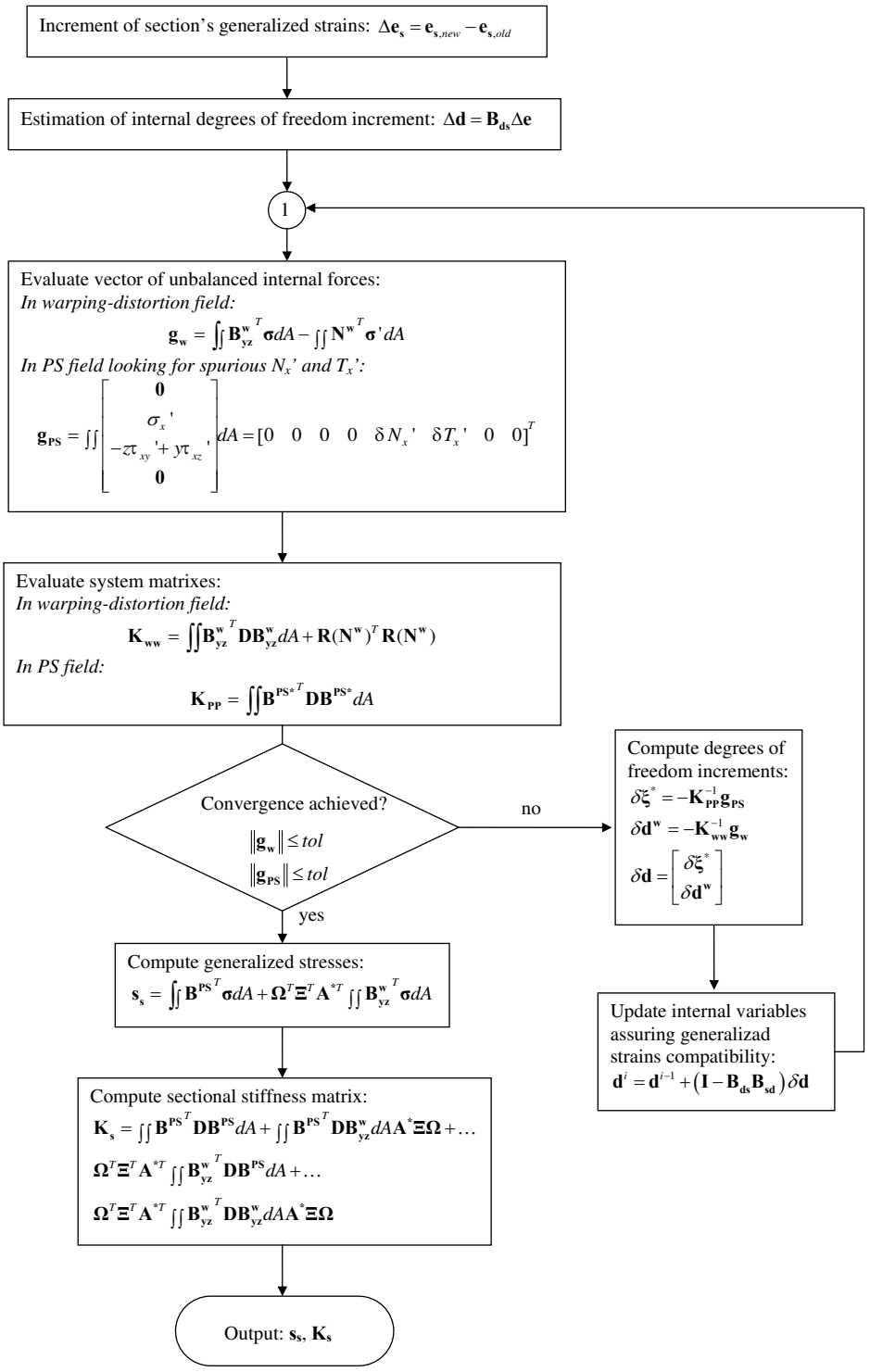

Figure 4.5: Sectional model flow chart.

full solid model of the structure but avoiding complex and expensive finite element computations.

It is an aim of this thesis to apply the proposed model to the study of reinforced concrete (RC) sections under fully coupled loading, more precisely skew bending-shear-torsion-axial force loading. A set of finite elements where implemented to discretize the section's domain. The typical components of a reinforced concrete frame element are projected into the section's plane, the components are then represented by the corresponding bidimensional objects, see figure 4.6.

In this way, a 2D plane element can be used to represent solid parts of the frame, like can be the concrete matrix. Line elements in the section's plane represents lateral reinforcements that can be or not inclined with respect to the section's plane (not contained in the section's plane). Line elements can also simulate a family of lateral reinforcements with different inclinations that might have the same projection on the section. Finally, point elements are used to simulate longitudinal reinforcements that rather intersects the section's plane.

4.4.1 2D finite elements for matrix of solid material

Bidimensional elements are employed to simulate solid parts of the cross section. The 2D element type currently available in the written compute code is a four nodes quadrilateral with three degrees of freedom at each node corresponding to the three-dimensional components of the distortion part of the section displacement.

Additional degrees of freedom include the four components of the PS section's generalized strains ($\mathbf{e}_s$) and their derivatives ($\mathbf{e}'_s$) all cast in the $\boldsymbol{\xi}^*$ vector. This gives a total of twenty degrees of freedom for each element. It must be noticed, however, that the eight degrees of freedom in $\boldsymbol{\xi}^*$ are common to all elements in the section.

For distortion interpolation, first order Lagrange polynomials are used. Distortion strains ($\boldsymbol{\varepsilon}^w$) are interpolated by means of the corresponding $\mathbf{B}^w_{yz}$

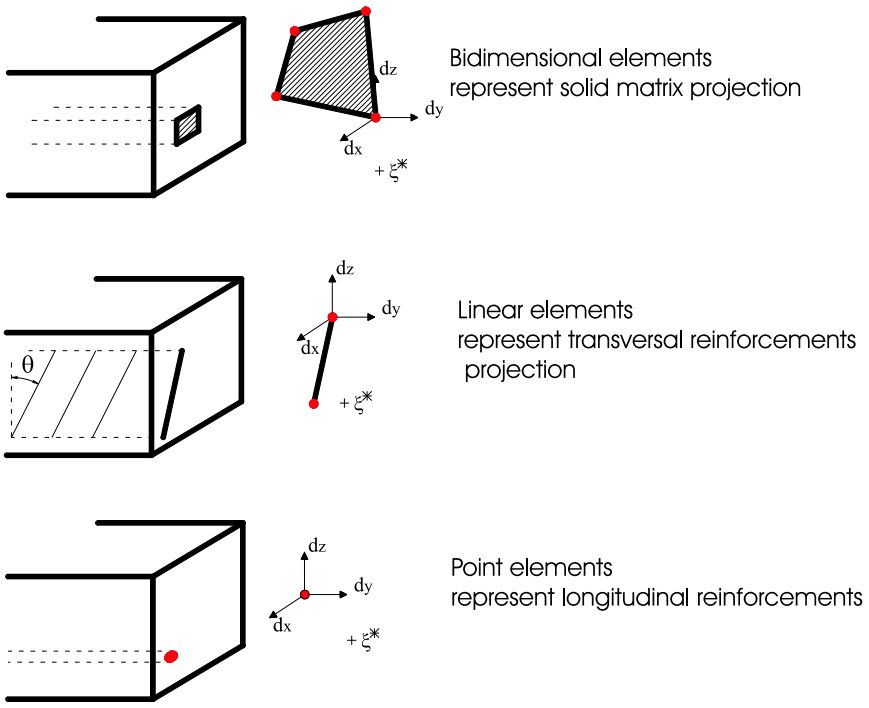

Figure 4.6: In-plane elements implemented for sectional discretization.

matrix, see equation (4.2). Gauss-Legendre quadrature with four integration points was used to integrate over these elements.

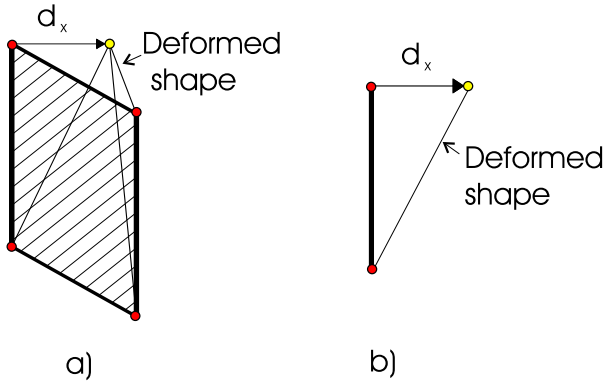

Figure 4.7: Linear shape functions: a) 2D element b)1D element

4.4.2 1D finite elements for lateral reinforcements

Unidemensional elements uses linear Lagrange polynomials as shape functions with two nodes making a total of fourteen degrees of freedom; three nodal values of distortion at each node and the eight generalized quantities in $\boldsymbol{\xi}^*$. A Gauss-Legendre quadrature with a single integration point was used.

To perform the surface integrals defined above along the line elements some special considerations must be taken. For instance, consider the integration of the first term in $\mathbf{K}_{ww}$ matrix (4.9):

$$\mathbf{K}_{ww} = \iint_A \mathbf{B}_{yz}^{w\ T} \mathbf{D} \mathbf{B}_{yz}^{w} dA$$

Considering that, as a good approximation, a reinforcing bar will respond uniaxially with a tangent modulus E_s in the direction of its longitudinal axis, that, in general will have an inclination. One can write its constitutive matrix in the section's reference coordinate system as:

$$\mathbf{D} = \mathbf{n}_\varepsilon^T E_s \mathbf{n}_\varepsilon$$

where:

$$\mathbf{n}_\varepsilon = \left[l^2, m^2, n^2, 2lm, 2ln, 2mn \right]$$

is a vector that transforms a strain tensor, defined in the reference coordinate system, to the axial strain in the direction defined by the directional cosines: l, m, n. Consequently, $\mathbf{n}_\varepsilon$ also rotates an axial stress in the previous direction, to the reference coordinate system.

The differential of area in the $Y - Z$ of this bar can be deduced by dividing the volume that corresponds to a differential projected length, see figure 4.8, by the bar spacing along X direction.

$$dA = \frac{dVol}{S_x} = \frac{A_{\boldsymbol{\phi}}}{\cos \boldsymbol{\theta} S_x} dl \tag{4.37}$$

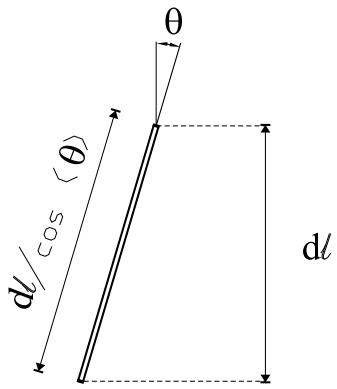

Figure 4.8: Differential volume of an inclined bar

where $A_{\boldsymbol{\phi}}$, S_x are the bar's cross section and spacing along X direction. The inclination angle with respect to the cross section's plane is $\boldsymbol{\theta}$, see figure 4.9, and dl is the differential of length projected in the section's plane.

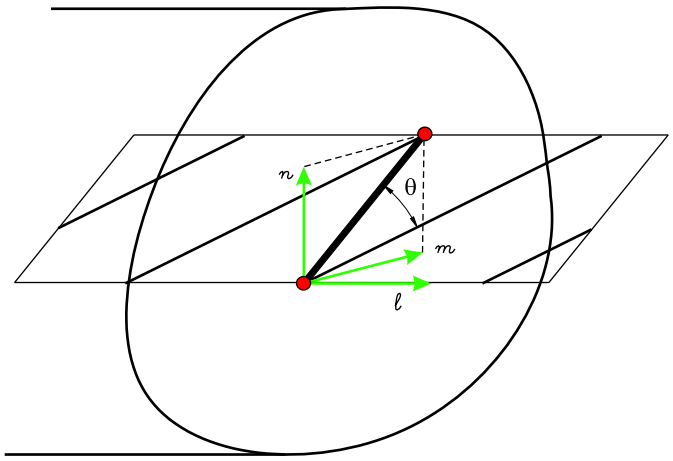

Figure 4.9: Angle between bars and the section's plane

By means of the chain rule, the derivatives in the strain interpolation matrixes $\mathbf{B}^w_{yz}$ will be computed in the following fashion:

$$\begin{aligned} \frac{\partial}{\partial y} &= \frac{m}{\cos\boldsymbol{\theta}}\frac{\partial}{\partial l} \\ \frac{\partial}{\partial z} &= \frac{n}{\cos\boldsymbol{\theta}}\frac{\partial}{\partial l} \end{aligned} \tag{4.38}$$

4.4.3 1D finite elements for double lateral reinforcements

A multi-bars 1D element is also available. This element is useful to simulate set of bars with different space inclination, but with the same projection on the section's plane, as can be the case of truss type reinforcements, see figure 4.10.

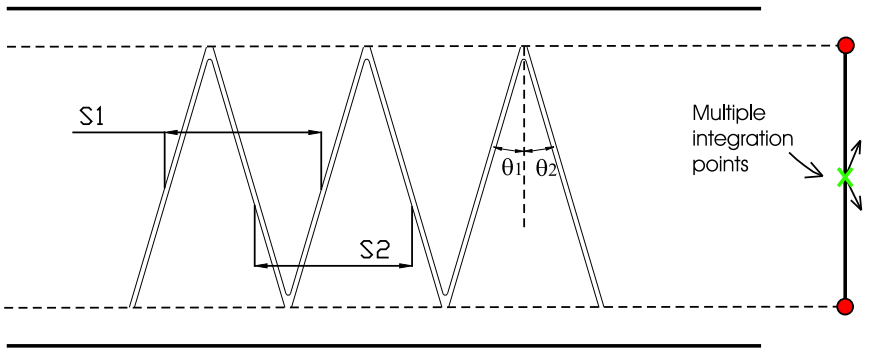

Figure 4.10: Multiple reinforcements line element

The implementation of this element is straight forward starting from the single bar element. Also linear Lagrange polynomials and Gauss-Legendre quadrature, are employed in this element. Different bars with their corresponding inclination angles, area and material properties are handled as different integration points, located in the same position. Each integral is evaluated independently at each gauss point; then all integrals are added.

4.4.4 Point finite elements for longitudinal reinforcements

Finally, a point element was implemented to simulate longitudinal reinforcements that intersects the section's plane in a single point. Longitudinal bars by a certain area of reinforcing material concentrated in a single point, the shape or the extension that the bar's cross-section represents in the total beam section is then neglected.

Consequently, the distortion field on single point elements will have a single point value. As seen in the figure 4.11 , the point element will have a warping-distortion value following the section's deformation, nevertheless

no variation of the warping-distortion field is possible inside the element's domain.

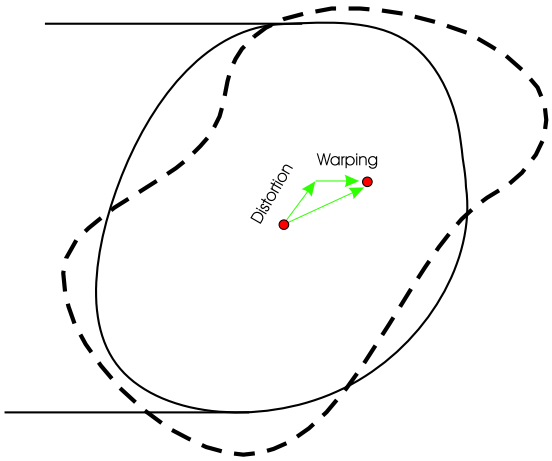

Figure 4.11: Warping-distortion in a point element

Recalling that the Saint-Venant type of warping has been considered, the warping variation along element's length is neglected. Then, it follows that longitudinal strains in the axial direction due to section's warping and distortion are always null and so will be for this element. Only the PS component is present in the strain and stress tensors.

4.5 Closure

The solution of the complementary equilibrium problem in the sectional level might require complex computations in the general case, specially in the case of arbitrary shaped sections and non-linear problems. To allow a suitable and versatile application of the sectional model proposed in chapter 3 a numerical implementation using the finite element method was carried out in this chapter.

Firstly it was necessary to apply the generic expression presented in chapter 3 to the finite element context. The algorithm of the sectional model was then presented. Finally, the implementation into three type of finite elements were shown. These elements are the minimum requirement to rep-

resent a typical reinforced concrete section: *concrete matrix*, *transverse* and *longitudinal reinforcements*.

From the resulting numerical model a computer code named *TINSA* was written, whose name corresponds to the acronym of *Total Interaction Non-linear Sectional Analysis*. The code was written in *Matlab* using some basic techniques from object oriented programming philosophy easing the interaction with other structural objects and the future expansion of the code. *Matlab* was chosen at this level of development because it is a powerful tool for handling matrix expressions and graphics and allows for a structurated programming with independently developed functions. In the future, a stand-along application can be compiled or easily translated to a more efficient language such as *C*, *C++* or *FORTRAN*.

Additionally, a compact structural analysis toolbox was witting including a non-linear structural solver with some aids to ease or accelerate convergency, such as: *automatic increments generation* based on convergence difficulty in the previous sub-step, *line searches* and *displacement control*. These techniques were properly implemented in the solver although they are not described in this document since they are not a development of the author but rather part of the state of the art tools for non-linear analysis. Exhaustive information on these topics can be found in many books on Non-linear finite element analysis books such as: Crisfield (1991), (1998); Bathe (1998), Belytschko et al. (2001), among others.

The toolbox also includes a library of material constitutive models that are independent of the elements used. The toolbox structure easily permits the future inclusion of new elements and materials models. They might be independently developed if they are written respecting simple standards in the *input-output* interface, thus becoming a new object of the toolbox.

The next chapter describes a set of developed and implemented material models.

Chapter 5

Materials modeling

5.1 Introduction

In the current chapter constitutive models developed to simulate the behaviour of some types of materials are described. A total of four material models were developed and implemented in the numerical toolbox. In this chapter, the name of the implemented object in quotation marks is included together with each section's name when it is the case.

The first two materials to be described include linear elastic orthotropic behaviour and a linear-brittle material with cracked induced anisotropy. These models are good and simple representations of orthotropic materials in elastic range, such as composite materials and concrete under service loads.

A complete triaxial non-linear model for plain concrete was also developed. The model allows for cracked induced anisotropy by means of a rotating crack approach. Behaviour under complex loading such as Poisson effects, strength enhancement due to confinement and the effects of concrete strength in the non-linear $\sigma - \varepsilon$ curve are considered by means of state-of-the-art specific models. Cyclic loading in concrete is possible. It exhibits plastic compression behaviour previous to crushing, i.e. unloading and reloading with initial stiffness. In tension, concrete presents anisotropic

damage represented by a damage tensor.

The series is completed with an uniaxial elastoplastic model to simulate the stress-strain relationship of reinforcing steel. This material allows for cyclic loading including kinematic strain-hardening to account for Bauschinger effect.

5.2 Orthotropic linear elastic material: "OrthoElastic"

The simplest constitutive model implemented is an orthotropic linear elastic solid. This solid material has three orthogonal principal directions defined by a set of three unit vectors: $\vec{e}_1$, $\vec{e}_2$ and $\vec{e}_3$. An isotropic linear elastic material has not been implemented since it is a special case of the orthotropic linear elastic solid which reduces to the former when all three principal material directions have the same material properties.

Several physical bodies can be represented by this constitutive law, ranging from stratified soils or rocks, brick masonry to modern composite materials in elastic range.

Pre-strain is possible in this material thanks to a pre-strain tensor given as input.

Along each principal direction, i, the solid has a linear elastic behaviour with elastic modulus E_i. Three shear modulus define the stiffness to shear distortion in a plane. An arbitrary shear modulus G_{ij} represents the shear stress required to produce a unit shear strain in the plane $i - j$.

The set of material properties is completed by three Poisson coefficients: ν_{12}, ν_{13} and ν_{23}. A generic coefficient ν_{ij} represents the free strain along direction j when a stress is applied along direction i.

To guarantee symmetry in the constitutive matrix, the following three complement Poisson coefficients are internally computed, according to Reddy (1996).

$$\begin{aligned}\nu_{21} &= \nu_{12}\frac{E_2}{E_1}\\ \nu_{31} &= \nu_{13}\frac{E_3}{E_1}\\ \nu_{32} &= \nu_{23}\frac{E_3}{E_2}\end{aligned} \tag{5.1}$$

The material constitutive matrix can be computed as follows:

$$D_{12} = \frac{1}{\Omega}\begin{bmatrix} E_1(1-\nu_{23}\nu_{32}) & E_1(\nu_{21}+\nu_{23}\nu_{31}) & E_1(\nu_{31}+\nu_{21}\nu_{32}) & 0 & 0 & 0\\ E_2(\nu_{12}+\nu_{13}\nu_{32}) & E_2(1-\nu_{13}\nu_{31}) & E_2(\nu_{32}+\nu_{12}\nu_{31}) & 0 & 0 & 0\\ E_3(\nu_{13}+\nu_{12}\nu_{23}) & E_3(\nu_{23}+\nu_{13}\nu_{21}) & E_3(1-\nu_{12}\nu_{21}) & 0 & 0 & 0\\ 0 & 0 & 0 & \Omega G_{12} & 0 & 0\\ 0 & 0 & 0 & 0 & \Omega G_{13} & 0\\ 0 & 0 & 0 & 0 & 0 & \Omega G_{23}\end{bmatrix} \tag{5.2}$$

Where:

$$\Omega = 1-\nu_{21}\nu_{12}-\nu_{31}\nu_{13}-\nu_{32}\nu_{23}-\nu_{12}\nu_{23}\nu_{31}-\nu_{21}\nu_{32}\nu_{13}$$

5.3 Elastic linear-brittle material: "L3DSCT"

An isotropic linear material with brittle failure in tension and compression has been developed and implemented. Material responds to a Rankine type failure surface with different strengths in tension and compression, referred as f_t and f_c respectively, see figure 5.1.

Initially the material behaves as isotropic linear elastic, until the failure surface is reached. When in a principal stress direction the strength is exceeded, the resisted stress and the corresponding elastic modulus drop to zero as indicated in figure 5.2. At this state, the behaviour is orthotropic with material principal directions are not fixed but rather vary according directions of the principal stresses.

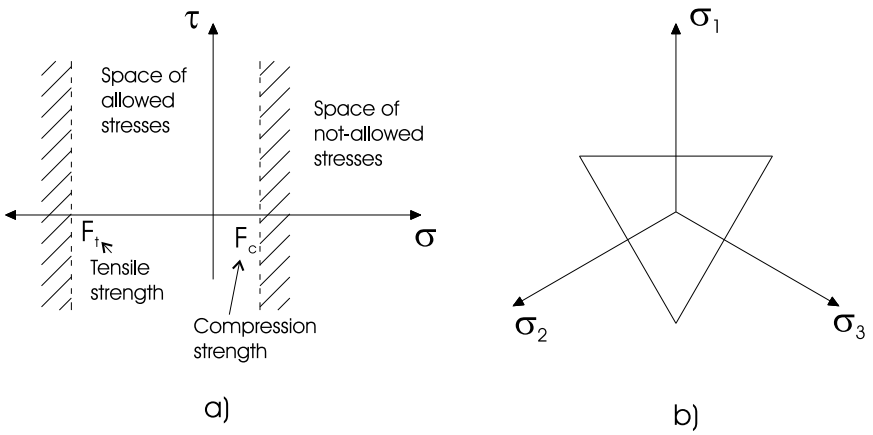

Figure 5.1: Rankine type failure surface. a) $\sigma - \tau$ space, b) Deviatoric view in $\sigma_1 - \sigma_2 - \sigma_3$ space.

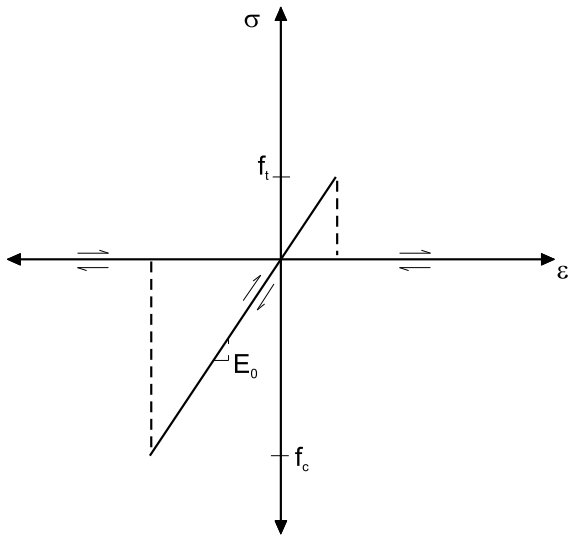

Figure 5.2: Elastic linear-brittle $\sigma - \varepsilon$ law.

The isotropic state is characterized by a single elastic modulus E_0 and a Poisson coefficient ν_0.

In all cases, the constitutive matrix is evaluated as in equation (5.2). Where the principal direction's elastic modulus can be either E_0 or null depending if the directional state is elastic or not respectively. Poisson in principal planes (ν_{ij}) coefficients are evaluated as follows to satisfy symmetry condition in the constitutive matrix.

$$\nu_{ij} = \begin{cases} \nu_0, \forall i < j \\ \nu_{ji}\dfrac{E_i}{E_j}, \forall i > j \end{cases} \tag{5.3}$$

Shear modulus in each principal plane G_{ij} is computed to assure consistency on the principal directions of stress and strain tensors before and after the current load step. Bazant equation (5.4) has been adopted for these case:

$$Gij = \frac{1}{2}\frac{\sigma_i - \sigma_j}{\varepsilon_i - \varepsilon_j} \tag{5.4}$$

5.4 Constitutive model for concrete: "OU3DC"

A non linear hypoelastic constitutive model is employed for modelling concrete material. The model allows, among other capabilities, for 3D loading, tension cracking with stiffness degradation, non linear compression loading considering the effect of concrete strength, etc. In the current section, the constitutive model is extensively described.

5.4.1 Hypotheses

Inelastic concrete is modeled as an orthotropic material whose behaviour along each principal loading direction is governed by an equivalent uniaxial non-linear relationship between stress and mechanical strain. The concept of mechanical strain is described bellow.

Material's principal directions are always coincident to the ones of the principal stress tensor, hence they are allowed to rotate in order to simulate the crack induced anisotropy phenomenon sketched in figure 2.11.

Mechanical and non-mechanical strains

Total strain in a material point is assumed to be the sum of a mechanical part, which is directly related to the stress, and a strain offset that is referred to as non-mechanical since it is not directly related to stresses. Although this offset may be a source of secondary stresses due to compatibility requirements. The same decomposition is also applicable to the strain rates as indicates equation (5.5).

$$\begin{aligned} \boldsymbol{\varepsilon} &= \boldsymbol{\varepsilon}^m + \boldsymbol{\varepsilon}^{nm} \\ \dot{\boldsymbol{\varepsilon}} &= \dot{\boldsymbol{\varepsilon}}^m + \dot{\boldsymbol{\varepsilon}}^{nm} \end{aligned} \tag{5.5}$$

All type of free deformations, or strains offstets, such as creep, shrinkage or thermal displacements may be handled as non-mechanical strains by adding them as shown in equation (5.6). Since stress-strain relationship along each direction is considered as uniaxial, Poisson strains must be considered as a free strain to be added to the non-mechanical ones. In the context of this work, the only non-mechanical strain to be considered will be the Poisson strains; although, all other strains offsets can be treated in the same manner.

$$\boldsymbol{\varepsilon}^{nm} = \boldsymbol{\varepsilon}^c + \boldsymbol{\varepsilon}^s + \boldsymbol{\varepsilon}^t + \boldsymbol{\varepsilon}^\nu + \dots \tag{5.6}$$

The mechanical strain is related to the direct instantaneous application of stresses to the material. It is assumed that the mechanical strain is composed of two addends, equation (5.7). Namely an elastic part ($\boldsymbol{\varepsilon}^e$) which is completely recoverable after the applied stress is removed. The second term corresponds to a plastic strain ($\boldsymbol{\varepsilon}^p$) which remains in the material after unloading.

$$\boldsymbol{\varepsilon}^m = \boldsymbol{\varepsilon}^e + \boldsymbol{\varepsilon}^p \tag{5.7}$$

Loading, unloading and reloading concepts

Inelastic materials like concrete and steel exhibit different $\sigma - \varepsilon$ behaviour when they are loaded for the first time or in strain range that was previously reached. This situation makes necessary to distinguish between *new-loading* and *unloading-reloading* states.

For the present constitutive model, loading state is defined independently in each principal direction by means of an envelope (backbone) $\sigma - \varepsilon$ curve. When a virgin material is loaded it follows the backbone curve while when it is unloaded to a smaller strain level, the material will follow a typically different $\sigma - \varepsilon$ law.

When reloading the material will follow a different $\sigma - \varepsilon$ curve until the threshold, defined by of the backbone curve, is reached again. If load is augmented after this point, a *new-loading* state will take place again.

In the constitutive model here described, both unloading and reloading take place along linear $\sigma - \varepsilon$ curves. The tangent of the unloading-reloading branch might differ in tension and compression loading. While in the latter unloading-reloading curve will always take place using the elastic modulus, in tension the tangent modulus will degrade after concrete cracking with a damage performance.

5.4.2 Compression behaviour

When loading in compression, the relationship between stress and the mechanical strain follows the non linear equation of Collins and Porasz (1989), see equation 5.8, as backbone envelope.

This curve is capable of reproducing the influence of concrete strength on the shape of the σ-ε curve, being suitable to simulate both normal and high strength concretes.

$$\sigma_i = \sigma_i^p = f_{ci}\frac{\varepsilon_i^m}{\varepsilon_{0,i}}\frac{n}{n-1+\left(\frac{\varepsilon_i^m}{\varepsilon_{0,i}}\right)^{nk}}$$
$$n = \frac{E_0}{E_0 + \frac{f_{ci}}{\varepsilon_{0,i}}} \tag{5.8}$$
$$k = \begin{cases} 1, \forall \dfrac{\varepsilon_i^m}{\varepsilon_{0,i}} \leq 1 \\ 0.67 + \dfrac{f_c}{62}, \forall \dfrac{\varepsilon_i^m}{\varepsilon_{0,i}} > 1 \ [MPa] \end{cases}$$

Where E_0 is the initial modulus of concrete, f_{ci} and $\varepsilon_{0,i}$ are the current strength and the corresponding strain at peak stress on direction i. These two quantities are to be computed considering the 3D stress state as will be explained below, in section 5.4.4.

The parameter f_c is the uniaxial compression strength in MPa. It controls the shape of the curve by means of the parameter k, see figure 5.3. The variable σ^p represents a stress situated in the non linear backbone curve.

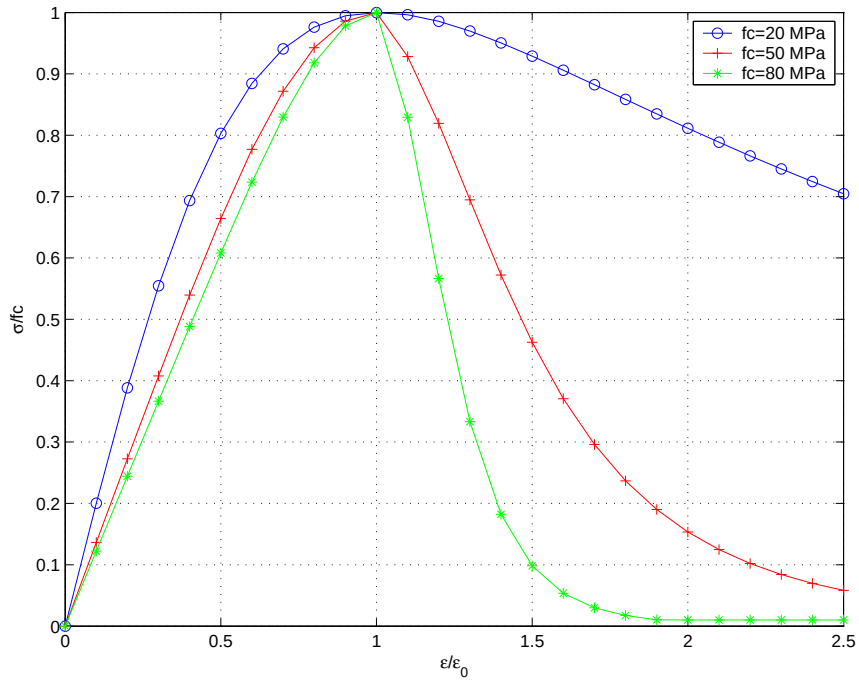

Figure 5.3: Collins and Porasz family of normalized curves $(\sigma/f_c, \varepsilon/\varepsilon_0)$

During new loading in compression the plastic strain in the corresponding directions increases, see figure 5.4. The value of the plastic strain along each principal direction must be updated after new loading has occurred. This updated value is computed depending on the last stress value reached in the backbone curve, see equation (5.9).

$$\varepsilon_i^p = \varepsilon_i^m - \frac{\sigma_i}{E_0} \tag{5.9}$$

When unloading and reloading in compression concrete $\sigma - \varepsilon$ curve is linear according to equation (5.4), without any increase of plastic strain. This state is valid until the backbone is reached again, then the state is that of new loading.

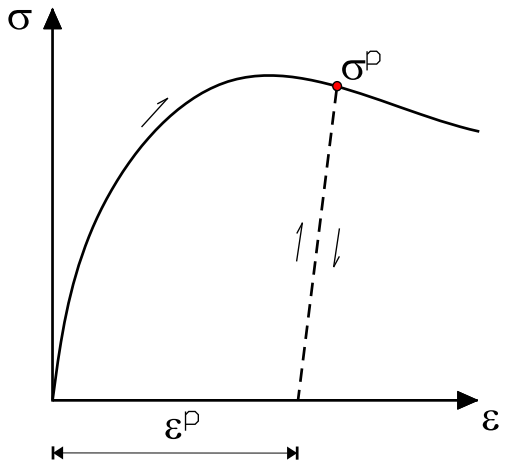

Figure 5.4: Compression cyclic behaviour

$$\sigma_i = E_0 \left(\varepsilon_i^m - \varepsilon_i^p\right) = E_0 \varepsilon_i^e \tag{5.10}$$

5.4.3 Tension behaviour

Before cracking, concrete is considered to behave linearly. The same equation of unloading-reloading (5.10) is considered valid in this situation. When the current cracking stress is reached in a tensile principal direction a strain

softening behaviour begins. The non-linear equation equivalent to the proposed by Cervenka (1985), equation (5.11), has been adopted as the tension backbone envelope in each tensile principal direction.

$$\sigma_i = f_{t,i}\left[1 - \left(\frac{\varepsilon_i^e}{c}\right)^{k_2}\right] \geq 0, \forall \varepsilon_i^e > \frac{f_{t,i}}{E_0} \tag{5.11}$$

Where c represents the strain at which tension stress is reduced to zero, k_2 is a coefficient defining the shape of the softening curve. These two parameters are employed to control the shape of tension stiffening in concrete. Typical values for c are between 0.004 and 0.005; for k_2 typically 0.5 is used; see CEB (1996).

After cracking has occurred, and when the elastic strain is positive, the crack is considered active. In the direction in which a crack is active, the material exhibits damage. This means that less effective material collaborates in stress transferring, as seen in figure 5.4. Hence the longitudinal stiffness is degraded in tension loading and unloading regimes following equation (5.12).

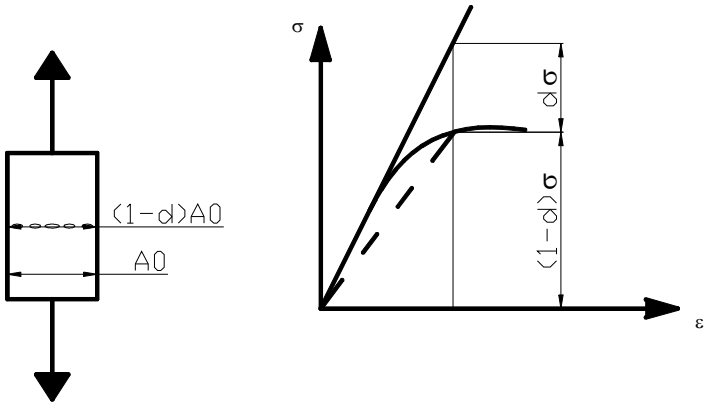

Figure 5.5: Schematic representation of damage process

$$\sigma_i = (1 - d_i)\, E_0\, (\varepsilon_i^e) \tag{5.12}$$

Where d_i is the damage variable in the loading direction, understood as the fraction of the material that is no longer effective in i direction. While unloading and reloading, damage is fixed but when the tension stress is on the backbone curve, the damage variable increases in the respective direction. The new damage is computed as:

$$d_i = 1 - \frac{\sigma_i^p}{E_0 \varepsilon_i^e} \tag{5.13}$$

The damage variable is bounded to a maximum value of one; consequently the tangent modulus has a lower bound of zero. A close $\sigma - \varepsilon$ loop in tension will be as shown in figure 5.6.

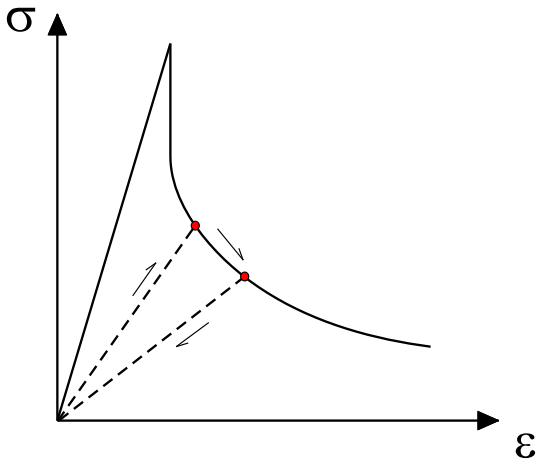

Figure 5.6: Tension cyclic behaviour

5.4.4 Triaxial characteristics: Failure surface

3D strength

Concrete strength under a general triaxial stress state is defined by means of a failure surface. Many failure theories are available for concrete and geomaterials, see Chen (1982). In the implemented code, failure surfaces are independent of the constitutive model. Any failure surface can be programmed in a separated code. In this section only the five parameters

surface of Willam and Warnke (1975). will be presented since it was the implemented surface for this work.

The reasons why this surface was chosen are because its excellent capabilities for reproducing the behaviour of concrete under a wide range of loading at low and high hydrostatic stress levels as exposed bellow.

The main characteristics of this surface are: curve parabolic meridians on the renduric plane distinguishing between tension and compression meridians. When cutting the deviatoric plane a smooth and convex curve is always obtained, as shown in 5.8. Its shape in the deviatoric plane features a transition from a more or less triangular shape for low hydrostatic stress levels, tending to the Rankine failure surface, and more or less circular shape for high hydrostatic stress, tending to the Drucker-Prager failure surface.

A compression meridian, defined by fixed similarity angles (θ) of 60°, 180° and 300°, is given by:

$$\frac{r_c}{\sqrt{5}f_c} = b_0 + b_1\frac{\sigma_m}{f_c} + b_2\left(\frac{\sigma_m}{f_c}\right)^2$$

A tensile meridian, defined by fixed similarity angles (θ) of 0°, 120° and 240°, is given by:

$$\frac{r_t}{\sqrt{5}f_c} = a_0 + a_1\frac{\sigma_m}{f_c} + a_2\left(\frac{\sigma_m}{f_c}\right)^2$$

where the a's and b's terms are coefficients to be adjusted from the five parameters defining the surface, as will be shown next, and:

$$\sigma_m = \frac{1}{3}\left(\sigma_x + \sigma_y + \sigma_z\right) = \frac{1}{3}I_1$$

is the mean value of the stress components,

$$\cos\left(3\theta\right) = \frac{3\sqrt{3}}{2}\frac{J_3}{\sqrt{J_2^3}} = \frac{\sqrt{2}J_3}{\tau_{oct}^3}$$

is the orientation angle in the deviatoric plane or angle of similarity:

$$r = \sqrt{2J_2} = \sqrt{3}\tau_{oct}$$

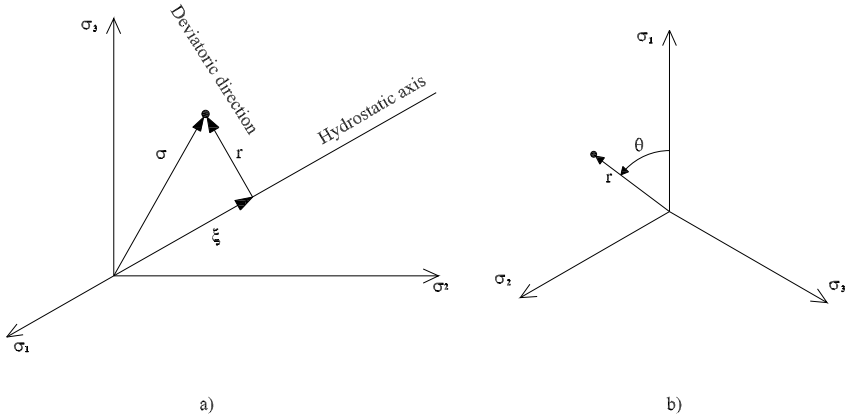

Figure 5.7: Geometric representation of a stress tensor. a) Space view, b) deviatoric view.

is a measure of the deviatoric stress, geometrically it is the distance from the stress to the hydrostatic axis. Figure 5.7 shows a geometrical representation of a tensor in the space of it principal directions.

The surface is defined by extending the two basic meridians by means of elliptic interpolation between them. Therefore, for an arbitrary angle of similarity, $r(\sigma_m, \theta))$ is given by:

$$r(\sigma_m, \theta) = \frac{c_1 + c_2 c_3}{c_4}$$

where:

$$c_1 = 2r_c\left(r_c^2 - r_t^2\right)\cos\theta$$

$$c_2 = r_c\left(2r_t - r_c\right)$$

$$c_3 = \sqrt{4\left(r_c^2 - r_t^2\right)\cos\theta^2 + 5r_t^2 - 4r_c r_t}$$

$$c_4 = 4\left(r_c^2 - r_t^2\right)\cos\theta^2 + \left(r_c - 2r_t\right)^2$$

Coefficients a_0, a_1, a_2, b_0, b_1 and b_2 are function of five material parameters which correspond to five points in the failure surface. The five parameters of the Willam and Warnke failure surface are defined in table 5.1. Substituting these parameters as points in the failure surface one can isolate the required

Table 5.1: Parameters of the Willam and Warnke failure surface

Uniaxial compression strength	f_c
Uniaxial tension strength	$\bar{f}_t = \frac{f_t}{f_c}$
Biaxial compression strength	$\bar{f_{bc}} = \frac{f_{bc}}{f_c}$
Point in tensile meridian ($\theta = 0\,^\circ$)	$\left(\bar{\xi_1}, \bar{r_1}\right) = \left(\frac{\xi_1}{f_c}, \frac{r_1}{f_c}\right)$
Point in compression meridian ($\theta = 60\,^\circ$)	$\left(\bar{\xi_2}, \bar{r_2}\right) = \left(\frac{\xi_2}{f_c}, \frac{r_2}{f_c}\right)$

coefficients which finally they are computed as follows as shown in Chen (1982):

Tensile meridian

$$a_2 = \frac{\sqrt{\frac{6}{5}}\bar{\xi_1}\left(\bar{f}_t - \bar{f_{bc}}\right) - \sqrt{\frac{6}{5}}\bar{f}_t\bar{f_{bc}} + \bar{r_1}\left(2\bar{f_{bc}} + \bar{f}_t\right)}{\left(2\bar{f_{bc}} + \bar{f}_t\right)\left(\bar{\xi_1}^2 - \frac{2}{3}\bar{f_{bc}}\bar{\xi_1} + \frac{1}{3}\bar{f}_t\bar{\xi_1} - \frac{2}{9}\bar{f}_t\bar{f_{bc}}\right)}$$

$$a_1 = \frac{1}{3}\left(2\bar{f_{bc}} - \bar{f}t\right)a_2 + \sqrt{\frac{6}{5}}\frac{\bar{f}_t - \bar{f_{bc}}}{2\bar{f_{bc}} + \bar{f}_t}$$

$$a_0 = \frac{2}{3}\bar{f_{bc}}a_1 - \frac{4}{9}\bar{f_{bc}}^2 a_2 + \sqrt{\frac{2}{15}}\bar{f_{bc}}$$

Compression meridian

$$\rho = \frac{-a_1 - \sqrt{a_1^2 - 4a_0a_2}}{2a_2}$$

$$b_2 = \frac{\bar{r_2}\left(\rho + \frac{1}{3}\right)\sqrt{\frac{2}{15}}\left(\rho + \bar{\xi_2}\right)}{\left(\bar{\xi_2} + \rho\right)\left(\bar{\xi_2} - \frac{1}{3}\right)\left(\rho + \frac{1}{3}\right)}$$

$$b_1 = \left(\bar{\xi_2} + \frac{1}{3}\right)b_2 + \frac{\sqrt{\frac{6}{5}} - 3\bar{r_2}}{3\bar{\xi_2} - 1}$$

$$b_0 = -\rho b_1 - \rho^2 b_2$$

Figure 5.8 shows a general view of the failure surface and its renduric and diviatoric planes. These characteristics make the surface suitable for both low and high confinements.

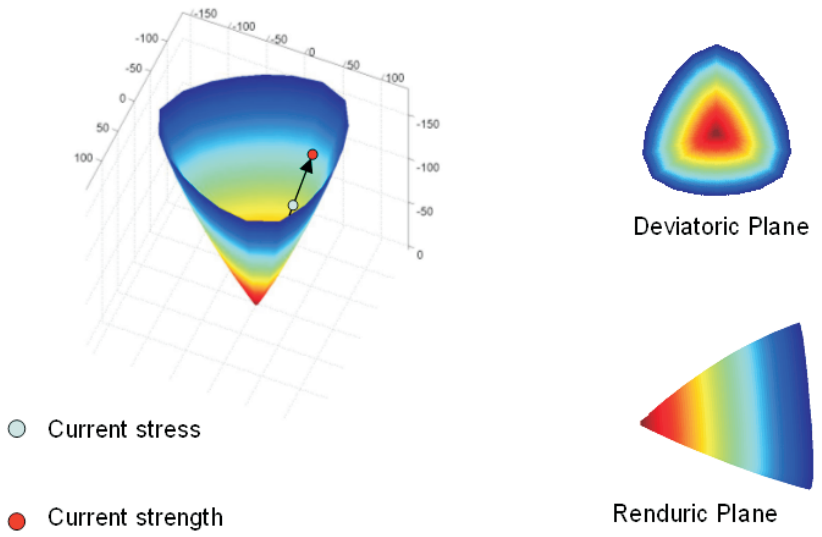

Figure 5.8: View of the Willam and Warnke failure surface

To determine the current strength first a trial stress is computed assuming elastic loading using equations (6) or (8) for compression or tension directions respectively. The 3D elastic stress is plotted on the failure surface's space. Along the imaginary line connecting the elastic stress and the origin, the intersection with the failure surface is searched. If the elastic stress falls inside the surface, then it is projected until the surface is reached. If otherwise the stress is outside the surface, then it projected backwards to the surface.

Each intersection point, figure 5.8, defines the current strength in all three principal directions for tension or compression.

Strain at peak load

The strain at peak stress depends on the degree of confinement. If the strength on a principal direction is enhanced compared to the uniaxial strength because of confinement, the strain at peak stress is computed from the following equation, Mander et al (1988).

$$\varepsilon_{0,i} = \varepsilon_0 \left[1 + 5 \left(\frac{f_{c,i}}{f_c} - 1 \right) \right], \forall f_{ci} > f_c \tag{5.14}$$

If strength is reduced because the combined tension-compression state is dominating, strain at peak stress is reduced as:

$$\varepsilon_{0,i} = \varepsilon_0 \frac{f_{c,i}}{f_c}, \forall f_{ci} \leq f_c \tag{5.15}$$

On the previous equations f_c and ε_0 are the uniaxial strength and the corresponding strain at peak stress. $f_{c,i}$ and $\varepsilon_{0,i}$ are the 3D strength and the corresponding peak strain in i direction respectively.

5.4.5 Poisson strains

It has been said that stress-strain relation is considered uniaxial on each principal direction. Nevertheless, on the orthogonal directions of loading free strain is produced due to Poisson effect. Poisson strains may be computed from the mechanical strains as:

$$\begin{bmatrix} \varepsilon_1^\nu \\ \varepsilon_2^\nu \\ \varepsilon_3^\nu \end{bmatrix} - \begin{bmatrix} 0 & \nu_2 & \nu_3 \\ \nu_1 & 0 & \nu_3 \\ \nu_1 & \nu_2 & 0 \end{bmatrix} \begin{bmatrix} \varepsilon_1^m \\ \varepsilon_2^m \\ \varepsilon_3^m \end{bmatrix} \tag{5.16}$$

For high loads the Poisson coefficient is non-linear; it is being possible to express it as a function of the current mechanical strain. non-linear equations for the Poisson coefficient can be found in Chen (1982), Vecchio (1992) and Montoya et al. (2001). The expression adopted in this paper is the third degree polynomial function described in Chen (1982), equation 5.17, which is an adjustment of the experimental data of Kupfer et al (1969) proposed by Elwi and Murray (1979).

$$\nu_i = \nu_0 \left[1 + 1.3763 \frac{\varepsilon_i^m}{\varepsilon_{0,i}} - 5.36 \left(\frac{\varepsilon_i^m}{\varepsilon_{0,i}} \right)^2 + 8.586 \left(\frac{\varepsilon_i^m}{\varepsilon_{0,i}} \right)^3 \right] \leq 0.5 \tag{5.17}$$

Where ν_0 is the initial Poisson coefficient.

5.4.6 Constitutive matrix

The previous stress-strain relations are functions of the mechanical strain or the elastic part of it, i.e. they are not functions of the complete strain tensor on equation (2). In deducing an expression for the constitutive matrix of equation (16) we shall assume that the increment of total strain, equation (17), is such that the non mechanical part of it does not change.

$$D_{ij} = \frac{\partial \sigma_i}{\partial \varepsilon_j} \tag{5.18}$$

$$\dot{\boldsymbol{\varepsilon}} = \dot{\boldsymbol{\varepsilon}}^m + \dot{\boldsymbol{\varepsilon}}^{nm} = \dot{\boldsymbol{\varepsilon}}^e + \dot{\boldsymbol{\varepsilon}}^p + \dot{\boldsymbol{\varepsilon}}^{nm} \tag{5.19}$$

The latter is only an approximation since some so-called non mechanical strains depend, directly or indirectly, on the applied load or mechanical strain. This is the case, for example, of creep or Poisson strains. Thus if an increment of mechanical strain takes place it is to expect an indirect variation of the non mechanical part. By neglecting this secondary increment of total strain, equation (18) is considered valid enough for the purpose of computing the constitutive matrix. The constitutive modulus resulting is an approximation of the exact one. Non mechanical strains are, nevertheless, considered for compatibility conditions. During iteration procedure, the error on using an approximate constitutive matrix is eliminated.

$$\dot{\boldsymbol{\varepsilon}} \approx \dot{\boldsymbol{\varepsilon}}^m \tag{5.20}$$

On compression loading, i.e. when compression stress is located within the backbone curve, the longitudinal modulus on the corresponding direction used is:

$$E_i = \frac{\sigma_i^p}{\varepsilon_i^m} \tag{5.21}$$

During unloading and reloading in compression, the initial elastic modulus is used in the corresponding direction:

$$E_i = E_0 \tag{5.22}$$

On tension loading damage is considered. The longitudinal modulus to be used for new loading or unloading is the one in equation (21). Before cracking the damage variable is zero, therefore equations (21) and (20) are initially equivalent.

$$E_i = (1 - d_i)\, E_0 \tag{5.23}$$

In the case of the shear modulus, the following equation proposed by Bažant (1983) for rotating-crack models is adopted, equation (5.24). It was deduced from the condition that on the predicted step the principal directions of both stress and strain keep being coincident.

$$G_{ij} = \frac{1}{2} \frac{\sigma_i - \sigma_j}{\varepsilon_i - \varepsilon_j} \tag{5.24}$$

On the principal directions, the constitutive matrix will be:

$$\mathbf{D}_{12} = \begin{bmatrix} E_1 & 0 & 0 & 0 & 0 & 0 \\ 0 & E_2 & 0 & 0 & 0 & 0 \\ 0 & 0 & E_3 & 0 & 0 & 0 \\ 0 & 0 & 0 & G_{12} & 0 & 0 \\ 0 & 0 & 0 & 0 & G_{13} & 0 \\ 0 & 0 & 0 & 0 & 0 & G_{23} \end{bmatrix} \tag{5.25}$$

This matrix is rotated to the global orientation in the way (23) indicates. As can be seen this matrix is orthotropic with principal angles depending on the applied stress.

$$\mathbf{D} = \mathbf{T}_\varepsilon^T \mathbf{D}_{12} \mathbf{T}_\varepsilon \tag{5.26}$$

In the previous equation, T_ε is the transformation matrix that rotates the strain tensor from the global coordinate system $X-Y$ to the principal direction $1-2$. The transposed of this matrix coincides with the transformation

matrix that rotates a stress tensor in direction $1-2$ to direction $X-Y$. This matrix will be given below in section 5.4.7.

5.4.7 State update algorithm

The concrete model described above needs three history variables for each loading direction: plastic strain, tension damage, strain offsets (in this case only Poisson strain).

Because of triaxial load history, the principal directions may change from one state to another. When this happens, the state variables values should be coherent with previous and new load directions.

To handle this problem, state variables are stored as tensors on a fixed global coordinate system in an incremental fashion as proposed by Vecchio (1999). When the new state variables are computed as above, their incremental variable on each direction may be computed as:

$$\dot{\boldsymbol{\varepsilon}}^{p}_{12} = \boldsymbol{\varepsilon}^{p}_{12,new} - \boldsymbol{\varepsilon}^{p}_{12,old} \tag{5.27}$$

$$\dot{\boldsymbol{\varepsilon}}^{\nu}_{12} = \boldsymbol{\varepsilon}^{\nu}_{12,new} - \boldsymbol{\varepsilon}^{\nu}_{12,old} \tag{5.28}$$

$$\dot{d}_{12} = d_{12,new} - d_{12,old} \tag{5.29}$$

These increment values are accumulated in the global coordinate system:

$$\boldsymbol{\varepsilon}^{p}_{XY} = \boldsymbol{\varepsilon}^{p}_{XY,old} - \mathbf{T}^{T}_{\sigma}\dot{\boldsymbol{\varepsilon}}^{p}_{12} \tag{5.30}$$

$$\boldsymbol{\varepsilon}^{\nu}_{XY} = \boldsymbol{\varepsilon}^{\nu}_{XY,old} - \mathbf{T}^{T}_{\sigma}\dot{\boldsymbol{\varepsilon}}^{\nu}_{12} \tag{5.31}$$

$$d_{XY} = d_{XY,old} - \mathbf{T}^{T}_{\varepsilon}\dot{d}_{12} \tag{5.32}$$

Where:

$$\mathbf{T}_{\varepsilon} = \begin{bmatrix} l_1^2 & m_1^2 & n_1^2 & l_1m_1 & l_1n_1 & m_1n_1 \\ l_2^2 & m_2^2 & n_2^2 & l_2m_2 & l_2n_2 & m_2n_2 \\ l_3^2 & m_3^2 & n_3^2 & l_3m_3 & l_3n_3 & m_3n_3 \\ 2l_1l_2 & 2m_1m_2 & 2n_1n_2 & l_1m_2+l_2m_1 & l_1n_2+l_2n_1 & m_1n_2+m_2n_1 \\ 2l_1l_3 & 2m_1m_3 & 2n_1n_3 & l_1m_3+l_3m_1 & l_1n_3+l_3n_1 & m_1n_3+m_3n_1 \\ 2l_2l_3 & 2m_2m_3 & 2n_2n_3 & l_2m_3+l_3m_2 & l_2n_3+l_3n_2 & m_2n_3+m_3n_2 \end{bmatrix} \tag{5.33}$$

$$\mathbf{T}_\sigma = \begin{bmatrix} l_1^2 & m_1^2 & n_1^2 & 2l_1m_1 & 2l_1n_1 & 2m_1n_1 \\ l_2^2 & m_2^2 & n_2^2 & 2l_2m_2 & 2l_2n_2 & 2m_2n_2 \\ l_3^2 & m_3^2 & n_3^2 & 2l_3m_3 & 2l_3n_3 & 2m_3n_3 \\ l_1l_2 & m_1m_2 & n_1n_2 & l_1m_2+l_2m_1 & l_1n_2+l_2n_1 & m_1n_2+m_2n_1 \\ l_1l_3 & m_1m_3 & n_1n_3 & l_1m_3+l_3m_1 & l_1n_3+l_3n_1 & m_1n_3+m_3n_1 \\ l_2l_3 & m_2m_3 & n_2n_3 & l_2m_3+l_3m_2 & l_2n_3+l_3n_2 & m_2n_3+m_3n_2 \end{bmatrix} \tag{5.34}$$

The unit vector along principal direction i is

$$\vec{\mathbf{e}}_i = \begin{bmatrix} l_i & m_i & n_i \end{bmatrix}^T$$

l_i, m_i and n_i are the corresponding directional cosines.

T_ε is a matrix that rotates the engineering strain tensor from the global coordinate system to the current system of principal loading. T_σ rotates the engineering stress tensor from the global coordinate system to the current system of principal loading.

It can be shown that $T_\varepsilon^{-1} = T_\sigma^T$ and $T_\sigma^{-1} = T_\varepsilon^T$. Therefore, to rotate strains from the local principal coordinate system to the global coordinate system T_σ^T is used, T_ε^T is used to rotate stresses back to the global system.

In the new time step the history variables on the principal directions are obtained from the stored tensors in the global coordinate system:

$$\boldsymbol{\varepsilon}_{12}^P = T_\varepsilon \boldsymbol{\varepsilon}_{XY}^p \tag{5.35}$$

$$\boldsymbol{\varepsilon}_{12}^\nu = T_\varepsilon \boldsymbol{\varepsilon}_{XY}^\nu \tag{5.36}$$

$$d_{12} = T_\sigma d_{XY} \tag{5.37}$$

The procedure described above is schematized in the flow chart of figures 5.9 and 5.10.

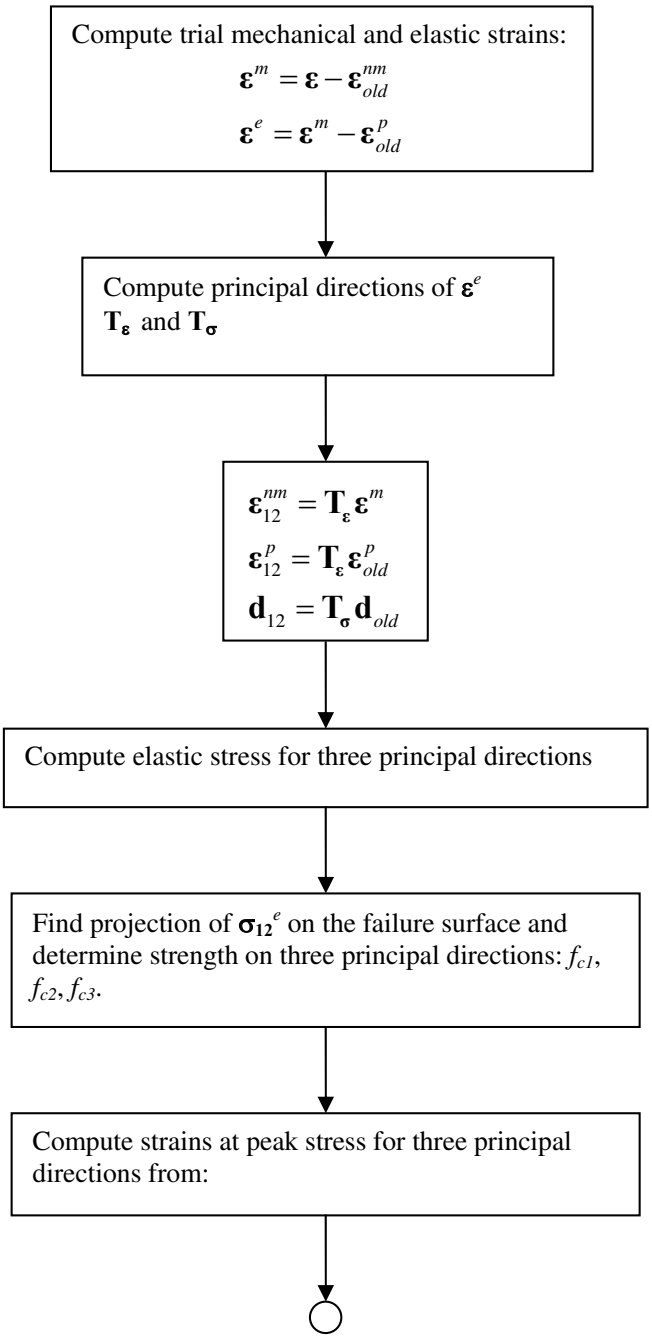

Figure 5.9: Concrete constitutive model flow chart (1)

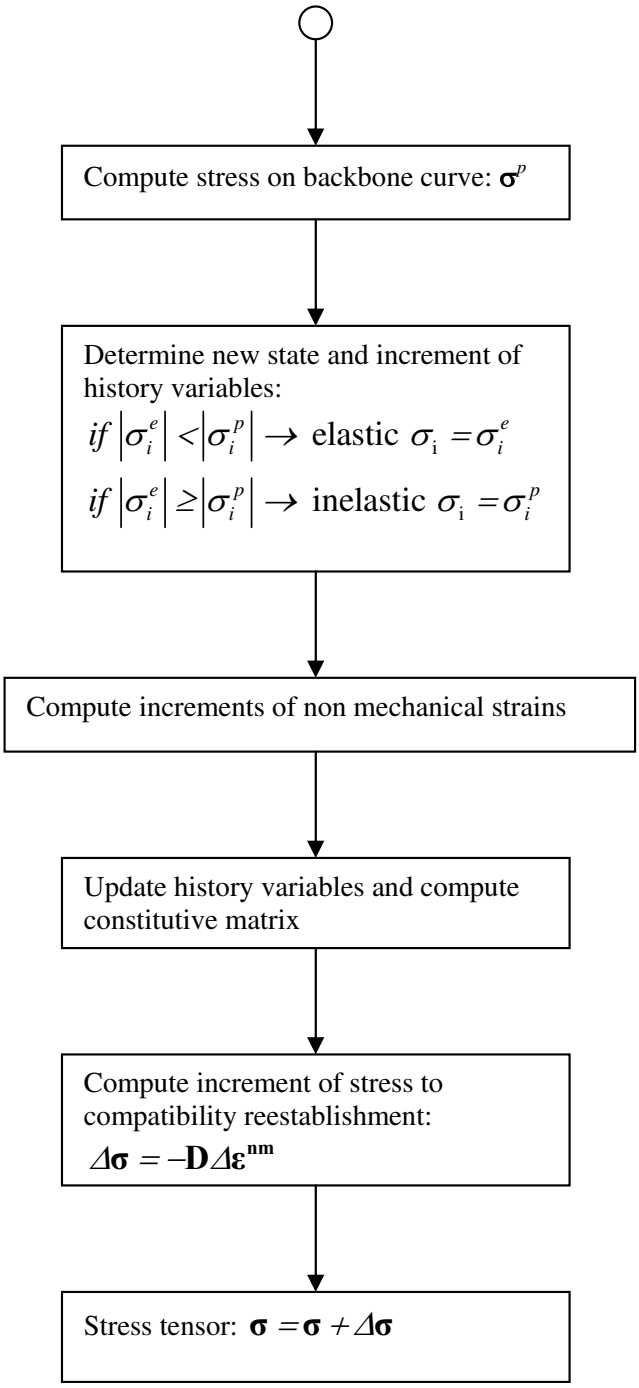

Figure 5.10: Concrete constitutive model flow chart (2)

5.4.8 Material response

To investigate the capabilities of the proposed constitutive model in reproducing the monotonic and cyclic behaviour of concrete, a set of tests were performed and will be presented next.

Biaxial compression loading

Figure shows the predicted response of three different concrete strengths under increasing proportional confinement rates. It was aimed to represent the behaviour of what can be called *"normal strength"*, *"moderete strength"* and *"high strength"* concretes. These grades of strength were respectively represented by $30MPa$, $50MPa$ and $80MPa$ concretes.

The three specimens were montonically loaded in two principal directions according to the following pattern:

$$\sigma_1 = \sigma_x$$
$$\sigma_2 = \alpha\sigma_x$$
$$\sigma_3 = 0$$

were α took the values 0, 0.05 and 0.1.

Figure 5.11 shows that the model predicts similar strength enhancements for all three types of concrete although different evolution of the $\sigma - \varepsilon$ law. It is noticed that the higher the concrete strength, the model predicts lower relative tangent modulus than in the case of a normal strength concrete.

Confined shear loading test

Shear loading in concrete is a rather complex phenomenon. Before cracking, concrete is able to resist shear as a couple of compression and tension stresses in two orthogonal directions usually located in a system rotated 45° from the direction of the shear stress. The first difference compared to a purely isotropic linear material is that, due the different behaviour in tension and

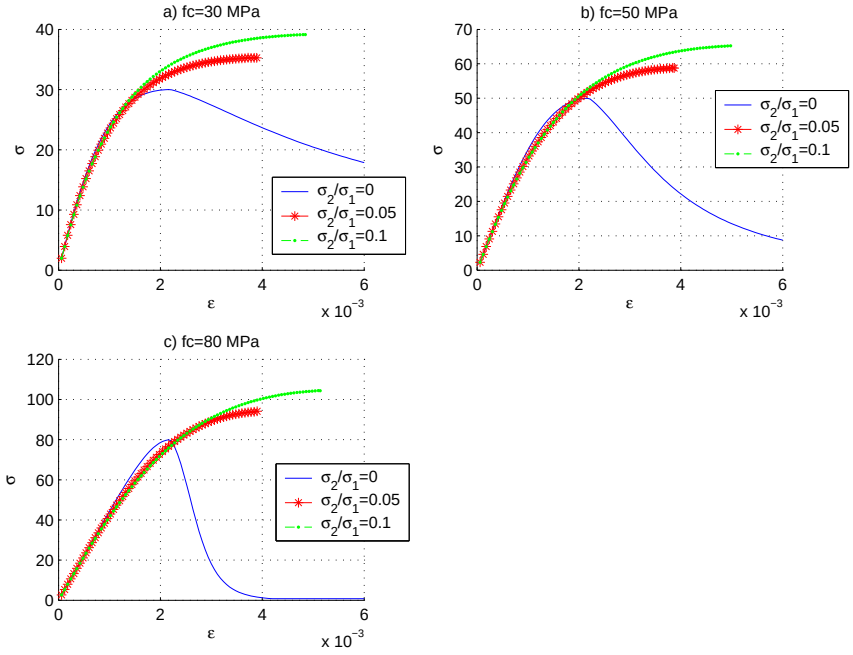

Figure 5.11: Confined compression loading for different concrete strengths (compression positive). a) 30 MPa, b) 50 MPa and c) 80 MPa

compression, the shear performance of concrete is not uncoupled to the normal stresses behaviour.

Even before cracking, although in a considerable minor amount, this effect is present since concrete is almost linear in tension until cracking stress while in compression presents non-linear $\sigma - \varepsilon$ behaviour from the very first moment. This phenomenon can be neglected compared to the post-cracked behaviour were tension and compression differences are considerable greater an so is the dependence of the shear performance to the concomitant normal stresses.

Figure 5.12 shows several simulations in a $30MPa$ concrete subjected to monotonic shear loading with proportional concomitant normal stresses in the two in-plane direction. Slightly differences in the $\tau - \gamma$ curve can be seen before cracking as mentioned in the previous above.

The influence of the concomitant normal stresses in the cracking shear stress is notorious in the same figure (5.12). After this point, concrete presents a

strain-softening behaviour.

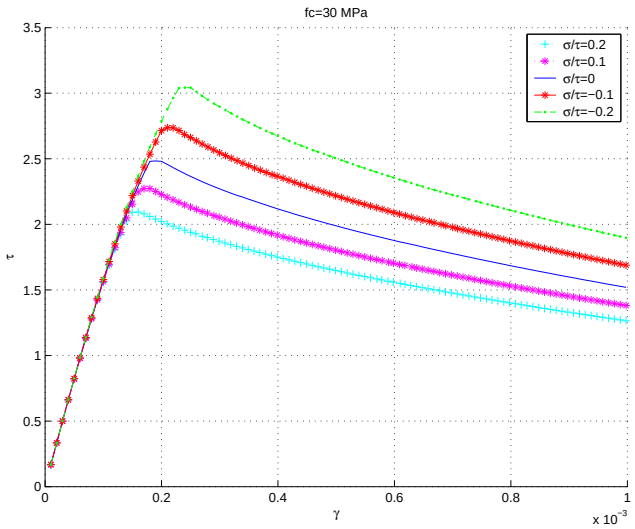

Figure 5.12: Shear loading with different confinement stress ($\sigma = \sigma_x = \sigma_y$).

Cyclic compression test

Figure 5.13 shows a uniaxial cyclic compression loading of $30MPa$ strength concrete. While loading concrete responds with the non-linear $\sigma - \varepsilon$ law described above. Figure 5.14 shows the plastic strains as a function of the total strains. Note that variations of plastic strains only take place during *new-loading* state.

When unloading and reloading, compressed concrete responds linearly. In this situation plastic strain do not change as seen in figure 5.14.

Cyclic tension test

Under tensile loading, concrete is linear elastic until cracking stress is reached. After this point it exhibits strain-softening and strain-softening as shown in figure 5.15. Unloading and reloading present linear behaviour according to a degrading longitudinal modulus affected by the normal component of the damage tensor projected to the loading directions. In this case, the loading

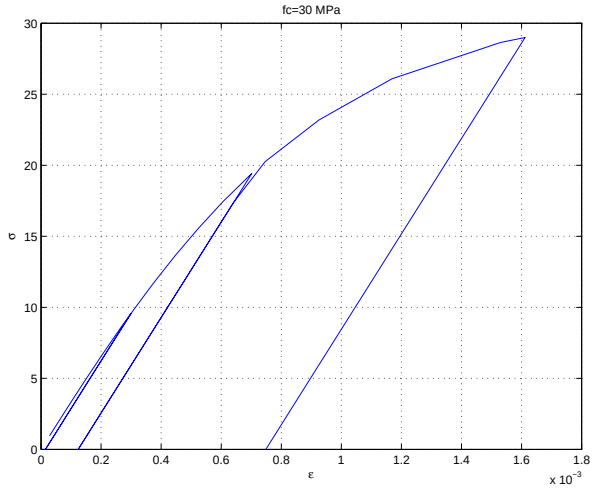

Figure 5.13: Stress-strain loops under uniaxial cyclic compression (compression positive).

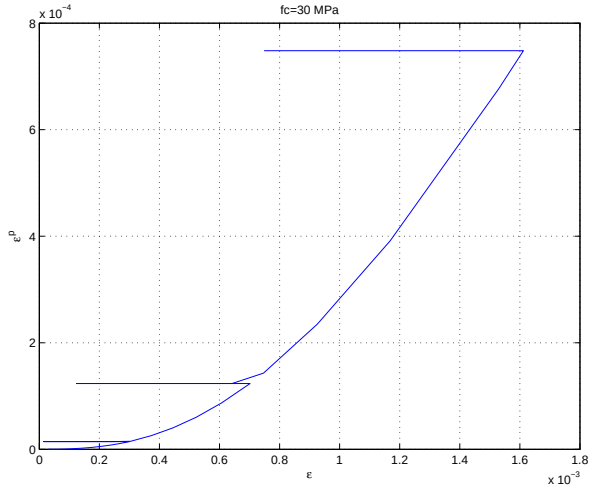

Figure 5.14: Plastic strain-total strain under uniaxial cyclic compression (compression positive).

direction does not change so damage tensor has a single component in the whole process.

In figure 5.16 it is shown the evolution of the relevant damage component. Note that the variable is asymptotic increasing to a maximum of one, which corresponds to total degradation. While unloading and reloading damage remains constant as an irreversible process.

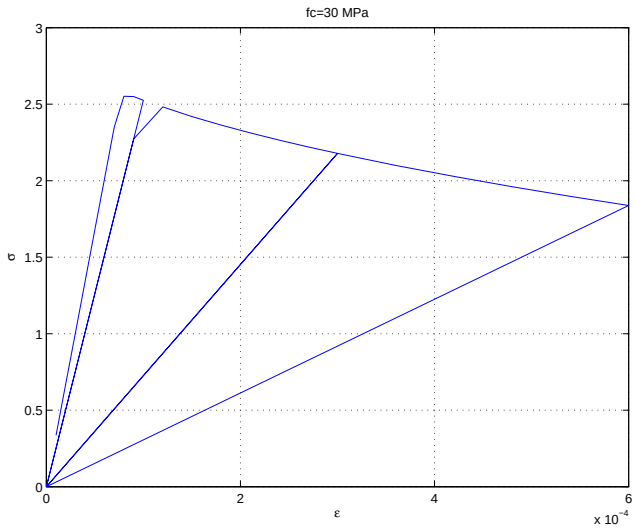

Figure 5.15: Stress-strain loops under uniaxial cyclic tension.

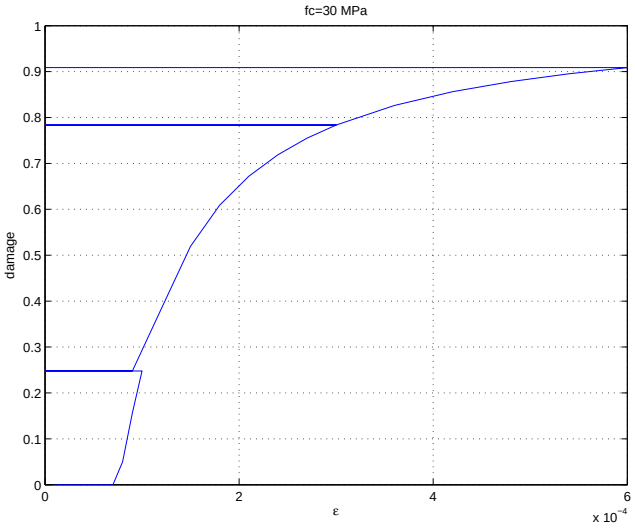

Figure 5.16: Damage-strain under uniaxial cyclic tension.

Cyclic pure shear test

Cyclic pure shear loading of a $30MPa$ concrete is shown in figure 5.17. A slight non-linear behaviour can be noticed in the $\tau - \gamma$ curve before cracking occurs. After cracking, strain softening is noticed.

It can be seen that cyclic loading is strongly characterized by tensile damage behaviour being dominant in comparison to the compression in the orthogonal principal direction. Because of this, shear resistance under unconfined loading degrades in the same way as the tension strength when increasing cycles.

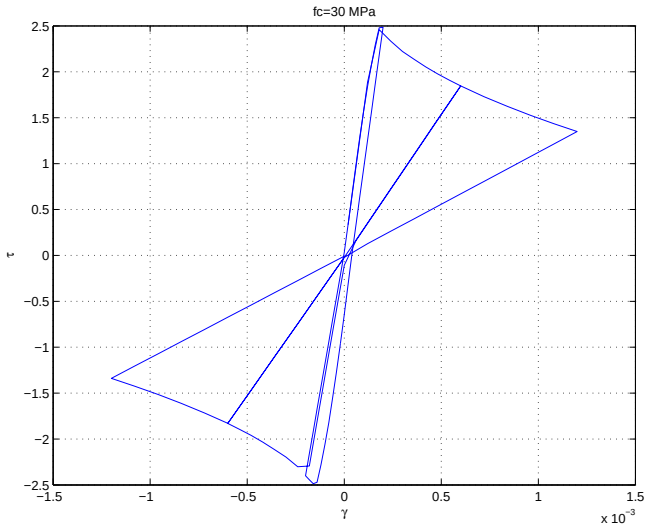

Figure 5.17: Shear stress-strain loops under zero confinement loading.

In this loading condition, principal tensile directions are alternating producing directional damage in the damage tensor as can be seen in figure 5.18 which is a representation of the damage tensor for different loading steps. Each figure represents, in polar coordinates, the magnitude of the normal component of the damage tensor projected in the direction given by the angular coordinate.

Figure 5.18.a show the damage tensor in one of the first load steps, prior to the first loading reversal. It is noticed that the damaged tensor has a principal direction in 45° with respect to the applied shear, corresponding

to the tensile principal stress component. When moving from this direction, the influence of the applied damage gradually decreases until reaching the principal compression direction at $-45\,^{\circ}$.

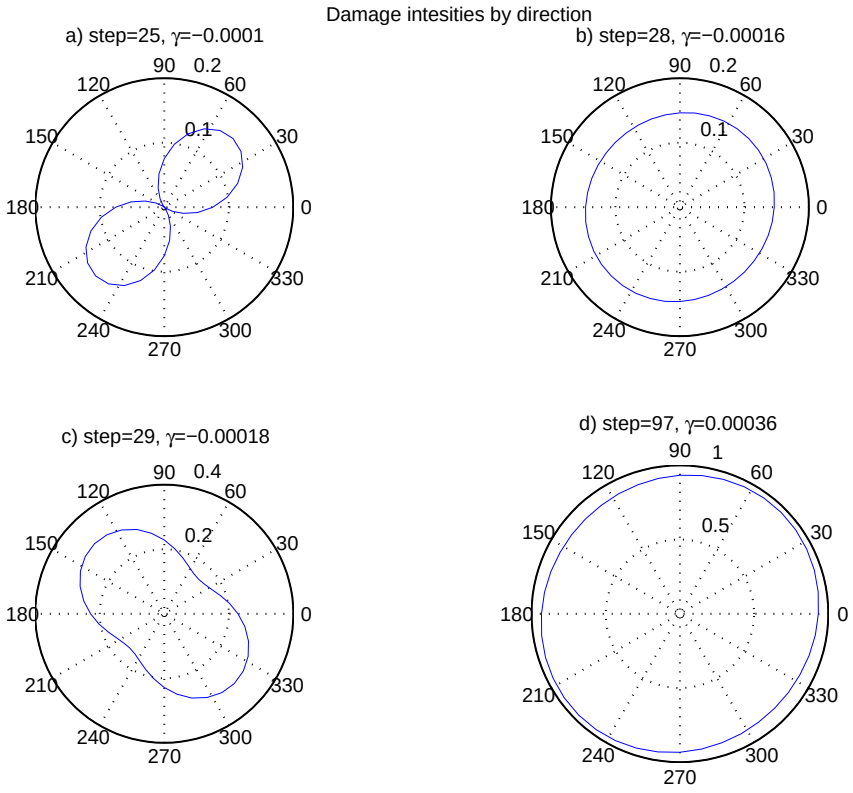

Figure 5.18: Evolution of damage tensor's intensity and direction

After load reversal, cracking in the opposite direction is also reached and so damage in the orthogonal direction. Eventually, practically isotropic damage can be achieved as shown in figure 5.18.b and 5.18.d. Figure 5.18.c is an example of a typical state were it has occured damage in all directions but there is a principal damage direction.

Cyclic confined shear test

As mentioned above, shear performance of cracked concrete is strongly dependent on the concomitant normal stresses. The following two tests correspond to cyclic shear forces with to limit type of concomitant normal

stresses, proportional normal stress and constant compression.

Figure 5.19 shows the predicted response of a $30MPa$ concrete under proportional stress in the same plane as the shear load is applied, in figure 5.20 the corresponding concomitant normal stress is presented. The overall response has similar characteristics as the pure shear cyclic loading: strain softening after cracking and degrading stiffness. There is, however, a remarkable difference in the hysteretic loops in the first and fourth quadrants, corresponding to compression and tension concomitant normal stresses respectively, both in the maximum and sustainable shear strains.

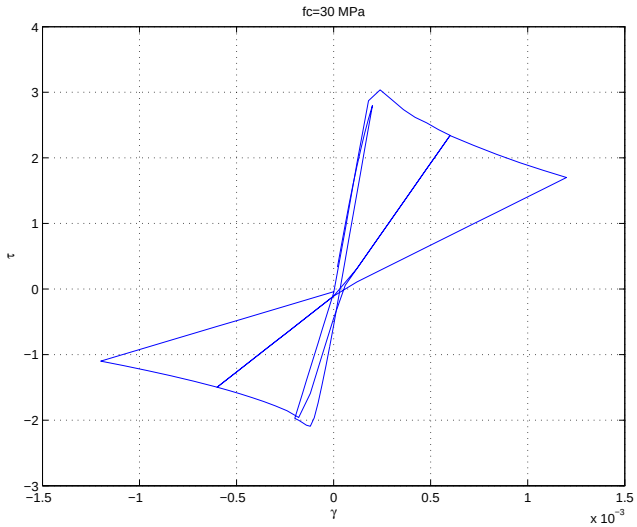

Figure 5.19: Shear stress-strain loops under proportional confinement loading.

It should be mentioned that while proportional loading enhances shear behaviour when the concomitant stress is in compression, the overall response still shows damage and stiffness degradation making the $\sigma - \varepsilon$ to follow a secant to the origin in each loading loop. However, when concomitant stress is a fixed compression during the whole cyclic loading differences are evident as seen in figure 5.21.

Plastic components in shear strains are more evident, although still small, due to higher principal compressions. The typical cyclic loop shows an almost linear zone where some plastic strains are developed and a second zone

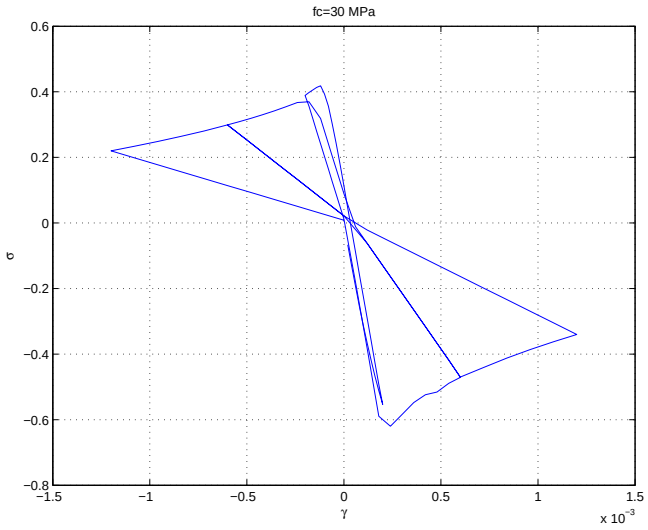

Figure 5.20: Axial stress-shear strain loops under proportional confinement loading.

where the lower principal direction is decompressed. In this stage, higher shear stresses are sustained until cracking occurs, then concrete begins a strain-softening process with damage and degrading stiffness.

The difference now is that it does not reaches the origin but the shear stress that starts the decompression. Degradation tends asymptotically to the decompression shear stress. Where degradation is complete, material will almost have a bilinear behaviour, with loading and unloading following the same path.

The two previous simulations are *ideal* loading conditions that are not exactly reproduced in a concrete cross-section with transverse reinforcement. The typical situation is in between the two presented examples, since stirrups will present, in elastic regime, a proportional concomitant confinement. However, this proportional stress does not have a constant proportionality coefficient, since it is always compressive no matter the sign of the shear stress. On the other hand, stirrups stress also depend on other parameters such as cracks angle, longitudinal reinforcements, other applied forces, section's shape, etc. The exact cyclic behaviour will be given by the interaction of all these parameters that will be a result of the sectional model

after satisfaction of the *warping-distortion problem* described in the previous chapters.

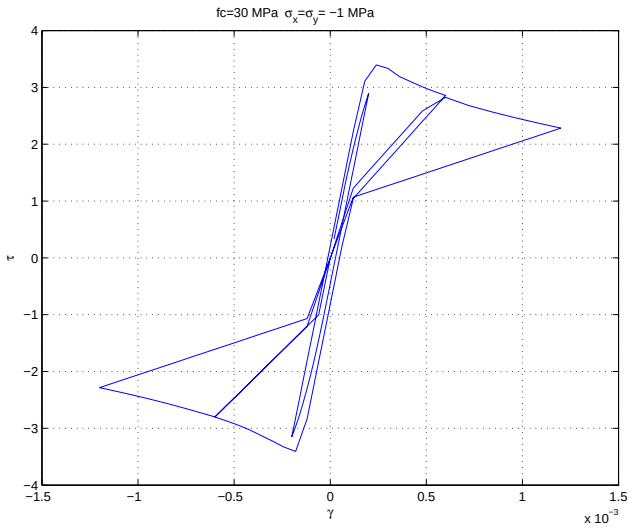

Figure 5.21: Shear stress-strain loops under fixed confinement load.

5.5 Constitutive model for reinforcing steel: "BilPla-Cyclic"

To simulate the behaviour of reinforcing steel bars an uniaxial constitutive model is used. The model is a bilinear elasto-plastic constitutive law that allows for kinematic strain hardening and cyclic loading by means of an scalar state variable to store the plastic strain. An extensive description of the constitutive law is given below.

5.5.1 Hypotheses

The non-linear behaviour of steel reinforcement is considered only to resist normal stresses, therefore an uniaxial $\sigma - \varepsilon$ law has been considered sufficient for these elements.

Elastic offsets, such as temperature strains or steel relaxation can be treated as non-mechanical strains in the same way as it was done for concrete, see

section 5.4. The concepts of mechanical and non-mechanical strains are also useful for this material to store all elastic offsets.

Steel pre-strains is also possible by means of a non-mechanical strain.

As for concrete, a state of new-loading is defined when the current (σ, ε) is loading along the envelope curve. A unloading state will be defined when loaded to a smaller strain level than the one in the current state. A reloading state will occur if the material is loaded to a higher strain level but the (σ, ε) point is not on the backbone curve.

5.5.2 Elastoplastic behaviour

Steel is simulated using a bilinear elastoplastic model with kinematical hardening. For the simulation of reinforcement bars it will be sufficient an uniaxial equation like the one in figure 5.22. Its bilinear backbone curve is characterized by three parameters: an elastic modulus E_0, a plastic modulus E_1 and a yielding stress f_y.

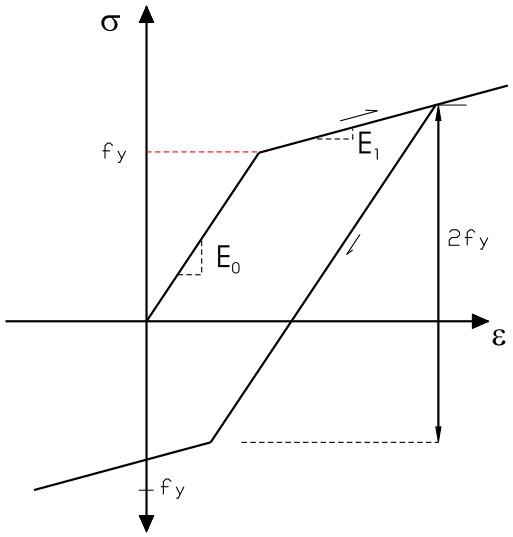

Figure 5.22: Stress-strain law for steel

5.5.3 State update algorithm

A single scalar history variable is needed to store the plastic strain. The scheme to follow in the state evaluation in a material point of reinforcement steel is described bellow.

The first step is to compute the elastic strain and stress given an incremental strain. A trial elastic strain is taken as the difference of the new strain and the current plastic strain:

$$\varepsilon^e = \varepsilon - \varepsilon^p \tag{5.38}$$

The trial stress is given by the following equation.

$$\sigma^e = E_0 \varepsilon^e \tag{5.39}$$

This trial stress has to be compared with the current elastic yielding stress, which according is evaluated considering a kinematical hardening rule as follows:

$$\sigma^p = sign\left(\varepsilon^p\right) f_y + \varepsilon^p E_1 \tag{5.40}$$

In the previous equations E_0 and E_1 are the elastic and yielding modulus respectively.

If the inequation (5.41) is true, the trial state will be valid. Then the actual stress will be equal to the trial elastic strain σ^e. If on the contrary inequation (5.42) holds, the material will be yielding and the trial state will have to be corrected.

$$|\sigma^e| < |\sigma^p| \rightarrow elastic, \sigma = \sigma^e \tag{5.41}$$

$$|\sigma^e| \geq |\sigma^p| \rightarrow plastic \tag{5.42}$$

If the material is yielding, equation (5.42) is true, then the plastic strain changes in the following amount, see figure 5.23.

$$\dot{\varepsilon}^p = \frac{\sigma^e - \sigma^p}{E_0} \tag{5.43}$$

In the same way, the correct stress will be given by equation (5.44) as can be explained after figure 5.23.

$$\sigma = \sigma^p + E_1 \dot{\varepsilon}^p \tag{5.44}$$

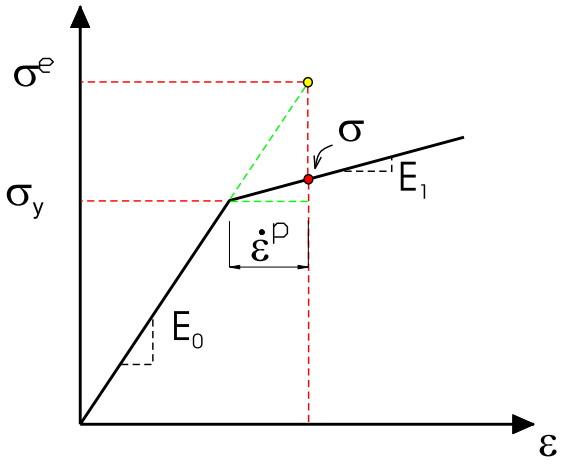

Figure 5.23: State updating during yielding

5.5.4 Material response

To investigate the capabilities of the proposed constitutive model to reproduce accurately the behaviour of reinforcing steel is a uniaxial loading test is presented next. An elastic modulus of $E_s = 2E5MPa$ and yielding stress of $f_y = 500MPa$ where considered. During yielding, a hardening modulus of $E_1 = 0.01E_s$ was used.

The response of the proposed uniaxial constitutive model can be seen in figure 5.24; where a cyclic tension-compression strain history has been applied to the material. In the same figure, the evolution of the internal variables during the cyclic loading are also shown. It can be seen that, as expected, plastic strains are only changing during material yielding and they are sustained until a new yielding state, in tension or compression, is occurred.

Kinematic hardening is noticed in both $\sigma - \varepsilon$ hysteretic loop and $\sigma - time$ curve.

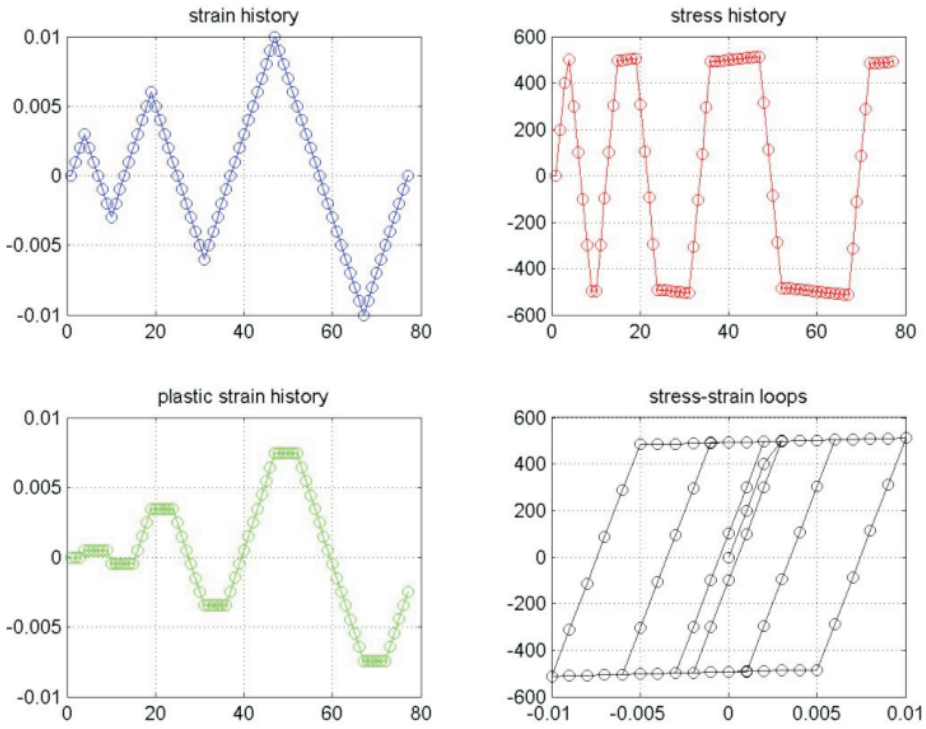

Figure 5.24: Cyclic behaviour of reinforcing steel

Chapter 6

Validation and case studies

6.1 Introduction

In this chapter, a series of case studies of sections under combined loading are analysed using the proposed model and the developed program. Two objectives have motivated this analyses: to verify the accuracy of the results provided by the proposed scheme comparing to theoretical or experimental solutions and to show the model's ability to reproduce complex situations of combined loading that conventional fiber cross-section formulations fail to capture.

The model was proved to simulate complex interactions that occurs under shear or torsion loading combined with normal forces and bending moments. These type of actions in general results in the warping and distortion of the original section's shape, phenomena accuratly caught by the proposal.

In the particular case of RC beams, it is shown how, because of the capabilities of the model to hanlde material non-linearity, crack-induced effects are properly simulated satisfying internal fiber equilibrium and further implications in the full non-linear behaviour until failure is reached.

The presented case studies are subdivided into two groups:

1. Theoretical case studies: where the model is used to analyse proposed

examples, for which analytical closed form solutions are available or the phenomenological behaviour has been observed although a close form solution might not be available, in order to compare the theoretical and the numerically predicted results.

2. Experimental case studies: where the model is employed to reproduce experimental investigations. Advantage of the numerical model is taken to show the evolution of internal variables and fields that are difficult or impossible to measure in laboratory tests, makeing easer the understanding of the simulated processes.

6.2 Theoretical case studies

A total of five theoretical examples are presented in the following section for which either closed form solutions or well-established models are available or the complex phenomenological response has been observed. The examples are presented starting from an equilateral triangular section made of an isotropic elastic material under pure torsion. The exact solution of this problem is known and can be found in Timoshenko and Goodier (1972).

An also linear but anisotropic problem is presented next in the form of two different composite laminate wide beams under bending and shear loading. The problem is compared to a *middle-plane* solution that can be found in Reedy (1996).

A set of theoretical case-studies on RC sections are then presented. The first one is an investigation on a cantilever RC element with a point lateral load. The element was subdivided into a series of sections and subsequently analysed. Elemental response was obtained by integration along all cross-sections.

The influence of the concomitant shear force on the moment-curvature curves of an RC section is investigated in the next case.

Finally, a square concrete section confined with stirrups was loaded in compression, all load stages including cover spalling were reproduced. Ultimate

load was compared with the predicted by the well-established model of Mander et al. (1988).

6.2.1 Triangular section under pure torsion

An isotropic linear elastic section with an equilateral triangular cross section of $200mm$ height is analysed under torsion loading; see figure 6.1. The applied torsional load corresponds to a torsional curvature of $1E-6\frac{rad}{mm}$.

The material properties considered in this analysis are summarized in table 6.1. The aim of this example is to show the capabilities of the proposed model in reproducing theoretical problems whose solutions are known in a closed form. The analytical solution of this problem can be found in Timoshenko and Goodier (1972); the cited authors utilized the membrane analogy to solve the problem.

It is known that, since section is not circular its correct solution is not given by Navier torsion theory, which is included in the plain section space of solutions (PS) mentioned in previous chapters. But section's warping must be takien into account to obtain a correct strain-stress field satisfying both compatibility and equilibrium conditions. Figure 6.2 shows the predicted sectional warping.

Table 6.1: Material properties of equilateral triangular section

E (Elastic modulus)	$30,000MPa$
G (Shear modulus)	$12,500MPa$
ν (Poisson coefficient)	0.2

Figure 6.3.a shows the predicted vertical component of the shear stress field, τ_{xz}. In figure 6.3.b the bidimensional shear flow can be appreciated; one may note in this figure how shear the vertices of the triangle correspond to singularity points where shear stresses must be vanished in order to satisfy boundary conditions. The proposed model was able to reproduce this field with enough accuracy as can be concluded from table 6.2 were numerical

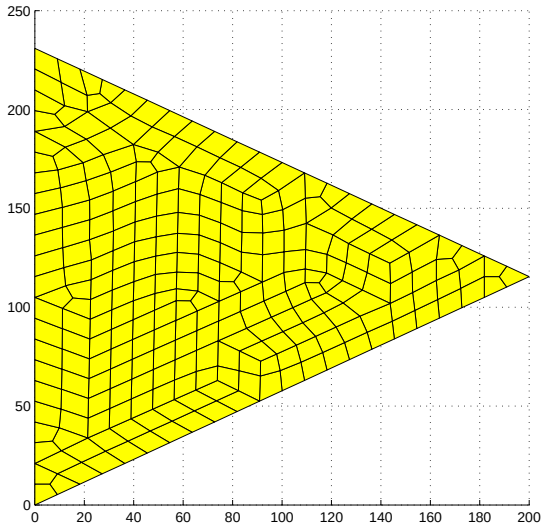

Figure 6.1: Equilateral triangle. Undeformed shape and finite element mesh.

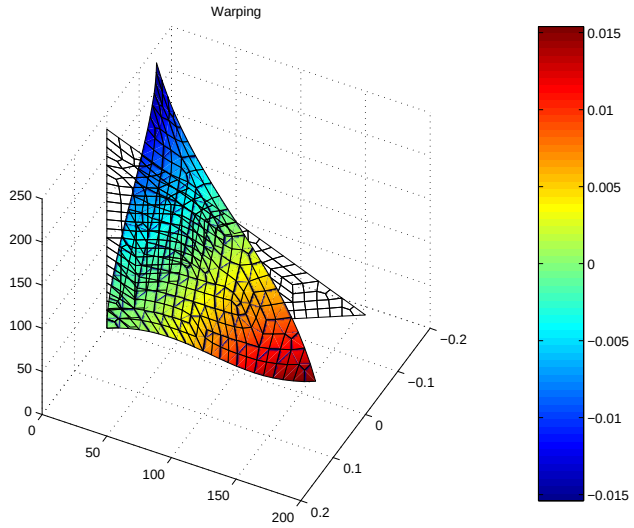

Figure 6.2: Warping of equilateral triangle.

and closed form solutions are compared both for the maximum τ_{xz} and the integrated torsional moment.

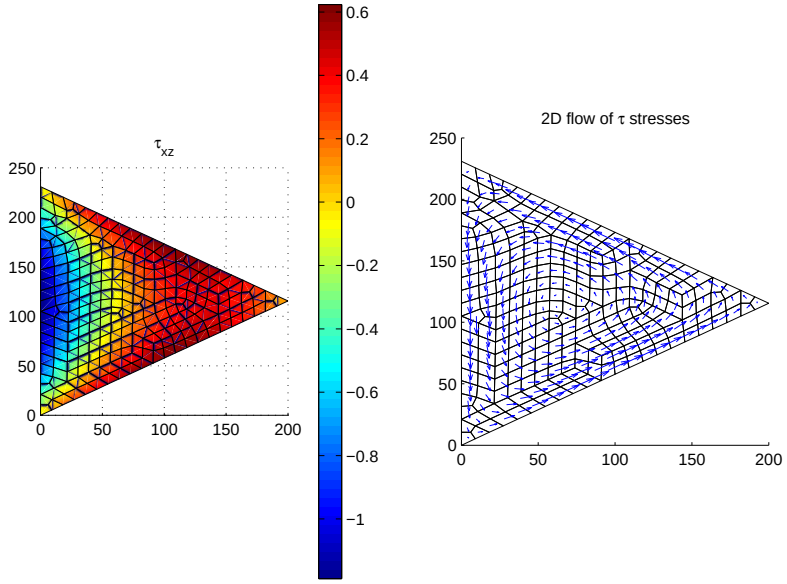

Figure 6.3: Shear stresses in equilateral triangle. a) τ_{xz} stresses; b) shear stress flow.

Table 6.2: Comparison between theoretical and numerical solutions of a triangular isotropic section under torsion.

	Theoretical value	Numerical value	Error
$T[KNm]$	0.7698	0.7725	0.34%
$\tau_{xz}[MPa]$	1.1881	1.1880	0.01%

6.2.2 Composite laminate beam under coupled bending and shear

To investigate the capability of the proposed formulation to deal with sections made of anisotropic materials, two specimens made of composite orthotropic plates assemblies under three point loading will be analyzed next,

figure 6.4. The solution of these beams is presented by Reddy (1996) using a one dimensional solution characterized by the beam's middle plane.

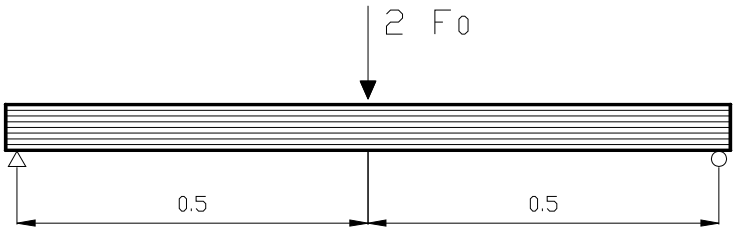

Figure 6.4: Composite beam loading scheme.

The dimensions, material's properties and loads of the two specimens' sections are the same but have different ply arrangements, as shown in figure 6.5. Lamination schemes are commonly denoted by listing the fiber orientation angle of each ply from bottom to top; if the stack is symmetric about the midplane, it is possible to list only half of the plies and add a S subscript to denote symmetry. With this notation, the schemes for sections 1 and 2 are respectively $(0/45/-45/90)_S$ and $(90/45/-45/0)_S$.

The section's dimensions are: $b = 0.2$, $h = 0.1$. The critical section is located in the element's midspan; in this point, the internal forces are a vertical shear force F_0 and a bending moment $0.5F_0$. Solutions will be presented in terms of normalized stresses in the following form:

$$\bar{\sigma} = \sigma \frac{bh}{F_0}$$

In the same manner, the materials properties are normalized with respect to the elastic modulus in the material direction $2-2$ like in table 6.3.

The mesh employed for both sections is the one seen in figure 6.5.c. Figures 6.6.a and 6.6.b show the warping-distortion state of both sections.

The influence of the plies distribution both in normal stresses and shear stresses is evident. It is known that, because of the orthotropy of the plies, auto-equilibrated shear stresses appear to maintain the sectional integrity, producing that under any arbitrary load, even though it is a pure normal

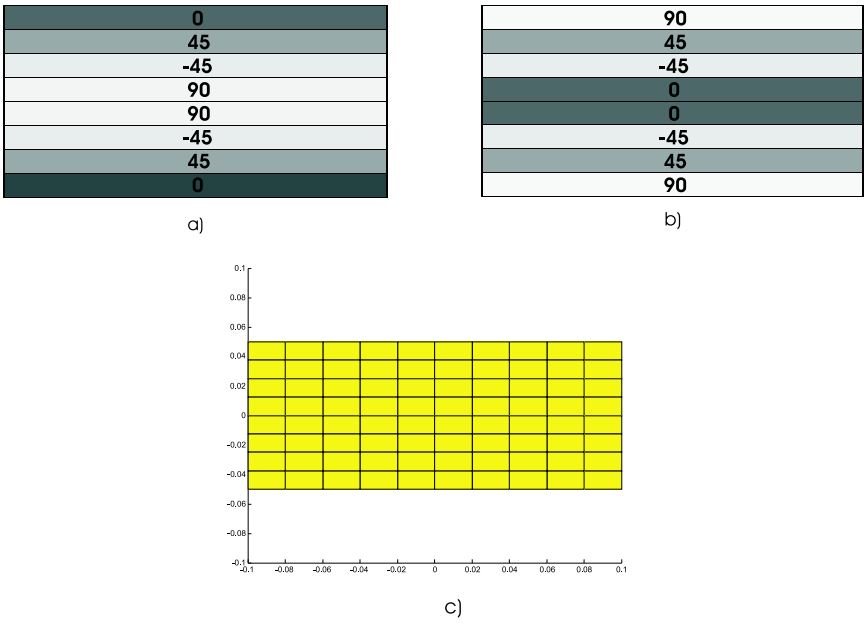

Figure 6.5: Composite cross-sections analyzed. a) section 1; b) section 2; c) finite element mesh.

Table 6.3: Material properties of composite plies.

$\frac{E_1}{E_2}$	25
E_2, E_3	1
$\frac{G_{12}}{E_2}, \frac{G_{13}}{E_2}$	0.5
$\frac{G_{23}}{E_2}$	0.2
$\nu_{12}, \nu_{13}, \nu_{23}$	0.25

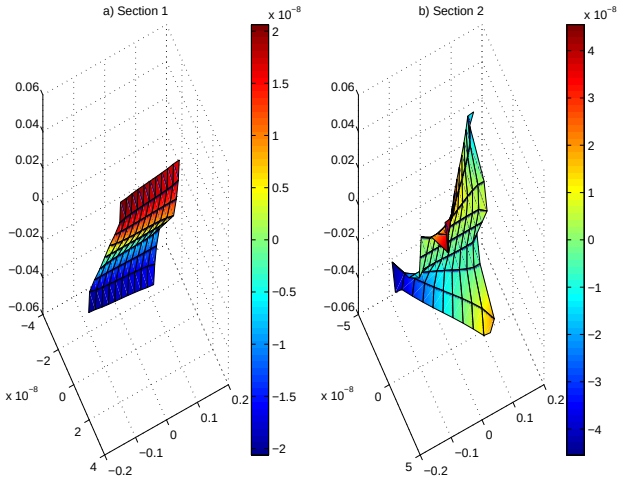

Figure 6.6: Sectional distortion under loading. a) section 1; b) section 2.

force or shear force, distortion and warping occur as the general case. This fact can be seen in figure 6.7 were the six distortion-warping modes of section 2 have been plotted. These modes correspond to the sectional distortion after a unit value of the indicated generalized degree of freedom is applied. Note that, even for the normal generalized strains, axial strain and bending curvatures, the cross section experiments distortion.

As noticed from figure 6.6, warping modes of sections 1 and 2 differ being the last one more influenced by coupled effects between bending and torsion. This statement can be confirmed from the two sections' stiffness matrixes reproduced in equations (6.1) and (6.2) respectively. While $0\,^\circ$ layers are located in an optimun position to resist bending moments in section 1, in section 2, they are located close to the midplane. In the second case, bending moment is mainly resisted by the $\pm 45\,^\circ$ plies. Horizontal shear stresses and out-of-plane stresses, produced because the orthotropic material is not loaded along its principal directions (as schematically indicated in figure 6.8), are higher in the second beam.

The section gets distorted to maintain inter-fiber equilibrium . In figure 6.9 it is seen that these auto-equilibrated shear stresses are as much as ten times higher in section number two, reflecting the stronger bending-torsion

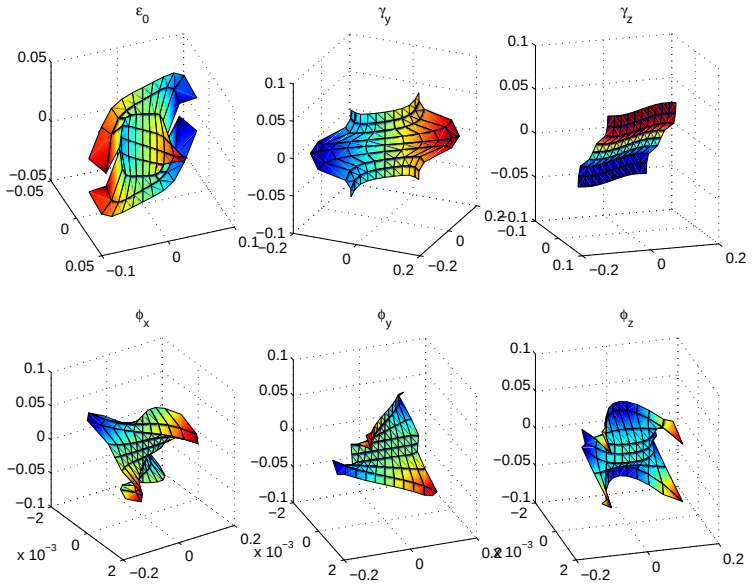

Figure 6.7: Warping-distortion modes for the six generalized strains in section 2.

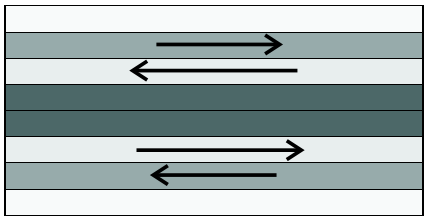

Figure 6.8: Sketch of the horizontal shear stresses developed in the $\pm 45^\circ$ plies.

coupling.

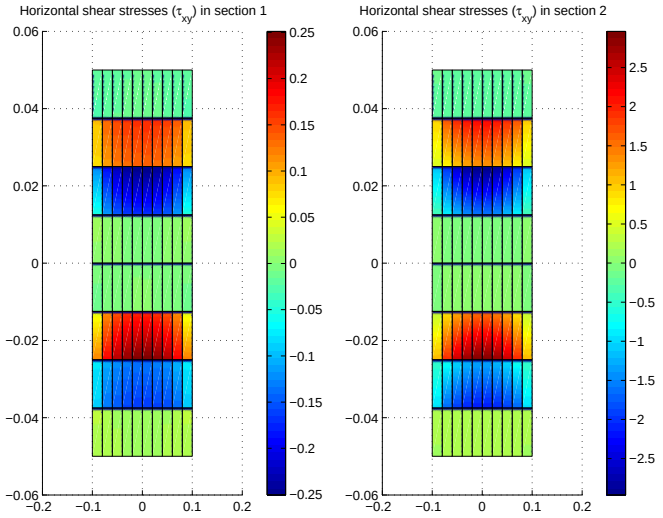

Figure 6.9: Shear stress field (τ_{xy}). a) section 1; b) section 2.

$$\mathbf{K}_{S1} = \begin{bmatrix} 1.61E5 & -8.61E3 & 0 & 0 & 0 & 0 \\ -8.61E3 & 8.12E4 & 0 & 0 & 0 & 0 \\ 0 & 0 & 6.04E3 & 0 & 0 & 0 \\ 0 & 0 & 0 & 3.32E1 & -2.76 & 0 \\ 0 & 0 & 0 & -2.76 & 2.57E2 & 0 \\ 0 & 0 & 0 & 0 & 0 & 5.08E2 \end{bmatrix} \quad (6.1)$$

$$\mathbf{K}_{S2} = \begin{bmatrix} 1.60E5 & 8.36E3 & 0 & 0 & 0 & 0 \\ 8.36E3 & 8.16E4 & 0 & 0 & 0 & 0 \\ 0 & 0 & 1.06E4 & 0 & 0 & 0 \\ 0 & 0 & 0 & 4.69E1 & -6.72 & 0 \\ 0 & 0 & 0 & -6.72 & 3.98E1 & 0 \\ 0 & 0 & 0 & 0 & 0 & 5.07E2 \end{bmatrix} \quad (6.2)$$

In figure 6.10 the normal stress field (σ_x) is shown for both analysed cases; figure 6.10.b evidences slightly higher edge effects on section 2 than in section

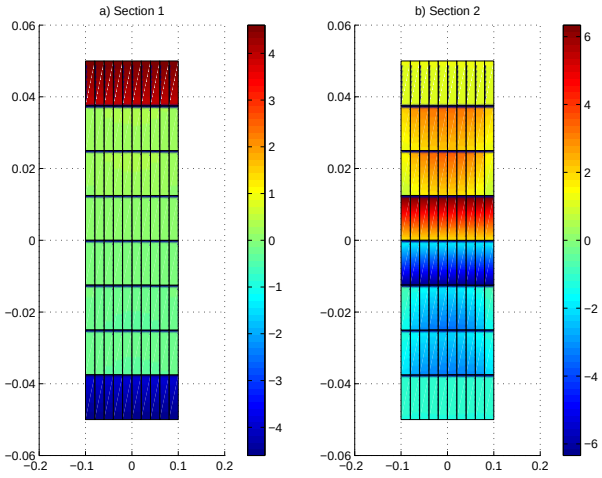

Figure 6.10: Normal stress field (σ_x). a) section 1; b) section 2.

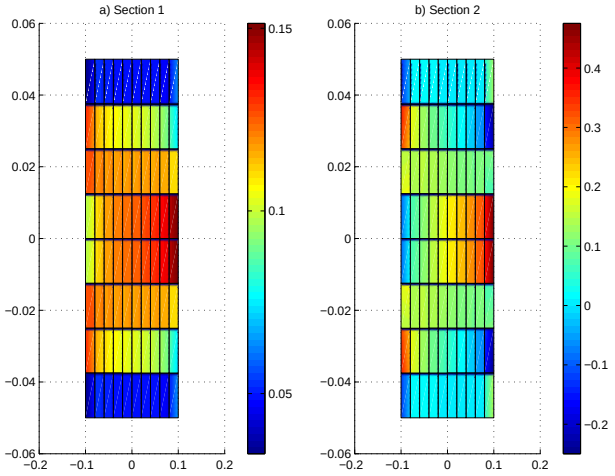

Figure 6.11: Shear stress field (τ_{xz}). a) section 1; b) section 2.

1. Nevertheless, these effects are more marked in both sections in the case of the vertical shear stress field (τ_{xz}), see figure 6.11.

Figures 6.12 and 6.13 represent vertical cuts of the σ_x and τ_{xz} fields respectively. The analytical middle plane solution found by Reddy (1996) has been also plotted in a blue wide line. Perfect coincidence exists between Reddy's middle plane solution and the cut passing through the zero ordinate both for normal and shear stresses. However, middle plane solution is not capable of reproducing edge effects captured by the proposed model, as shown in the figures.

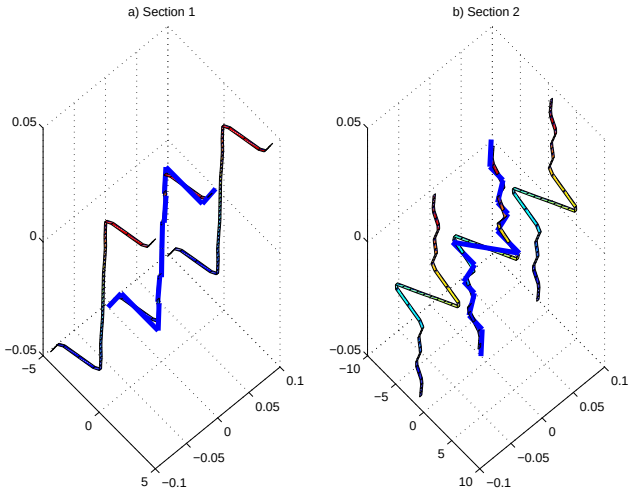

Figure 6.12: Vertical cuts of σ_x field and comparison with theoretical solution (wide blue line). a) section 1; b) section 2.

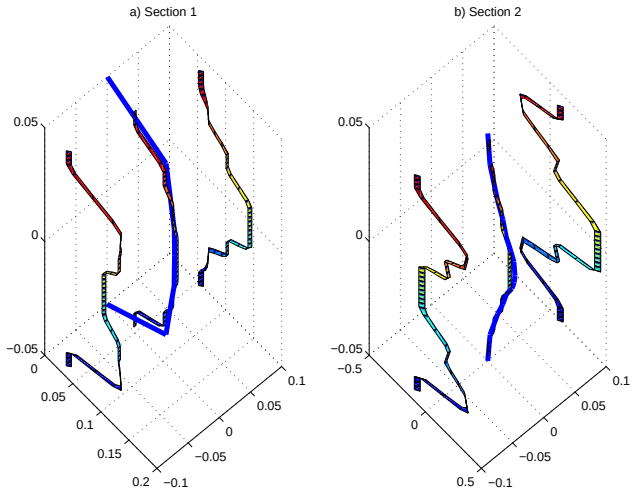

Figure 6.13: Vertical cuts of τ_{xz} field and comparison with theoretical solution (wide blue line). a) section 1; b) section 2.

6.2.3 RC cantilever

A reinforced concrete cantilever of $3000mm$ long is subjected to an horizontal point load in the free end as shown in figure 6.14.a. The cross section of figure 6.14.b is constant along the length of the element. The section was discretized in layers with the mesh of figure 6.14.c.

The material properties used in this example are summarized in table 6.4. The longitudinal reinforcement was assumed to have a plastic modulus of $2000MPa$ (not shown in the table).

Along its length, the element has been subdivided in ten increments producing eleven control sections. The overall response of the structure is obtained by numerical integration each section. In this situation all sections are subjected to a combination of bending moment and shear load. The objective of this case study is to investigate the non-liner behaviour of this simple structure considering the shear-bending interaction effects in non-linear regime. Is in these type of cases where the proposed model is a powerful and interesting tool.

Table 6.4: Material properties of the RC cantilever.

Concrete	f_c	$28.2MPa$
	f_t	$1.75MPa$
	E_c	$25600MPa$
	ν	0.2
Longitudinal steel	f_y	$442MPa$
	E_s	$200,000MPa$
Transversal steel	f_y	$400MPa$
	E_s	$200,000MPa$

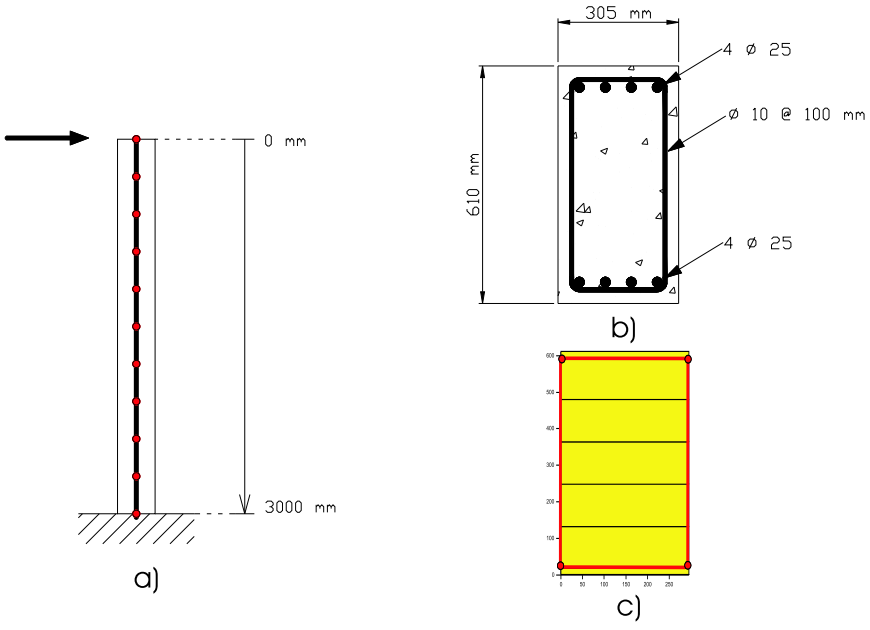

Figure 6.14: RC cantilever. a) test configuration, b) cross section, c)section discretization.

Figure 6.15.a shows the force-displacement response of the cantilever identifying the flexural, shear and total deformations. It is a common assumption in most of the non-linear formulation of frame elements to maintain shear stiffness fixed and linear elastic along the whole non-linear process, attributing all non-linearities to bending. In figure 6.15.b the contribution of shear deformation to the total displacement of the cantilever free end has been plotted. It is shown that this assumption is not accurate in zones where strong shear and moments exist together.

At early load stages, it is shown that shear displacements are around 3% of the total deformation. This was expected due to the slender aspect ratio of the element and usually shear deformation will be neglected. Early cracks are due to flexural loading, thus bending stiffness is reduced while shear stiffness remain constant, being coincident with regular non-linear frame element formulations as mentioned above. If shear cracks appear, as did happen for a displacement of around $3mm$, the situation changes completely. Shear stiffness degrades faster than bending stiffness does, thus shear contribution to total displacement increases to levels that can not be neglected any more (exceeding 10%) until the section yields in bending.

The distribution of the sectional curvature and shear deformation along the beam length if presented in figures 6.16 for different load levels. In order to make the shape of the generalized strains law more noticeable, the ordinates have been normalized to a unit maximum value.

Both curvature and shear deformation follow similar laws as the corresponding internal forces distribution for low level forces, i.e. linear for bending moments and constant for shear forces. For high level loads, curvatures tend to concentrate at the fixed end forming a plastic hinge that spreads in length under increasing loading (figure 6.16.a) until collapse.

The distribution of shear strains changes rapidly after cracking has occurred. Even at load of $70KN$, when bending curvatures are still almost linear, it can be seen that shear strains are already not following the same (constant) distribution as the shear forces. In figure 6.17 the stress at the middle height of stirrups is shown along the length. Even for a constant shear

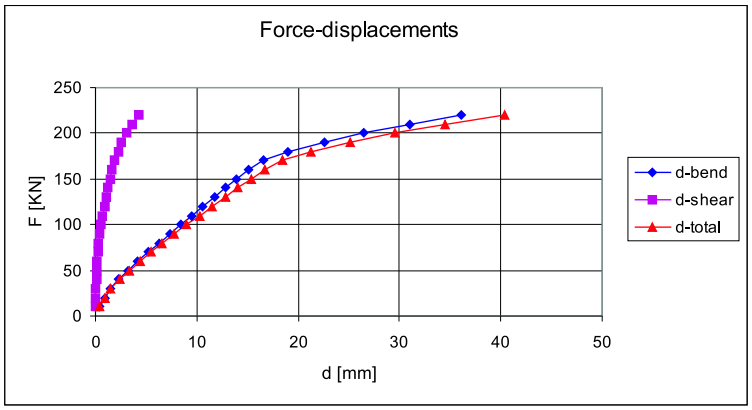

a)

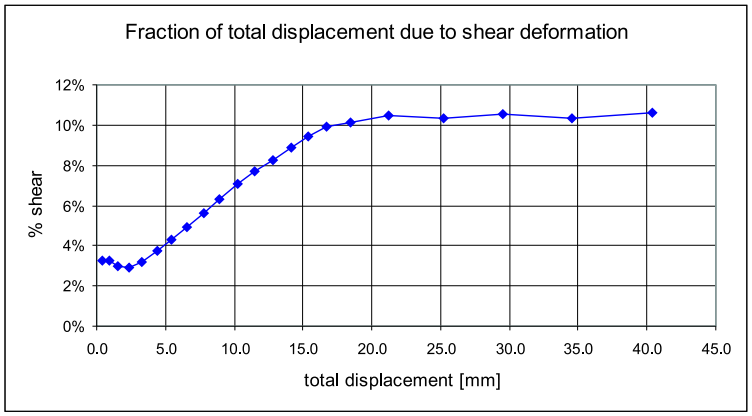

b)

Figure 6.15: RC cantilever force-displacement. a) bending, shear and total displacements, b) contribution of shear deformation to total displacement.

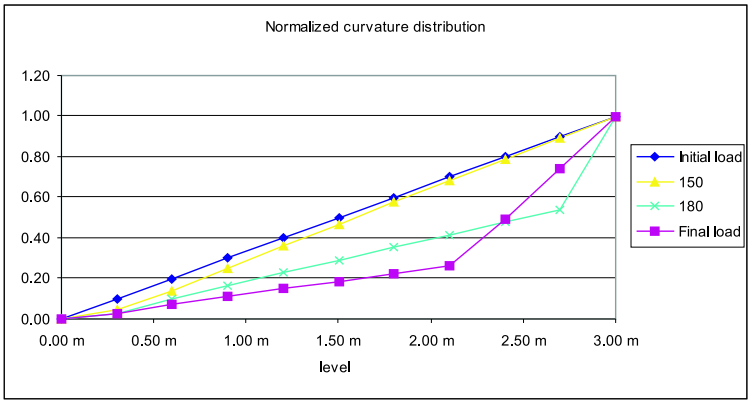

a)

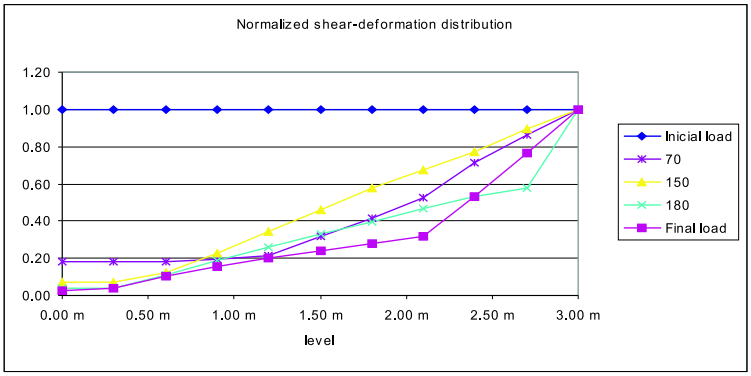

b)

Figure 6.16: RC cantilever strain distribution along length. a) normalized curvature distribution, b) normalized generalized shear strain distribution.

load, stirrups stresses are concentrated at the fixed end, where maximum moments are localized.

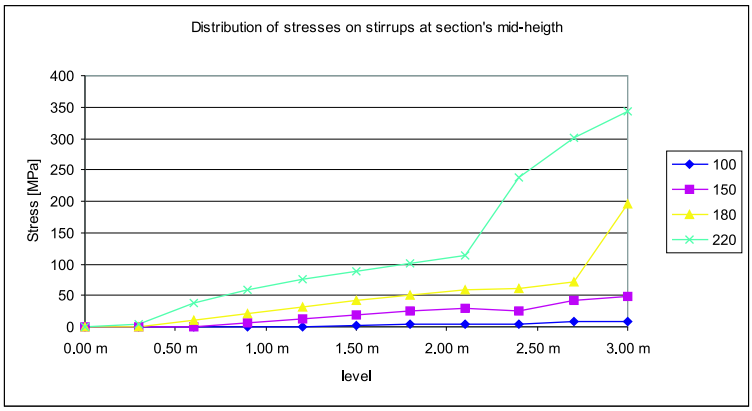

Figure 6.17: RC cantilever stirrups stress distribution along length.

A series of stress distributions are shown in figure 6.18 for different load levels. It is interesting to note a crack-induced anitostropy effect under shear-bending loading that occurs in the tensile zone. This situation is seen in figure 6.18.a for high load intensities when compression stresses occur below the neutral axis. These normal stresses correspond to the horizontal component of the diagonal strut forces necessary to resist the applied shear force as explained in figure 6.19.c.

During loading, the critical section (figure 6.18) goes through different shear resistance schemes. In figure 6.19 the main stages are represented. The first stage represents the behaviour before cracking where the section can be considered as isotropic, as can be confirmed in figure 6.18, this is the situation for a load level of $10KN$.

At a certain level, the element cracked in flexure. The traditional hypotheses of *Strength of Materials* predicts, under decoupled shear-normal stresses assumptions, a stress distribution as in figure 6.19.b. As has been commented, this result is not completely correct; nevertheless it can be acceptable at relatively low loads, see stress distributions at $100KN$ in figure 6.18. This is possible because at this load level, softening tensile stress is relevant in the transfer of shear stresses and diagonal compression stresses are relatively

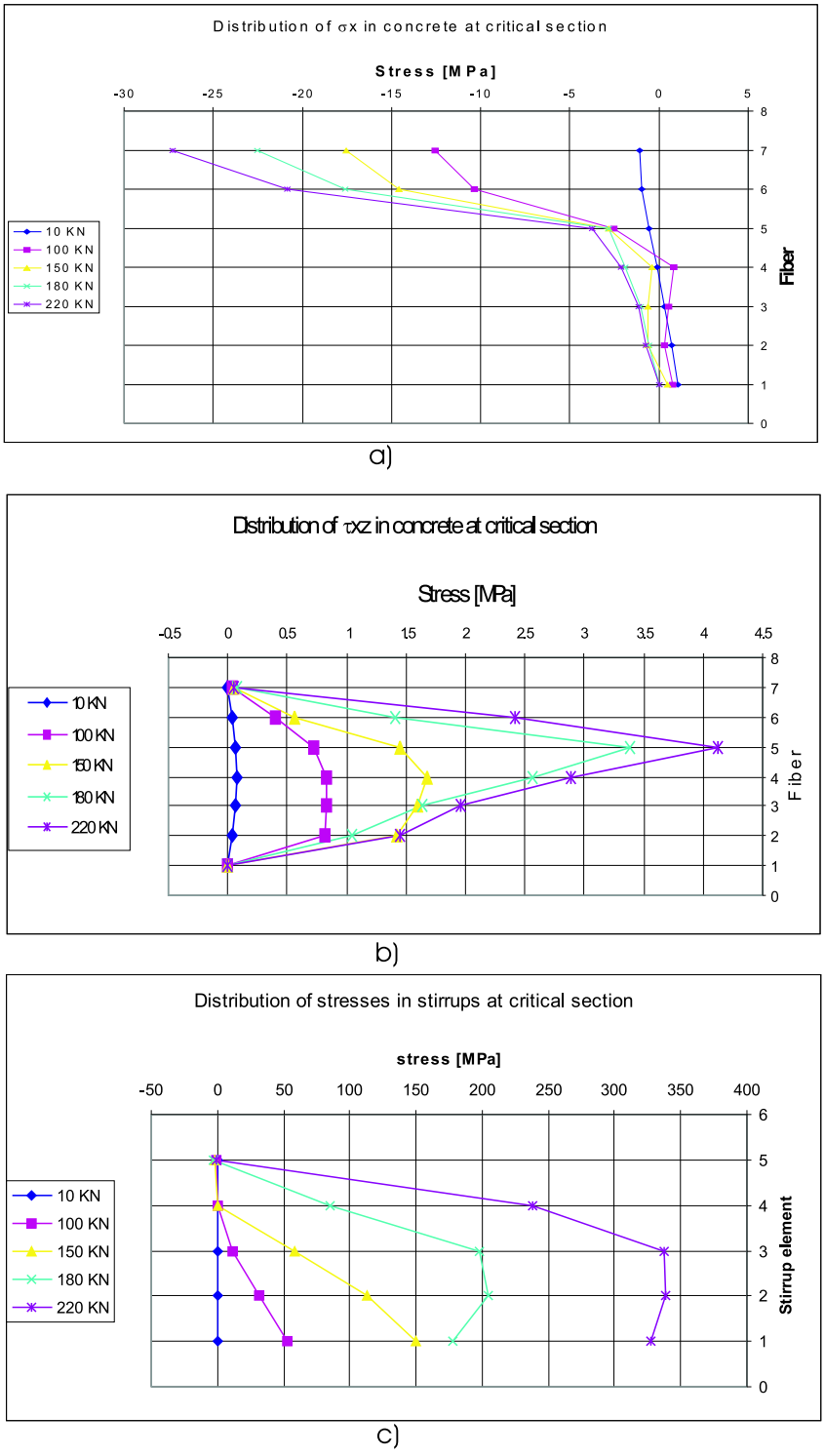

Figure 6.18: RC cantilever stresses in the fixed-end section. a) normal stresses, b) shear stresses, c) stresses in stirrups.

small, thus *Strength of Materials* hypotheses are acceptable.

When shear force is increased, the effects of anisotropic cracked-concrete are more apparent. Cracks in the tension zone become wider and transfer of shear stresses is limited. Softened tensile stresses get smaller thus in order to transfer shear stresses compression confinement is required. These compression is supplied by diagonal compression and steel reinforcements. The actual stress distribution is like the one sketched in figure 6.19.c. This mechanism is noted in the analysed element from a load of $150KN$.

When longitudinal reinforcements yield, the new increments of shear forces are mainly sustained by the shear capacity in the compression zone. The mechanism is evident for loads $180KN$ and $220KN$. Strains keep growing and concentrating in the tensile zone; however, since cracking are extensive, the increment of new shear stresses is considerably less than in the compression zone.

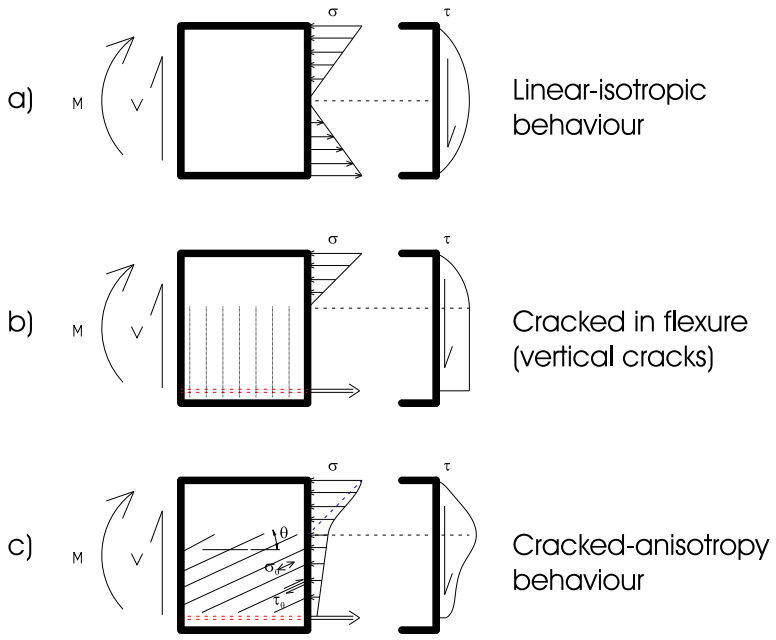

Figure 6.19: In-plane normal and shear stresses distribution under different material hypotheses: a) linear-isotropic, b) cracked isotropic, c) cracked with anisotropic behaviour.

6.2.4 Moment-curvature of a RC section with concomitant shear forces

The influence of a concomitant shear force in the non-linear characteristics of an RC section will be investigated in the following case study. Usually, the more important non-linear response of a frame section is considered to be governed by its moment-curvature ($M-\phi$) diagram, on which some characteristic points can be identified (cracking, yielding and failure). Further, the non-linear performance can be quantified by means of the curvature ductility ($\mu = \frac{\phi_u}{\phi_y}$), which measures the section's deformation capacity in the inelastic regime while sustaining the loading.

A concomitant axial compression is known to influence the $M-\phi$ diagram. In general, it reduces the section's ductility and increase the resisting moment until moderate values of the axial load, a high axial force reduces the resisting moment. Results that can be easily obtained by means of a fiber-sectional model using only the Navier-Bernoulli kinematics. These aspects are specially relevant for the geometric-second order behaviour of compression members (Bairan, 1999) and for the seismic performance of columns (Moreno et al., 2004).

On the other hand, the effects of a concomitant tangential force is not easy to evaluate, it is evident that the traditional fiber-sectinal analysis is unable of doing it.

It has been traditionally assumed (Park and Paulay, 1978) that moderate shear forces on "*well-designed*" sections should not significantly affect the moment-curvature diagram. However, it is difficult to objectively stablish the limits for this statement and the qualitative and quantitative consequencies of high shear forces, see Bairan and Mari (2004). Moreover, as previously mentioned (see chapter 1) and noticed from the previous case study (section 6.2.3) the influence of shear forces gain importance in the non-linear range.

The same cross-section used in section 6.2.3 will be analysed next to obtain the $M-\phi$ curves under different levels of shear forces quantified as the shear

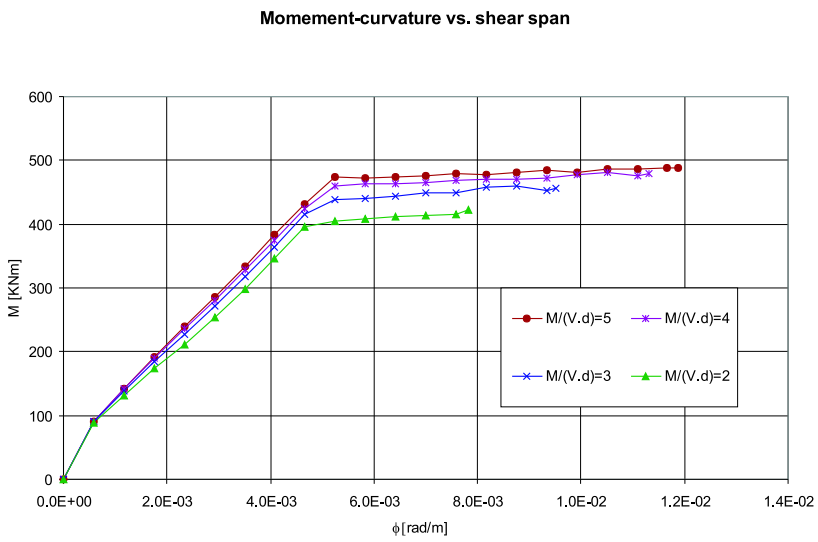

Figure 6.20: Moment-curvatures curves for various shear-spans

span to effective depth ratio ($\frac{M}{Vd}$). The section's geometry and discretization are the same as sketched in figure 6.14.b and 6.14.c, the materials properties are summarized in table 6.4. In this study, a lower plastic modulus, of $200MPa$, was used for the longitudinal reinforcements.

The obtained $M-\phi$ diagrams for shear to span ratios ($\frac{M}{Vd}$) of $2, 3, 4$ and 5 (considered as flexure dominated), are shown in figure 6.20.

It can be noticed that for increasing shear force (reducing shear span) all non-linear characteristics are altered, specially for $\frac{M}{Vd} \leq 3$. Reduction of ultimate bending moment and ductility are evident, but also are affected the yielding moment, post-cracked bending stiffness and the hardening of the inelastic branch.

Figure 6.21 shows the yielding and the ultimate bending-shear interaction diagrams for this section. Note that the higher the shear force, the distance between the two limit surfaces increases. The definition of the yielding point is based on a biliniear representation of the moment-curvature that has the same ultimate moment and curvature strain energy (area under the curve) as the original curve.

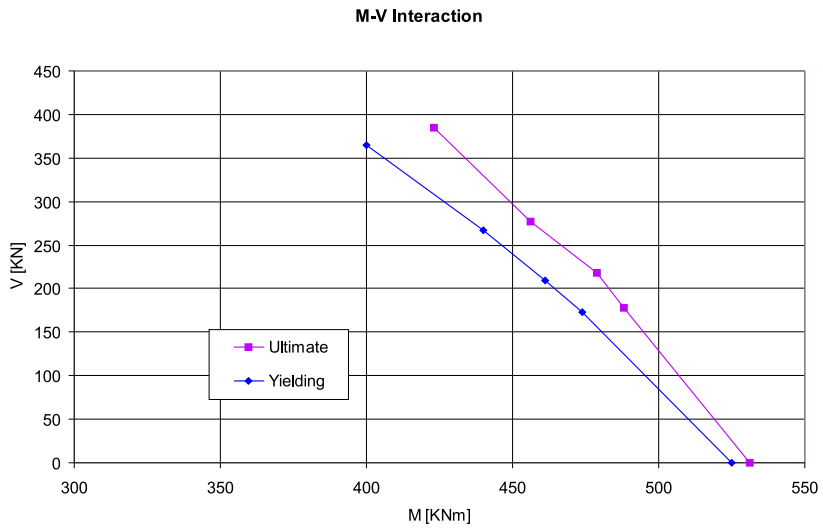

Figure 6.21: Bending-shear interaction diagrams for yielding and failure loads.

Having identified the yielding point, the ductility can be computed for each case. As shown in figure 6.22 ductility is reduced on increasing shear. Only the four computed points are shown, however it is known that the curve has a lower bound of 1 and a upper bound at the pure bending ductility.

The effect of shear force on the flexure stiffness is to reduce it in the elastic range as seen in figure 6.23; but at the same time it increases the inelastic stiffness and therefore the curve's hardening, see figure 6.24. Under very high shear forces, a convex shape is prediceted in the pre-yielding branch of the moment-curvature, see the $\frac{M}{Vd} = 2$ curve in figure 6.20. This was also noticed for non-proportional loading with more marked convex shapes, see Bairan and Mari (2004).

The effect can be explained as an influence of the diagonal compression field on the integration of the bending moment. Note in figure 6.20 that until a curvature close to $0.002\frac{rad}{m}$ the $M - \phi$ curve softens, this is attributed to an augmenting inclination angle of the diagonal compression field. As this angle differs from the element's axis, the diagonal compression influences less on the σ_x stress component and hence on the effective inertia of the

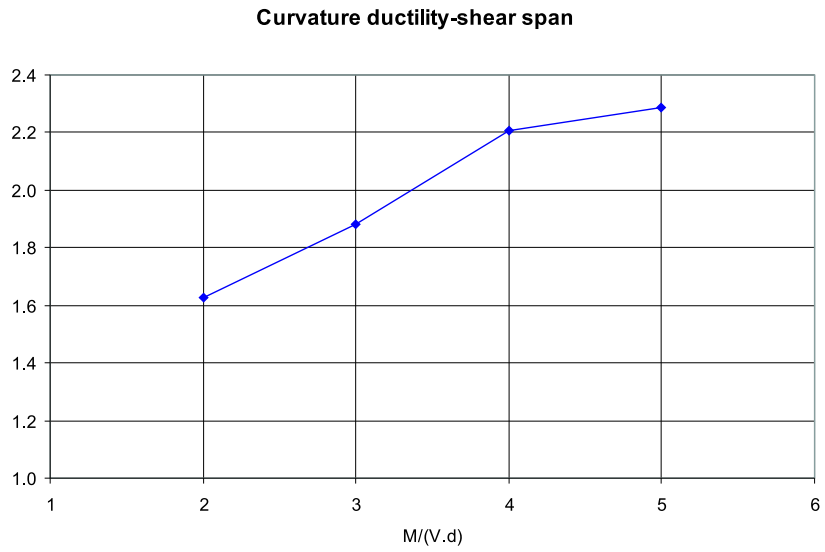

Figure 6.22: Influence of the shear-span ration on the curvature ductility ($\mu = \frac{\phi_u}{\phi_y}$).

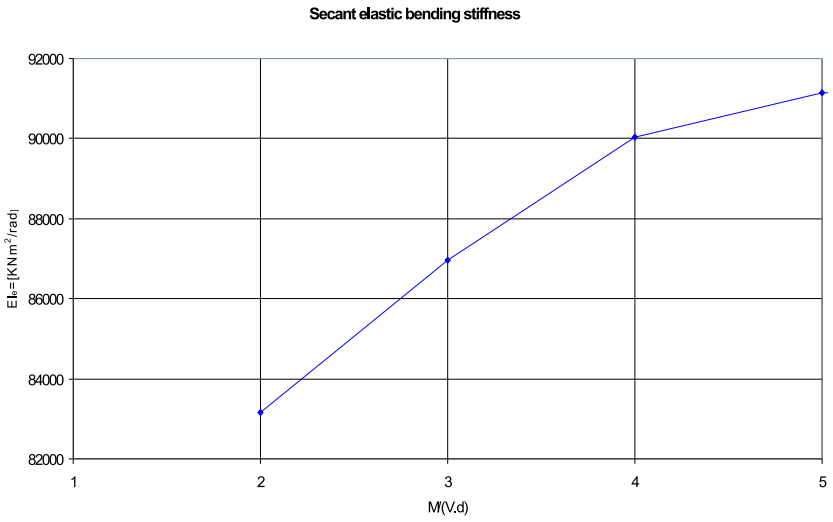

Figure 6.23: Influence of the shear-span ratio on secant bending stiffness.

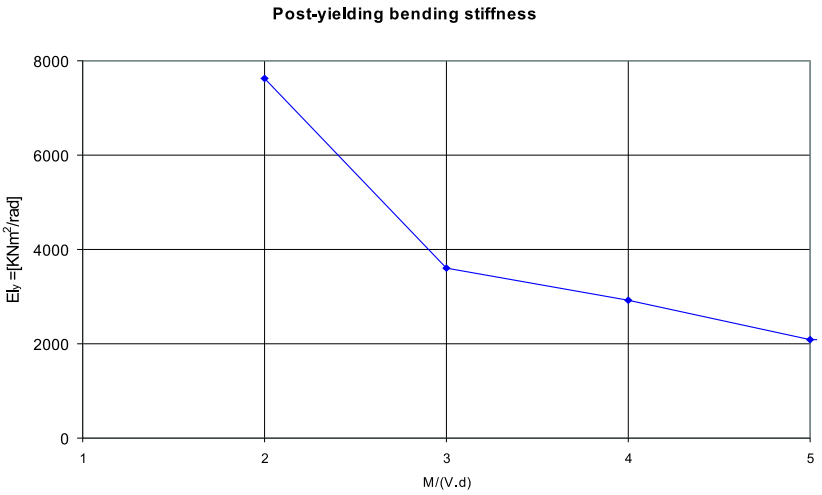

Figure 6.24: Influence of the shear-span ratio on flexure hardening.

beam.

In figure 6.25 the inclination angle of the principal compression stress has been plotted for two fibers in the tension side (their coordinates are shown in figure). After the mentioned curvature value, the $M - \phi$ diagram tends to recover some of its stiffness. Figure 6.25 shows that this corresponds to a reduction of the inclination angle thus to a higher component on the σ_x field and effective inertia.

The fact that the shear force affects the longitudinal reinforcements in order to equilibrate the diagonal compressions is a well accepted fact. This is considered in some design provisions by prolonging these bars a certain distance from that predicted by the bending moment diagrams. The spanish design code requires that the longitudinal reinforcement is designed for an increment of stress in addition to the predicted by the applied moment. Since the proposed model jointly considers both actions, this effect is catched automatically as can be seen in figure 6.26.a. Here, the strains in the longitudinal bars have been plotted together with the bending moments for different shear forces. It can be confirmed that for a given bending moment an additional strain is present due to the shear force advancing the yielding.

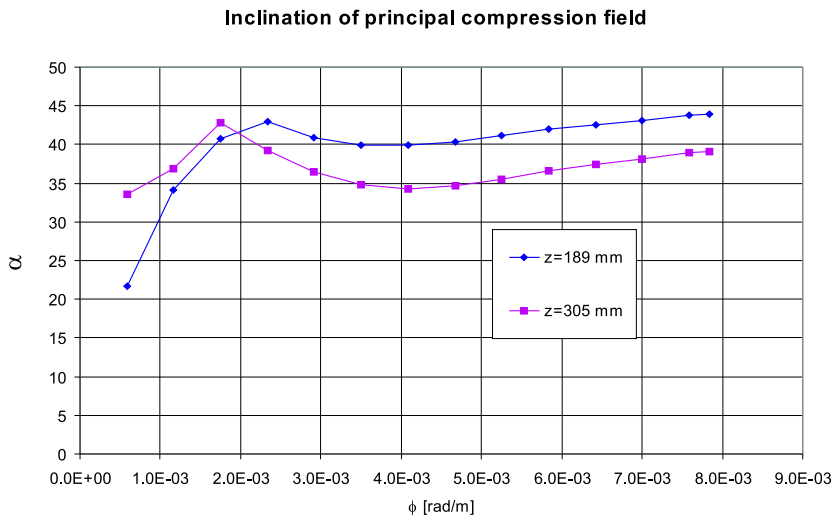

Figure 6.25: Compression field inclination at two crackes fibers for $\frac{M}{Vd} = 2$

However, as the shear force affects the longitudinal reinforcements, the bending moment also influences the stresses on the transverse reinforcement. This fact is not yet recognized by the design codes though it has been experimentally observed. It is also a consequence of the inclined compression on the cracked side of the beam interacting with the normal forces and the bending moments. The effect is also reproduced by the proposed sectional model as seen in figure 6.26.b.

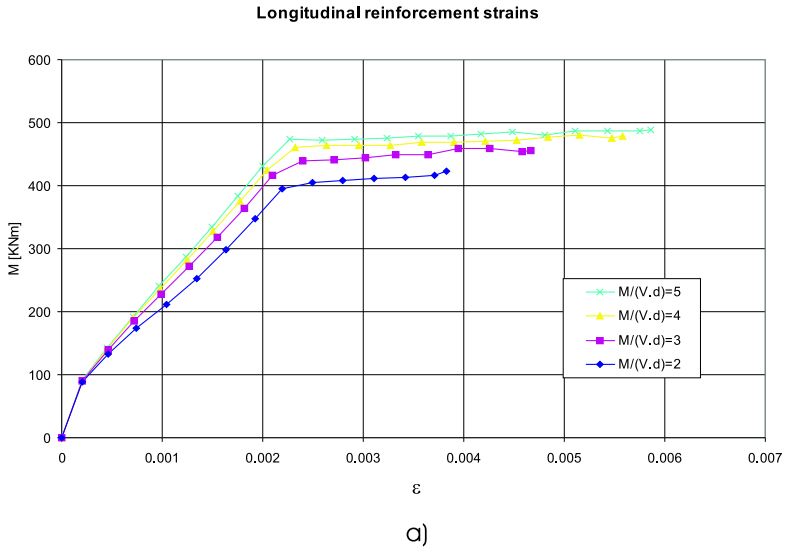

a)

b)

Figure 6.26: Shear span influence on different reinforcements, a) strains in longitudinal reinforcements, b) strains in transverse reinforcements.

6.2.5 Confinement of a RC section

A square RC section of $120mm$ side is analyzed under compression load. The section is confined with closed stirrups of a theoretical area of $61.5mm^2$ each $100mm$, considered smeared for what conserns the numerical model. Section core is a square of $100mm$ side. Concrete unaixial strength was taken as $f_c = 30MPa$. Stirrups yielding stress is $f_y = 340MPa$, with an elastic modulus of $E_s = 200,000MPa$ and a yielded modulus of $E_1 = 20MPa$.

The cross section discretization is presented in figure 6.27. With these parameters the theoretical failure load for the unconfined section is $432KN$. The theoretical ultimate load of the confined-core, considering complete spalling of concrete cover, computed after the analytical model of Mander et al (1988), is $390KN$; a confinement effectiveness coefficient of 0.333 was used for these hand calculations.

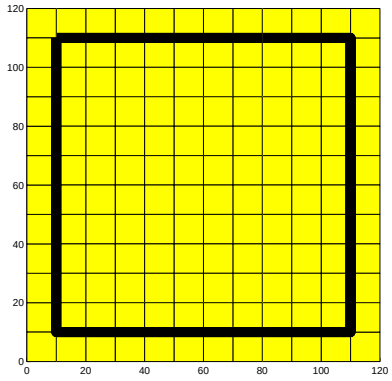

Figure 6.27: Cross section and finite element mesh.

In figure 6.28 the predicted force-strain deformation is shown, where a set of six load stages are identified. In figure 6.29 these load stages are represented in the form of normal stress fields and sectional distortion.

Two peak loads can be noticed in the force-strain curve. The first one corresponds to the maximum load of the not spalled section, stage III. However, even though confinement has not been completely developed, some confined zones exists mainly on the core corners; for this reason, the first peak load is slightly higher than the one computed as an unconfined section.

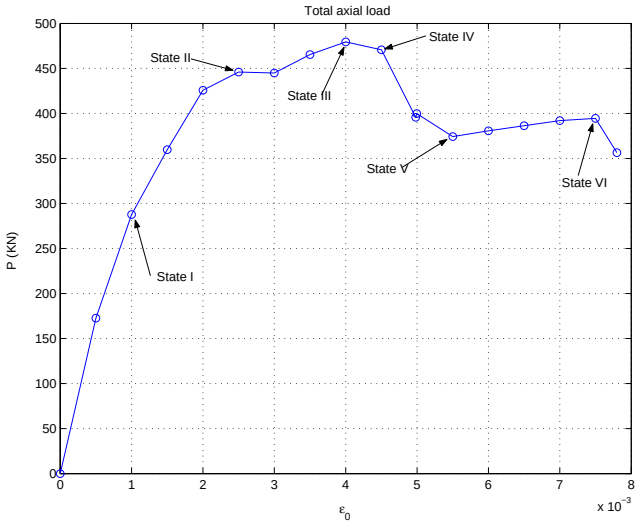

Figure 6.28: Axial force-strain.

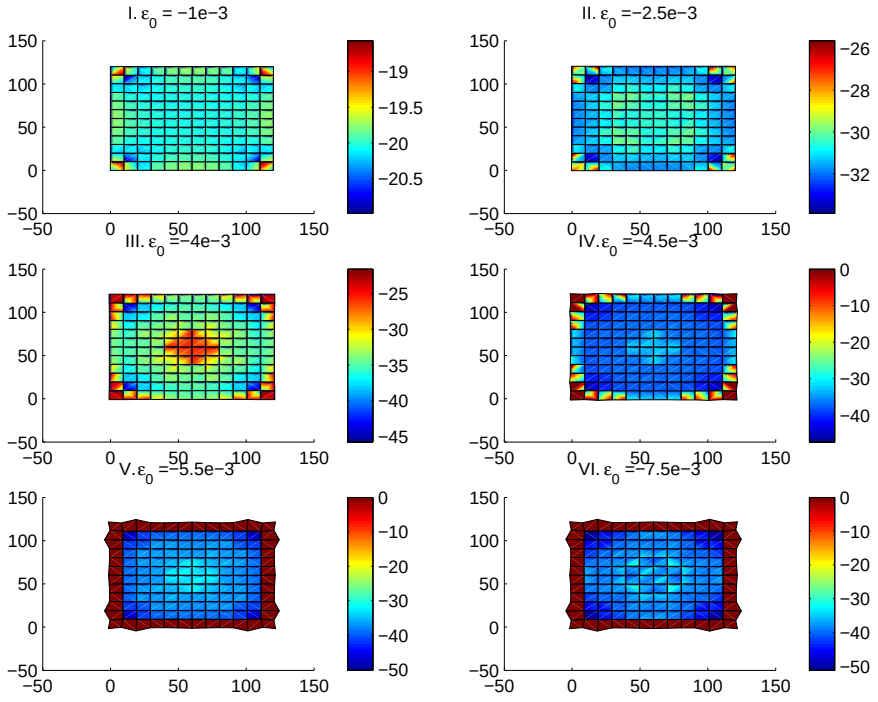

Figure 6.29: Sectional distortion and σ_x distribution at certain load states.

As seen in figure 6.28, after this stage, cover spalling develops rapidly and softening occurs in the force-strain curve. Such effects can be properly captured by the proposed model.

After complete spalling, a positive stiffness branch takes place since the confined core is capable of resist higher stresses. A second peak load is reached at stage VI. In figure 6.30 both stress and strain of the stirrups are plotted as a function of the normal axial strain. It is shown that stirrups begin to yield at load stage V.

Note that excellent correlation exists between confined core load predicted by the model and the one predicted by the confinement analytical model of Mander et al. (1988).

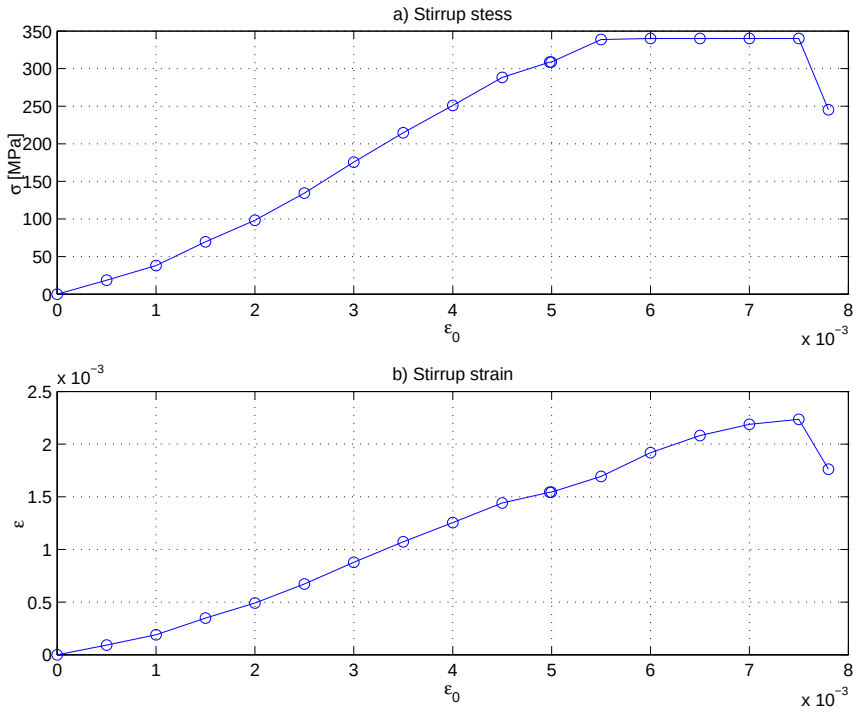

Figure 6.30: Stirrup response. a) $\sigma - \varepsilon_0$, b) $\varepsilon - \varepsilon_0$.

6.3 Experimental case studies

In this section four sets of examples are presented for which experimental information on RC elements is available in the literature. The first case study deals with the problem of estimating the cracked torsional stiffness. The elastic linear-brittle material L3DSCT presented in section 5.3 was used to simulate crack effects in tension and linear compression in concrete. This example is compared with the un-cracked and cracked stiffness predicted by a well-established analytical formulation, Lampert (1972), corroborated by a series of experimental tests carried out by Collins and Lampert (1972); in fact, the cross section analysed corresponds to one of the specimens tested by the mentioned authors.

The next two verification examples correspond to typical combined load cases on RC elements, namely: combined bending-torsion and bending-shear. Though these load combinations are typical in almost all type of RC structures, there is not a unique rational formulation to properly design and estimate the behaviour under such loads; instead, they are designed under rather empirical or semi-empirical models.

The fourth set corresponds to a type of one-way RC slabs of common use in Spain with unidirectional ribs and whose lateral reinforcement is a basic 3D steel truss.

6.3.1 Torsion stiffness of a RC section

In this section the proposed model is employed to compute the torsional stiffness of a RC spandrel beam section tested by Collins and Lampert (1972) after which they developed a formulation for estimating the cracked and un-cracked torsional stiffness of the critical concrete section. In figure 6.31 the analyzed section and the corresponding discretization are shown.

The obtained stiffness are compared to the analytical model developed by Lampert (1972):

$$GJ_{cr} = \frac{E_s \left(b_0 h_0\right)^2 A_h}{2 \left(b_0 + h_0\right) s} \left(1 + m\right) \tag{6.3}$$

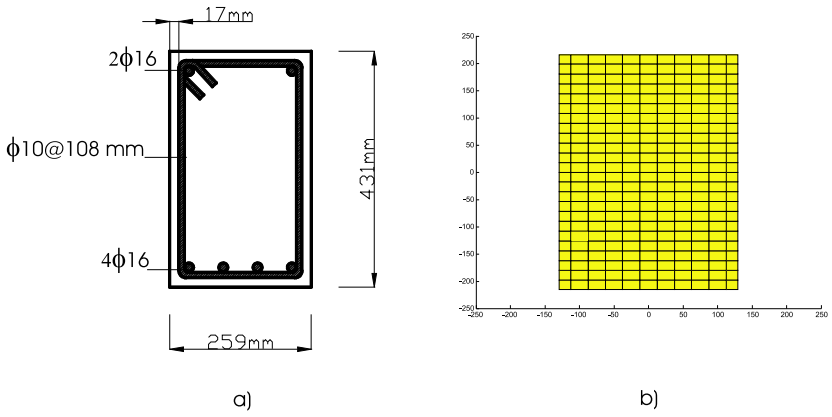

Figure 6.31: Studied section. a) dimensions and details, b) finite element mesh.

where A_h is the cross-sectional area of the hoop bar, b_0 and h_0 are the horizontal and vertical directions between the corners bars respectively, s is the hoops' spacing, m is the volume ratio of longitudinal reinforcement with respect to the hoop reinforcement and E_s is the steel's elastic modulus.

This equation has been proved to be a well established formulation to predict torsional stiffness at first yielding, thus with uniform cracking and low tension stiffening influence. For this reason the elastic linear-brittle material L3DSCT presented in section 5.3 was used to simulate crack effects in tension and linear compression in concrete. The materials properties relevant in this study are the elastic modulus of both concrete and steel, summarized in table 6.5.

Table 6.5: Material properties for RC section under pure torsion

E_c	$25,364MPa$
E_s	$200,000MPa$

It is well known that the mechanism of torsion resistance of reinforced concrete sections shows strong variations when comparing to the pre-cracked and post-cracked situations, Hsu (1984). Before cracking, RC may be accu-

rately considered as an elastic and homogeneous material. In this situation, neither the transverse nor the longitudinal reinforcements collaborate to the section torsion resistance. Because concrete exhibits low tensile strength, the material cracks at a certain load and therefore the previous mechanism can not be sustainable. After cracking, concrete is only capable of resisting compression stresses; concrete will behave as orthotropic with material principal directions depending on the principal stress directions. See figure 6.32

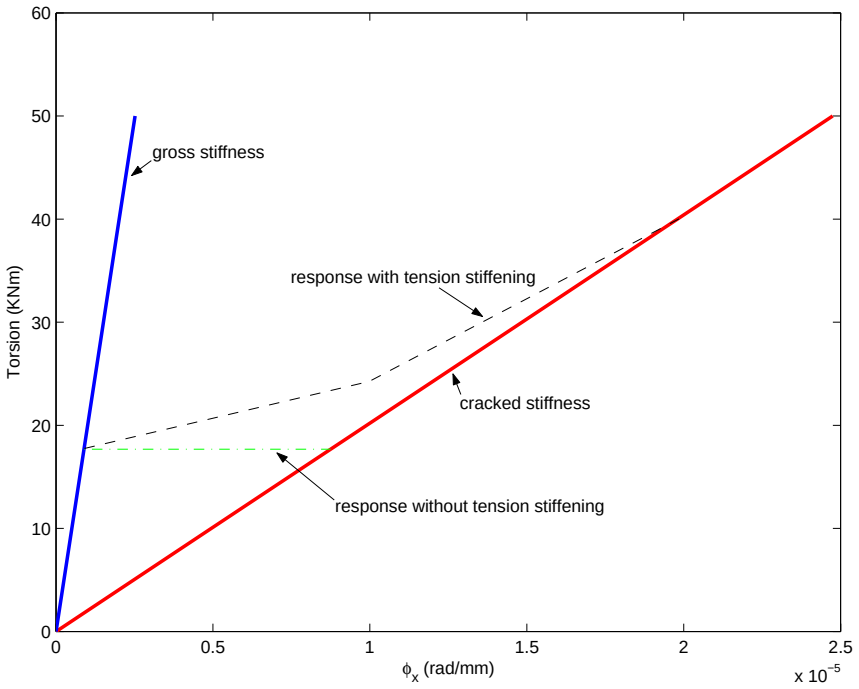

Figure 6.32: Un-cracked-cracked torsion-curvature relationship.

If torque is increased after cracking, a new resistant mechanism is developed in which longitudinal and transverse reinforcements are determinant. It has been demonstrated, and used as basic hypothesis by many modern structural codes, that a cracked RC section under pure torsion can be assimilated to a thin-walled section. The determination of the equivalent wall-thickness is not a trivial task and still is not a closed problem. Although it is known to depend on section's geometry and reinforcement arrangement, codes guidelines are not objective enough for this problem. Empirical expressions are

proposed for the minimum and maximum values of the equivalent thickness, as is the case of the spanish code EHE (1999), but it is left to the designer the responsibility of choosing the final value.

In figure 6.33 the shear stresses flow predicted by the model for the un-cracked and cracked sections are shown.

The proposed model was capable of reproducing the phenomenon of thin-walled effective section automatically without imposing additional hypothesis other than no tensile resistance on concrete (by means of the appropriate constitutive model) and the inherent hypothesis of the model already described in the previous chapters.

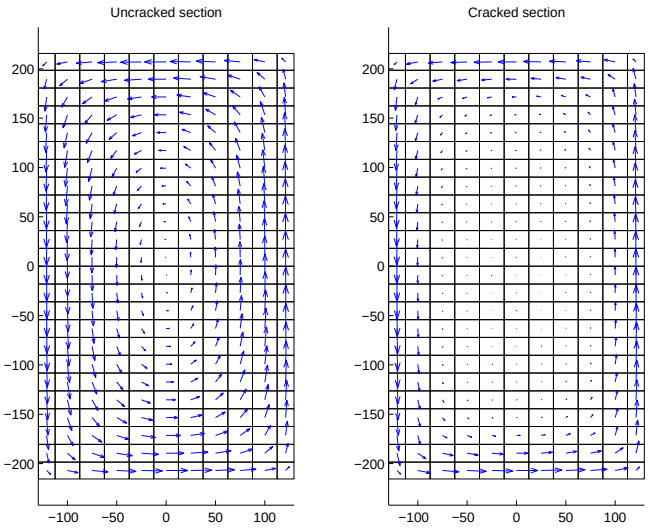

Figure 6.33: Shear stress flow. a) Un-cracked section, b) Cracked section.

Warping of the cracked section is shown in figure 6.34 together with the field of vertical shear stresses. Relevant differences exist among the deformation of the un-cracked and cracked sections. The most obvious one is the fact that although un-cracked section does warps, its shape is not distorted as does happens to the cracked section. This is plotted in figure 6.35 together with the principal compression stress field. Again the tubular thin-walled equivalent section is evident in figure 6.35.b.

Another difference of the two warping fields is related to the equivalent

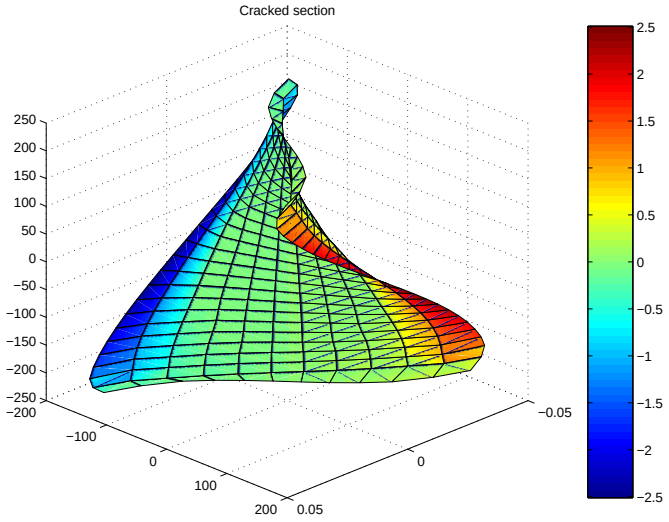

Figure 6.34: Warping and τ_{xz} field in cracked section.

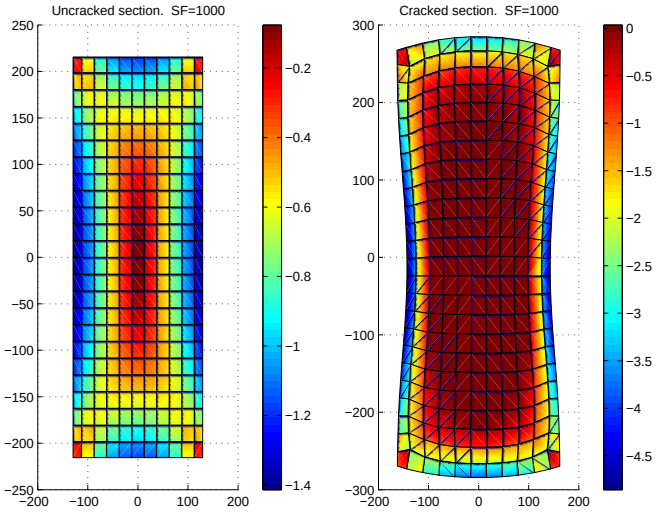

Figure 6.35: Cross-section distortion and compression stress field. a) Uncracked section , b) Cracked section.

section's shape and the influence of the reinforcing steel. To appreciate this fact a lateral view of the deformed sections are presented in figure 6.36. Note that the influence of reinforcement is poor and imperceptible since the warped shape is perfectly symmetric with a zero value in the middle height. On the other hand, the unsymmetrical distribution of the top and bottom longitudinal reinforcements is evident in figure 6.36.b.

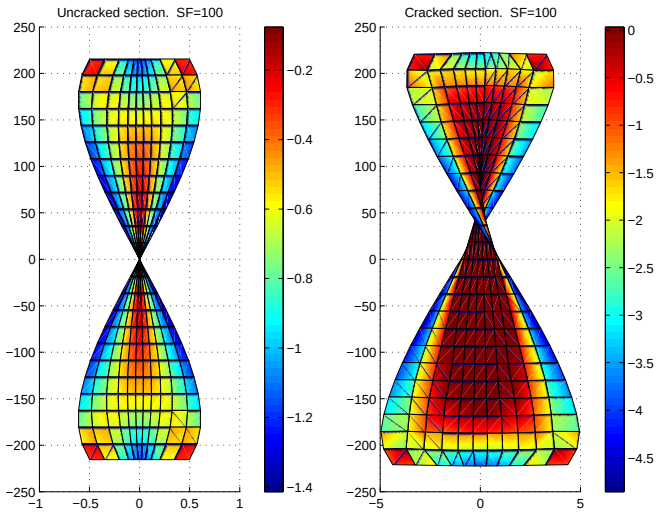

Figure 6.36: Cross-section distortion and compression stress field. a) Uncracked section , b) Cracked section.

Stresses in lateral steels are plotted in figure 6.37, vertical and horizontal branches are distinguished. As expected from the rectangular shape of the section, vertical branches is more demanded.

Torsion-bending-axial coupling are apparent from figure 6.38 where stresses in longitudinal reinforcements are plotted against torsion curvature. Both top and bottom bars are positive loaded when a pure torsion is applied indicating the torsion-axial load coupling arising from the cracked pattern. The fact that top bars are more loaded than the bottom ones reflects the increment of bending-curvature, hence flexure-torison coupling directly related to the asymmetric reinforcement scheme used (bottom steel ratio is higher than top ratio).

Force couplings due to the cracked pattern can be perfectly verified if one

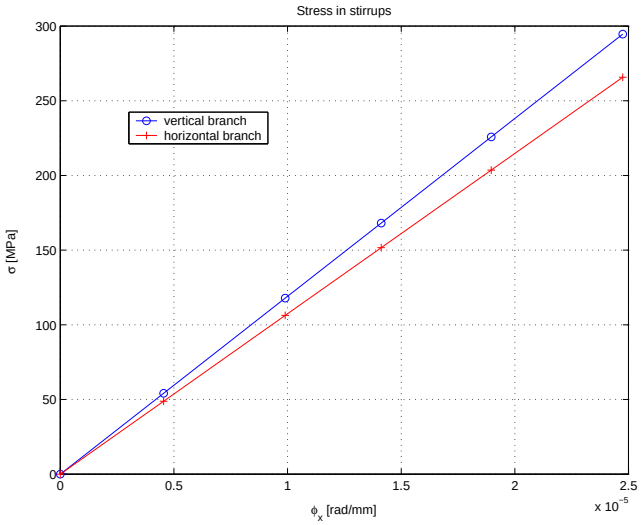

Figure 6.37: Stress in stirrups for the cracked section against torsion curvature.

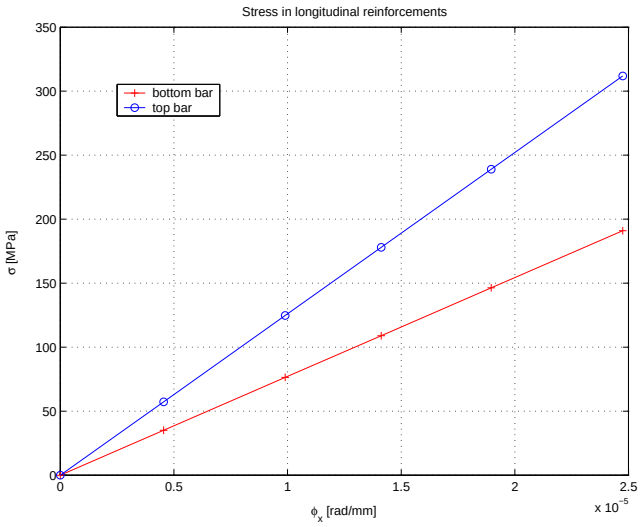

Figure 6.38: Stress in longitudinal reinforcement for the cracked section against torsion curvature.

compare both stiffness matrixes: for un-cracked section, equation 6.4, and cracked section 6.5. The degrees of freedom in these matrixes are organized as: $\varepsilon_o, \gamma_y, \gamma_z, \phi_x, \phi_y, \phi_z$.

Focusing on the gross section matrix, equation 6.4, note that as for typical isotropic sections, normal forces (axial load and bending moments) are uncoupled from tangential forces (shear forces and torsion). Torsion is slightly coupled to the shear force along Y direction since, do to the difference between bottom and top reinforcements, there is a little difference between the center of shear forces and point the reference point. A similar statement can be said with respect to the coupling of bending moment in direction $Y-Y$ (M_y) and the axial load (N_x).

$$\mathbf{K}_s = \begin{bmatrix} 3.06E09 & 0 & 0 & 0 & -1.57E10 & 0 \\ 0 & 1.17E09 & 0 & 3.17E08 & 0 & 0 \\ 0 & 0 & 1.21E09 & 0 & 0 & 0 \\ 0 & 3.17E08 & 0 & 1.98E13 & 0 & 0 \\ -1.57E10 & 0 & 0 & 0 & 5.31E13 & 0 \\ 0 & 0 & 0 & 0 & 0 & 1.79E13 \end{bmatrix} \tag{6.4}$$

On the other hand, the cracked section's stiffness matrix, equation 6.5 shows, besides the expected smaller stiffness values, general coupling between normal and tangential forces. This effect is produced because cracks are inclined with respect to the section's plane.

$$\mathbf{K}_s = \begin{bmatrix} 6.22E08 & -1.31E07 & 0 & -3.04E10 & -2.46E10 & 0 \\ -1.31E07 & 1.15E08 & 0 & 2.42E09 & 2.57E10 & 0 \\ 0 & 0 & 1.80E08 & 0 & 0 & 2.19E10 \\ -3.04E10 & 2.42E09 & 0 & 3.58E12 & 8.38E11 & 0 \\ -2.46E10 & 2.57E10 & 0 & 8.38E11 & 1.88E13 & 0 \\ 0 & 0 & 2.19E10 & 0 & 0 & 5.99E12 \end{bmatrix} \tag{6.5}$$

Lampert's model for cracked torsion stiffness considers pure torsion. Therefore, to compute this value one must condensate degrees of freedom 1, 2, 3, 5 and 6 of the previous sectional matrixes. Results are compared in table 6.6. Good agreement was obtained. It has to be mentioned that the proposed model offers a far more complete information of the torsional stiffness, since the interaction between all degrees of freedom is also obtained.

Table 6.6: Torsion stiffness comparison.

	Collins & Lampert	Numerical value	Error
Gross stiffness K_{Tg}	$19,940 KNm^2$	$19,851 KNm^2$	0.45%
Cracked stiffness K_{Tc}	$2,200 KNm^2$	$2,020 KNm^2$	8.2%

6.3.2 RC sections under combined bending-torsion

In this section a series of RC beams under different combinations of bending-torsion loading are analysed. The numerical solutions of the proposed model are compared to the results of an experimental campaign carried out by Onsongo (1978). Figure 6.39 shows the general test setup, internal forces diagrams as well as the beam's cross-section and mesh employed.

The tests were carried out varying the lengths X_M and X_T in order to reproduce different torsion-moment relations. The campaign included two different sets namely: TBO for over-reinforced beams designed to fail on concrete compression and TBU for under-reinforced beams designed to fail on steel tension. The analyzed sets are summarized in table 6.7, where R stands for the torsion-bending ratio in the interaction diagram.

All beam tested had the same reinforcement shown in figure 6.39.c. The failure mode was controlled by varying the concrete strength. Materials properties considered are summarized in table 6.8.

In figure 6.40.a and 6.40.b the predicted interaction diagrams for both, over-reinforced and under-reinforced sets, are plotted together with the experimentally obtained diagrams. Figures 6.41.a and 6.41.b show the numerical

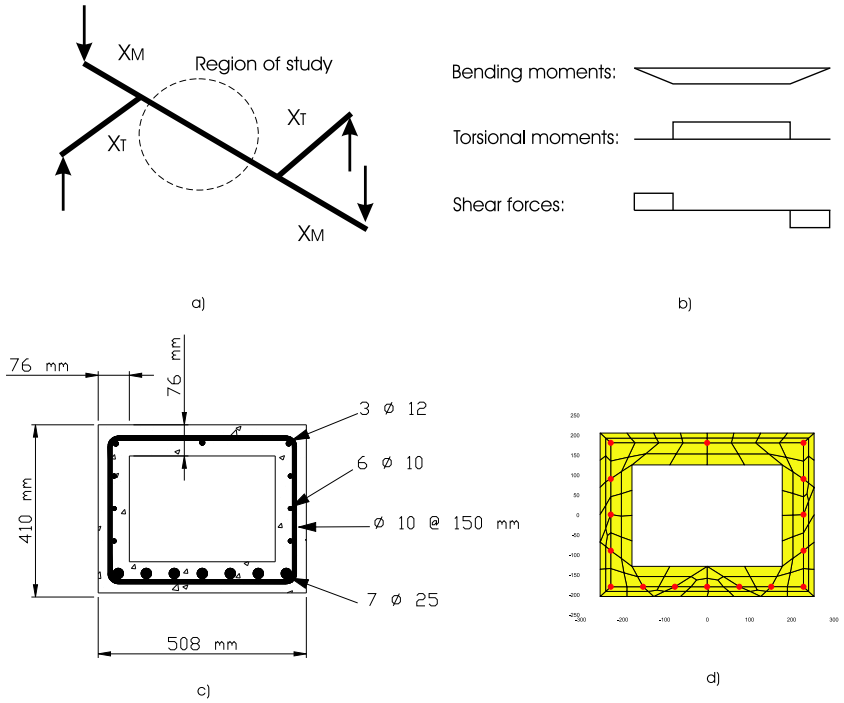

Figure 6.39: Onsongo tests for bending-torsion interaction. a) test setup, b) internal forces distribution, c) typical cross-section reinforcement, d) cross-section mesh.

Table 6.7: Series of bending-torsion tests modeled

	TBO series $f_c = 20MPa$				TBU series $f_c = 35MPa$			
	TBO1	TBO2	TBO3	TBO4	TBU1	TBU2	TBU3	TBU4
$X_T(m)$	0.000	0.610	1.200	1.911	0.000	0.616	1.200	1.911
$X_M(m)$	2.321	2.321	1.711	1.254	2.359	2.359	1.724	1.267
$R = \frac{T}{M}$	0.000	0.261	0.701	1.524	0.000	0.261	0.696	1.509

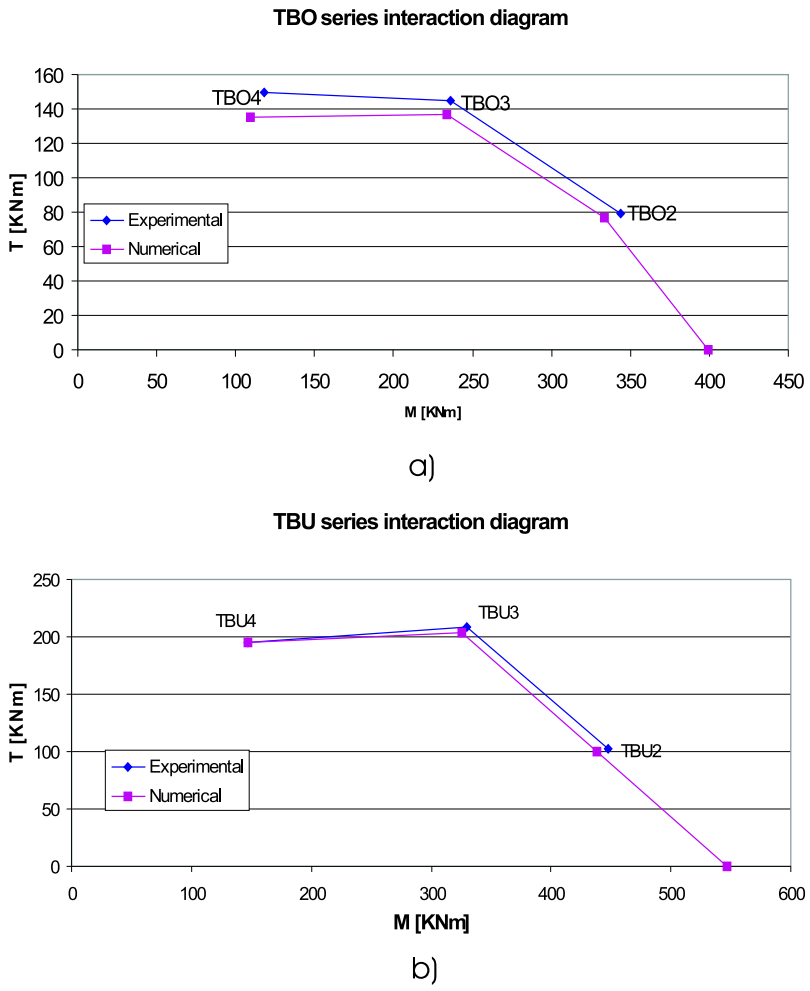

Figure 6.40: Bending-torsion interaction diagrams. a) Over-reinforced section, b) Under-reinforced section.

Table 6.8: Material properties for bending-torsion tests

f_c (TBO beams)	$20MPa$
f_t (TBO beams)	$2MPa$
f_c (TBU beams)	$35MPa$
f_t (TBU beams)	$3.5MPa$
f_y ($\phi 10$)	$400MPa$
f_y ($\phi 12$)	$393MPa$
f_y ($\phi 25$)	$436MPa$
E_s	$200,000MPa$

and experimental $T-\phi_x$ curves for $TBO4$ and $TBU2$ beams are plotted. In general the proposed model showed good correlation with the experimental data.

To show the predicted stress fields, in figure 6.42 the principal compression stress distribution is plotted for beam $TBO4$. At a cracked load stage it is shown that compression normal stresses (σ_x) are present all along the section's perimeter due to the presence of shear stresses in a cracked domain. This situation is clearly appreciated in figure 6.42 where horizontal and vertical cuts on the σ_x field were performed along the flanges and webs respectively.

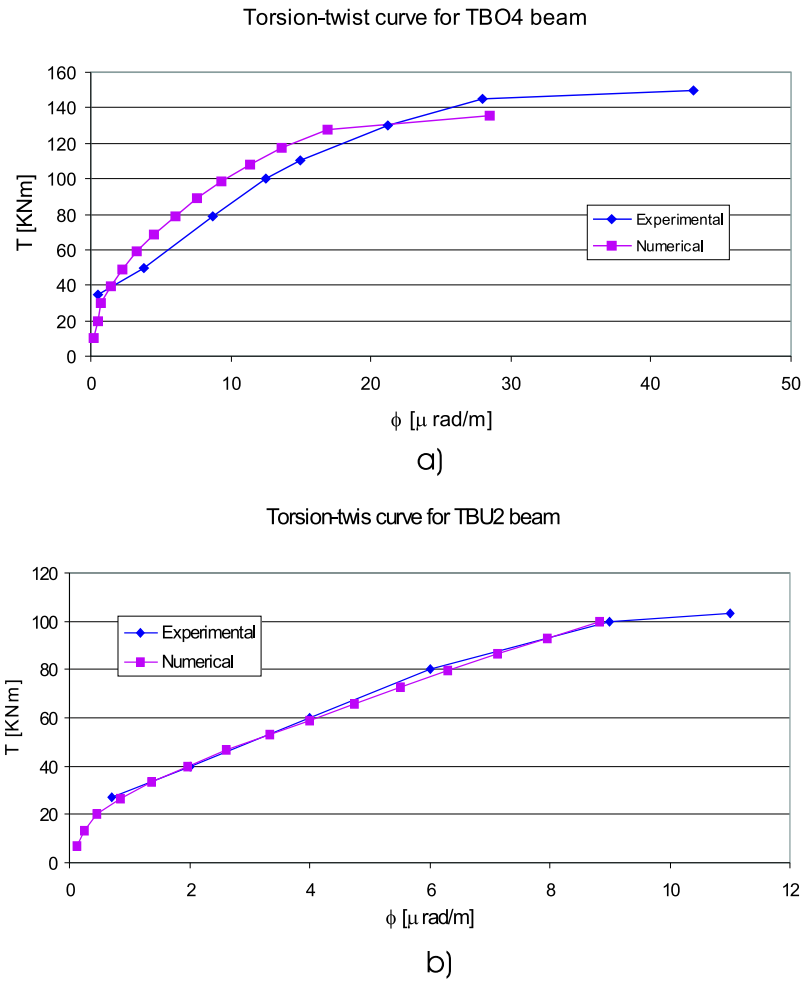

Figure 6.41: Experimental and numerical torsion-curvature curves. a) Over-reinforced section, b) Under-reinforced section.

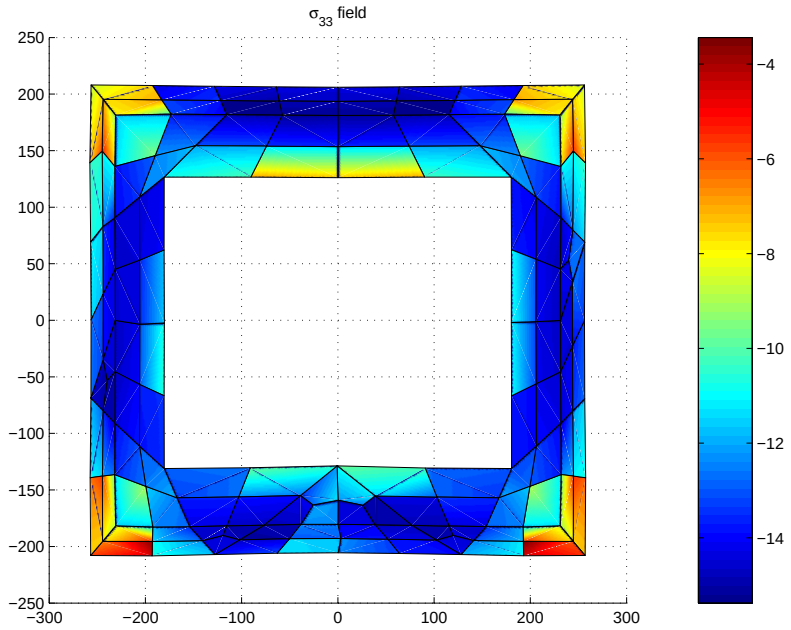

Figure 6.42: Computed principal compressions field in TBO4 beam at step 13.

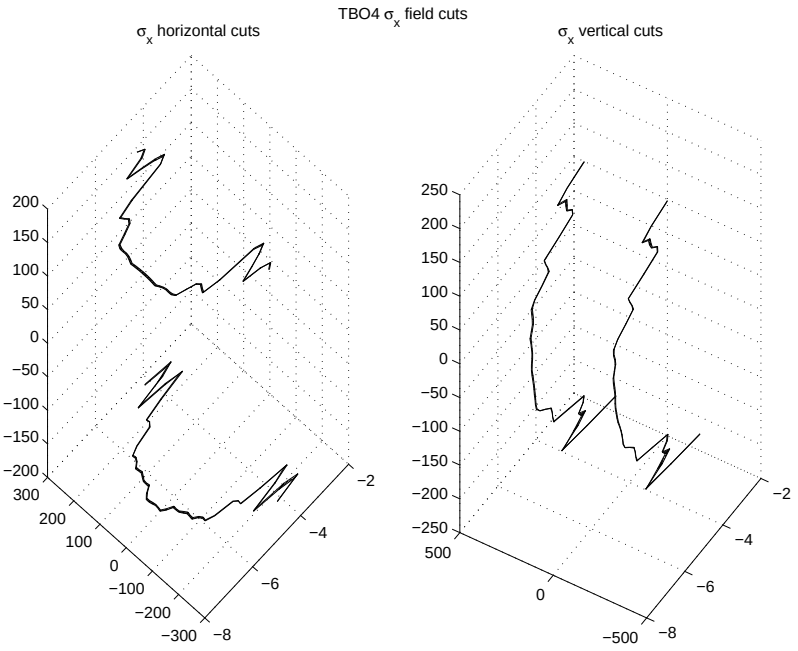

Figure 6.43: Cuts on the longitudinal stress field (σ_x) at step 13. a) horizontal cuts along flanges, b) vertical cuts along webs.

6.3.3 RC sections under shear loading

In this section, the developed model is tested under shear loading of RC sections. Two types of experimental tests are used to corroborate the predicted numerical results. The first type corresponds to a normal strength concrete beam under shear loading tested by Kani (1977). The second type of beams corresponds to a shear loading campaign on high strength concrete, Cladera (2002).

Normal strength reinforced concrete beams (Kani tests)

The test setup is shown in figure 6.44, together with the critical cross section definition and the sectional discretization used. The materials properties considered are indicated in table 6.9.

Table 6.9: Material properties for shear test of normal strength concrete beam.

Concrete	f_c	$28.2MPa$
	f_t	$1.75MPa$
	E_c	$25600MPa$
	ν	0.2
Longitudinal steel	f_y	$442MPa$
	E_s	$200,000MPa$
Transversal steel	f_y	$400MPa$
	E_s	$200,000MPa$

The test was thought so the region of study is localized between positive and negative bending moments of equal magnitude. The goal is to reproduce an inflection point in the middle of the study region where only shear forces exist.

The test was designed so that a section of null moment but non-zero shear force exists in the middle of the region of study. This was achieved by

assuring that the analyzed zone was bounded by moments of different signs and the same magnitude at every time. The objective was to evaluate the pure shear strength of the element.

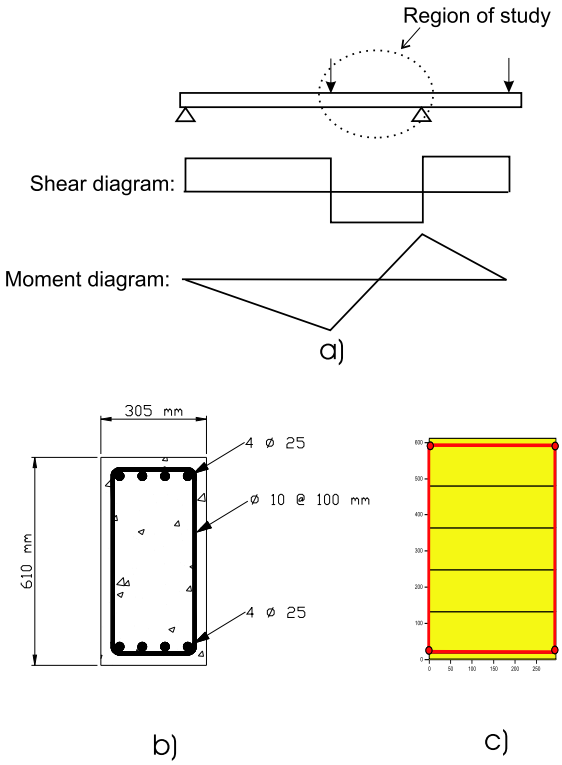

Figure 6.44: Pure shear loading test. a) test setup, b) cross-section, c) cross-section mesh.

The experimental results and the numerical prediction of the proposed model are plotted in figure 6.45 showing good correlation.

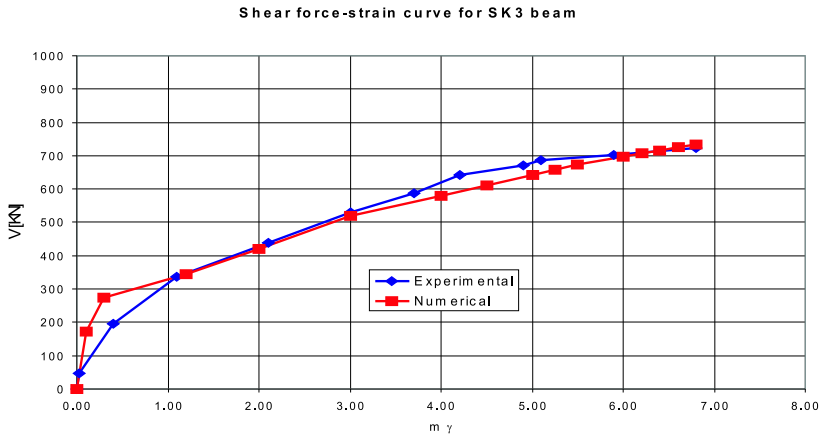

Figure 6.45: Experimental and numerical shear force-strain curve normal strength beam.

High strength reinforced concrete beams (Cladera tests)

In the following, some experimental high-strength RC beams tested under shear loading by Cladera (2002) are analyzed. The test setup consisted in a simple supported beam with a single load in the middle-span at a distance $a = \frac{M}{V} = 3d$ from the support,see figure 6.46. Under this conditions, all sections of the beams are subjected to combination of shear and bending moments with a critical section in the middle span. Nevertheless, this section is influenced by the presence of the applied load making it to behave as a $D - Region$ rather than according to beam theories.

Because of this, the critical section was considered to be located a distance equal to the beam's height from the applied load. Thus in the numerical analysis of the critical section, shear forces and bending moments were applied with a fixed ratio of $\frac{M}{V} = 680mm$.

In figure 6.47 the experimental set $H50$ of RC beams, with a concrete strength $f_c = 50MPa$, is presented together with the typical mesh used for the numerical study. In this work, only the study of three of such beams is presented, corresponding to the specimens $H501$, $H502$ and $H505$.

Specimen $H502$ beam was reinforced with stirrups to resist shear loads, and

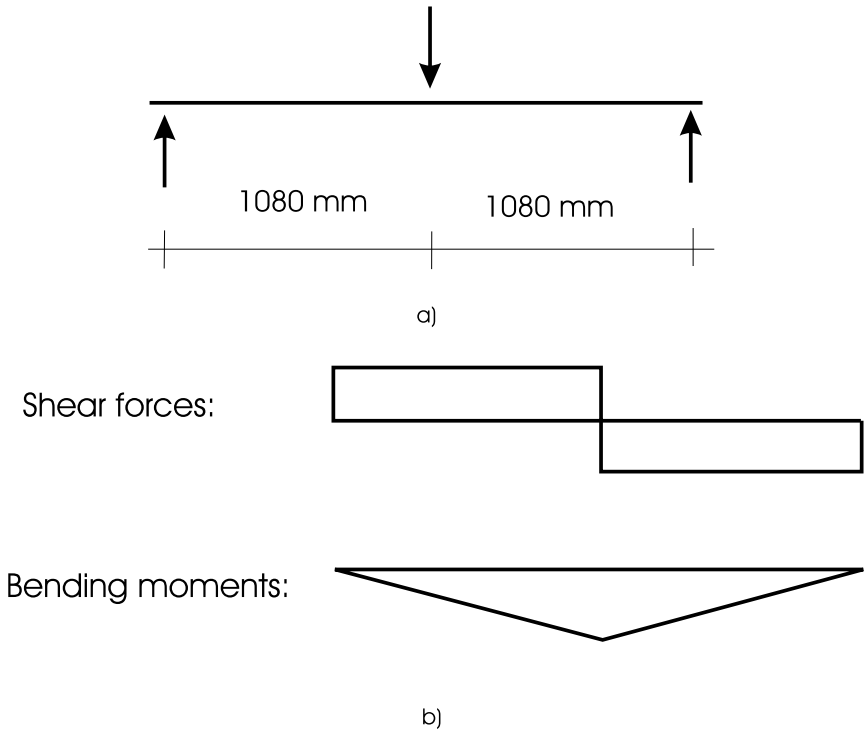

Figure 6.46: Shear-bending tests. a) test setup, b) internal forces diagrams.

was designed to assure the yielding of stirrups. On the other hand, both specimens $H501$ and $H505$ were beams without transversal reinforcement and the same main longitudinal reinforcement. The difference between these two beams is that specimen $H505$ had skin longitudinal reinforcement along its height in contrast with beam $H501$.

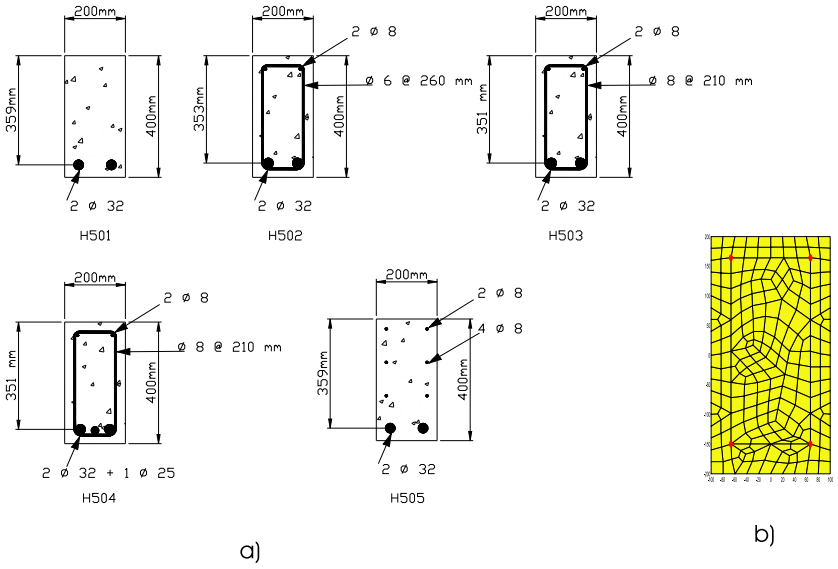

Figure 6.47: Set of beams analyzed. a) cross sections, b) typical cross-section mesh.

In figure 6.48 the numerical and experimental $V-\gamma$ curves are plotted for the three beams analyzed. Excellent agreement among numerical and predicted solutions is observed for beams $H501$ and $H505$, figures 6.48.a and 6.48.c. Good agreement in the non-linear response was obtained for Beam $H502$. The model predicts well the yielding load and plateau including the observed hardening up to 90% of the experimental failure load.

In figure 6.49 the shear force is plotted with respect to longitudinal bottom reinforcement and stirrup strains comparing the predicted results of the model with a series of experimentally measured strains by means of strain-gauges. In figure 6.49.b the plot includes two measures of the same stirrup at half the section's depth and at $50mm$ from the bottom edge. The possition of the strain gauges in the beam is shown in figure 6.50.

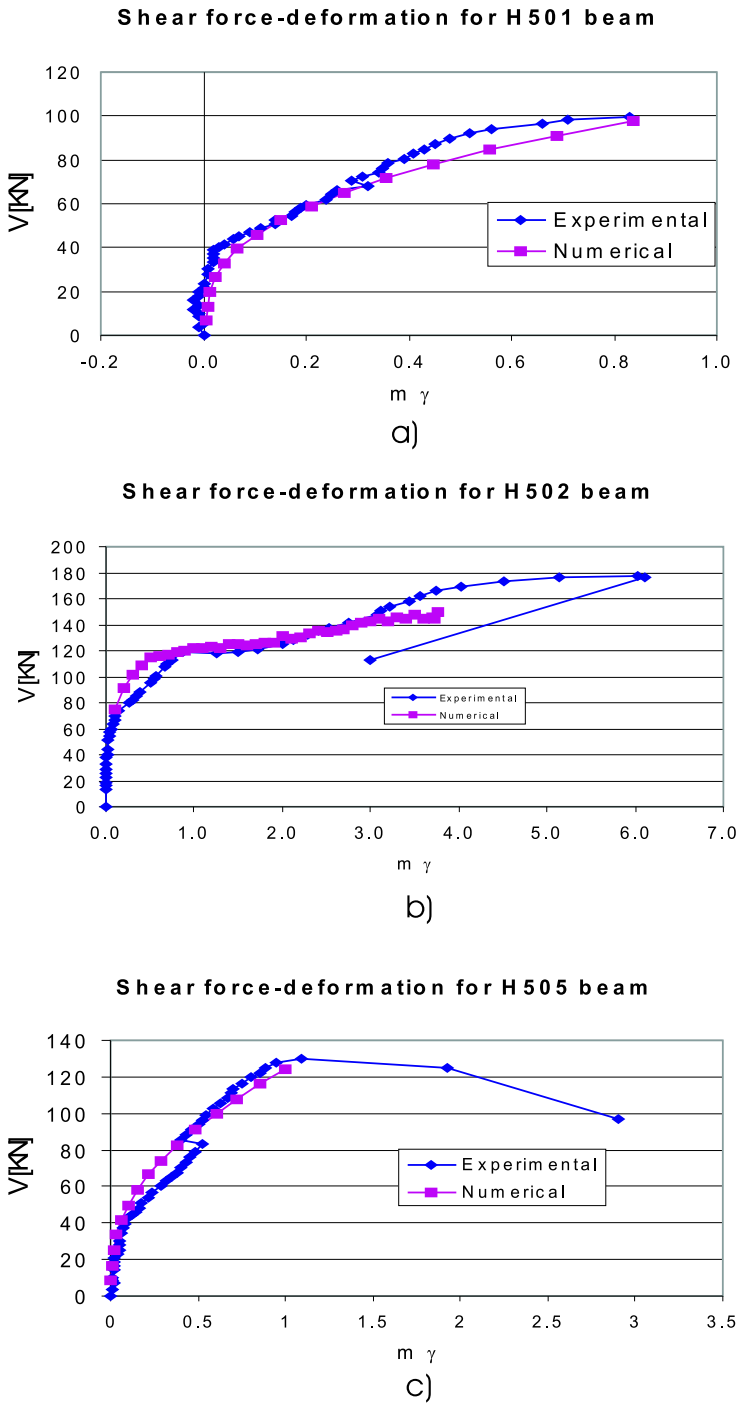

Figure 6.48: Experimental and numerical shear force-deformation curves. a) H501 beam, b) H502 beam, c) H505 beam.

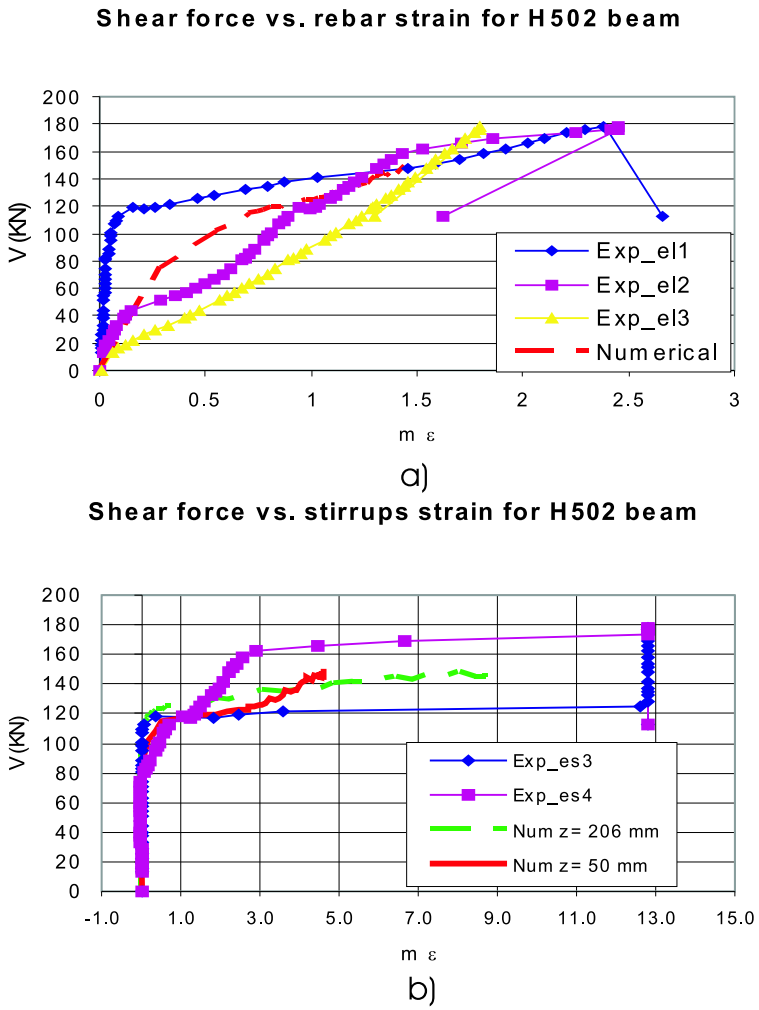

Figure 6.49: Experimental and numerical shear force vs. various reinforcement strain for H502 beam. a) shear vs. longitudinal bars strain, b) shear vs. stirrups strain.

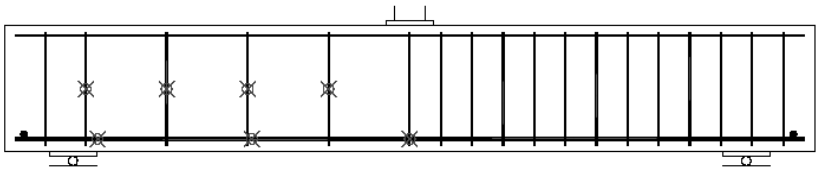

Figure 6.50: Typical location of strain gauges. *Cladera (2002)*

Specimens $H501$ and $H502$ can be used to illustrate the differences in the stress fields of sections with and without lateral reinforcement for shear resistance and with equivalent bending reinforcements. With this objective the corresponding σ_x and τ_{xz} fields are plotted just before failure, in figures 6.51 and 6.52 respectively. Figures 6.53 and 6.54 show vertical cuts of the normal and shear stress fields. Three cuts were performed to specimens $H501$ and $H502$, one along the center line and two close to the section's edge.

The specimen with stirrups, $H502$, presents a more uniform distribution of both normal and shear stresses in the cracked zone than the specimen without transversal reinforcement. In beam $H501$, figures 6.51.a and 6.53.a, it can be seen a concentration of compression normal stresses (originated from the horizontal component of the generated diagonal diagonal compression field) around the two tensile reinforcements, while they tend to disappear in the center lower zone. This is interpreted as the effect of the bidimensional shear field flowing to the longitudinal steel to get anchored. Distribution of shear stresses tend be higher on the compressed zone of the beam and around the perimeter in the tension zone, as confirm from figures 6.52.a and 6.54.a. It is interesting to notice the marked influence of the diagonally compression field in the cracked concrete of $H502$ which can be seen in figures 6.51.b, 6.53.b.

To show the influence of skin longitudinal reinforcements, two vertical cuts of the vertical shear fields are plotted in figure 6.55 for $H501$ and $H505$ specimens. These cuts correspond to the penultimate load step before failure. It is observed that skin reinforcement, figure 6.55.b allows the upper fibers of the cracked region to collaborate more in shear resistance than in case of null skin reinforcement. As a result, section $H505$ resists 20% more than the failure load of section $H501$.

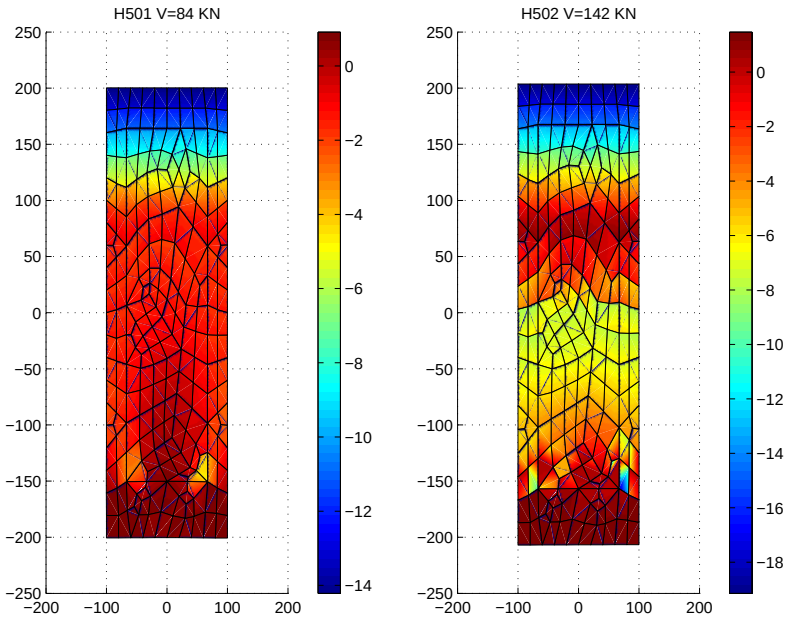

Figure 6.51: Computed σ_x stress field at a high level load. a) H501 beam, b) H502 beam.

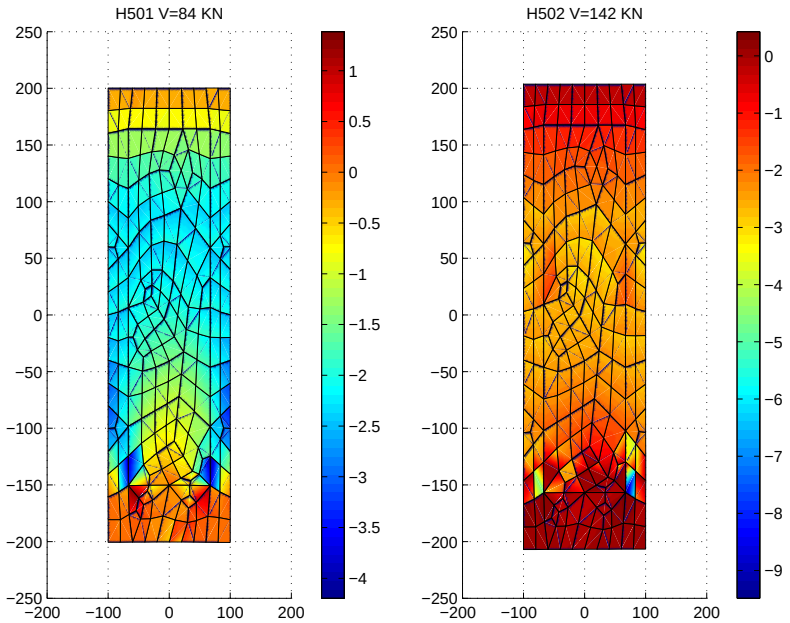

Figure 6.52: Computed $\tau_{xz}x$ stress field at a high level load. a) H501 beam, b) H502 beam.

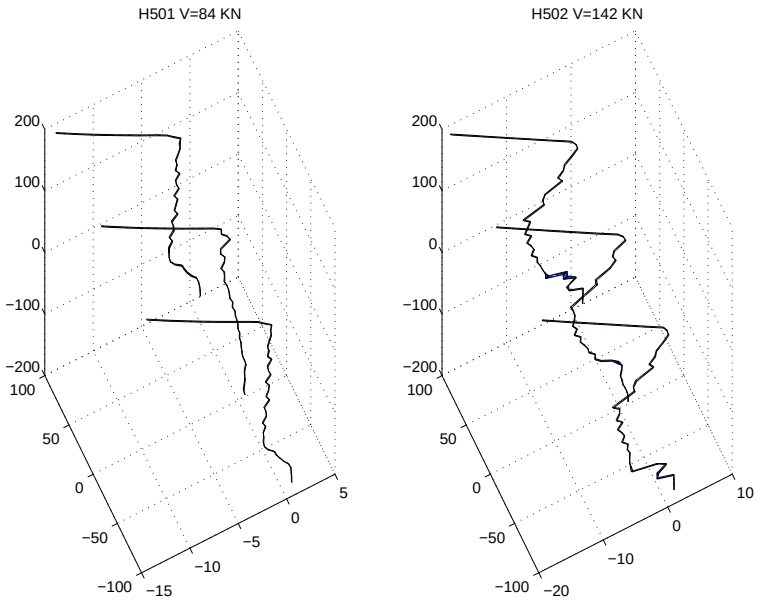

Figure 6.53: Vertical cuts in the τ_{xz} stress field at a high level load. a) H501 beam, b) H502 beam.

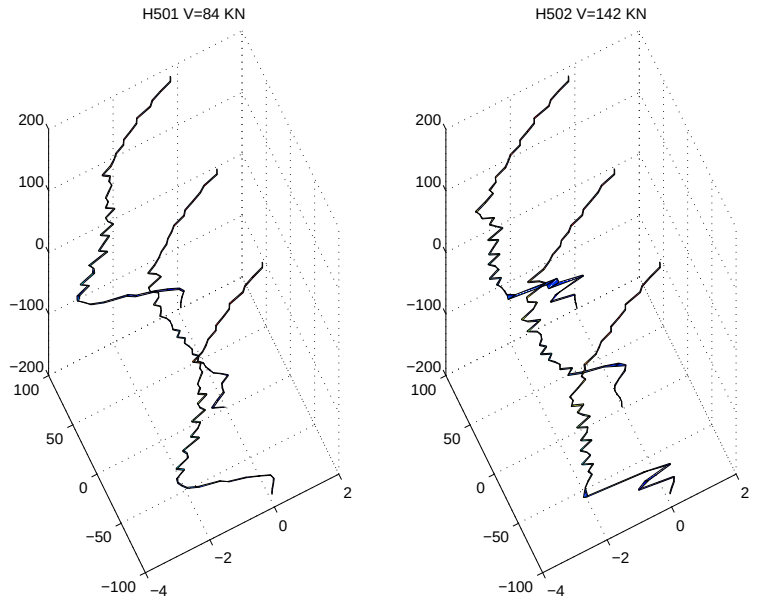

Figure 6.54: Vertical cuts in the τ_{xz} stress field at a high level load. a) H501 beam, b) H502 beam.

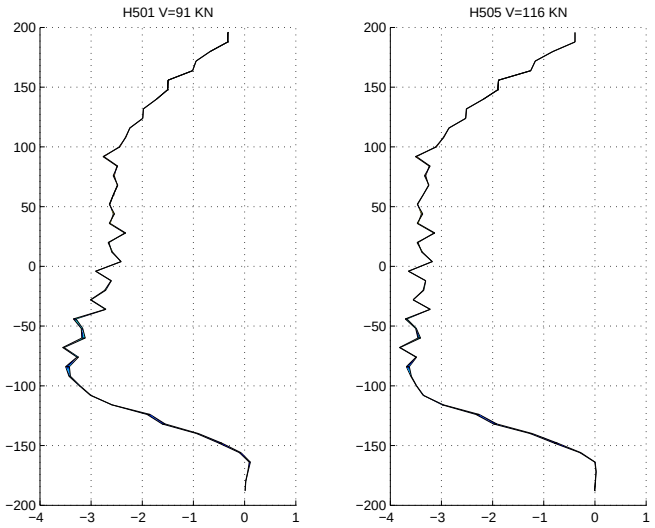

Figure 6.55: Vertical cut in the τ_{xz} stress field in the section's perimeter at a high level load. a) H501 beam, b) H505 beam.

6.3.4 Behaviour of RC ribbed-slabs with basic truss reinforcements

In the following case study, the behaviour of an one-way RC ribbed-slab of common use in Spain will be investigated using the proposed sectional analysis formulation. Thes main characteristic of this structural type is the use of a basic 3D steel truss as shear reinforcement.

An experimental campaign was carried out in the *Structural Technology Laboratory* of the Technical University of Catalonia, Mari et al. (2005), on two sets of two nominal identical specimens each. Sets one and two correspond to a truss height of $200mm$ and $225mm$ respectively.

Test setup and typical cross-sections of both types of beams are shown in figures 6.56 and 6.57. After the tests were conducted, the proposed numerical model was used to reproduce the response of the critical sections and to achieve a better understanding of the behaviour of such beams.

In the present analysis only one rib of each element type was modeled. The cross-section meshes used for the two types of beams are presented in figure

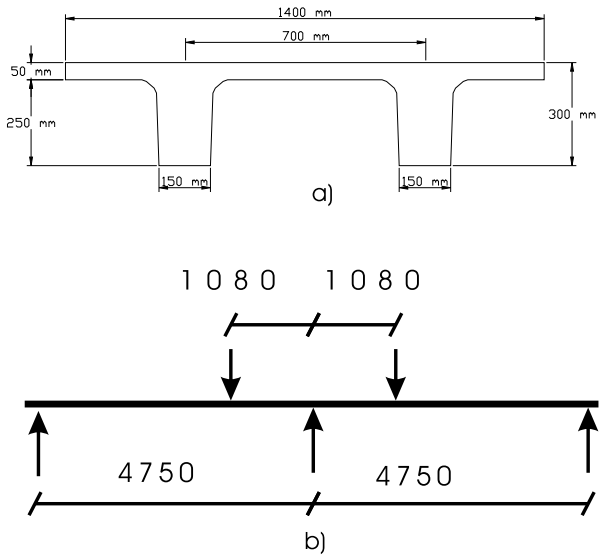

Figure 6.56: One way slab test setup.

6.58. The actual material properties of the beams were obtained by means of characterization tests. The mean values are summarized in table 6.10.

Table 6.10: Material properties for one-way slabs.

	Type 1: 200mm truss	Type 2: 225mm truss
f_c	35.1MPa	35.1MPa
f_t	3.47MPa	3.47MPa
f_y (Truss steel)	809MPa	778MPa
f_y (Long. steel)	588MPa	661MPa

In figure 6.59 a comparison between the experimental and numerical results are shown for both types of beams in the form of total shear (for the two ribs element) against strains in inclined bars of the truss reinforcements. Relatively high dispersions exist on the measured strains for the same applied shear force. In figure 6.59 it is only shown the mean, the maximum and minimum experimental truss strains together with the prediction of the

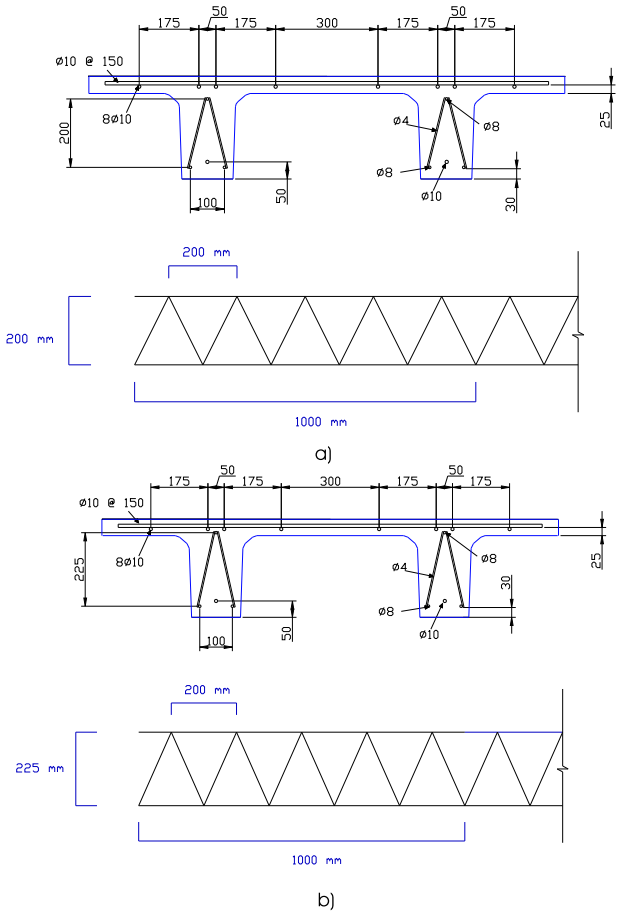

Figure 6.57: One way slabs cross-sections. a) Type 1 beam, b) Type 2 beam.

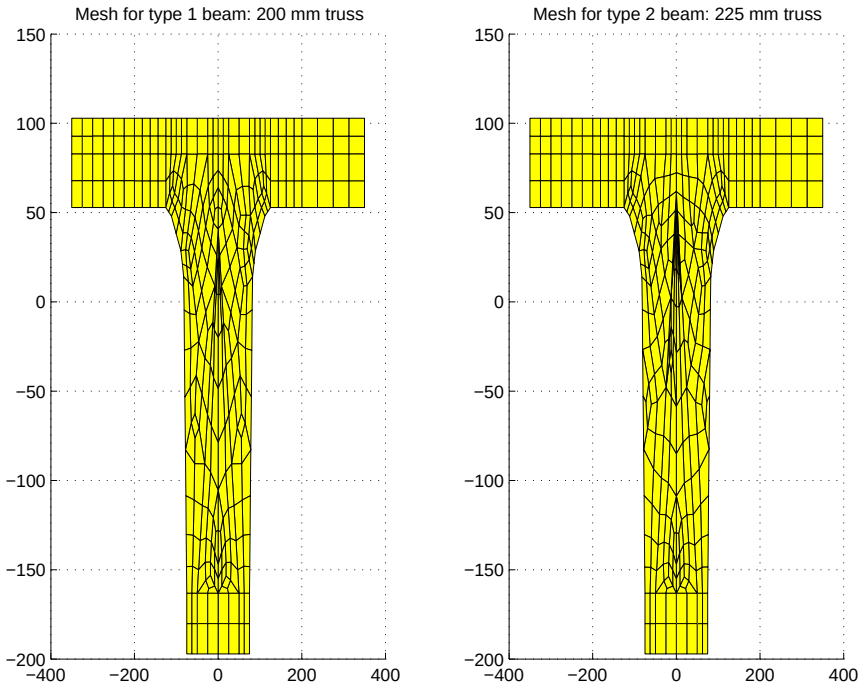

Figure 6.58: One way slabs cross-section mesh. a) Type 1 beam, b) Type 2 beam.

proposed model.

This dispersion can be attributed to the fact that, because of the geometry of the steel truss used as shear reinforcements, spacing of each truss branch is unusually large. Thus cracking occurs in a rather discrete fashion with large spacing and widths. Therefore, if a truss branch is crossed by a crack it will be considerably more loaded than another branch. The expected variability of cracking patterns and concrete tension behaviour justifies the observed dispersion.

The constitutive model used in this analysis (section 5.4) is based under the assumption that cracked concrete can be simulated as new material were cracking is a continuum material property. Therefore, cracking is considered *smeared* instead of discrete. Although patterns characterized by few and wide cracks, as the one obtained in this experiment, are not strictly consistent with this material hypotheses, the model presented good agreement with the average observed behaviour, see figures 6.59.a and 6.59.b.

In figure 6.60 views of the two distort sections and the normal stress field are shown for a load step close to failure. The vertical shear stress fields corresponding to this stage are shown in figure 6.61.

It is remarkable that the shallow truss produces a more uniform shear stress distribution, being more effective than the tall one. This effect can also be seen in figures 6.62 and 6.63 where cuts on the vertical shear distribution in the web and flange have been plotted together with the horizontal shear distribution on the flange. In spite of the large spacing of the transverse reinforcemet, their influence can be appreciated.

The estimation of the values of stresses in the inclined truss branches are plotted in figure 6.64. The left branch corresponds to the truss member with positive inclination with respect to the element axis, hence it is loaded with negative stresses under the applied load. The branch on the right is representing the elements with negative inclination, therefore loaded with positive stresses.

As the shallow-truss beam, type 1, branch inclination is closer to the theo-

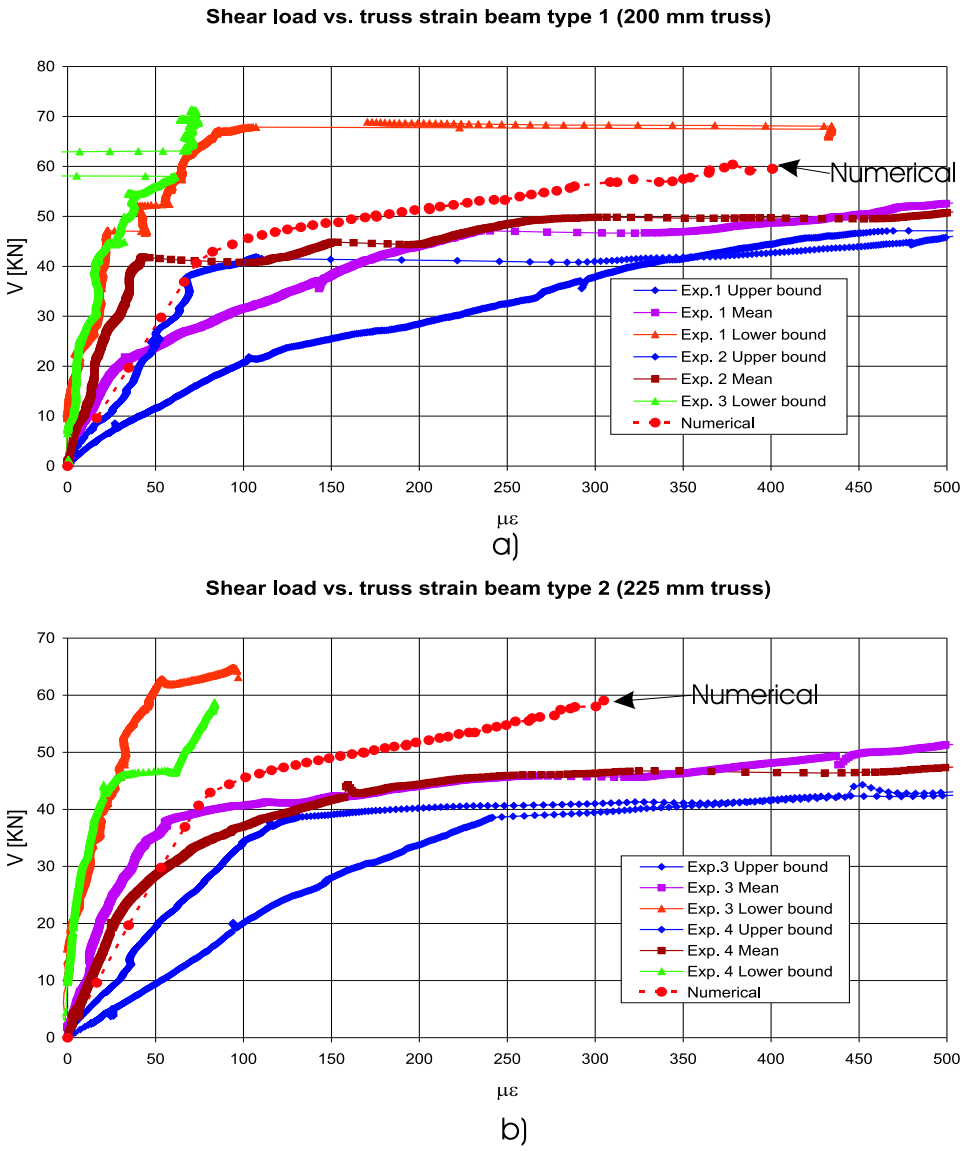

Figure 6.59: Shear force - truss strain curves. a) Type 1 beam, b) Type 2 beam.

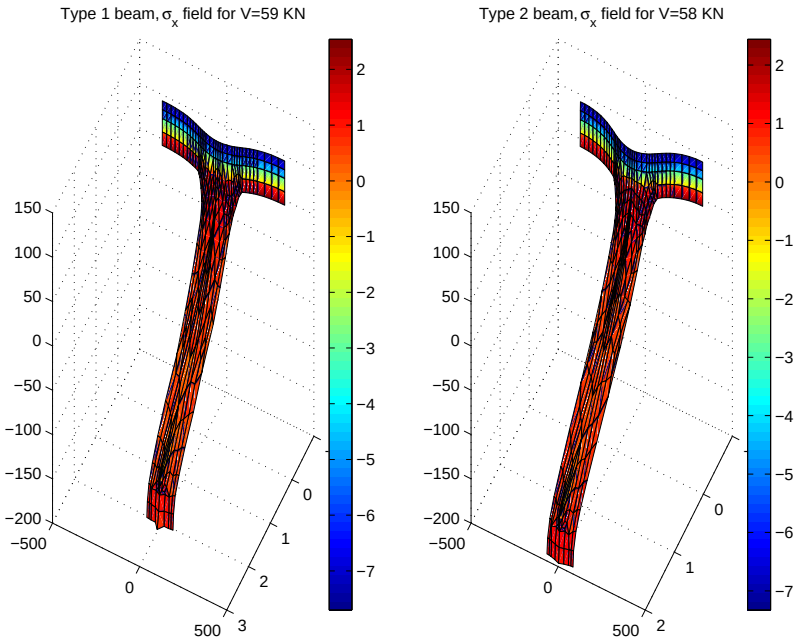

Figure 6.60: Normal stress field (σ_x) and warping. a) Type 1 beam, b) Type 2 beam.

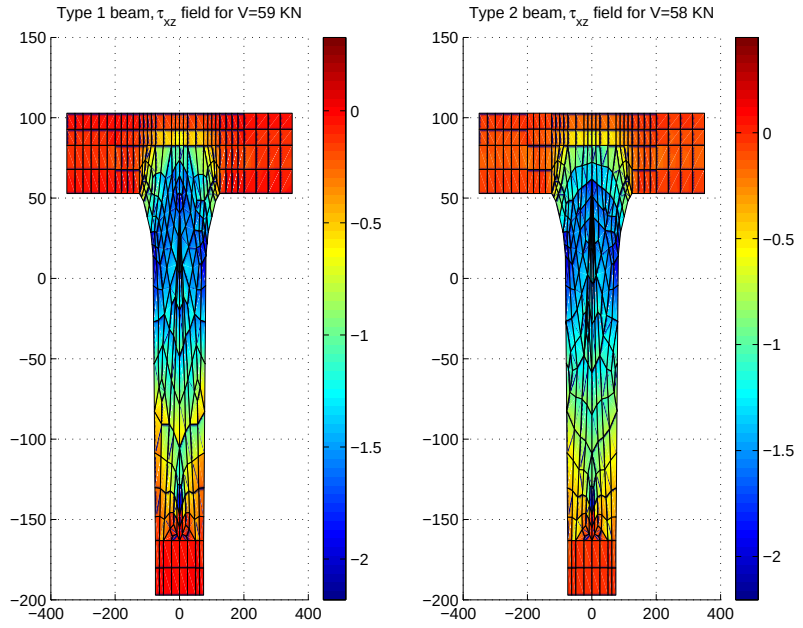

Figure 6.61: Vertical shear stress field (τ_{xz}). a) Type 1 beam, b) Type 2 beam.

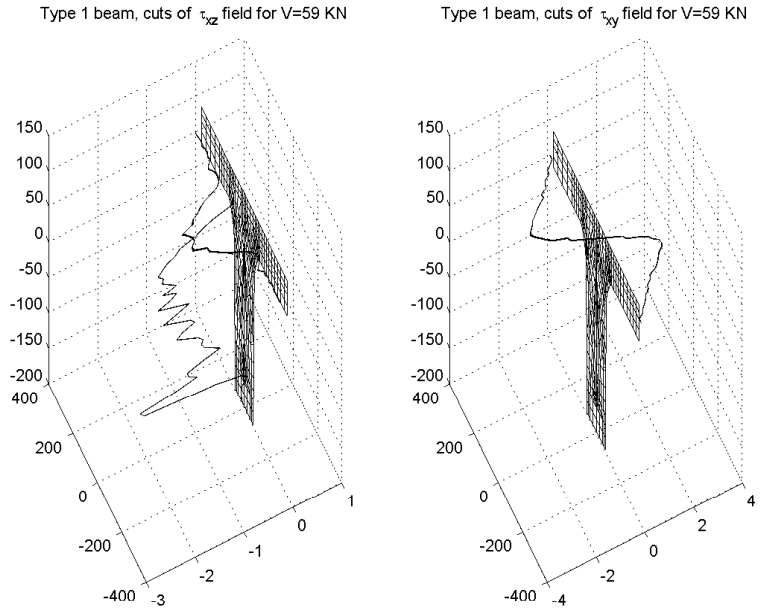

Figure 6.62: Cuts on shear stress field for type 1 beam. a) Vertical shear stress (τ_{xz}), b) Horizontal shear stress (τ_{xy})

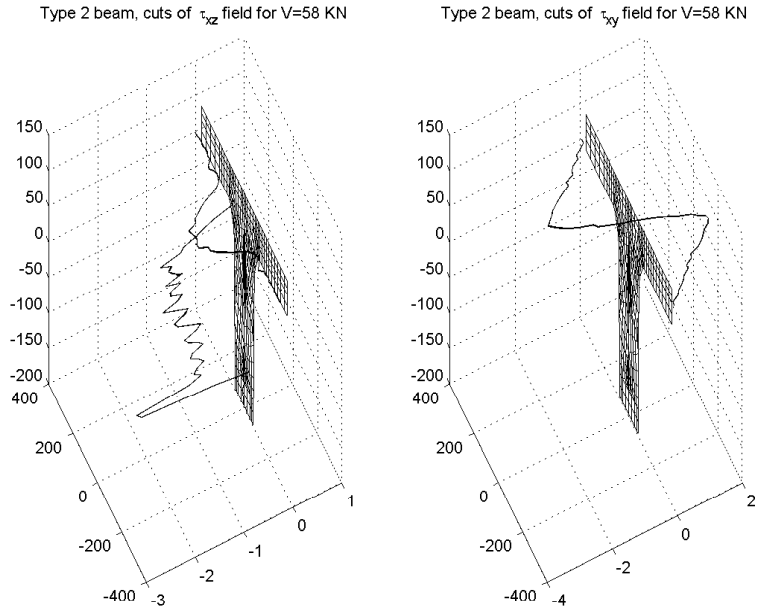

Figure 6.63: Cuts on shear stress field for type 2 beam. a) Vertical shear stress (τ_{xz}), b) Horizontal shear stress (τ_{xy})

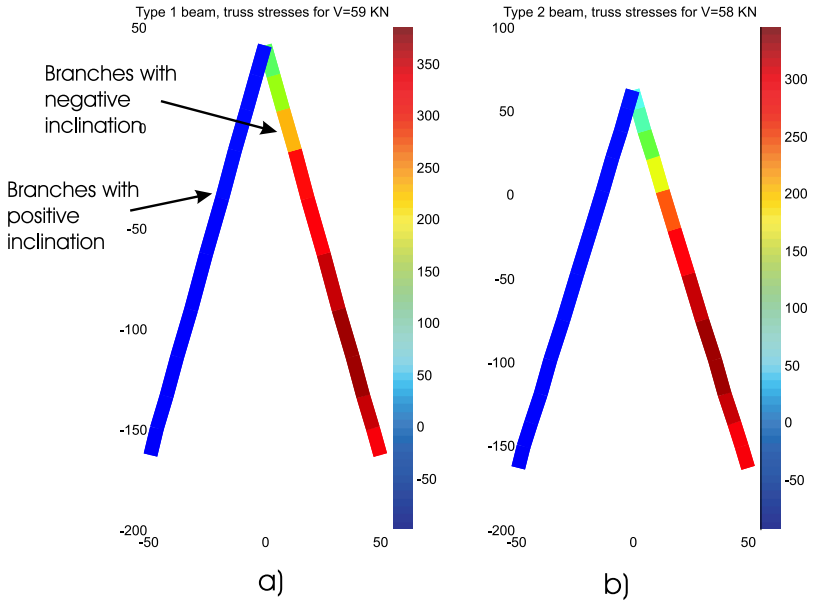

Figure 6.64: Stresses in truss reinforcement. a) Type 1 beam, b) Type 2 beam.

retical optimum direction of 45 °, higher levels of stress can be seen in figure 6.64.a with respect to figure 6.64.b.

Chapter 7

Conclusions

7.1 Global results

The main objective of this thesis is to extend the fiber-like cross-section analysis of frame elements so that it is able of capture the coupling effects between the six possible stress resultants under 3D loading: normal force, biaxial shear force, torsion and biaxial bending moment. In addition, the resulting methodology must be applicable to the non-linear analysis of reinforced concrete elements of any cross-section shape and reinforcement arrangement. These requirements introduce important difficulties compared to the bidimensional shear-bending interaction analysis or trhee-dimensional coupling under bending and axial load as were highlighted in section 1.1 of this thesis.

At the ending of this research, it is considered that both general and specific objectives stated in section 1.2 were achived with the desired generality, thoroughness and formality.

The global results of this research can be summarized in the following:

1. A generalized cross-section formulation, valid for any material behaviour and capable of reproducing the coupling effects, under any combination of internal forces, without renouncing to a bidimensional sec-

tional domain.

2. The implementation of the proposed formulation in a finite element scheme and the development of a computer program for non-linear structural analysis that contains the proposed cross-section model.

3. A series of constitutive material models, particularly a 3D non-linear constitutive model for cracked concrete capable of non-linear Poisson deformation, confinement enhancement, cyclic loading and prepared for non-mechanical strain offsets.

4. A series of investigations on the detailed coupled behaviour RC sections under different combinations of normal and tangential loadings, thus contributing to the understanding of the resistance mechanism of reinforced concrete and cross-section mechanics.

7.2 General conclusions

The general conclusions derived from this research are the following:

1. By means of the adequate cross-section kinematics, three-dimensional and local stress states can be reproduced in the scope of a cross-section analysis in the 2D domain. This is valid for any material, section's geometry and load combination.

2. A variational formulation was proposed that complements the standard set of beam equilibrium equation and enhances the solution obtained from a frame analysis to 3D equilibrium. It can be used to express the sectional warping-distortion kinematics as a function of the beam genaralized strains.

3. The developed model assures internal fiber equilibrium under 3D loading. The equilibrium is evaluated locally using a single cross-section in a differential form (no dual-sectional analysis is required). As a result the sectional model is independent of any frame element formulation and only required input are generalized strains at a single point.

4. For complex materials, such as cracked RC concrete, local stress distributions and coupling effects between concrete matrix, transverse and longitudinal reinforcements can be propertly captured at the sectional analysis level.

In summary, it can be stated that combining a one-dimensional structural model (by means of beam-column elements), the proposed two-dimensional model of the cross-section and a three-dimensional constitutive equation, it is possible to reproduce three-dimensional phenomena without need of 3D solid discretization of the geometry.

The specific conclusions obtained from the different stages of this research are described in the next section.

7.3 Specific conclusions

7.3.1 Integration of the response of RC sections under coupled 3D loading

1. Constitutive models of the smeared-cracks type are a feasible approach to take into account the directional response of cracked concrete under combined normal-tangential loading in a cross-section analysis.

2. Unlike to the distribution of normal strains, which is well characterized by the plane-section hypothesis, the distribution of tangential and out-of-plane strains and stresses depend on the section's shape and material response. In the case of reinforced concrete sections, these patterns vary with the evolution of concrete damage and reinforcement yielding.

3. When constituent materials present anisotropic response, inter-fiber equilibrium can not be satisfied without considering the section's distortion.

4. Shear and torsion resistance mechanisms of cracked reinfoced concrete sections with transverse reinforcements are possible because the sec-

tion's shape distorts. Therefore, a correct distortion kinematics is essential for a rational evaluation of the bearing mechanims in all loading range.

5. The proposed formulation is based on a consistent decomposition of the full 3D equilibrium problem into the beam equilibrium problem ("*equilibrium at the structural level*") and a complementary orthogonal solution ("*equilibrium at the sectional level*") to account for the inter-fiber equilibrium problem lost in beam problem. The complementary problem is solved within the cross-section domain, by means of static condensation it is posed as a function of the structural level problem. Therefore, the sectional model does not requires additional input variables.

6. A sectional stiffness matrix was derived based on the proposed formulation. It reflects the internal forces coupling effects observed in cracked-concrete elements consistently with the principles of mechanics (energy conservation, internal equilibrium and compatitibility). In general, the matrix has terms outside of the principal diagonal for any degree of freedom, depending on the anisotropic material arrangement or crack pattern in the case of RC. If the constitutive relation used produces a symmetric constitutive matrix, the sectional stiffness matrix will also be symmetric.

7.3.2 Implemented constitutive models

1. A concrete material model was implemented in order to realistically simulate its three-dimensional behaviour considering cyclic loadings. It presents stiffness degradation (damage-like) in tension and residual strains (plastic-like) in compression. Full three-dimensional non-linear behaviour is achieved by means of a non-linear Poisson coefficients and a three-dimensional failure surface. Effects of the concrete strength is taken into account in the compression backbone stress-strain curve.

2. Response directionality can be traced during general loading by means of non-isotropic damage and plastic strain tensors. The former allows

to store the tensile stiffness degradation in all directions in a compact form. In the same manner, the residual compression strains are stored in all diretions by means of the plastic strain tensor.

3. All developed materials model allow for elastic offset strains, therefore creep, shrinkage and other non-stress related deformations as well as prestrains can be further implemented.

4. Concrete and steel constitutive models were tested under single-point stress-strain loading combinations obtaining good agreement with the expected phenomenological responses.

7.3.3 Case studies

1. A series of case studies were carried out and presented in chapter 6. The model was employed to simulate theoretical and experimental case studies of different combinations of tangential and normal forces. The results were in good agreement with the known theoretical response and the experimental observations.

2. The model was proveed capable of automatically reproduce some effects that other sectional formulations would require additional hypotheses to approximately do so. This is the case of local and free-edge effects in composite laminates, evolution of confinement and cover spalling under axial loading, cracked torsion stiffness and the correct shear flow pattern under cracked torsion and shear considering the reinforcements arrangement.

3. The importance of shear deformation on the displacement of a RC frame element is variable under non-linear loading. Particularly, it was shown that for slender RC elements, with small shear deformation contribution in the elastic analysis, after cracking it can increase up to non-neglectable values (exceeding 10% for the case studied).

4. Under inclined cracking, a component of the diagonal compression field is present in the distribution of normal stresses in the tensile zone. This effect can be beneficial to the bending stiffness.

5. High concomitant shear forces reduce the secant bending stiffness, ductility, ultimate and yielding bending moments. However, hardening tends to increase.

6. In the same way that tangential forces affect the stresses at the longitudinal reinforcements under inclined crack patterns, normal forces and bending moments influence the stresses at the transverse reinforcements. This effect was reproduced by the proposed model.

7. Experimentally obtained bending-torsion interaction diagrams were reproduced with good accuracy, both for underreinforced and overreinforced elements. For the rectangular sections studied, it was shown that up to about 40% or 60% of the ultimate bending moment, torsion resistance is essentially the same as for pure torsion. After this point torsion resistance decreases to zero for the ultimate bending moment.

8. As shown in the case study of the ribbed-slab with truss-like transverse reinfocements (section 6.3.4), very large spacing of transverse reinforcements results in rather discreate cracking patterns and considerably dispersed strains in such bars. These types of arrangements are not consistent with the sectional analysis concept. However, the predicted response of the transverse reinforcements was a mean value of the experimental observation.

7.4 Recomendations for future studies

The present research work has opened many possibilities for future studies, both under the theoretical and practical viewpoints, some of these are summarized in the following:

- To study the overall non-linear response of complete frame structural systems considering the influence of strong tangential internal forces. Particularlly, the seismic response of concrete structures and other cyclic actions producing high tangential internal forces are of interest.

- To study the behaviour of repaired structures and the use of composite materials in strengthening of frame elements. The role of coupled shear and torsion internal forces in the developement of secondary failure modes and the overall ductility can be investigated.

- To study the behaviour of structures made mainly of composite materials considering local stresses effects that traditional sectional analysis are not capable of reproducing.

- To study the confinement of hollow-core and complex shaped sections, usually used as columns and bridge piers.

- To investigate the confinement of high-strength concrete elements.

- To develop simplified rational models for shear and torsion resistance accounting for irregular section's shapes. In particular, the case of variable section's width in the shear resistance should be considered.

- To develop simplified and rational proceedures to evaluate the shear-torsion bearing mechanism of sequentially constructed concrete elements with more than one type of concrete.

- To enhance the sectional model to consider reinforcements bond-slip by means of a rational scheme, similar to the one used in this thesis to include tangential generalized stresses. Furhter, the influence of this phenomenon on the sectional response under tangential forces can be studied, specially on the post-yielded state.

- To include the variation of warping and distortion with respect to the frame element's axis. This will allow to simulate higher order effects such as shear-lag and warping-torsion.

- To develop a "*D-region*" element to simulate the non-linear response of joints and the effect of point loads in the scope of frame element analysis.

References

AASHTO (2001). "*AASHTO LRFD Bridge Design Specifications*". American Association of State Highway and Transportation, Ed. 1998 (2001 Interin Revisions).

Abbas S., Scordelis, A. C. (1993). "*Nonlinear geometric, material and time-dependent analysis of segmentally erected three-dimensional cable stay bridges*", Report UCB/SEMM-93/09. University of California, Berkeley.

ACI-318 (1999). "*ACI Building Code Requirements for Reinforced Concrete*". American Concrete Institute, Detroit.

ASCE-ACI Committee 445 (1998). "Recent approaches to shear design of structural concrete". *ASCE J. of Structural Eng.*, Vol. 124, No. 12, 1375-1417.

Auricchio, F., Sacco, E. (1999). "Partial-mixed formulation and refined models for the analysis of composite laminates within a FSDT". *Composite Structures*. Vol 46, 103-113.

Auricchio, F., Sacco, E. (2003). "Refined first-order shear deformation theory models for composite laminates". *ASME J. Applied Mechanics*. Vol 70, 381-390.

Bažant, Z. P, (1983). "Comment on orthotropic models for concrete and

geomaterials". *ASCE J. of Structural Eng.*, Vol. 109, No. 3, 849-865.

Bažant, Z. P., Oh, B. H. (1983). "Crack band theory for fracture of concrete". *Mat. and Structures*, Vol. 93, 16(93), 155-177.

Bažant, Z. P., Prat, P. C. (1988). "Microplane model for brittle-plastic material: I. Theory". *ASCE J. Eng. Mechanics*, Vol. 114, No. 10, 1672-1688.

Backlund, J. (1976). "Large deflection analysis of elasto-platic beams and frames". *Int. J. Mechanical Science*, Vol. 18, 269-277.

Bairan, J. M. (1999). "*Efectos de segundo orden y no-linealidad en soportes de hormigón armado (Non-linear and second order effects on reinforced concrete piers)*", Master Thesis, University of Cantabria, Cantabria.

Bairan, J. M., Mari, A. R. (2004). "Non-linear interaction of normal and tangential internal forces on 3D RC beam-column structural systems". *13th World Conference on Earthquake Engineering*, Vancouver, paper No. 840.

Balan, T., Filippou, F.C., Popov, E. (1997). "Constitutive model for 3D cyclic analysis of concrete structures". *ASCE J. of Structural Eng.*, Vol. 123, No. 12, 143-153.

Barbero, E. J. (1998). "*Introduction to composite materials design*". Taylor & Francis, London, pp. 336.

Barbero, E. J. (1992). "3-D Finite element for laminated composites with 2-D kinematics constraints". *Computers & Structures*, Vol. 45, pp. 263-271.

Baron, F. (1961). "Matrix analysis of structures curved in space". *ASCE J. of Structural Division*, Vol. 87, 17-38.

Bathe, K.-J. (1996). "*Finite element procedures*". Prentice-Hall, Inc., New

Jersey, pp. 1037.

Belarbi, A., Hsu, T. T. (1994). "Constitutive laws of concrete in tension and reinforcing bars stiffened by concrete". *ACI Structural J.*, Vol. 91, No. 4, 465-474.

Belarbi, A., Hsu, T. T. (1995). "Constitutive laws of softened concrete in biaxial tension-compression". *ACI Structural J.*, Vol. 92, No. 5, 562-573.

Belletti, B., Cerioni, R., Iori, I. (2001). "Physical approach for reinforced-concrete (PARC) membrane elements". *ASCE J. of Structural Eng.*, Vol. 127, No. 12, 1412-1426.

Belytschko, T., Liu, W. K., Moran, B. (2001). "*Nonlinear finite elements for continua and structures*". John Wiley & Sons, LTD, Chichester, pp. 650.

Bentz, E. (2000). "*Sectional analysis of reinforced concrete members*", Doctoral Thesis, University of Toronto, Toronto, pp. 184.

Bentz, E.C. (2005). "Explaining the riddle of tension stiffening models for shear panel experiments". *ASCE J. of Structural Eng.*, Vol. 131, No. 9, 1422-1425.

Bigaj, A. J. (1999). "*Structural dependence of rotation capacity of plastic hinges in RC beams and slabs*", Doctoral Thesis, Technical University of Delft, Delft, pp. 230.

Buckle, I. G., Jackson, A. T. (1981). "*A filamented beam element for the nonlinear analysis of reinforced concrete shells with edge beams*". University of Auckland, New Zeland.

Carol, I. and Murcia, J. (1989). "Nonlinear time-dependent analysis of planar frames using and *exact* formulation - I Theory". *Computers and Structures*, Vol .33, No. 1, 79-87.

Carol, I., Bažant, Z. P., Pract, P. C. (1990). "*New explicit microplane model for concrete: theoretical aspects and unified implementation for constitutive verification and F. E. Analysis*". Report No. GT015/1990, School of Civil Eng., Universitat Politècnica de Catalunya, Barcelona, pp. 29.

Carrascon, S., Mari, A. R., Carol, I. (1987). "*Analisis instantáneo y diferido de puentes curvos de hormigón armado y pretensado (Instantaneous and time-dependent analysis of reinforced and prestresses concrete curve bridges)*". Publication ES-015, Depart. of Construction Eng., Universitat Politècnica de Catalunya, Barcelona.

Carrera, E. (1999). "Multilayered shell theories accounting for a layer-wise mixed description. Part I: Governing equations". *AIAA J.*, Vol. 37, pp. 1117-1124.

CEB (1996). "*RC elements under cyclic loading: State of the art report*", Comité Euro-International du Béton, Bulletin d'indormation 230, Thomas Telford, London, pp. 190.

Cervenka, V. (1985). "Constitutive model for cracked reinforced concrete". *ACI Journal*, Vol. 82, No. 6, 877-882.

Cesnick, C. E. S., Hodges, D. H. (1994). "Variational-Asymptotical Analysis of Initially Twisted and Curved Composite Beams". *Int. J. for Eng. Analysis and Design*, Vol. 1, No. 2, 177-187.

Chan, E. C.-Y. (1983). "*Nonlinear geometric, material and time dependent analysis of reinforced concrete shells with edge beams*", Doctoral Thesis, University of California, Berkeley, pp. 361.

Chen, W. F. (1982). "*Plasticity in reinforced concrete*", McGarw Hill Book Co., Inc., New York, pp. 474.

Cladera, A. (2002). "'*Shear design of reinforced high-strength concrete beams*", Doctoral Thesis, Universitat Politècnica de Catalunya, Barcelona, pp. 168.

Cobo, D., Burgueño, R., Seible, F., Marí, A. R. (2000). "Use of advanced composite materials in the design of a cable stay brigde". *Hormigón y Acero*, No. 216, 2nd trimester. Spain.

Collins and Lampert (1972). "Redistribution of moments at cracking - the key to simpler torsion design". *Analysis of Structural Systems for Torsion*, ACI Publication SP-35, American Concrete Institute, Detroit, 343-383.

Collins, M. P., Mitchell, D. (1987). "*Prestressed concrete basics*". Canadian Prestressed Concrete Institute.

Collins, M. P., Porasz, A. (1989). "*Shear design for high-strength concrete*". Comité Euro-International du Béton, Bulletin d'Information, No. 193, 77-83.

Crisfield, M. A. (1991). "*Non-linear finite element analysis of solids and structures. Volume 1: Essentials*". John Wiley & Sons, LTD, Chichester, pp. 345.

Crisfield, M. A. (1998). "*Non-linear finite element analysis of solids and structures. Volume 2: Advanced topics*". John Wiley & Sons, LTD, Chichester, pp. 494.

Cruz, P. J. S., Marí, A. R., Roca, P. (1998). "Nonlinear time-dependent analysis of segmentally constructed structures". *ASCE J. of Structural Eng.*, Vol. 124, No. 3, 278-287.

Debernardi, P. G., Taliano., M. (2002). "On evaluation of rotation capacity for reinforced concrete beams". *ACI Structural J.*, Vol. 99, No. 3, 360-368.

EHE (1999). "*Instrucción de hormigón estructural (Structural concrete code*

requirements)". Ministerio de Fomento, Madrid, pp. 470.

Elwi, A. A., Murray, D. W. (1979). "A 3D hypoelastic concrete constitutive relationship". *ASCE J. Eng. Mechanics Division*, Vol. 105, No. 4, 623-641.

Fam A., Musiker D., Kowalsky M.J., and Rizkalla S. (2002). "In-Plane Testing of a Damaged Masonry Wall Repaired with FRP", *Advanced Composite Letters*, Vol. 11, No. 6.

Ghali, A., Elbadry, M. M. (1985). "User's manual and computer program CPF: Cracked plane frames in prestressed concrete". Department of Civil Engineering, The University of Calgary, Research Report CE 85-2, Calgary.

Grelat, A. (1978). "Comportament non linéaire et stabilité des ossatures en béton armé". *Annales de l'Inst. Tech. du Batiment et des Travaux Publics*. Vol. 111, No. 1, 19-36.

Hsu, T. T. (1984). "*Torsion of reinforced concrete*". Van No.strand Reinhold. New York, pp. 515.

Jefferson, A. (2000). "Anisotropic damage model derived from random fibre network". *European congress on Computational Methods in Applied Sciences and Engineering, ECCOMAS 2000*. Barcelona.

Kang, Y. I., Scordelis, A. C. (1980). "Nonlinear analysis of prestressed concrete frames". *ASCE J. of Structural Division*, Vol. 106, 445-462.

Kang, Y. I., Scordelis, A. C. (1990). "Non-linear segmental analysis of reinforced and prestressed concrete bridges". *3rd. International conference on short and medium span bridges*, Toronto, 229-240.

Kani, M. (1977). "*An experimental investigation of reinforced and prestressed beams in shear*", Master Thesis, University of Toronto, Toronto.

Ketchum, M. A. (1986). "*Redistribution of stresses in segmentally erected prestressed concrete bridges*", Report UCB-SESM 86/07. University of califonia, Berkeley.

Kupfer, H. B., Hilsdorf, H. K., Rüsch, H. (1969). "Behavior of concrete under biaxial stresses". *J. ACI*, Vol. 66, No. 8, 656-666.

Lampert, P. (1972). "Postcracking stiffness of reinforced concrete beams in torsion and bending". *Analysis of Structural Systems for Torsion*, ACI Publication SP-35, American Concrete Institute, Detroit, 384-432.

Lopez, A. (1987). "*Estudio de la evolución hasta la rotura de tableros continuos de puentes de hormigón pretensado de planta curva o esviada (Study on the evolution till failure of the structural behaviour of curved or skew continuous prestressed concrete bridge decks.)*". Doctoral Thesis, Universitat Politècnica de Catalunya, Barcelona.

Luccioni, B., Oller, S. (2003). "A directional damage model". *Comp. Methods in App. Mechanical Eng.*, 1119-1145.

Mander, J. B., Priestley, M. J. N., Park, R. (1988). "Theoretical stress-strain model for confined concrete". *ASCE J. of Structural Eng.*, Vol. 114, No. 8, 1804-1825.

Mansour, M., Lee, J.-Y., Hsu, T. T. (2001). "Cyclic stress-strain curves of concrete and steel in membrane elements". *ASCE J. of Structural Eng.*, Vol. 127, No. 12, 1402-1411.

Mari, A. R. (1984). "*Nonlinear geometric, material and time dependent analysis of three-dimensional reinforced and prestressed concrete frames*", Report No. UCB/SESM-84/12, University of California, Berkeley, pp. 142.

Mari, A. R. (2000). "Numerical simulation of the segmental construction

of three dimensional concrete frames". *Eng. Structures*, Vol. 22, No. 6, 585-596.

Mari, A., Perez, G., Viladomat, G., De la Torre, M. (2005). "Resistencia a cortante de forjados unidireccionales construidos in situ con armadura básica en celosia (Shear strength of one-way slabs built in-situ with truss-like basic transverse reinforcements)". *III Congreso de ACHE de puentes y estructuras* (*in press*), Zaragoza.

Mazars, J. (1982). "Mechanical damage and fracture of concrete structures". *Advances in fracture research*, Vol. 4, Pergamon press, Oxford, pp. 1499-1506.

Mitchell, D., Collins, M. P. (1974). "Diagonal compression field theory - A rational model for structural concrete in pure torsion". *Journal of American Concrete Institute*, Vol. 71, 396-408.

Molins, C. (1996). "*Un modelo para el analisis del comportamiento resistente de construcciones de obra de fabrica (A model for the strength analysis of masonry structures)*", Doctoral Thesis, Universitat Politècnica de Catalunya, Barcelona, pp. 268.

Molins, C., Roca, P., Barbat, A. H. (1995). "Una formulacion matricial generalizada. Parte 2: Análisis dinámico (A generalized matrix formulation. Part 2: Dynamic analysis)". *Revista internacional de métodos numéricos para cálculo y diseño en ingeniería*, Vol. 11, No. 1, 23-36.

Molins, C., Roca, P., Mari, A. R. (1995). "One dimensional elements for the static and dynamic analysis of historic spatial structures". *Spatial Structures: Heritage, Present and Future*, SGEditorial, 1245-1252, Padua.

Montoya, E., Vecchio, F. J., Sheikh, S. A. (2001). "Compression field modeling of confined concrete". *Structural Engineering and Mechanics*, Vol. 12, No. 3, 231-248.

Moreno R., Bairan J. M., Pujades L., Aparicio A. and Barbat A. (2004). *"Probabilistic assessment of the seismic behaviour of reinforced concrete framed buildings"*, *Hormigón y Acero*, Vol. 232, 2nd trimester, pp. 125-136.

Murcia, J., Herkenhoffm L. (1994). "Time dependent analysis of continuous bridges composed by precast elements". *Hormigón y Acero.* Vol. 192, 55-71.

Nettles, A. T. (1994). "*Basic mechanics of laminated composite plates*". NASA Reference Publication 1351, Marshall Space Flight Center, Alabama, pp. 102.

Oller, E., Cobo, D., Mari, A. R. (2004). "Flexural srengthening of RC beams using composite materials. End anchorage study", *Hormigón y Acero*, No. 232, 2nd trimester, Spain.

Oller, S. (Ed.) (2002) "*Analisis y calculo de estructuras de materiales compuestos (Analysis and computation of composite materials structures)*". Cimne, Barcelona, pp. 576.

Onsongo, W. M. (1978). "*The diagonal compression field theory for reinforced concrete beams subjected to combined torsion, flexure and axial load*", Doctoral Thesis, University of Toronto, Toronto, pp. 246.

Palermo, D., Vecchio, F. J. (2003). "Compression field modeling of reinforced concrete subjected to reversed loading: Formulation". *ACI Structural J.*, Vol. 100, No. 5, 616-625.

Pang, X.-B., Hsu, T. T. (1995). "Behaviour of reinforced concrete membrane elements in shear". *ACI Structural J.*, Vol. 92, No. 6, 665-679.

Pang, X.-B., Hsu, T. T. (1996). "Fixed-angle softened truss model for reinforced concrete". *ACI Structural J.*, Vol. 93, No. 2, 197-207.

Park, R., Paulay, T. (1994). "*Estructuras de concrete reforzado (Reinforced concrete structures)*". Ed. Limusa, Mexico, pp.796.

Paulay, T., Priestley, M. J. N. (1992). "*Seismic design of reinforced concrete and masonry buildings*". Wiley, New York, pp. 768.

Petrangeli, M., Ozbolt, J. (1996). "Smeared crack approaches-material modeling". *ASCE J. of Eng. Mechanics*, Vol. 122, No. 6, 545-554.

Petrangeli, M., Pinto, P. E., Ciampi, V. (1999). "Fiber element for cyclic bending and shear of RC structures. I: Theory". *ASCE J. Eng. Mechanics*, Vol. 125, No. 9, 994-1009.

Priestley, M. J. N., Seible, F. and Calvi, G.M. (1996). "*Seismic Design and Retrofit of Bridges*", John Wiley & Sons, Inc. New York.

Rahal, K. N., Collins, M. P. (2003). "Combined torsion and bending in reinforced and prestressed concrete beams". *ACI Structural J.*, Vol. 100, No. 2, 157-165.

Rahal, K. N., Collins, M. P. (1994). "Analysis of sections subjected to combined shear and torsion - A theoretical model". *ACI Structural J.*, Vol. 92, No. 4, 459-469.

Ranzo, G. (2000). "*Experimental and numerical studies on the seismic performance of beam-column RC structural members subjected to high shear*", Doctoral Thesis, University of Rome "'La Sapienza", Rome, pp.238.

Recupero, A., D'Aveni, A., Ghersi, A. (2003). "N-M-V interaction domains for box and I-shaped reinforced concrete members". *ASCE J. of Structural Eng.*, Vol. 100, No. 1, 113-119.

Recupero, A., D'Aveni, A., Ghersi, A. (2005). "Bending moment-shear force

interaction domains for prestessed concrete beams". *ASCE J. of Structural Eng.*, Vol. 131, No. 9, 1413-1421.

Reddy, J. N. (1996). "*Mechanics of laminated composite plates*". CRC Press, Boca Raton, FL., pp. 800.

Reddy, J.N. (1997). "On locking-free shear deformable beam finite elements". *Comput. Methods App. Mech. Eng.*, Vol. 149, 113-132.

Saouridis, C. Mazars, J. (1992). "Prediction of the failure ans size effect in concrete via a bi-scale damage approach". *Eng. Comp.*, Vol.9, 329-344.

Selby, R. G., Vecchio, F. J. (1997). "A constitutive model for analysis of reinforced concrete solids". *Canadian Journal of Civil Engineering*, Vol. 24, 460-470.

Simo, J. C., Ju, J. W., Pister, K. S., Taylor, R. L. (1988). "Assesment of cap model: consistent return algorithms and rate-depedent extension". *ASCE J. Eng. Mechanics*, Vol. 114, 191-218.

Sobrino, J. A., Pulido, M. D. G. (2002). "Towards advanced composite material footbridges". *Structural Eng. International*, SEI 2/2002, May, 2002.

Spacone, E., Ciampi, V., Filippou, F. C. (1996). "Mixed formulation of No.nlinear beam finite element". *Computers & Structures*, Vol. 58, No. 1, pp.71-83.

Timoshenko, S. T., Goodier, J. N. (1972). "*Teoria de la elasticidad (Theory of elasticity)*". Ed. Urmo, Bilbao, pp. 549.

Ulm, F. J., Clement, J.L., Guggenberger, J. (1994). "Recent advances in 3-D nonlinear FE-analysis or R/C and P/C beam structures". *Proc. ASCE Structures Congress XII*, Atlanta (GA), New York, 427-1433.

Vecchio, F. J. (1992). "Finite element modeling of concrete expansion and confinement". *ASCE J. of Structural Eng.*, Vol. 118, No. 9, 2390-2406.

Vecchio, F. J. (1999). "Towards cyclic load modeling of reinforced concrete". *ACI Structural J.*, Vol. 96, No. 2, 132-202.

Vecchio, F. J. (2000). "Disturbed stress field model for reinforced concrete: Formulation". *ASCE J. of Structural Eng.*, Vol. 126, No. 9, 1070-1077.

Vecchio, F. J. (2001). "Disturbed stress field model for reinforced concrete: Implementation". *ASCE J. of Structural Eng.*, Vol. 127, No. 1, 12-20.

Vecchio, F. J., Collins, M. P. (1982). "*Response of reinforced concrete to in-plane shear and normal stresses*", Publication No. 82-03, Department of Civil Engineering, University of Toronto, pp. 332.

Vecchio, F. J., Collins, M. P. (1986). "The modified compression-field theory for reinforced concrete elements subjected to shear". *ACI Journal*, Vol. 83, No. 2, 1375-1417.

Vecchio, F. J., Collins, M. P. (1988). "Predicting the response of reinforced concrete beams subjected to shear using the modified compression field theory". *ACI Structural J.*, Vol. 85, No. 3, pp. 258-268.

Vecchio, F. J., Lai, P., Schim, W., Ng, J. (2001). "Disturbed stress field model for reinforced concrete: Implementation". *ASCE J. of Structural Eng.*, Vol. 127, No. 4, 350-358.

Vecchio, F. J., Selby, R. G. (1991). "Toward compression-field analysis of reinforced concrete solids". *ASCE J. of Structural Eng.*, Vol. 117, No. 6, 1740-1758.

Walraven, J. C. (1981). "Fundamental analysis of aggregate interlock".

ASCE J. of Structural Division., Vol. 108, 2254-2270.

Willam, K. J., Warnke, E. P. (1975). "Constitutive model for the triaxial behavior of concrete". *Proc. Int. Assn. for Bridge and Structural Eng.*, Vol. 19, 1-30.

Yu, W., Volovoi, V., Hodges, D., Hong, X. (2002). "Validation of the variational asymptotic beam sectional analysis (VABS)". *AIAA Journal*, Vol. 40, No. 10, 2105-2113.

Zhu, R., Hsu, T. T., Lee, J.-Y. (2002). "Rational shear modulus for smeared-crack analysis of reinforced concrete". *ACI Structural J.*, Vol. 98, No. 4, 443-450.